1 Introduction

Since its completion in 1989, the Beijing electron-positron collider (BEPC) and its detector, the Beijing Spectrometer (BES), have been in operation successfully for 13 years. There has been an upgrade in 1996 for both the machine (still called BEPC afterwards) and the detector (called BESII afterwards), leading to a significant improvement of performance. A variety of important physics results from J/ψ, ψ', τ, D and D_s data were obtained and more than 50 papers were published on world-class journals. Table 1-1 list all data collected at BESI and BESII.

Table 1-1 Data collected at BESI and BESII

	Ecm (GeV)	**Physics**	**Data**
BESI	3.1	J/ψ	7.8×10^6
	3.69	ψ(2S)	3.96×10^6
	4.03	τ	1.0×10^5
	4.03	Ds, D	$22.3pb^{-1}$
	~3.55 (m_τ scan)	m_τ	$5pb^{-1}$
BESII	2-5 (R scan)	R value	6+85 points
	3.1	J/ψ	5.8×10^7
	3.69	ψ(2S)	1.4×10^7
	3.77	ψ(3770)	~$20pb^{-1}$

The rich physics program of the BES experiment includes light hadron spectroscopy, charmonium spectrum, charm meson decay properties, QCD, tau physics, rare decays, search of glueball and other non-pure quark states, etc. These results played an important role towards our understanding of the Standard Model, and they are unique at the boundary between the perturbative and non-perturbative regime of QCD. Here we list a few major physics results in the last 13 years.

1) Precision measurement of the tau mass. The central value shifted by 3σ and the error was reduced by a factor of 10 with respect to previous measurements. This result removed doubt to the lepton universality at that time and proved that tau is indeed a normal lepton as described by the Standard Model.

2) Precision measurement of R values in 2-5 GeV region. This measurement reduced the previous error by a factor of 2-3, resulted in a prediction of higher Higgs mass, better compared with results from direct searches at LEP. It also reduced the error of QED prediction for g-2, provided a profound implication to the latest BNL

g-2 experiment.

3) Study of $\psi(2S)$ decays. Observed for the first time several new decay channels of $\psi(2S)$ and $\chi_{CJ,}$ such as $\psi(2S)\to\tau^+\tau^-$ and baryon-antibaryon pairs, etc.; Confirmed the vector-pseudoscalor suppression in $\psi(2S)$ to ρπ, $K^{*+}\overline{K}^-$ +c.c. decays and observed for the first time the vector-tensor suppression in decay channels ωf_2, ρa_2, $K^{*0}\overline{K_2}^{*,0}$+c.c. and $\phi f_2^{'}$. Observed a large isospin violation effect in decays $\rho\pi$, $\omega\pi^0$, $K^+\overline{K}^{*-}$ (892)+c.c., $K^0\overline{K}^{*0}$ (892)+c.c., etc.

4) Study of D and Ds decays. Observed for the first time the pure leptonic decays of D meson and measured branching ratios of D(Ds)→μν, the above branching ratios lead to the measurement of decay constants f_D and f_{Ds}; the model independent measurement of Ds→φπ.

5) Study of J/ψ decays. Many measurements were published from BESI data. With the world largest J/ψ data sample for BESII, more results are expected.

There are many other important measurements well received by the community and Table 1-2 lists our results referenced by the Particle Data Group.

Table 1-2 Results referenced by the particle data group

Particles	References
η (1440)	3
f_2 (1525)	2
f_0 (1710)	7
η_2 (1870)	2
f_2 (1950)	2
f_I (2220)	11
τ	2
$D^{\pm}$	2
D_s	5
η_c (1S)	1
J/ψ (1S)	33
χ_{c0} (1P)	13
χ_{c1}(1P)	8
χ_{c2} (1P)	12
ψ (2S)	12
ψ (3836)	1
Total	116

BEPCII is a high luminosity, multi-bunch collider, which requires a comparable high quality detector with the modern detector technology. On the one hand, the existing BESII detector is facing severe aging problems, and its electronics and data acquisition system do not support the multi-bunch mode; on the other hand, a factor of 100 increases of statistics requires a corresponding reduction of systematic errors. Therefore a modern detector, BESIII, has to be built to meet the following requirements:

1) Very good photon energy resolution, good angle resolution for photon measurement. Crystal calorimeter, such as CsI, is one of the best choice.

2) Accurate 4-momenta measurement of low momentum charged particles. A drift chamber based on He gas is one of the best choice.

3) Good hadron identification capabilities. Both Cherenkov detector and

Time-of-Flight system can meet our requirements.

4) A modern data acquisition system and the front-end electronics system based on the pipeline technique, which can accommodate multi-bunch mode.

The choice of the detector components is based on physics requirements, existing experience in the collaboration, budgetary and schedule constraints, etc. Fig.1-1 shows the schematics of the BESIII detector, which consists of the following components:

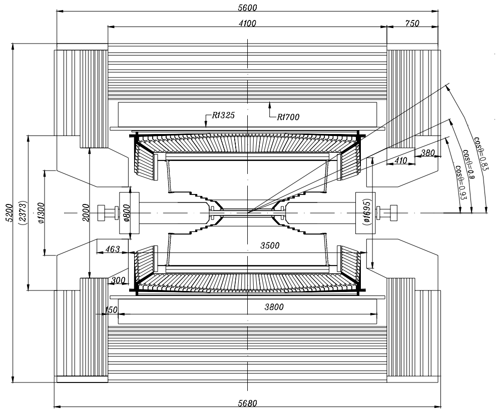

Fig.1-1 Schematic drawing of the BESIII detector

1) A He gas based drift chamber with a single wire resolution better than 130μm;

2) A CsI calorimeter with an energy resolution better than 2.5%@1 GeV;

3) A Time-of-Flight system with a time resolution better than 100 ps;

4) A super-conducting solenoid magnet with a field of 1.0 Tesla;

5) A RPC based muon chamber system.

Details of each sub-detector will be discussed in subsequent sections. Table 1-3 shows the comparison of the BESII and BESIII detector.

Table 1-3 Detector parameters comparison

Sub-system	**BESIII**	**BESII**
MDC	□ σ_{xy} = 130 μm	250 μm
	Δ P/P=0.5% @ 1GeV SC magnet	2.4%@1GeV
	□ $\sigma_{dE/dx}$= (6-7) %	8.5%
EM Calorimeter	□ ΔE/E = 2.5% @ 1 GeV □ σ_z = 0.6cm @ 1 GeV	20%@1GeV 3cm @ 1 GeV
TOF detector	σ_T(ps)=100 ps barrel 110 ps endcap	180 ps barrel 350 ps endcap
μ counters	9 layers	3 layers
Magnet	1.0 tesla	0.4 tesla

2 Physics Motivations

The success of the Standard model, especially of the electroweak interactions, has been proved by many of the precision measurements performed at LEP and other places. New physics are expected either at higher energies or from precision measurements at lower energies. The former was represented by currently running experiments at Tevatron and the constructing ones at LHC, while the latter is by those experiments at "factories", such as KLOE at the ϕ factory DA ϕ NE, and those at the B-factories at KEK and SLAC. The ϕ factory mainly studies the strange quark, and the B-factories are focused on the study of CP violation from the third generation quark, b quark. At the energy region in between, namely the τ -charm energy region, a high luminosity accelerator is still not realized although it is being proposed since 80's of the last century.

Another component of the standard model — quantum chromodynamics (QCD), has been tested extensively at the high momentum transfer by lots of high precision experiments, while at low energies, it is rather difficult to be tested due to its non-perturbative nature. In particular, gluonic matters like glueballs and hybrids, have not been predicted with a list of very clear distinctive properties, although they are a straight forward prediction of the non-abelian nature of the QCD theory. Lattice QCD (LQCD) starting from the first principle of QCD, can in principle get correct predictions for any strong process, but unfortunately, it is limited by the computing power and some other technical difficulties. It is expected that the LQCD calculation can approach a precision of a few percent in a few years, which will help the comparison between theoretic predictions and experimental results to a better situation. In the mean time, the reliability of the LQCD calculation should be checked and calibrated by high precision measurements. Charmed mesons, tau lepton and charmonium states exactly lie in the most important energy region where LQCD plays important roles, therefore experimental studies of these physics, which can be both measured and calculated in high precision, are extremely important in developing the QCD predictions based on LQCD.

The upgrade of BEPC/BESII, currently working at the tau-charm energy region, to BEPCII/BESIII with a peak luminosity of 10^{33}cm^{-2}s^{-1} at the $D\overline{D}$ threshold, will certainly supply the possibility of high precision measurements in the two physics areas mentioned above, and the outcome would help to develop particle physics substantially.

2.1 Study of Electroweak Interactions

The BESIII experiment working at the tau-charm energy region will test electroweak interactions with a very high precision in both quark and lepton sectors.

2.1.1 Precision Measurement of CKM Matrix Elements

Quarks coupling to the weak interacting intermediate bosons are not mass eigenstates. This phenomena results in a transition matrix between weak interaction eigenstates and quark mass eigenstates. This was first proposed by Cabibbo[1], and extended by Kabayashi and Maskawa to the three-generation case[2]. The matrix is then called CKM matrix,

$$\begin{pmatrix} d' \\ s' \\ b' \end{pmatrix} = \begin{pmatrix} V_{ud} & V_{us} & V_{ub} \\ V_{cd} & V_{cs} & V_{cb} \\ V_{td} & V_{ts} & V_{tb} \end{pmatrix} \begin{pmatrix} d \\ s \\ b \end{pmatrix}$$

where $\begin{pmatrix} d' \\ s' \\ b' \end{pmatrix}$ is the weak interaction eigenstates, $\begin{pmatrix} d \\ s \\ b \end{pmatrix}$ is the mass eigenstates, and V is a unitary matrix, which can be expressed by three mixing angles and one phase. As basic parameters of the standard model, the precision measurement of the matrix elements is of fundamental importance. From them, the completeness and effectiveness of theory can be guaranteed.

Among those matrix elements relevant to the charm quark, V_{cs} and V_{cd} can be measured from the pure leptonic or semileptonic decays of Ds and D, and a precision of 1.6% and 1.8% can be achieved respectively at BESIII due to the large statistics and very high purity. V_{cb} which can be measured from B decays with D or D* in the final states, will benefit from the high precision measurements of the absolute D decay branching fractions, so to reduce the error from the tagging modes of B decays. With a combined efforts of both B factories and unquenched LQCD calculation of the form factor, V_{cb} can be measured to a precision of 3% .

In determining the matrix elements V_{td} and V_{ts} from measuring $B_d\overline{B}_d$ and $B_s\overline{B}_s$ mixing, the decay constants f_{Bd} and f_{Bs} from theoretical calculations are used, since measurements of these two quantities are impossible at the moment. The known best way for improving the precision of the decay constant calculation is to calibrate the LQCD calculation of the decay constants of D and Ds—f_D and f_{Ds} with high precision measurements. From the pure leptonic decays of D and Ds, the decay constants can be measured to a precision of 2% or less, this will help a lot in improving the precision of V_{td} and V_{ts} measurements.

Since there are only four free parameters in the CKM matrix, the high precision measurements of all the matrix elements can be used as a check of the unitarity and normality condition of the matrix. Any significant deviation of measured values from the expectation may indicate the incompleteness of the CKM matrix, so to give a hint of the existence of new physics. Otherwise, if matrix elements satisfy all the requirements of the standard model, the mixing angles and the phase can be extracted from the measured values, and a higher precision transition matrix can be obtained.

2.1.2 Lepton Universality

Due to the high selection efficiency and the high purity of the $\tau^+\tau^-$ sample at Z^0 peak, the tau physics study at Z^0 energy has the advantage of small systematic error for channels with large branching fractions. While at B factories, the large statistics of the $\tau^+\tau^-$ sample makes the study of channels with small branching ratios as well as the search for rare decays and new physics more suitable. At $\tau^+\tau^-$ threshold, however, it has its own advantages due to the fact that $\tau^+\tau^-$ pairs are produced at very low velocity. It can be used for some special physics studies, including the precision measurement of the tau lepton mass for the test of the lepton universality and interaction properties between the slowly moving tau pairs produced near threshold.

The lepton universality is a basic, but very strong assumption in the standard Model. The assumption has been tested in very high precision with pure leptonic and semi-leptonic decays of taus and muons. Following the procedure of the tau mass measurement at BESI with the cross section measurement near the threshold, but with a much large statistics, BESIII can achieve a precision of 0.1MeV, an improvement of a factor 3 compared with that of the current world average. The precision will be far beyond what people can reach in tau lifetime and tau leptonic branching fraction measurements in the near future, and provide a foundation for a more precise test of the universality.

It should be noted that the $\tau^+\tau^-$ cross section near the threshold has been calculated to $O(\alpha^4)$ in theory, taking into account the initial state radiation, Coulumb interaction between the tau pair and the high precision vacuum polarization estimation from hadron contributions. The precision is declared to be better than 0.1%[5], which can guarantee the final precision of the tau mass measurement where the observed $\tau^+\tau^-$ production cross section as a function of tau mass was fit to the theoretical calculation. At the mean time, the measured cross section can be used to test the theoretical calculation of the cross section, especially the non-relativistic QED (NRQED) calculation of the $\tau^+\tau^-$ interaction. This will supply us a better understanding of the $\tau^+\tau^-$ interaction near the threshold.

2.2 Study of Strong Interactions

Due to the non-perturbative nature of the strong interaction at the tau-charm energy region, almost all the theoretical calculations in this energy range have large uncertainties. LQCD will provide high precision predictions in a few years. But due to the limitation of computing capacity and complexity, the results will still be quite limited. As a consequence, all kinds of phenomenology models will still exist for a pretty long period of time, and even play important roles in some cases for the interpretation of experimental results. The study of QCD in the tau-charm energy region includes following aspects: determination of basic QCD parameters such as the strong coupling constant a_s, the mass of the charm quark m_c, the high precision measurement of the light hadron spectroscopy, searching for gluonic states such as glueballs and hybrids, and the study of charmonium physics by measuring the production and decay properties of the charmonium states to test and develop QCD calculations.

2.2.1 Precision Measurement of Basic QCD Parameters

In principle, the strong coupling constant α_s can be measured in any strong interaction process provided there exist good measurable quantities and reliable theoretical calculations. At BESIII, the most probable processes which may give high precision measurements of α_s include: inclusive J/ψ radiative decays, τ decays and hadronic cross section measurements (R value).

The α_s at c-quark mass can be measured with inclusive J/ψ radiative decays, but the precision depends strongly on that of theoretical predictions, as well as that of the charm quark mass. The former one is expected to be taken care of by the development of LQCD, while the latter one can be determined by the much accurate charmonium spectroscopy and high precision theoretical calculations.

The measurement of α_s with tau decays currently gives the best precision at a mass scale as low as the tau mass, by using the high precision measurement of the leptonic branching ratios and spectral functions, with the help of the Operator Product Extension in the theoretical calculation. Although it is very hard to improve the tau decay branching ratios at BESIII, the measurement of the spectral function with different systematic effects from previous experiments will contribute to the estimate of the strong coupling constant at the tau mass, as well as a test of running of the strong coupling constant at energies below the tau mass.

Because QCD only contributes to the correction term of the R value, it is not easy to get a high precision α_s measurement with the R data. However since the statistical error will be completely negligible at BESIII for the R value measurement at any energy point and systematic errors excluding common ones are very small, the running of the strong coupling constant at the tau-charm energy region can be tested with a high precision.

Furthermore, high precision measurement of R can be used to further improve calculations of the hadronic contribution in vacuum polarization, so to decrease the systematic uncertainties in the calculation of the abnormal magnetic moment of muon, $a_\mu=(g-2)\mu$, and the running of the fine structure constant, α, and so on.

2.2.2 Study of the Light Hadron Spectroscopy

Hadronic states are the basic components of the QCD at low energies, they reflect the strong interaction between quarks within the states. Although the study has a very long history, the understanding of the nature of interactions is rather poor, especially not accurate. In addition, QCD predicts the existence of gluonic states like glueballs and hybrids, which have not been experimentally observed or identified unambiguously. It is still one of the hot topics in particle physics in recent years.

The radiative decay of J/ψ is considered as one of the best places for glueball production naïvely, and lots of experimental searches have been performed with the collected J/ψ data. Since glueballs are in the same mass range as normal hadronic states, and there is no conclusive signature predicted, their identification is very difficult, although some candidates were reported over a long period of time. At BESIII, the J/ψ sample will be two orders of magnitudes more than that currently collected, and the detector has a better acceptance and resolution, a much more sophisticated partial wave analysis (PWA) for those interesting decay channels can be performed. It is not impossible to systematically study the production and decay properties of the identified glueballs to test the QCD expectations provided glueballs are identified. At the mean time, other QCD predicted non q-qbar states like hybrids and four-quark states can be searched and studied with J/ψ decays. As an important by-product, systematic studies of normal meson states, high precision measurements of resonance parameters, production and decay properties of light mesons will play important roles in the test and development of the QCD in non-perturbative domain, especially in the development of the LQCD to which the high precision data will be a good calibration. Also, the experimental study of the baryonic states with J/ψ and possibly other charmonium decays will result in a better understanding of the strong interactions between mesons and baryons, so to supply interesting information for nuclear physics.

It should be noted that, although glueballs are expected to be substantially produced in J/ψ radiative decays, the study of other hadronic states can be done in a very different environment, such as in J/ψ hadronic decays, non-leptonic decays of D or Ds, the decays of ψ(2S) and the charmonium production from ψ(2S) decays, as well as the semi-leptonic decays of the tau lepton.

2.2.3 Charmonium Physics

J/ψ 、ψ(2S)、ψ(3770) and the charmonium states from their decays can be used to test the QCD by measuring their production and decay properties with the large data sample. The potential model and the non-relativistic QCD (NRQCD) color-octet mechanism play important roles in production and decays of quarkonium states, and lots of detailed information of the theory, including some crucial input parameters like the color-octet matrix elements need to be determined from experiments. A systematic study of the charmonium states below $D\overline{D}$ threshold will hence provide theoretical input parameters and further test other predictions from the theory.

The P wave spin singlet $^1P_1$ state has been predicted soon after the discovery of the charmonium, but searches for this state have not be given solid results although candidates have been reported by a few experiments. This state will help us to understand the details of the potential between quark pairs in the charmonium states, and will complete the charmonium spectrum below $D\overline{D}$ threshold. The high precision measurement of the resonance parameters of other charmonium states, together with their production rates and decay modes, will supply substantial experimental information for testing theoretical models, and help the development of theories.

It should be noted that the large data sample collected at the B factories can be used for the charmonium physics study, including the search for the missing charmonium spin-singlet states, but the systematic study of these states will be better performed at BESIII since the data sample is much large and the background level is lower.

The study of the charmonium decay dynamics is another important topic. It has been revealed that the charmonium spin-triplet state J/ψ and its radially excited state ψ(2s) have very different decay patterns in some of the hadonic channels, compared with the naïve QCD prediction. The vector-pseudoscalor (VP) decays of ψ(2s) were found to be significantly suppressed related to the decays of J/ψ, the so called "$\rho\pi$ puzzle". Further experimental study shows that not only the VP mode, but also the vector-tensor (VT) decay mode is suppressed, although the strength is a bit weaker. Current experimental studies are still limited by the statistics. At BESIII, the large data samples at J/ψ 、 $\psi(2S)$ and $\psi(3770)$ resonances and the nearby continuum will allow the measurements of all the interesting hadronic decay modes to a level similar to that of electromagnetic interactions, and different decay rates of these three charmonium states with different quantum numbers can be compared after non-resonance contributions subtracted. It is possible then to explain how the QCD works in charmonium decays, and to understand finally the "$\rho\pi$ puzzle".

2.3 Search for New Physics

Rare decays and processes not allowed by the standard Model can be searched for with the high statistics data sample to detect new physics or give constraints of new physics contributions. At the tau-charm energy region, there are lots of possibilities to search for new physics effect. Here we only list the single D_S or D production, lepton and baryon number violation processes in J/ψ decays, $D^0\overline{D^0}$ mixing and the flavor changing neutral current (FCNC) with D data.

2.3.1 J/ψ Decays

In standard model, the weak decays of J/ψ to single D_S or D has the branching ratio of the order of 10^{-8}. At BESIII, with 10^{10} J/ψ events in one year's running, the decays can be observed and the test of the direct theoretical prediction can be made. Most importantly, if the observed production rate deviates significantly from the expectation, either enhanced or suppressed, it indicates the existence of other dynamics, or new physics.

In standard model, the lepton number and the baryon number are conserved exactly. Very stringent limits have been set from Z^0、 τ and μ decays. With the large data sample at BESIII, the upper limits of $J/\psi \to e\mu$ 、 $e\tau$ 、 $\mu\tau$ 、 ep、 μp、 τp and so on can be set to the level of 10^{-9}, so to give a stringent limit for theories beyond the standard model, or restrict the parameter space of non-standard models.

It has been pointed out long time ago that the spin correlation between two separated spin half particles can be used to measure the Bell's inequality so that to test the quantum theory[6]. A few hundred $\eta_c \to \Lambda\overline{\Lambda}$ were expected to give a good precision, while a much larger $\eta_c \to \Lambda\overline{\Lambda}$ sample can be obtained at BESIII. A careful study will give an unambiguous answer to the question, and supply the first test of the Bell's inequality in particle physics.

2.3.2 D Decays

The Standard Model predicts a very small $D^0\overline{D^0}$ mixing probability and a small direct CP violation in D_S or D decays, while new physics may enhance the effect dramatically. A careful study of $D^0\overline{D^0}$ mixing from $\psi(3770)$ decays can reach a mixing probability of 10^{-4}, which, although still far away from the standard model prediction of 10^{-9}, give a constraint to new physics contributions.

The new physics search can also be performed through the measurement of FCNC modes. Standard model predicts the decay rates of D→πe^+e^-、$\pi\mu^+\mu^-$、ρe^+e^-、$\rho\mu^+\mu^-$ being of the order of 10^{-6} [7]，which can be reached with the BESIII statistics. The test of these predictions with experimental measurements will reveal possible effects due to new physics.

In summary, the construction of a high luminosity accelerator and high performance detector at tau-charm energy region opens a new window for high precision measurements of the electroweak interactions through the study of the charm mesons and the tau lepton, high precision study of the perturbative and non-perturbative QCD with J/ψ and other charmonium decays, and new physics searches. All these studies will supply more high quality tests of the standard model and give constraints to or hints on the new physics.

In the following sections, detailed study of physics reach at BESIII is discussed, with some simulation results.

Reference

[1] N．Cabibbo，Phy．Rev．Lett．10，531(1963)．
[2] M．Kobayashi and T．Maskawa，Prog．Theo．Phys．49, 652(1973)．
[3] M．Artuso, Nucl．Instrum．Meth．A462 , 307(2001)．
[4] S．R．Sharpe, hep-lat/9811006, Plenary talk at ICHEP98．
[5] P．Ruiz-Femenia and A．Pich,　Phys．Rev．D64，053001(2001)．
[6] N．A．Toernqvist, Found. Of　Phys., 11, 171(1981)．
[7] G．Burdman et. al., hep-ph/0112235．

3 Physics Reach of the BESIII

3.1 Event Statistics

The designed peak luminosity of BEPCII is $10^{33}cm^{-2}s^{-1}$ at 1.89 GeV, which is the highest in the tau-charm region ever planned. An unprecedented large number of physics events is expected, giving us opportunities to obtain important physics results.

The number of expected events, N, is given by

$$N = \sigma \cdot L \cdot T,$$

where L is the luminosity, σ the cross section of the interested physics process, and T the integral of the data taking time. In the following calculations, we will use the average luminosity, $L = 0.5 \cdot L_{peak}$, to take into account the effect of the beam lifetime and the injection time. T is taken as 10^7 seconds per year for real data taking time.

In calculating the total cross section, the spread of the center-of-mass energy of BEPCII, $\Delta = 2.73\sqrt{2}E_b^2 \times 10^{-4}$, was taken into account and the maximum coverage of the solid angle of the detector, $\cos\theta_{max} = 0.93$, was chosen. The resulting total cross section was shown in Fig.3.1-1[1]. As seen in Fig.(a), The Bhabha and the two-gamma final state cross sections are dominant except at J/ψ and ψ' peak. As shown in Fig.(b) and (c), the total cross section including QED and other continuum processes is more than 4300nb at J/ψ and 1300nb at ψ'. This estimate can be cross checked at BES, where the resonance cross sections are 3100nb and 700nb, from J/ψ resonance scan at BESI and ψ' resonance scan at BESII, respectively. The center-of-mass energy spreads were (0.964±0.008)MeV and (1.305±0.002)MeV, respectively, similar to the designed goal of BEPCII.

The physics event rate at BEPCII is enormous, about 2600Hz at J/ψ, 1300Hz at ψ', and 300-600Hz for dominant QED processes at other energy points. The event number accumulated for each kind of physics in one year of running is shown in Table 3.1-1.

Table 3.1-1 Number of events expected for one year of running

Physics Channel	Center-of-mass Energy (GeV)	Peak Luminosity ($10^{33}cm^{-2}s^{-1}$)	Physics cross section(nb)	Number of Events per Year
J/ψ	3.097	0.6	~3400	10×10^9
τ	3.67	1.0	~2.4	12×10^6
ψ'	3.686	1.0	~640	3.0×10^9
D	3.770	1.0	~5	25×10^6
D_s	4.030	0.6	~0.32	1.0×10^6
D_s	4.140	0.6	~0.67	2.0×10^6

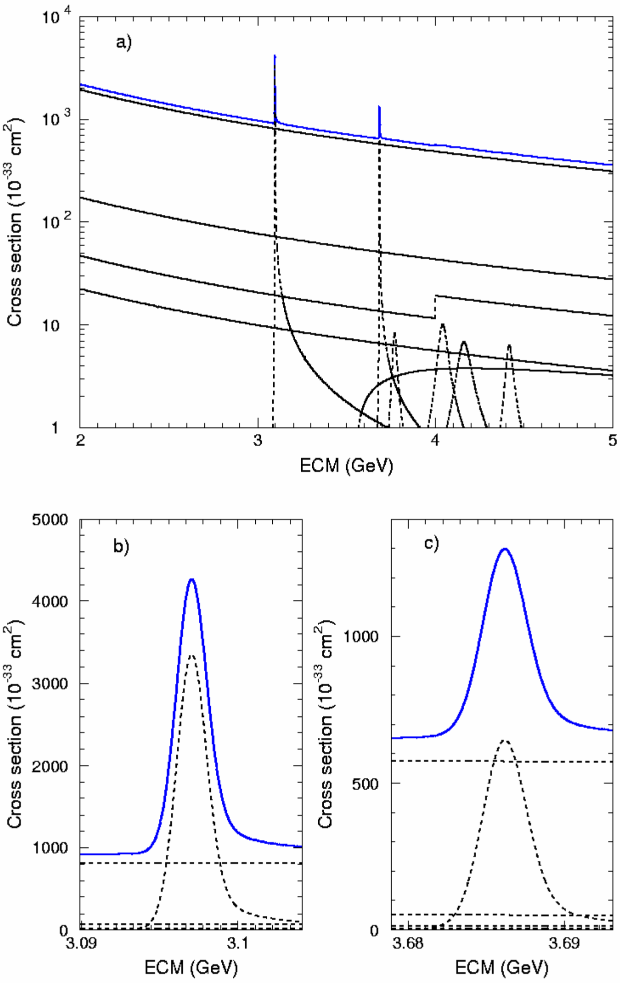

Fig. 3.1-1

Fig. 3.1-1 Cross sections in the τ-charm energy range. (a) Total cross sections of all physics processes. From top to bottom at 5.0GeV: Bhabha, two-gamma final state, non-resonance hadron production, dimuon and τ pair production. From left to right: resonance of J/ψ, ψ', ψ'', $\psi(4040)$, $\psi(4160)$ and $\psi(4415)$; (b) Total cross section, resonance cross section and other processes at J/ψ; (c) Total cross section, resonance cross section and other processes at ψ'.

Reference

[1] Yuan Changzheng *et al.*, “τ -charm physics and restriction to the accelerator and detector design”, to be published in High Energy Phys. and Nucl. Phys. (in Chinese)

Monte Carlo Simulation

The BESIII Monte Carlo study is based on the existing BESII software package[1] with some modifications. All physics processes are simulated based on the existing generators from the BESII[2], including J/ψ 、 ψ' 、D and Ds. The detector response to particles are simulated based on the CERN developed software package Geant3.21[3].

Since the full simulation using GEANT needs a lot of CPU time, it is unpractical in some cases when a large data sample is needed. A fast simulation program based on parameters from full simulation was established and simple smearing was performed to obtain fast simulation results.

FULL Simulation

The detector geometry built in the GEANT software is shown in Fig.3.2-1. It consist of a Be beam pipe, a Main Drift Chamber(MDC), a Time-of-Flight system (TOF), and an electromagnetic calorimeter(EMC) made of CsI crystals, a superconducting magnet and a 9 layers μ chamber system.

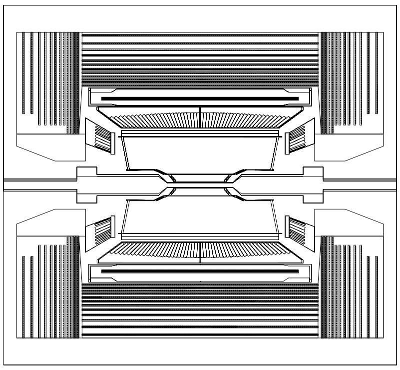

Fig. 3.2-1 Geometry of the detector

1. MDC

Although GEANT is used to track particles' transport in MDC, we use the software package TRACKERR [4] to calculate the MDC error matrix and to smear the output parameters. TRACKERR can give the resolution and error matrix at an given momentum and polar angle, which are then used to sample the quantities $1/P_{XY}$, θ and tg(λ) according to the Gaussian distribution. Fig.3.2-2 shows the momentum resolution of electrons at 1.5 GeV. It can be seen that the momentum resolution is 1.2%. In MDC, a track is marked as lost if the hit number is less than 20.

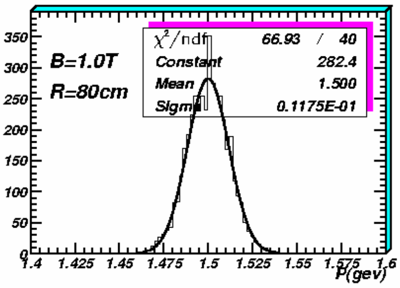

Fig. 3.2-2 Distribution of output momentum of electrons at 1.5GeV

Since the simulation results from GEANT directly for the thin gas is not satisfactory at this initial stage, the dE/dx of the MDC is obtained from a simple Gaussian sampling with a trancated mean value calculated from the theoretical prediction [5] and a resolution of 7%. Fig.3.2-3 shows the dE/dx distribution for five different particles, wherein the incident momentum is distributed uniformly.

The beam size with σ_Z=1.5cm and σ_{XY}=0.1cm, based on the accelerator design has been taken into account. In addition, the vertex reconstruction uncertainty is taken as σ_Z=0.3cm and σ_{XY}=0.02cm.

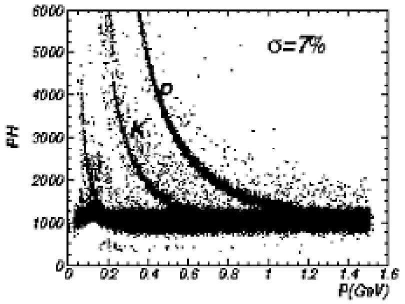

Fig. 3.2-3 dE/dX as a function Momentum for p,K,π, e

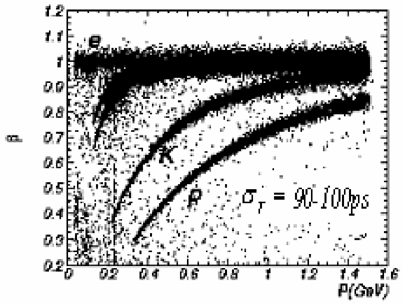

Fig. 3.2-4 β as a function of Momentum for p,K,π, e

2. TOF

Same as above, the flight time of particles is obtained by smearing the flight time from the vertex to TOF counters given by GEANT with a resolution of 85ps for the barrel and 100ps for endcaps. Fig.3.2-4 shows the distribution of the velocity β of barrel at different momentum for various particles. Effects of secondary particles, such as δ rays and back-scatterings have been simulated and they are not significant. Fig.3.2-5 shows the particle identification efficiency for π/K/p using TOF and dE/dx information at different momentum for various particles. Fig.3.2-6 gives the mis-identification probabilities as a function of momentum, which in most of cases are less than 10%.

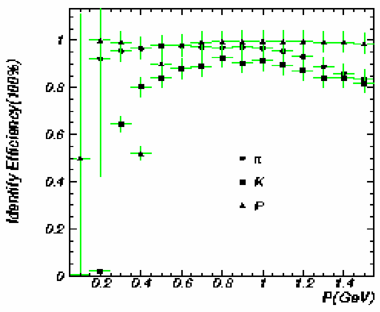

Fig. 3.2-5 PID efficiency

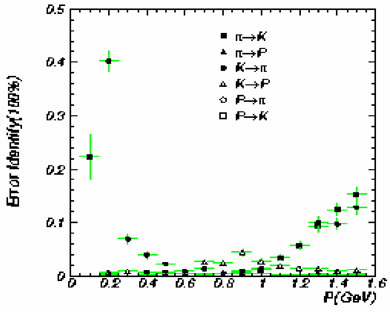

Fig. 3.2-6 mis-ID ratios

3. EMC

The energy deposit in the CsI electromagnetic calorimeter is simulated using the GEANT program. For an electromagnetic shower, more than 90% of energy is deposited in a 3x3 crystal matrix, with about 80% in the central crystal, if hitting at the center of the central crystal. In addition, a 0.2 MeV electronic noise is added to each crystal. The shower leakage into the sensitive area of photodiodes producing a large signal is also simulated based on our laboratory measurements.

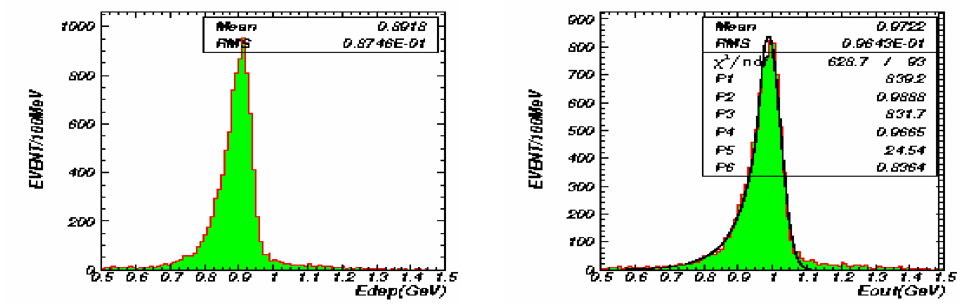

（a）before calibration (b) after calibration

Fig. 3.2-7 Energy deposit of 1.0 GeV photons in the CsI calorimeter

Fig.3.2-7 shows the energy deposit of 1.0GeV photons in 3x3 crystals, the long tail is due to the leakage of secondary particles. A calibration constant to bring the most probable energy deposit back to the nominal value is applied. An asymmetric function [6]

$$F(E)=\begin{cases} p_1 e^{-p_3(E-p_2)^2}\langle E\geq p_4\rangle \\ p_1 e^{-p_3(p_4-p_2)^2} e^{-p_5(E-p_4)^{p6}}\langle E<p_4\rangle \end{cases}$$

is used to fit the energy distribution and the resolution is obtained by $\sigma = \frac{FWHM}{2.35}$.

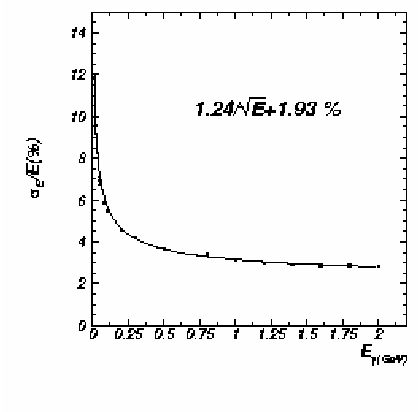

Fig. 3.2-8 Simulated energy resolution

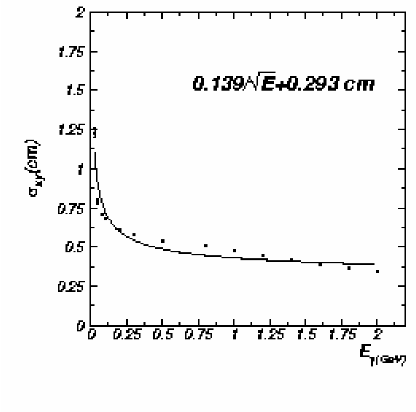

Fig. 3.2-9 Simulated position resolution

Fig.3.2-8 shows the resolution as a function of the photon energy. Another fitting method gives $\frac{\sigma_E}{E} = \left(\frac{1.492}{\sqrt{E(GeV)}} \oplus 2.754 \right)(\%)$. The photons' incident position on the front surface of crystal is determined by the center of gravity of showers projected onto the surface. For photons emitted isotropically, the position resolution σ_{XY} as a function of photon energy is shown in Fig.3.2-9. Similarly, another fitting method gives $\sigma_{XY} = \left(\frac{0.1985}{\sqrt{E(GeV)}} \oplus 0.3735 \right)(cm)$.

4. μ Counter

Particles such as muons and pions can be identified in the μ counter using hits information. Multiple hits in the same layer are considered as the pattern of pions, while single hit in each layer indicates a muon. Fig.3.2-10 gives the identification efficiency for muons and the mis-identification probability for pions. Since the optimization is not final, it is believed that the capability of the μ counter would be better than what is shown here, especially at the transition position between the barrel and the endcap. Further studies will be performed.

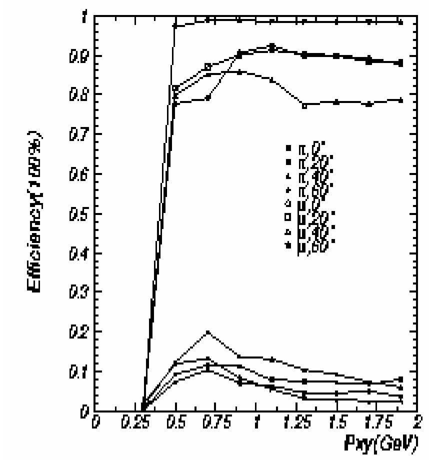

Fig. 3.2-10 Identification efficiency for μ and mis-ID probability of π as μ

FAST Simulation

The fast simulation is based on the performance parameters of sub-detectors. For MDC, these parameters are obtained by using the TRACKERR program, the same as in the full simulation. For TOF, they are obtained by smearing the flight time, the flight distance and the hit position assuming helix movement of particles. For calorimeter, we sample the photons' energy from tables of distributions obtained from the full simulation. For each incident and deposited energy, a two-dimensional probability table is given. Fig.3.2-11 compares the deposit energy distributions of fast (histogram) and full(shadowed area) simulations for 1.0 GeV photons. The photon direction is smeared with the angle resolution. Since it is difficult to calculate the multiple-scattering and the hadronic interactions in the μ counter and its absorber material, the μ counter simulation is not included temporarily in the fast simulation.

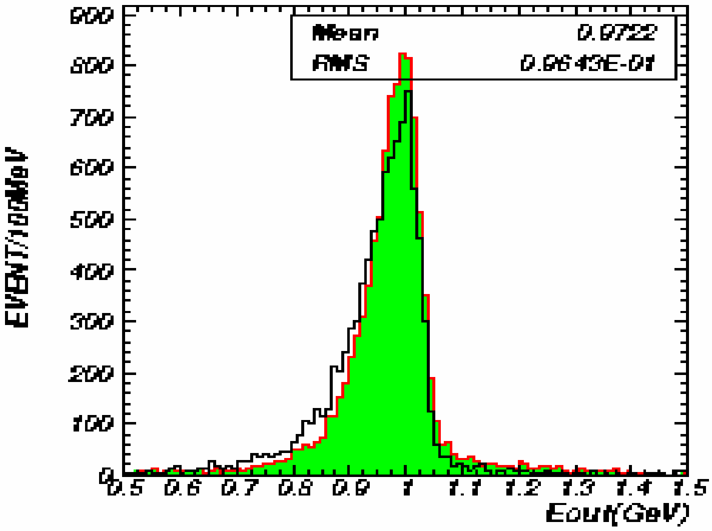

Fig.3.2-11 Comparison of full and fast simulation for 1GeV photons in EMC

Reference

[1] Wang Taijie et al. BES software note，Feb.1989;

[2] J.C.Chen et al. Phys. Rev. D62 (2000) 034003-1;

[3] Application Software Group,GEANT User's Guide,Program Library W5013. CERN, 1993;

[4] Walt Innes，BABAR Note#360，Feb.1998;

[5] Particle Data Group, Review of Particle Physics, July 2000;

[6] J.A.Bakken et al. L3 Note 1712，March 1995.

3.2 Charmed Meson Physics

Charmed mesons D^0, D^+ and D^+_s are the bound states of $c\bar{q}$ ($\bar{q}=\bar{u},\bar{d},\bar{s}$) quarks. The charm quark is sufficiently massive so that some aspects of perturbative QCD are applicable both in their productions and decays. Since the weak couplings of the charm quark are theoretically determined in the standard model with three generations of quarks, charm decays offer a clean laboratory to study strong interactions at the boundary between the perturbative and nonperturbative regime. There are three classes of charmed meson decays: pure leptonic, semileptonic and non-leptonic decays. BEPCII will operate at 2-4.2GeV, providing a best place to study the charm physics. In this report, we use the general BESIII software as described above to generate a total of $80pb^{-1}$ $D\bar{D}$ data at $\psi(3770)$ and

$500\text{pb}^{-1}\ D_S^{\pm}D_S^{\mp}$ data at $\sqrt{s} = 4.03\text{GeV}$, to study the physics reach of the designed BEPCII/BESIII [1].

3.2.1 Pure Leptonic Charmed Meson Decays

For the pseudoscalar charmed D^+ and D^+_s mesons, the decay rates of $D^+_{(s)} \to \mu^+ \nu$ can be rigorously calculated in the Standard Model, as given in the following:

$$Br(D^+_{(s)} \to l^+ \upsilon_l) = \tau_{D^+_{(s)}} \frac{G_F^2}{8\pi} f^2_{D_{(s)}} m_{D^+_{(s)}} |V_{cd(s)}|^2 \, m_l^2 \left(1 - \frac{m_l^2}{m^2_{D^+_{(s)}}}\right)^2, \qquad (1)$$

where $|V_{cd(s)}|$ is the CKM matrix element and $f_{D(s)}$ are the so-called decay constants, which contain all the information of nonperturbative QCD in leptonic decays. The m^2_l term represents the helicity suppression of the leptonic decays of the pseudoscalar mesons.

f_D and f_{Ds} are two fundamental constants in particle physics. They describe the overlapping of the wave function of mesons at the origin and play an important role in predicting the branching fractions of semileptonic and nonleptonic decays, and in understanding hadronic wave functions and the second order weak processes, such as the $D\overline{D}$ mixing and the CP violation. Although f_D and f_{Ds} are very important, they are poorly known since it is much more difficult to measure them than to measure f_π and f_K via leptonic decays $D^+ \to \mu^+ \nu$ and $D^+_s \to \mu^+ \nu$ due to the fact that leptonic decay branching fractions become smaller as the masses $m_{D(s)}$ become larger. At present the measured branching fractions $Br(D^+ \to \mu^+ \nu) = (8^{+17}_{-5}) \times 10^{-4}$ and $Br(D^+_s \to \mu^+ \nu) = (4.6 \pm 1.9) \times 10^{-3}$ have very large errors[2], especially for Cabbibo supressed decay $D^+ \to \mu^+ \nu$ whose braching ratio quoted by the PDG is based on one event observed at BES at 4.03GeV.

Theoretical evaluation of the decay constants relies on nonperturbative methods of QCD such as QCD sum rules[3-7], chiral perturbation theory, Bethe-Salpeter equation[11] and lattice gauge calculations[8-10]. Typically, they all predict f_D around 200 MeV (taking f_π =130 MeV). The ratio of f_{Ds}/f_D calculated by QCD sum rules [12]and by the lattice gauge theory [9] are all about 1.3.

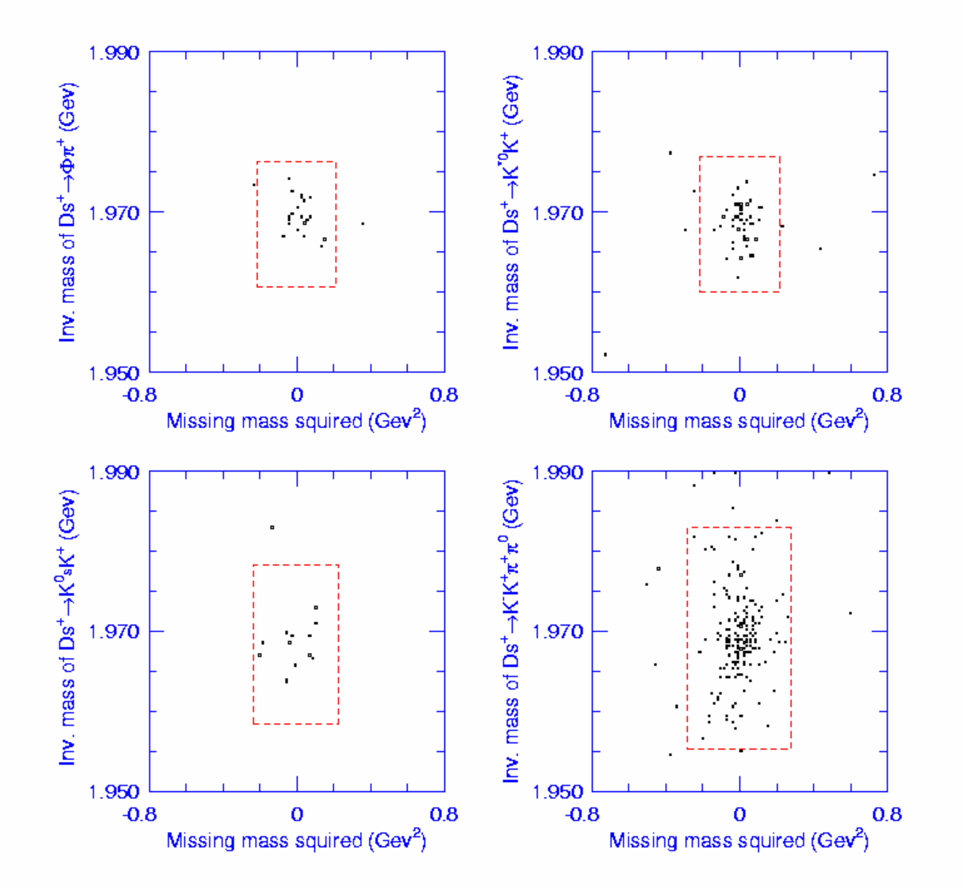

Fig.3.3-1. Missing mass squared vs the invariant mass distribution in $D_S^+ \to \mu^+\nu$

The high statistical data at BEPCII is expected to deliver accurate decay fractions of pure leptonic decays of charm mesons. Monte Carlo studies show that, ~450 events of $D^+ \to \mu^+\nu$ and ~ 450 events of $D^+_s \to \mu^+\nu$ will be obtained in $5fb^{-1}$ $\psi(3770)$ data and $3fb^{-1}$ $D_S^{\pm}D_S^{\mp}$ data. Fig.3.3-1 show the scatter plot of missing mass squared vs the invariant mass of single tags. The f_D and f_{Ds} can be extracted directly from the eqn.(1). Contributions from different error sources are listed in Table 3.3-1, which comes from the life time measurement of charm mesons($\Delta\tau/\tau$), the precision of CKM matrix elements($\Delta V/V$) and the error of the branching ratios($\Delta B/B$).

The life time measurement relies on results from fixed target and high energy experiments, while the CKM matrix elements (via the semileptonic decay of charm mesons) and the branching ratio of pure leptonic decays can be mearsured at BEPCII with a very high precision. Errors are dominated still by statistics.

Table 3.3-1. The measurement of decay constants of charm mesons

Decay mode	Decay constant	Branching ratio	Life time	CKM elements	Precision of decay constans
$D^+ \to \mu^+\nu$	f_D	2.4%	1.2%	1.8%	3.2%
$D_S^+ \to \mu^+\nu$	f_{D_s}	1.7%	1.8%	0.1%	2.5%

3.2.2 Semileptonic Decays and CKM Matrix Elements

The semileptonic decays of charmed mesons are more complicated than pure leptonic decays but simpler than the nonleptonic decays. For the process $D \to Xl\nu$, where X is a final state, the lepton part $l\nu$ can be factorized out. What is left is the matrix element of the weak current between D and X, $<X \mid j_u \mid D>$, where j_u is the weak current. The decay width of $D \to Xl\nu$ is also related to the CKM matrix element V_{cq} where q is the daughter quark after the transition of c by the emission of W boson and the q quark is combined with another quark in D mesons to form the meson X. In general the decay width Γ can be written as $\Gamma = |V_{cq}|^2 \overline{\Gamma}$ where $\overline{\Gamma}$ is proportional to $|<X \mid j_u \mid D>|^2$. Hence all the nonperturbative information is included in $\overline{\Gamma}$, which depends on the initial and final state hadronic wave functions and the hadronization mechanism. On the ground of Lorentz invariance, the matrix element $<X \mid j_u \mid D>$ can be decomposed as (for X a pseudoscalar meson)

$$< P | j_\mu | D >= \left(p_D + p_X - \frac{m_D^2 - m_X^2}{q^2} \right)_\mu F_1(q^2) + \frac{m_D^2 - m_X^2}{q^2} q_\mu F_0(q^2),$$

and (for X a vector meson)

$$\begin{aligned} < P | j_\mu | D >= & \frac{2}{m_D + m_V} \varepsilon_{\mu\nu\rho\sigma} \varepsilon^{*\nu} p_D^\rho p_V^\sigma V(q^2) \\ & + i\left(\varepsilon_\mu^* (m_D + m_V) A_1(q^2) - \frac{\varepsilon^* \cdot q}{m_D + m_V} (p_D + p_V)_\mu A_2(q^2) - \frac{\varepsilon^* \cdot q}{q^2} 2m_V q_\mu A_3(q^2) \right)_\mu \\ & + i \frac{\varepsilon^* \cdot q}{q^2} 2m_V q_\mu A_0(q^2), \end{aligned}$$

where p_D and p_X are the four momenta of D and X respectively and q is the momentum carried by $l\nu$. The form factors $F_1(q^2)$, $F_0(q^2)$, $V(q^2)$, $A_1(q^2)$,and $A_2(q^2)$ are governed by nonperturbative hadron dynamics and, therefor, are very difficult to calculate from the first principles of QCD. At the maximum recoil point q^2=0 the condition $F_1(0)=F_0(0)$ and $A_3(0)=A_0(0)$ must be satisfied. A_3 can be expressed in terms of A_1 and A_2

$$A_3(q^2)=\frac{m_D+m_V}{2m_V}A_1(q^2)-\frac{m_D-m_V}{2m_V}A_2(q^2).$$

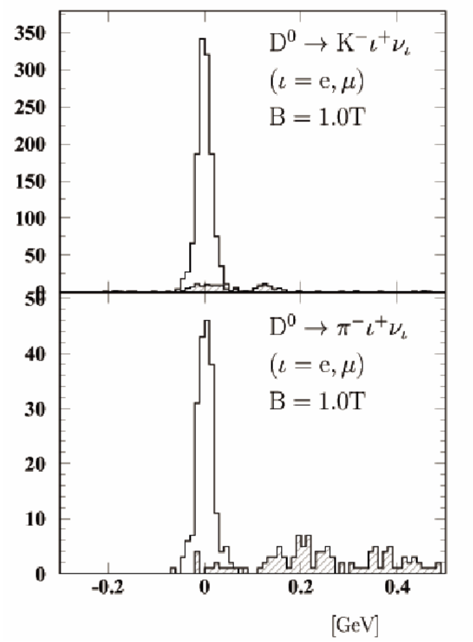

Fig. 3.3-2 The U distribution for the decay of $D^0 \to K^- e^+ \nu$ and $D^0 \to \pi^- e^+ \nu$. The shade represents contributions from backgrounds

At present, there are some phenomenological models to deal with these form factors[13-14]. Each of them has its own assumptions and hence limitations.

At BEPCII, the double tag method will be applied to study the semileptonic decays of charm mesons, which are produced with pairs at √s=3.77GeV, 4.03GeV and 4.14GeV. If we tag one charm meson via non-leptonic decay mode, we may tag the lepton and X in the recoil side. Since the neutrino from the semileptonic decay will escape the detector, and its mass is null, a kinematic varible $U=E_{missing}-P_{missing}$, where $E_{missing}$ and $P_{missing}$ are the missing energy and momentum of the whole system, is useful to reduce the background. Fig.3.3-2 shows the distribution of the variable for the decay of $D^0 \to K^- e^+ \nu$ and $D^0 \to \pi^- e^+ \nu$. The background are also shown in the figure. Table 3.3-2 lists statistical errors of the measurement of the branching ratios from one year's data of BEPCII.

Table 3.3-2 The measurement of the branching ratios of the semileptonic decays of charm mesons

Mode	Input Branching ratio	Efficiency	Stat. errors	CKM Elements
$D^0 \to K^- e^+ \nu$	3.4%	54.6%	0.6%	V_{cs}
$D^0 \to K^- \mu^+ \nu$		30.5%		
$D^0 \to \pi^- e^+ \nu$	0.4%	62.2%	1.6%	V_{cd}
$D^0 \to \pi^- \mu^+ \nu$		44.3%		
$D^+ \to \overline{K^0} e^+ \nu$	8.5%	6.7%	1.6%	V_{cs}
$D^+ \to \overline{K^0} \mu^+ \nu$		3.7%		

The elements of CKM matrix can be extracted from the branching ratios directly

$$\Gamma(D^0 \to K^- e^+ \nu) = \frac{B(D^0 \to K^- e^+ \nu)}{\tau_{D^0}} = \overline{\Gamma_s} \mid V_{cs} \mid^2$$

and

$$\Gamma(D^0 \to \pi^- e^+ \nu) = \frac{B(D^0 \to \pi^- e^+ \nu)}{\tau_{D^0}} = \overline{\Gamma_d} \mid V_{cd} \mid^2$$

and error of $\mid V_{cq} \mid$ is

$$\frac{\delta \mid V_{cq} \mid}{\mid V_{cq} \mid} = \sqrt{\left(\frac{\delta B}{2B}\right)^2 + \left(\frac{\delta \tau_{D^0}}{2\tau_{D^0}}\right)^2 + \left(\frac{\delta \overline{\Gamma_q}}{2\overline{\Gamma_q}}\right)^2}$$

Taking ~0.5% as the inefficiency of a single track, including the tracking and particle identification, the total systematic error of the measurement of the branching ratio is estimated to be ~1%. The precision of the lifetime is 0.7%, taken from PDG[2]. Comparing the error of branching ratios and the lifetime, we see that the error $\delta\overline{\Gamma_q}/\overline{\Gamma_q}$, coming from theoretical calculations, is dominant. Taking $\delta\overline{\Gamma_q}/\overline{\Gamma_q} = 3\%$, we obtain $\delta V_{cs}/V_{cs}$=1.6% and $\delta V_{cd}/V_{cd}$=1.8%.

Theoretical uncertainties are largely suppressed by taking the ratios such as $\Gamma(D \to \pi l \nu)/ \Gamma(D \to K l \nu)$ where the only uncertainty comes from SU(3) symmetry breaking. The systematic uncertainty from experiments will be supressed also, resulting a more reliable ratio V_{cd}/V_{cs} which can be obtained at BEPCII with an accuracy around 1.4%.

By measuring the inclusive semileptonic decays of the charmed meson $d\Gamma/dE_l$ where E_l is the lepton energy, the distribution function of heavy quarks, *f(x)*, can be extracted from the relation

$$\frac{d\Gamma}{dE_l} = \int dx f(x) \left(\frac{d\Gamma}{dE_l} \right)_{parton} .$$

At present, only a few ansatz for *f(x)* exists[16]. The precise measurement of *f(x)* can give important information about the inner structure of charmed mesons.

The analysis of the semileptonic decays of charmed mesons based on the high precision data to be obtained at BEPCII will surely help us to learn more about nonleptonic decay processes, where not only the matrix $<X \mid j_u \mid D>$ appears, but also the decay mechanism plays an important role. Just as in the case of pure leptonic decays, all the related theoretical techniques such as heavy quark expansion, QCD sum rules, Bethe-Salpeter equation, chiral perturbation theory and lattice gauge simulations will be tested.

3.2.3 Non-Leptonic Decays

Absolute branching ratios of $B(D^0 \to K^-\pi^+)$, $B(D^+ \to K^-\pi^+\pi^+)$ and $B(D^+_s \to \phi\pi^+)$ are the important normalization constants for the branching ratios of charm and B meson decays. At present, their errors are 2.3%, 7.7% and 25% respectively. At 2-4 GeV, charmed mesons are produced with pairs accompanied by small or no backgrounds, and the model dependent factors and backgrounds will be suppressed by using the double tag method, the beam energy constrained mass and the 4-C kinematic fit technique.

Fig. 3.3-3 show the reconstructed D^+ mass constrained by the known beam energy for the decay of $D^+ \to K^-\pi^+\pi^+$. In the Monte Carlo study, the decay mode $K^-\pi^+$, $K^-\pi^+\pi^+\pi^-$ and $K^-\pi^+\pi^0$ are used as the tag to measure the absolute branching ratio of $D^0 \to K^-\pi^+$, the decay modes $K^-\pi^+\pi^+$、$\overline{K^0}\pi^+$、$\overline{K^0}\pi^+\pi^+\pi^-$、$\overline{K^0}\pi^+\pi^0$ and $K^-\pi^+\pi^+\pi^0$ are used as the tag for $D^+ \to K^-\pi^+\pi^+$ and the decay mode $\varphi\pi^+$、$\overline{K^{*0}}K^+$、$\overline{K^0}K^+$、$K^-K^+\pi^+\pi^0$、$\eta\pi^+$ and $\eta'\pi^+$ used as the tag for $D^+_s \to \phi\pi^+$.

A large sample of single tags can be obtained at BEPCII, and the systematic uncertainty of single charged track and single photons can be limited to the level of ~0.5%, and backgrounds can be ignored at 3.77GeV. The experimental error of absolute branching ratios is then dominated by the number of double tags. Fig. 3.3-4 shows the invariant mass distributions of double tags. Statistical errors of the measurement of absolute branching ratios are listed in Table 3.3-3 and the number of observed double tag events in a $3\mathrm{fb}^{-1}$ $D_S^{\pm}D_S^{\mp}$ data sample are listed in Table 3.3-4.

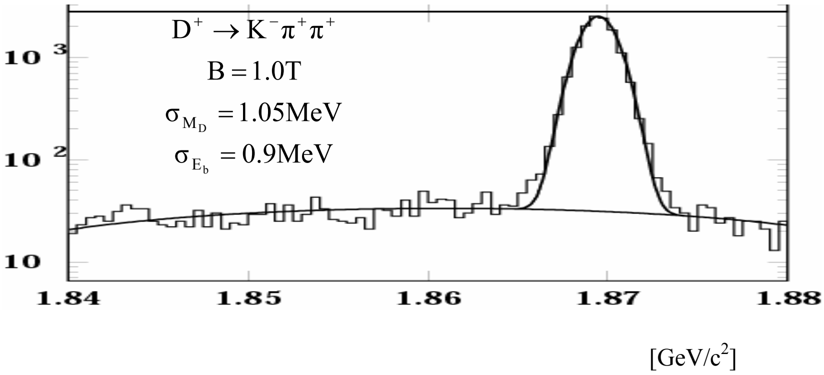

Fig.3.3-3 Reconstructed D^+ mass constrained by the beam energy for the decay of $D^+ \to K^-\pi^+\pi^+$

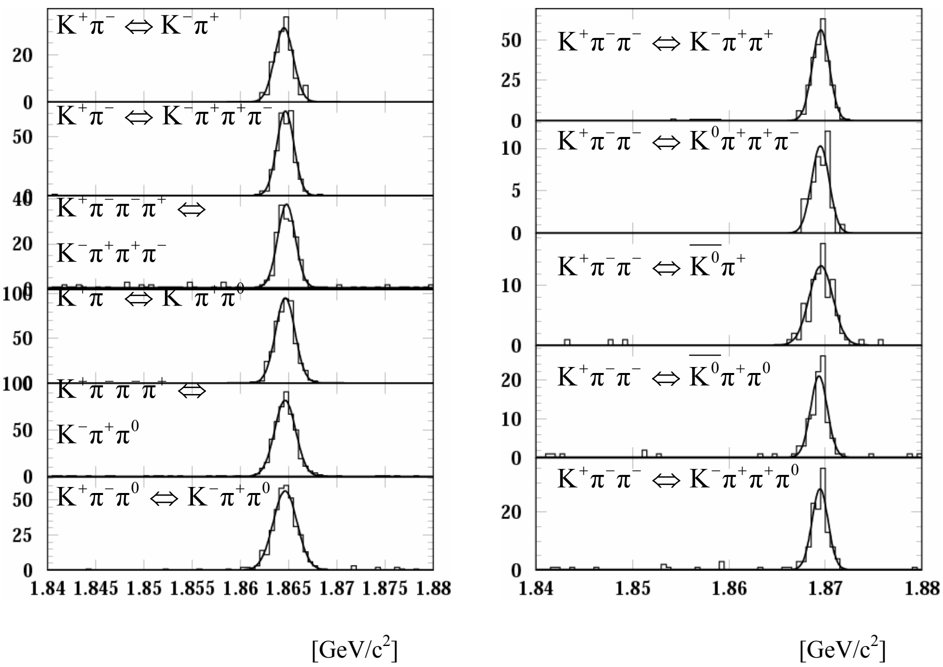

Fig. 3.3-4 Invariant mass distributions for D^0 and D^+ double tags

Table 3.3-3 Measurement precision of the absolute branching ratios of charmed mesons in a $5\mathrm{fb}^{-1}$ $\psi(3770)$ data sample

Mode	Input Branching Ratios	Detection efficiency	$\Delta B/B$
$K^-\pi^+$	3.7%	72.2%	~0.4%
$K^-\pi^+\pi^+\pi^-$	~7.8%	34.0%	
$K^-\pi^+\pi^0$	~12.0%	32.0%	
$K^-\pi^+\pi^+$	~7.7%	52.0%	~0.6%
$\overline{K^0}\pi^+$	2.8%	12.5%	
$\overline{K^0}\pi^+\pi^+\pi^-$	~5.6%	9.2%	
$\overline{K^0}\pi^+\pi^0$	~8.6%	7.9%	
$K^-\pi^+\pi^+\pi^0$	~5.0	22.5%	

Table 3.3-4 The number of observed double tag events in $5fb^{-1}$ $D_S^{\pm}D_S^{\mp}$ data taken at $\sqrt{s} = 4.03$

	$\varphi\pi^-$	$K^{*0}K^-$	K^0K^-	$K^-K^+\pi^-\pi^0$	$\eta\pi^+$ $\eta\to\gamma\gamma$	$\eta'\pi^+$ $\eta'\to\pi^+\pi^-\eta$
$\varphi\pi^+$	280					
$\overline{K^{*0}}K^+$	697	512				
$\overline{K^{)}}K^+$	303	370	95			
$K^-K^+\pi^+\pi^0$	820	1103	480	598		
$\eta\pi^+(\eta\to\gamma\gamma)$	213	290	123	313	40	
$\eta'\pi^+(\eta'\to\eta\pi^+\pi^-)$	173	233	100	253	67	27

Total D_s double tag events	7090	Statistical error $\Delta B/B$ of the branching ratio of $D_s^+ \to \phi\pi^+$	1.2%

The rich varity of available charm decay modes (meson and baryon decays, Cabbibo allowed, Cabbibo suppressed, and double Cabbibo suppressed decays) offers a possibility to study decay mechanism of the charm hadrons and to test different theoretical methods. For instance, there are six feynman diagrams for D meson decay, as shown in Fig. 3.3-5. As expected theoretically the decay through diagram (b) should be color suppressed because of the color mis-match, however, the present charm data show no color suppression. Theoretical speculations on the strength of the different diagrams (a)-(f) can be tested by the precision data. Another examples is $D^0 \to \overline{K^0}\phi$. At the quark level this decay can only go through diagram (c) in Fig. 3.3-5, i.e., the so-called exchange diagram, hence its branching fraction should be very small. Recent experimental data[2] shows that its Branching ratio is surprisingly large, $Br(D^0 \to \overline{K^0}\phi) = (8.6 \pm 1.0) \times 10^{-3} \approx 1\%$. There are theoretical arguements[17] saying that this is due to the final state interactions (rescattering), but up to now, this is not convincing yet. Again because of the rich varity, charm decays are ideal places for studying final state interactions. For example, if sufficiently large number of branching ratios are well measured, we can extract the size of contributing isospin amplitudes and their phase shifts.

Because charm hadrons are heavier than light hadrons but lighter than bottom hadrons, charm study will tell us how to apply and test different theoretical methods, such as QCD Sum Rule, Lattice Simulations of QCD, Heavy Quark Effective Theory, and $1/M_Q$ expansions, etc.

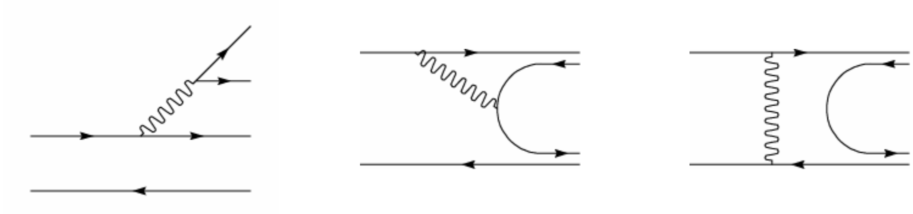

(a) (b) (c)

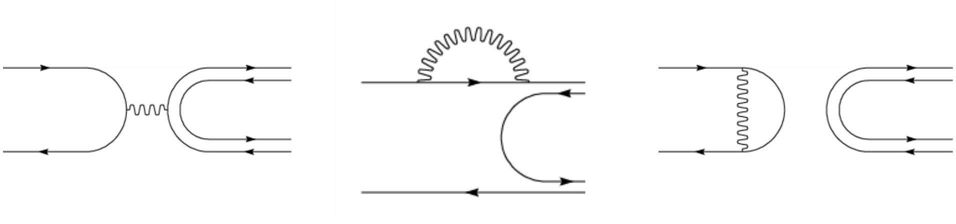

(d) (e) (f)

Fig. 3.3-5 Feynman diagram of charmed meson decays

3.2.4 $D^0 - \overline{D^0}$ Mixing

The process of particle–antiparticle mixing is a sensitive probe of the weak interaction in the neutral K, D, and B mesons. Since mixing is very sensitive to phenomena such as possible existence of a new quark generation, it is a good place to look for new physics. Although in the standard model, the mixing is expected to be small, the D^0 system is similar to the neutral Kaon and B^0 system that its mass eigen-states are different from its CP eigen-states. Taking the phase convention as $PC|D^0>=|\overline{D^0}>$, we can construct symmetric and asymmetric CP eigen states D_1 and D_2 respectively:

$$|D_1>=\frac{1}{\sqrt{2}}\left(|D^0>+|\overline{D^0}>\right), \qquad |D_2>=\frac{1}{\sqrt{2}}\left(|D^0>-|\overline{D^0}>\right).$$

The physical mass eigen states (also weak decay eigen states) can be described by

$$|D_S>=\frac{1}{\sqrt{2}}\left(|D_1>+\varepsilon|\overline{D_2}>\right), \qquad |D_L>=\frac{1}{\sqrt{2}}\left(|D_2>+\varepsilon|\overline{D_1}>\right)$$

In contrast to K_S, K_L,, here D_S, D_L have comparable lifetimes due to the large number of decay channels of the D mesons.

Experimentally we measure the mixing rate defined as

$$r_D=\frac{N(D^0\to\overline{D^0}\to Decays)}{N(D^0\to Decays)}\approx\frac{x^2+y^2}{2},$$

where $\chi=\Delta m/\Gamma$, $y=\Delta\Gamma/(2\Gamma)$, Δm and $\Delta\Gamma$ are the mass and width differences of D_S and D_L respectively.

At BEPCII, the $D^0\overline{D^0}$ pair can be produced in the electron positron annihilation at the center-of-mass energy of 3.77 GeV in the physics interaction $e^+e^-\to D^0\overline{D^0}$, where $D^0\overline{D^0}$ is in $C=-1$ state and can be described by

$$|D^0\overline{D^0}>=\frac{1}{\sqrt{2}}\left[D^0(\vec{k})\overline{D^0}(-\vec{k})-D^0(-\vec{k})\overline{D^0}(\vec{k})\right].$$

$\overline{D^0}\to K^+\pi^-$ is Cabbibo favored decay, but in principle $D^0\to K^+\pi^-$ can occur through Double Cabbibo suppressed Decay (DCSD). Since D^0, $\overline{D^0}$ have identical final states and can be regarded as identical particles, their coherent wave function should be symmetric and must have a charge parity C = +1. Therefore for C = -1 coherent state, DCSD can not contribute to $D^0\to K^+\pi^-$, and only the mixing $D^0\to\overline{D^0}\to K^+\pi^-$ contributes. Hence, we can tag $K^+\pi^-$ to measure $D^0-\overline{D^0}$ mixing free from DCSD contamination. The observation of the processes $e^+e^-\to D^0(\to K^-\pi^+)D^0(\to K^-\pi^+)$ or $e^+e^-\to\pi^0 D^0(\to K^-\pi^+)D^0(\to K^-\pi^+)$ would be an unambiguous evidence for the existence of $D^0-\overline{D^0}$ mixing. The final states of the above decay modes are very clean because all final particles are observed and D mass peak must be seen. Another method for measuring $D^0-\overline{D^0}$ mixing is to use the semileptonic decay, which is also free from DCSD contamination.

At BEPCII, we can search for $D^0-\overline{D^0}$ mixing through the process $e^+e^-\to D^0(\to K^-\pi^+)D^0(\to K^-\pi^+)$. A strict kinematic fit can result in the background absolutely free. The double semileptonic decays lost 2 neutrinos, making it less kinematically constrained. The background for $D^0(\to K^-\pi^+)D^0(\to K^-\pi^+)$ are dominated by the double mis-identification of *K* and *π*. The momentum of final particles are between 0.7 to 1.2 GeV for $D^0(\to K^+\pi^-)$. In this case, dE/dx is not good enough to distinguish K/π, while only TOF can be applied for the particle ID. A total of 100,000 Monte Carlo events of $e^+e^-\to D^0(\to K^-\pi^+)\overline{D^0}(\to K^+\pi^-)$ are generated for the study of the mixing at BEPCII, corresponding to about one year data taking. It shows that we may achieve a detection efficiency of ~40% with a misidentifaction probabilty of less than 10^{-4}.

In Standard Model, r_D is expected to be very small (~10^{-6}). BEPCII does not have the sensitivity to measure the r_D if the mixing is governed by the Standard Model. Several recent experiments and theoretical estimate claimed that[18-19] the mixing can be as large as 10^{-3}. BEPCII can approach to the order of 10^{-4} to test the theory.

Reference

[1] It is mainly based on "Feasibility Study Report on Beijing Tau-Charm Factory", IHEP-BTCF, Report-03, October, 1996.

[2] Particle Data Group, Review of Partcile Properties, Phys. Rev. D15(2000)543, 573

[3] T.M. Aliev and V.L. Eletsky, Yad. Fiz. 38, 1537(1983) [Sov. J. Nucl. Phys. 38,

936(1983)].

[4] M. Neubert, Phys. Rev. D45, 2451(1992).

[5] E. Bagan, P. Ball, V.M. Braun and H.G. Dosch, Phys. Lett. B278, 457(1992).

[6] S. Narison, Phys. Lett. B198, 104(1987)

[7] C.A. Domoinguez, Proceedings of the Third Workshop on the Tau-Charm Factory, Marbella, Spain, 1993, eds, J.Kirkby and R. Kirkby.

[8] C.W. Bernard, J.Labrenz and A. Soni, Nucl. Phys. B(Proc. Suppl.)30, 465(1993)

[9] A.Abada et al., Nucl. Phys. B376, 172(1992)

[10] G. Martinelli, Proceedings of the Third Workshop on the Tau-Charm Factory, Marbella, Spain, 1993, eds. J. Kirkby and R. Kirkby.

[11] Y.Dai, X.Guo, C.Huang and H.Jin, Commum. Theor. Phys. 24, 453(1995)

[12] M. Neubert, Phys. Rev. D46, 1076(1992)

[13] M.Bauer, B. Stech and M. Wirbel, Z. Phys. C34, 103(1987); ibid., 29, 637(1985); X.H. Guo and T. Huang, Phys. Rev. D43, 2931(1991); B. Grinstein, N. Isgur, and M. Wise, Phys. Rev. Lett. 56, 298(1986); C.W. Luo, T. Huang, X.H. Guo, J, P. Li and G.R. Lu, High Energy and Nucl. Phys. 18,601(1994); J.G. K0rner and G. Schuler, Z. Phys. C38, 511(1988).

[14] N.Isgur, D.Scora, B.Grinstein and M.Wise, Phys.rev. D39, 799(1989); T. Altomari and L. Wolfenstein, Phys. Rev. D37, 681(1988); P. Colangelo, G. Nardulli and L. Tedesco, Phys. Lett. B272, 344(1991)

[15]High Precision studies of charm. Tau, and QCD physics with CESR-c and CLEO-c. May 4, 2001.

[16] C.Peterson, D.Schlatter, J. Schmitt and G. Preparata, Phys. Lett. B172, 447(1986)

[17] J.F. Donoghue, Phys. Rev. D33, 1516(1986).

[18]Z.Z. Xing, Phys.Rev.D55. 196(1997)

[19]M.Gronau, Y. Grossman, J.L.Rosner, hep-ph/0103110

1.1 Light Hadron Spectroscopy

Our knowledge of mesons and in parallel, our understanding of the strong interactions has undergone several major revisions. Mesons were first introduced by Yukawa[1] with pions acting as the exchange boson responsible for the strong interaction between nucleons. With the advent of higher energy accelerators, more and more mesons and baryons appeared and it was recognized that the hadrons of a given J^{PC} can arrange themselves into representations of the SU(3) group. Zweig and Gell-Man[2] postulated that mesons and baryons were in fact composite objects with mesons made of a quark-antiquark and baryons made of three quarks. By taking this simple “naïve” quark model, the qualitative properties of hadrons were explained quite well. However, serious problems remained in the quark wavefunctions. For the spin 3/2 baryons, the constituent quarks’ spin and flavor wavefunctions were symmetric, in contradiction with expectations for fermions. This implies that either quarks obey some sort of different statistics or the ground state spatial wavefunction was asymmetric. To solve this problem, Greenberg[3] pointed out that quarks had another quantum number – color, which explained that quark wavefunctions could be asymmetrized. But still, there were considerable skepticisms about quark model due to the fact that the existence of quarks had never been observed. This situation had been changed until the discovery of J/ψ [4], which was interpreted as the bound state of a new heavy quark – charm. The quark model which incorporated the features of asymptotic freedom and confinement of quarks was able to reproduce the charmonium spectrum and describe the phenomenology of light quark spectroscopy rather well. All these developments in both experiments and theories are convincing enough that quarks were real objects and were the building blocks of hadronic matter.

Hadron spectroscopy is an ideal laboratory for the study of the internal structure of mesons and baryons, and so for the study of the strong interaction. Many experiments have been dedicating to the study of the hadron spectroscopy. The hadronic peripheral production, K^-p reaction by LASS, π^-p experiments by E852, GAMS, VES, and the experiment at KEK provided many data on the light meson spectroscopy. The pp central production at CERN, $p\bar{p}$ and $p\bar{n}$ annihilation at CERN and FNAL contributed much to the meson spectroscopy too. Crystal Ball, MARKIII, DM2, BES collaborations at e^+e^- storage rings and two photon collision experiments at CLEO and LEP have played and will continue to play an important role in the study of the hadronic spectroscopy. Most of the results of baryons and excited baryons came almost all from the old generation of πN experiments of more than 20 years ago. Considering its importance for the understanding of the baryon internal structure, a new generation of experiments on u-d quark N* baryons with electromagnetic probes (real photon and space-like virtual photon) has recently been started at new facilities such as Jefferson Lab, ELSA at Bonn, GRAAL at Grenoble and SPRING8 at KEK.

Our present understanding of the strong interactions is based on a non-Abelian gauge field theory, Quantum Chromodynamics (QCD) [5], which describes the interactions of quarks and gluons and thus predicts the existence of other types of hadrons with explicit gluonic degrees of freedom — glueballs and hybrids. Therefore, the observation of glueballs and hybrids is, to certain extent, a direct test of QCD, and the study on the hadron spectroscopy, as well as the glueball and hybrid spectroscopy will be a good laboratory for the study of the strong interactions in the strongly coupled non-perturbative regime.

1.1.1 Study of the Meson Spectroscopy

As an example, Fig. 3.4-1 and Fig. 3.4-2[6] show the comparison of Quark Model predictions with the experimental strange, charm and beauty meson spectra. The solid lines are the quark model predictions and the shaded regions are the experimental measurements with the bar widths representing the experimental uncertainty. One can see clearly that, for most part, the observed hadron properties are consistent with the predictions of the quark model. However, discrepancies between the experiments and the quark model exist, which may suggest interesting physics.

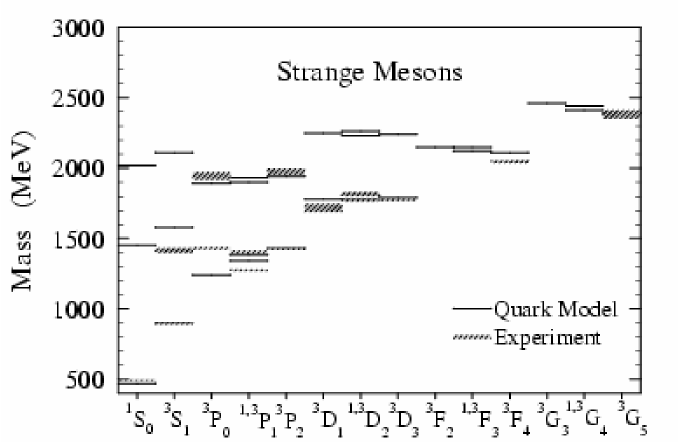

Fig.3.4-2 Comparison of Quark Model predictions with the experimental strange meson spectrum

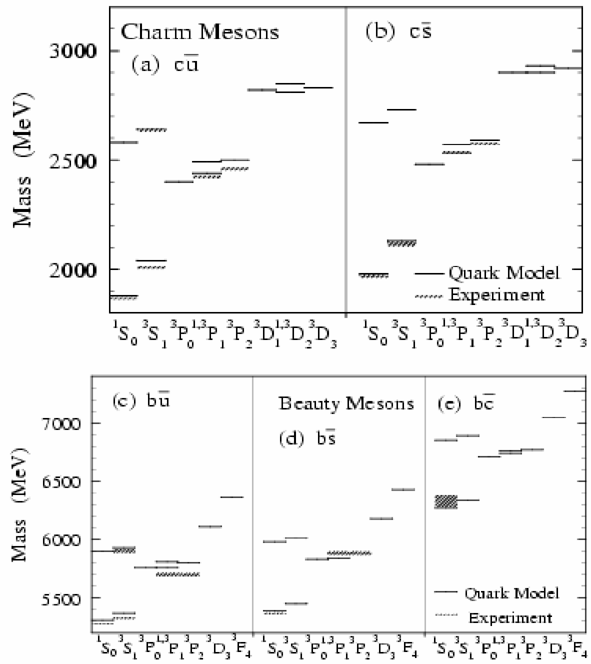

Fig. 3.4-1 Comparison of Quark Model predictions
with the charm and beauty spectra

The quark model can predict well the light meson spectrum and their decays, while disagreements still exist. Among them, some can be ascribed to be the natural limitation of the model when compared to the inherent complexity of QCD, but some may indeed point to the fundamental degrees of freedom needed to fully describe the hadron structure. Here, some of these disagreements are listed.

1. With a rather complete picture of the low mass $q\bar{q}$ states, it is becoming increasingly clear that some states have no place to be filled in $q\bar{q}$ sector. For example the low mass 0^{++} states have been confusing for many years and it turns out to be that there are too many 0^{++}, such as $f_0(1370)$, $f_0(1500)$, $f_0(1710)$ …

2. Two ground-state isoscalar 1^{++} states occur at 1240 and 1480 MeV in the quark model and are filled in by $f_1(1280)$ and f_1'(1530), thus the $f_1(1420)$ clearly appears as an extra state.

3. Extra 2^{++} states are observed.

4. There is a long time argument about whether 0^{++} $f_0(980)$ and $a_0(980)$ are $K\overline{K}$ molecular state or not.

5. Possible existence of the states with exotic quantum numbers

These states point to a need for a better understanding of the hadronic structure, perhaps by studying the relation between the $q\bar{q}$ meson properties and experimental observations or by enlarging the quarkonium picture to include gluonic degrees of freedom and multiquark states. So, more experimental information is needed for the understanding of meson spectroscopy.

1.1.2 Study of the Baryon Spectroscopy

The understanding of the internal quark-gluon structure of baryons is one of the most important tasks in both particle and nuclear physics. From theoretical point of view, since baryons represent the simplest system in which the three colors of QCD neutralize into colorless objects and the essential non-Abelian character of QCD is manifested, the systematic study of various baryon spectroscopy will provide us with critical insights into the nature of QCD in the confinement domain. The main source of information for the baryon internal structure is their mass spectra, production and decay rates. In recent years, Jefferson Lab in US, ELSA at Bonn, GRAAL at Grenoble and SPRING8 in Japan have started to study the baryon and excited baryon states. BES also studied N* production from J/ψ deca ys using 7.8M J/ψ data at BESI [7]. However, the available experimental information is still poor, especially for the excited baryon states with two strange quarks, e.g., Ξ*. Some phenomenological QCD-inspired models predict more than 30 such kinds of baryons, however only two are experimentally well settled.

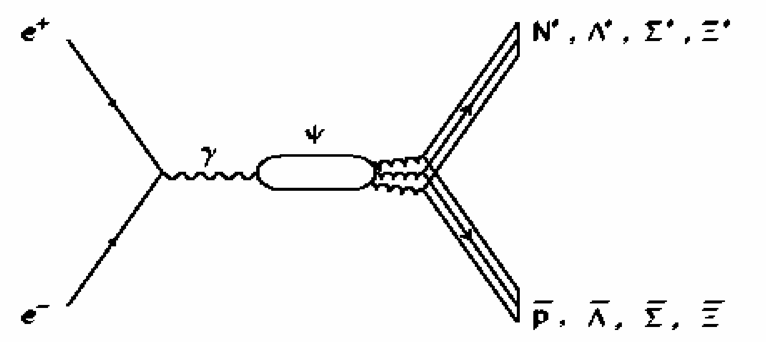

Fig. 3.4-3 Feynman diagram for $\bar{p}N^*, \bar{\Lambda}\Lambda^*, \bar{\Sigma}\Sigma^*$ and $\bar{\Xi}\Xi^*$ from e^+e^- collision through J/ψ

J/ψ decays provide us a good place for studying excited nucleon N* and excited hyperons, such as Λ*, Σ* and Ξ*. The Feynman diagram for $\bar{p}N^*, \bar{\Lambda}\Lambda^*, \bar{\Sigma}\Sigma^*$ and $\bar{\Xi}\Xi^*$ from e^+e^- collision through J/ψ is shown in Fig.3.4-3.

Since J/ψ decays through three gluons and that of gluons are flavor blind, the strange s quarks are produced at the same level as the non-strange u-d quarks. Therefore, $p\overline{p}, \Lambda\overline{\Lambda}, \Sigma^0\overline{\Sigma}^0$ and $\Xi\overline{\Xi}$ should be produced at similar branching ratios.

In fact, the Feynman graph in Fig.3.4-3 is almost identical to those describing the N* electro-production process when the direction of the time axis is rotated by 90°. The only difference is that the virtual photon here is time-like instead of space-like and it couples to NN* through a real vector charmonium meson J/ψ. So, all the N* decay channels which are presently under investigation in Jefferson Lab, ELSA, GRAAL at and SPRING8 with real photon or space-like virtual photon can also be studied at BES complementally with the time-like virtual photon. In addition, for $J/\psi \to N\overline{N}\pi$ and $N\overline{N}\pi\pi$, the $N\pi$ and $N\pi\pi$ systems are limited to be pure isospin 1/2 due to isospin conservation. This is a big advantage in studying N* resonances from J/ψ decays, compared with πN and γN experiments which suffer from the difficulty in the decomposition of isospin 1/2 and 3/2.

On theoretical side, the coupling of $J/\psi \to \overline{p}N^*$ provides a new way to probe the internal quark-gluon structure of the N* resonances. In the simple three-quark picture of baryons, as shown in Fig.3.4-3, three quark-antiquark pairs are created independently via a symmetric three-gluon intermediate state with no extra interaction other than the recombination process in the final state to form baryons. This is quite different from the mechanism underlying the N* production from the γN process where the photon couples to only one quark and asymmetric configuration of quarks is favored. Therefore the processes $J/\psi \to \overline{p}N^*$ and $\gamma p \to N^*$ should probe different aspects of the quark distributions inside baryons. Since J/ψ decay is a glue-rich process, it is also a very good place to hunt for hybrid baryons.

In Table 3.4-1, we listed some interesting J/ψ decay branching ratios, these channels are relatively easy to be reconstructed at BES. For example, for $K^-\Lambda\overline{\Xi}^+$, we can select events containing K^- and Λ with $\Lambda \to p\pi^-$, then from recoiling mass spectrum of $K^-\Lambda$, one can easily identify the very narrow $\overline{\Xi}^+$ peak. The $K^-\Lambda\overline{\Xi}^+$ channel is a very good place to study $\Xi^* \to K\Lambda$. For the three-body channels listed in Table 3.4-1, $J/\psi \to \Lambda\overline{\Sigma}^-\pi^+$ and $J/\psi \to pK^-\overline{\Lambda}$ can be used to study $\Lambda^* \to \Sigma\pi$ and NK and $J/\psi \to pK^-\overline{\Sigma}^0$ for $\Sigma^* \to \Lambda\pi$ and NK. With the channels including $\overline{p}$, we can also investigate $N^* \to K\Lambda$ 、$K\Sigma$ 、$N\pi$ 、$N\pi\pi$ 、$N\eta$ 、$N\eta'$ and $N\omega$ to search for “missing” excited nucleon states.

Table 3.4-1 Some interesting J/ψ decay branching ratios

Decays	$\Lambda\bar{\Lambda}$	$\Sigma^0\bar{\Sigma}^0$	$\Xi\bar{\Xi}$	$\Lambda\bar{\Sigma}^-\pi^+$	$pK^-\bar{\Lambda}$	$pK^-\bar{\Sigma}^0$
Br(10^{-3})	1.3±0.1	1.3±0.2	1.8±0.4	1.1±0.1	0.9±0.2	0.3±0.1
Decays	$p\bar{p}\pi^0$	$p\bar{p}\pi^+\pi^-$	$p\bar{p}\eta$	$p\bar{p}\eta'$	$p\bar{p}\omega$	$K^-\Lambda\bar{\Xi}^+$
Br(10^{-3})	1.1±0.1	6.0±0.5	2.1±0.2	0.9±0.4	1.3±0.3	

1.1.3 Glueball Search

After more than 20 years of theoretical effort, it has not yet been possible to calculate the glueball or hybrid spectrum from first principles, since Perturtative QCD cannot be applied at the hadron mass scale. Therefore, many QCD-based phenomenological models and calculations, such as bag models[8], flux-tube models[9], QCD sum rules[10] and lattice QCD[11] are developed to make predictions to the properties of glueballs and hybrids. Of them, lattice QCD is considered as more relevant since it originated from QCD, though it is very CPU time consuming and only numerical results can be obtained without any corresponding physical insight.

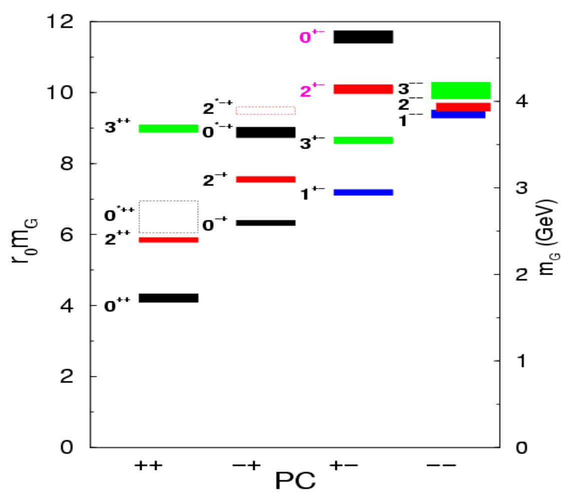

Fig. 3.4-4 The mass of glueball states from LQCD calculations[11].
The scale is set by r_0 with $1/r_0$=412(20) MeV.

Lattice QCD predictions for glueball masses in the quenched approximation, which neglects internal quark loops, are shown in Fig. 3.4-4. The lightest glueball is found to be 0^{++} with the mass from 1.5 GeV – 1.7 GeV, and the next lightest is 2^{++} with the mass around 2.24 GeV, from different groups' calculations. Naively, one can also expect that glueballs have the following signatures:

- no place in $q\bar{q}$ nonet
- enhanced production in gluon rich processes such as pp central production, J/ψ radiative decays and $p\bar{p}$ annihilation
- decay branching fractions incompatible with SU(3) predictions for $q\bar{q}$ states
- reduced $\gamma\gamma$ couplings

However, the glueball may mix with an ordinary $q\bar{q}$ meson that has the similar mass and the same quantum numbers, and thus it makes the identification of a glueball more complicated. Even so, there are some candidates of glueballs, such as $f_0(1500)$, $f_0(1710)$, $\xi(2230)$, etc.

a. Experimental Status of Some Glueball Candidates

- $f_0(1500)$

The $f_0(1500)$ was observed in many experiments, such as pion induced reaction $\pi^- p$, $p\bar{p}$ annihilation[12,13], central pp collisions [14,15] and J/ψ radiative decays[16,17] . Most of the data on $f_0(1500)$ was from Crystal Barrel collaboration, who resolved two scalar states in this mass region, and determined its decay branching ratios to a number of final states, including $\pi^0\pi^0$, $\eta\eta$, $\eta\eta'$, K_LK_L and $4\pi^0$, using $p\bar{p}$ annihilation at rest. It is also observed that in glueball suppressed processes of $\gamma\gamma$ collision to K_sK_s and $\pi^+\pi^-$, $f_0(1500)$ is absent. All of these favor $f_0(1500)$ being a non-$q\bar{q}$ state. If $f_0(1500)$ is a scalar glueball, it should be copiously produced in J/ψ radiative decays. However, $f_0(1500)$ was only observed in $J/\psi \to \gamma\pi^+\pi^-\pi^+\pi^-$ from MARKIII and BES J/ψ data. Therefore, searching for more decay modes of $f_0(1500)$, such as $\pi\pi$, $\eta\eta$, $\eta\eta'$ etc. and studying its spin-parity are important in determining the nature of $f_0(1500)$.

- $f_0(1710)$

The $f_0(1710)$ is a main competitor of $f_0(1500)$ for being the lightest 0^{++} glueball candidate due to its large production rate in gluon rich processes, such as J/ψ radiative decays, pp central production etc., and the predictions of lattice QCD. Table 3.4-2 lists the results of $f_0(1710)$ from different experiments. Apparently, different experiments gave different masses, widths and spin-parities.

The spin-parity of $f_0(1710)$ in the observed processes is crucial in determining whether $f_0(1710)$ is a $q\bar{q}$ or non-$q\bar{q}$ state. If J=0, then the $f_J(1710)$ and $f_0(1500)$ might well represent the glueball and the $s\bar{s}$ state, or more likely each is a mixture of both. However, if J=2, it will be difficult to assign a glueball status to $f_J(1710)$, since that would be at odds with all current lattice gauge calculations. Based on the present BESII 5.8×10^7 J/ψ data, the partial wave analyses are performed to $J/\psi \to \gamma K\overline{K}$ and $\gamma\pi^+\pi^-$ and the preliminary results show a dominant 0^{++} component in 1.7 GeV mass region for both channels. However, the analysis is limited by statistics and the absence of other channels, such as $J/\psi \to \gamma\pi^0\pi^0, \gamma\eta\eta, \gamma\eta\eta'$.

Table 3.4-2 History of $f_0(1710)$

Process	Collaboration	M (MeV)	Γ (MeV)	J^{PC}
$J/\psi \to \gamma\eta\eta$	CBAL (82)	1640 ± 50	200^{+100}_{-70}	2^{++}
$\pi^- p \to K_S^0 K_S^0 n$	BNL (82)	1771^{+77}_{-53}	200^{+156}_{-9}	0^{++}
$\pi^- N \to K_S^0 K_S^0 n$	FNAL (84)	1742 ± 15	57 ± 38	—
$\pi^- p \to \eta\eta N$	GAMS (86)	1755 ± 8	<50	0^{++}
$J/\psi \to \gamma K^+K^-$	MARKIII (87)	1720 ± 14	130 ± 20	2^{++}
$J/\psi \to \gamma K^+K^-$ $\gamma\pi^+\pi^-$	DM2 (88)	1707 ± 10 1698 ± 15	166 ± 33 136 ± 28	—
$pp \to p(K^+K^-)p$ $\to p(K_S^0 K_S^0)p$	WA76 (89)	1713 ± 10 1706 ± 10	181 ± 30 104 ± 30	2^{++}
$J/\psi \to \gamma K^+K^-$	MARKIII (91)	1710 ± 20	186 ± 30	0^{++}
$p\overline{p} \to \pi^0\eta\eta$	E760 (93)	1748 ± 10	264 ± 25	$(even)^{++}$
$J/\psi \to \gamma 4\pi$	MARKIII data D. Bugg (95)	1750 ± 15	160 ± 40	0^{++}
$J/\psi \to \gamma K^+K^-$	BES (96)	$1696 \pm 5^{+9}_{-34}$ $1781 \pm 8^{+10}_{-31}$	$103 \pm 18^{+30}_{-11}$ $85 \pm 24^{+22}_{-19}$	2^{++} 0^{++}
$J/\psi \to \gamma K\overline{K}$	MARKIII data Dunwoodie (97)	1704^{+16}_{-23}	124^{+52}_{-44}	0^{++}
$pp \to p(K\overline{K})p$	WA102 (99)	1730 ± 15	100 ± 25	0^{++}
$J/\psi \to \gamma 4\pi$	BES (2000)	1740^{+20}_{-25}	135^{+40}_{-25}	0^{++}

- $\xi(2230)$

The $\xi(2230)$ was first observed by the MARKIII collaboration in $J/\psi \to \gamma K\overline{K}$ [18]. Later, GAMS[19] reported a narrow structure at 2220 MeV/c^2 decaying into $\eta\eta'$ in the reaction $\pi^- p \to \eta\eta' n$ interactions at 38 GeV and 100 GeV. With 7.8×10^6 J/ψ events, BES[20] observed $\xi(2230)$ in $K\overline{K}$, $\pi\pi$ and $p\overline{p}$ channels but null signal in the later 5.8×10^7 J/ψ data sample $\xi(2230)$ was also not seen in the inclusive γ spectrum by Crystal Ball collaboration and $p\overline{p}$ annihilation in flight at CERN. In addition, stringent limits have been placed on the two-photon coupling of the ξ (2230) by the CLEO collaboration in the reactions $\gamma\gamma \to K_sK_s$[21] and $\gamma\gamma \to \pi^+\pi^-$ [22].

If we combine CERN $p\overline{p}$ scan result[23] $Br(\xi(2230)\to p\overline{p})\times Br(\xi(2230)\to K_sK_s)\leq 7.5\times10^{-5}$(95%C.L.) with the BES results[20]: $Br(J/\psi \to\gamma\xi)Br(\xi\to K_sK_s)=(2.7^{+1.1}_{-0.9}\pm0.8)\times10^{-5}$ and $Br(J/\psi \to\gamma\xi)Br(\xi\to p\overline{p})=(1.5^{+0.6}_{-0.5}\pm0.5)\times10^{-5}$, we have the lower bound $Br(J/\psi \to\gamma\xi) \geq (2.3 \pm 1.7)\times10^{-3}$. However, no $\xi(2230)$ was observed in the inclusive γ spectrum by Crystal Ball collaboration. One possibility is the branching ratio to $p\overline{p}$ being over estimated, and another possibility is that we haven't found more decay modes or the main decay modes of $\xi(2230)$. It is also possible that $\xi(2230)$ doesn't exist.

According to some theoretical predictions, $\xi(2230)$ can be strongly coupled to $\eta\eta'$, $\eta'\eta'$, provided it exists and is a glueball. In this case the final states of these channels have multi-prong and multi-photon. So, high statistics, good particle identification and good photon energy resolution are required to analyze these decays. On the other hand, the study of the inclusive γ spectrum directly becomes possible with a good photon energy resolution.

b. Glueball Search at BESIII/BEPCII

With the double-ring design, the luminosity of BEPCII will reach 10^{33}. Therefore, a large J/ψ event sample, e.g. 6×10^9 can be obtained in one year. On the other hand, BESII will be upgraded to BESIII. With a better particle identification, a much improved photon detection capability and a good charged tracks' momentum resolution, BESIII is able to study final states of all-neutral or multi-photon and multi-charged tracks.

As an example, we study $J/\psi \to\gamma\eta\eta'$ process to investigate $\xi(2230)$ assuming $Br(J/\psi \to\gamma\xi(2230))Br(\xi\to\eta\eta') \sim 3 \times 10^{-6}$, based on the design of BESIII/BEPCII .

Fig. 3.4-5 shows the expected $\eta\eta'$ invariant mass spectrum of 6×10^9 $J/\psi \to\gamma\eta\eta'$, $\eta\to\gamma\gamma$, $\eta'\to\gamma\rho^0$ events passing through BESIII detector. In addition to $\xi(2230)$, the possible $f_0(1500)$, $X(1910)$ and $X(2150)$ according to other experiments, as well as the background, are included in the simulation. ξ(2230) can be clearly seen here. The results of each resonance from Breit-wigner fit are shown in Table 3.4-3.

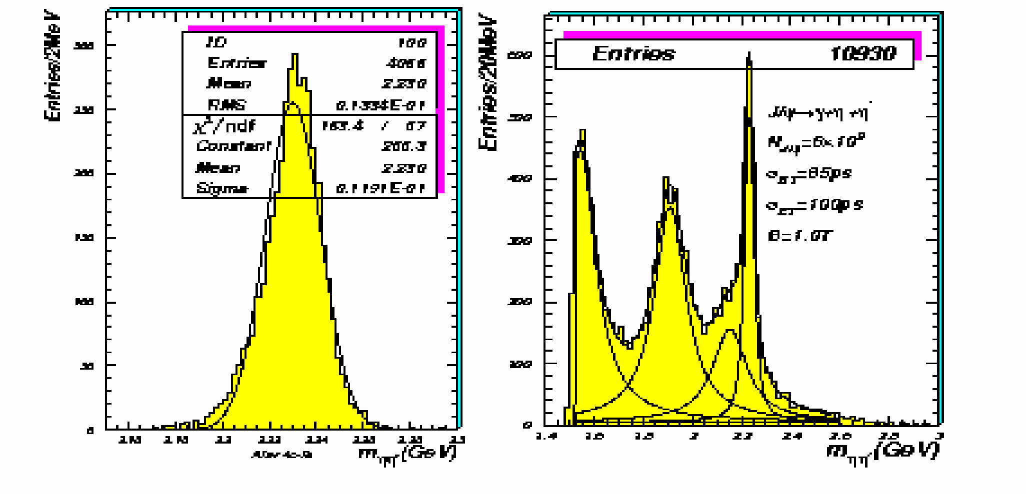

Fig. 3.4-5 ηη' invariant mass spectrum at B=1.0T

Table 3.4-3 The results of Breit-wigner fit

		Input	Output (B=1.0T)
	M(MeV)	1910.00	1909.40±2.40
X(1910)	Γ(MeV)	150.00	153.89±8.67
	Br($\times 10^{-6}$)	7.20	7.47±0.30
	M(MeV)	2150.00	2152.20±9.90
X(2150)	Γ(MeV)	157.00	167.13±21.00
	Br($\times 10^{-6}$)	3.60	3.66±0.33
	M(MeV)	2230.00	2231.20±1.05
ξ(2230)	Γ(MeV)	25.00	30.18±4.54
	Br($\times 10^{-6}$)	3.0	3.18±0.33

1.1.4 Hunting for Hybrid States at BESIII/BEPCII

Hybrid mesons are color-singlet mixture of constituent quarks and gluons, such as $q\bar{q}g$ bound states. The evidence of the existence of the hybrid mesons is also a direct proof of the existence of the gluonic degree of freedom and the validity of the QCD theory. The conventional wisdom is that it would be more fruitful to search for low mass hybrid mesons with exotic quantum numbers than to search for glueballs. Hybrids have the additional attraction that, unlike glueballs, they span complete flavour nonets and hence provide many possibilities for experimental detection. In addition, the lightest hybrid multiplet includes at least one J^{PC} exotics.

In searching for hybrids, there are two ways to distinguish them from conventional states. One approach is to look for an access of observed states over the number predicted by the quark model. The drawback to this method is that it depends on a good understanding of hadron spectroscopy in a mass region that is still rather murky. The experimental situation is not well settled that the phenomenological models have yet to be tested to the extent that a given state can be reliably ruled out as a conventional meson. The situation is further muddied by expected mixing between conventional $q\bar{q}$ states and hybrids with the same J^{PC} quantum numbers. The other approach is to search for the states with quantum numbers that cannot be accommodated in the quark model. The discovery of exotic quantum numbers would be definitely evidence of something new.

According to Quantum Field Theory, the J^{PC} of the ordinary $q\bar{q}$ mesons cannot be: 0^{+-}, 0^{--}, 1^{-+}, 2^{+-}, 3^{-+} ……These numbers are called exotic quantum numbers. The hybrid state with the exotic quantum numbers is called exotic meson or exotic state. Exotic mesons cannot be ordinary $q\bar{q}$ states, so they must be hybrids, glueballs or multiquark states.

From the theoretical estimation, we know that: $\Gamma(J/\psi \to \mathrm{MH}) > \Gamma(J/\psi \to \mathrm{MM'}) > \Gamma(J/\psi \to \mathrm{MG})$, where M stands for ordinary $q\bar{q}$ meson, G stands for glueball and H stands for hybrid. It means that the process of J/ψ hadronic decays to hybrid states will have relatively large branching ratios. So the J/ψ hadronic decay is an ideal place to study hybrid states and to search for exotic states.

Table 3.4-4 Experimental search for 1-+ in $\eta\pi$ final states

EXPS	LAB	REACTION	PBEAM(GEV/C)	YEAR
ICE	IHEP	$\pi^- p \to \eta\pi^0 n$	40	1981[24]
GAMS	CERN	$\pi^- p \to \eta\pi^0 n$	100	1988[25]
BENKEI	KEK	$\pi^- p \to \eta\pi^- p$	6.3	1993[26]
VES	IHEP	$\pi^- N \to \eta\pi^- X$	37	1993[27]
E852	BNL	$\pi^- p \to \eta\pi^- p$	18	1997[28]
CBL	CERN	$\bar{p}d \to \eta\pi^-\pi^0 p$		1998[29]

Some experiments have been working on the search of the hybrid states with the exotic quantum number 1^{-+}. All the experiments, listed in Table 3.4-4, observed a clear forward-backward asymmetry and each of them, except NICE, suggested or claimed the evidence of an exotic $J^{PC}=1^{-+}$ resonance $\hat{\rho}(1400)$. Of them, VES and E852 gave consistent results. In Crystal Barrels results on $\bar{p}d \to \eta\pi^-\pi^0 p$, the Dalitz plot is dominated by $\rho^- \to \pi^-\pi^0$, and there is a clear $\eta\pi$ P-wave which interferes with it. The fit to the Dalitz plot is improved when $\hat{\rho}(1400)$ is included and the mass and width of $\hat{\rho}$ are quite consistent with those from E852 experiment. E852 also found the evidence of another 1^{-+} exotic $\hat{\rho}(1600)$[30], decaying to $\rho\pi$, in $\pi^- p \to \pi^-\pi^+\pi^- p$ reaction, with the mass and width being 1593±8 MeV/c^2 and 168±20 MeV/c^2. Tentative evidence was put forward by the VES collaboration in $\eta'\pi$ from $\pi^- N \to \pi^-\eta' N$ process. VES saw a broad but resonant P_+ wave near this mass, however, the phase motion is not distinctive.

At BESIII/BEPCII, the decay of $J/\psi \to \rho\eta\pi$ can be studied to search for 1^{-+} exotic state. As an example, 6×10^9 $J/\psi \to \rho\eta\pi^0$ Monte Carlo events are generated to pass through BESIII detector. In the simulation, the possible $a_2(1320)$, 1^{-+} X(1390), $a_0(980)$ and 1^{-+} X(2300), as well as background are considered. A partial wave analysis (PWA) is performed to analyze this channel. Fig.3.4-7 shows the invariant mass spectrum of $\eta\pi^0$. In Fig.3.4-8, the contribution of $a_2(1320)$ and the scan results of its mass and width are plotted. The minimum of the scan curve stands for the mass or width of this resonance. The 1^{-+} X(1390) component is shown in Fig. 3.4-9. From this Monte Carlo study, we know that the angular distributions of $a_2(1320)$ and 1^{-+} X(1390) are very different due to their different spin-parities, even though the masses are in the same region. Partial wave analysis is able to separate components which have different spin-parities but at the same mass, when the statistics is enough and the resolution of the spectrum is good. With a large statistics, it is also possible to measure the phase motion of P-wave and so to give a more convincing evidence for the existence of a resonance.

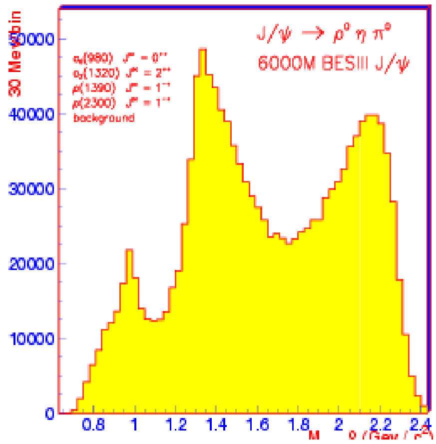

Fig.3.4-7 the invariant mass spectrum of $\eta\pi^0$

Some phenomenological models predict that the dominant decay channels of exotic mesons are $\pi b_1(1235)$ and $\pi f_1(1285)$. The dominant decay channel of b_1 is $\omega\pi$ and the dominant decay channels of f_1 are $\eta\pi\pi$ and 4π. So, it seems that these exotic states should appear in the invariant mass spectrum of 5π or $\eta 3\pi$. If these exotic states are produced through $J/\psi \to \rho X$, then we had to study the following decay channels: $J/\psi \to \rho X$, $X \to \pi\omega\pi$; $J/\psi \to \rho X$, $X \to 5\pi$; $J/\psi \to \rho X$, $X \to \eta 3\pi$. In addition, we can study iso-scalar exotic mesons through the following channels: $J/\psi \to \omega X$, $X \to \pi\, \pi(1300)$, $\pi(1300) \to \rho\pi$; $J/\psi \to \omega X$, $X \to \pi\, a_1(1260)$, $a_1(1260) \to \rho\pi$; $J/\psi \to \omega X$, $X \to K\, K_1(1400)$, $K_1(1400) \to K^*\pi$.

Since there are lots of neutral and charged tracks in each channel, a large coverage of solid angle is necessary to preserve a high event selection efficiency. Good energy resolution for neutral and charged tracks is also required to accurately measure the mass and width of these exotic states.

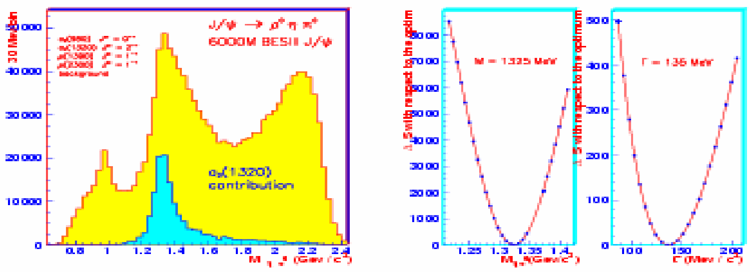

Fig. 3.4-8 The contribution of $a_2(1320)$ and the scan results of its mass and width

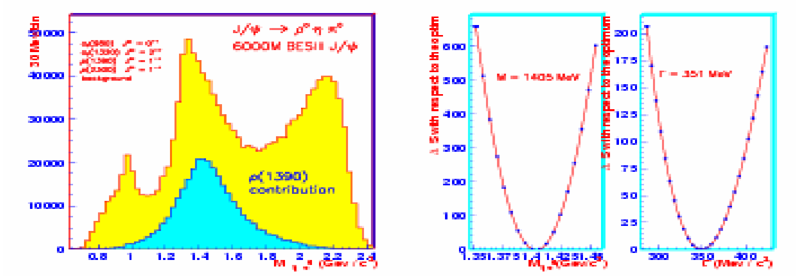

Fig. 3.4-9 The contribution of 1^{-+} X(1390) and the scan results of its mass and width

Reference

[1] Yukawa H., 1935, Proc. Phys-Mass. Soc. (Japan) 17, 48.

[2] Zweig, Z. 1964 CERN preprint 8419/ TH.412, 8182/TH.401

Gell-mann, M., Phys. Lett. 8 (1964) 214

[3] Greenberg, O.W., Phys. Rev. Lett., 13 (1964) 598

[4] Aubert, J. J., Phys. Rev. Lett., 33 (1974) 1404

Augustin, J. E., Phys. Rev. Lett., 33 (1974) 1406

[5] Fritzch, M., M. Gell-mann et. al., Phys. Lett. 47B (1971) 365

Weinberg, S., Phys. Rev. Lett. 31 (1973) 494

[6] Godfrey S., et al, Rev. Mod. Phys., 71 (1999) 1411

[7] BES Colalboration, Phys. Lett., B510 (2001) 75

[8] Barnes T., F. E. Close, et al., Nucl. Phys. B224 (1983) 241

[9] Isgur N., et al., Phys. Rev. D 31 (1985) 2910

[10] Latorre, J.L., et al., Phys. Lett. 147B (1984) 169

[11] Michael, C., et al., Nucl. Phys. B314 (1989) 347

Bali, et al., Phys. Lett., B309 (1993) 378

Morningstar, C., et al., Phys. Rev. D 56 (1997) 4043

[12] Amsler, C., et al., CBR collaboration, Phys. Lett., B340 (1994) 259

Amsler, C., et al., CBR collaboration, Phys. Lett., B355 (1995) 425

[13] Abele, A., et al., CBR collaboration, Phys. Lett. B380 (1996) 453

Abele, A., et al., CBR collaboration, Phys. Lett. B385 (1996) 425

Abele, A., et al., CBR collaboration, Nucl. Phys. A609 (1996) 562

[14] Antinori, F., et al., WA91 collaboration, Phys. Lett., B353 (1995) 589

[15] arberis, D., et al., WA102 collaboration, Phys. Lett., B413(1997) 217
[16] Bugg, D., et al., Phys. Lett., B353 (1995) 378
[17] Bai, J. Z., et al., BES collaboration, Phys. Lett. B472(2000)207
[18] Baltrusaitis, R. M., et al., Mark-III collaboration, Phys. Rev. Lett., 56(1986)107
[19] Alde, D., et al., GAMS collaboration, Phys. Lett., B177(1986) 120
[20] Bai, J. Z., et al., BES collaboration, Phys. Rev. Lett., 76(1996) 3502
Bai, J. Z., et al., BES collaboration, Phys. Rev. Lett., 81(1998) 1179
[21] Godang, R., et al., CLEO collaboration, Phys. Rev. Lett., 79(1997) 3829
[22] Alam, M.S., et al., CLEO collaboration, Phys. Rev. Lett., 81(1998) 3328
[23] Evangelista, C., et al., JETSET collaboration, Phys. Rev. D56 (1997) 3803
[24] Apel, W. D. et al., Nucl. Phys. B193 (1981) 269
[25] GAMS collaboration, Phys. Lett., B205 (1988) 397
[26] Aoyagi, H. et al., Phys. Lett., B314 (1993) 246
[27] VES collaboration, Phys. Lett., B313 (1993) 276
[28] Thompson, D.R., et al., E852 collaboration, Phys. Rev. Lett., 79(1997) 1630
[29] Crystal Barrel collaboration, Phys. Lett., B423 (1998) 175
[30] Adams, G., et al., E852 collaboration, Phys. Rev. Lett., 81(1999) 5760

2.3.3 QCD and Hadronic Production

2.3.3.1 Motivation

As an unique candidate theory of strong interactions, the quantum chromodynamics (QCD) has had many great achievements in the description of hadronic interactions. Although it can describe the evolutions of the quark and gluon phases with large momentum transfer, it can not give a complete theoretical calculations from the primary quarks and gluons to hadrons in final states, due to its non-Abelian asymptotic freedom nature. Owing to historical reasons in the process of the development of the high energy physics, the studies of theory and experiments in high energy region (higher than 10 GeV, such as at TASSO, PETRA and LEP) are rather complete. The perturbative evolutions of QCD is dominant in the process of hadronization, and the hadronization mechanism for a given production channel is not critical,the hadronic final states can keep main features of the perturbative evolution of quark-gluons.

On the other hand, the studies of QCD and hadronization in the intermediate to low energy region are rather poor or even blank in many aspects. In this energy region, the main experiments in the past decades are hadronic decays of τ leptons and the hadronic total cross section (R value). The quest for the applicable range of pQCD has attracted special attention both in theory and experiments. More and more signs show that pQCD may give reasonable predictions down to the energy of about 2-3GeV, but still there are many questions to be studied in detail.

The standard model (SM) is supported by all the precision experiments so far. A few precise quantities measured in experiments are needed as the input parameters when calculating the higher order radioactive corrections. One such example is the R value for the coupling constant $\alpha(s)$. The running coupling constant $\alpha(s)$ changes with energy s:

$$\alpha(s) = \frac{\alpha}{1-\Delta\alpha(s)} \ ,$$

where, α is the coupling value at zero momentum limit, term $\Delta\alpha(s)$ comes from the contribution of the vacuum polarization of photons, which contains three parts,

$$\Delta\alpha = \Delta\alpha_l + \Delta\alpha_{had}^{(5)} + \Delta\alpha_{top} \, .$$

It is easy to calculate $\Delta\alpha_l$ which accounts for the contribution of leptons, while

$\Delta\alpha_{top}$ from the top-quark is very small. $\Delta\alpha_{had}^{(5)}$ comes from the contributions of other five quarks $(d\bar{d}, u\bar{u}, s\bar{s}, c\bar{c}, b\bar{b})$, which can be calculated by the dispersion relation and the optical theorem. In the calculation of $\Delta\alpha_{had}^{(5)}$, the R value play an important role and its error is the dominant contribution to the uncertainty of $\Delta\alpha_{had}^{(5)}$. At present,

$$\Delta\alpha(M_Z^2) = (593.2 \pm 4.5) \times 10^{-4}, \qquad \Delta\alpha_{had}^{(5)}(M_Z^2) = (278.9 \pm 4.5) \times 10^{-4}.$$

The precision of $\Delta\alpha(M_Z^2)$ is improved dramatically when the R value from BESII[1] are used.

In the global fitting of the standard model, the uncertainties of the theoretical predictions for the top guark mass M_t and the Higgs mass M_H are about 4 GeV and 150 GeV respectively. These uncertainties are the obstacle for the determination of M_H in standard model. This is one of main reasons that theorists and experimentalists appeal to measure R value with high precision at intermediate energies. The central value of Higgs mass changes to 88 GeV from 60 GeV when R values of BEPC/BESII were used. The measurement of R value at BEPC/BESII has important impact to the search of Higgs.

The R value at intermediate energies is related also to the muon anomalous magnetic moment $(g-2)$, which is considered as the best experiment to test QED. The new BNL-821 experiment[2] gave a_μ=(g-2)/2=11659203(15)$\times 10^{-10}$, a precision at $1.3\,ppm$ level. The theoretical value[3] of anomalous magnetic moment may be written as the sum of several terms, $a_\mu^{th} = a_\mu^{QED} + a_\mu^{had} + a_\mu^{weak}$, where a_μ^{QED} is the contribution from QED with a precision of 0.025ppm, a_μ^{weak} from the weak interactions of W、Z and Higgs with a precision of 0.003ppm, a_μ^{had} from the hadronic contributions of vacuum polarization, which can not be calculated reliably by QCD directly. Instead, a_μ^{had} may be obtained by using the dispersion integral with experimental R values at intermediate energies as in put. Thus, the experimental error of the R value has significant influence to a_μ^{had}. The result $a_\mu^{th} = 11659159.6(6.7) \times 10^{-10}$ (0.57ppm), and $a_\mu^{had} =$ $673.9(6.7) \times 10^{-10}$ (0.57ppm) shows that the uncertainty of the theoretical calculation comes mainly from the error of a_μ^{had} induced by R value. The error of BNL-E821 experiment and the theoretical calculation is at the same level and the difference between theory and experiment is $a_\mu^{\exp} - a_\mu^{th}$=(43±16) $\times 10^{-10}$, therefore, an improvement of precision both in theory and experiments are neceessary.

2.3.3.2 R Measurement at BEPCII/BESIII

In the energy region where perturbative theory is still available, pQCD gives the prediction of $R_{QCD}(s)$, varying with energy. In the non-resonant region and above the heavy flavor production threshold, the R values measured in experiments agree well with the pQCD prediction. But at intermediate energies, the pQCD calculations and the treatment of mass-effects have not been well solved, theoretical and experimental values are inconsistent significantly. The effort to measure R with high precise is obviously urgent both for theory and experiment.

R value is defined as the ratio

$$R = \frac{\sigma_0(e^+e^- \to \gamma^* \to hadrons)}{\sigma_0(e^+e^- \to \gamma^* \to \mu^+\mu^-)} \equiv \frac{\sigma_0^{had}(s)}{\sigma_0^{\mu\mu}(s)},$$

where, $\sigma_0^{had}(s)$ is measured by experiments, and $\sigma_0^{\mu\mu}(s)$ is Born cross section of di-muon production calculated by QED, and s the center of mass energy. In the history of accelerator physics, almost all e^+e^+ collider measured R value, which is actually the absolute hadron production cross section. The measurement of R concerns the selection of hadronic events, the subtraction of all kinds of background, the measurement of the luminosity, reliable hadronization model and its Monte Carlo simulation, hadronic detection efficiency (acceptance), the calculation of initial state radiative corrections, etc.

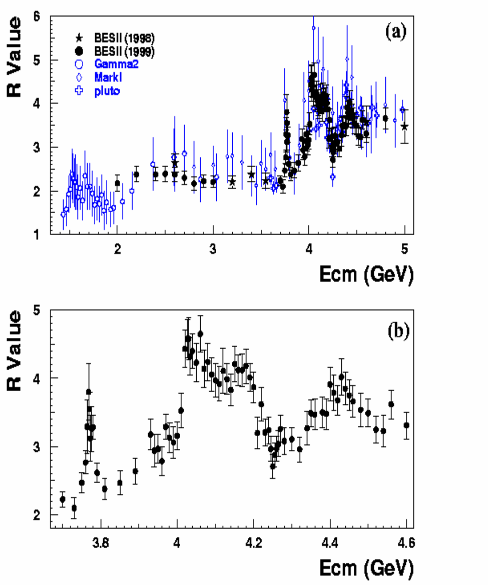

Fig.3.5-1 R value measured at BEPC/BESII

In 1998 and 1999, two scans of 6+85 energy points for R measurement were performed at BES[1], as shown in Fig.3.5-1. There are about 1000 – 2000 hadronic events for each point, and the total measurement error for each point is about 7%. Of course this successful experiment should not be the last measurement of R at BEPC/BES, it is necessary and inevitable to measure R with higher precise at BEPCII. Table 3.5-1 shows the impact of a better R measurement to $\Delta\alpha^{(5)}_{had}(M_z^2)$, in the case of no significant improvement in other energy regions, particularly below 2 GeV. It is clear that a reduction of R measurement error from 6% to 2-3% is very important, particularly taken into account the possibility that there may be improvement in the energy region below 2 GeV in the near future.

Table 3.5-1 The error of R and the corresponding uncertainty to $\Delta\alpha^{(5)}_{had}(M_Z^2)$

The error of R in $2-5GeV$	$\Delta\alpha^{(5)}_{had}(M_Z^2)$
5.9%	0.02761 ± 0.00036
3%	0.02761 ± 0.00030
2%	0.02761 ± 0.00029

The forthcoming BEPCII will run in the energy region of 2 – 4 GeV with a much higher luminosity , and BESIII has a better space and momentum resolution and good particle identification capabilities. A Monte Carlo simulation shows that a much improved efficiency and a reduction of systematic error can be expected. Fig. 3.5-2 shows the hadron efficiency as a function of cos θ and total energy deposited in CsI Calorimeter. Table 3.5-2 list the expected error of R measurement at BEPCII/BESIII with a comparison to that at BEPC/BESII.

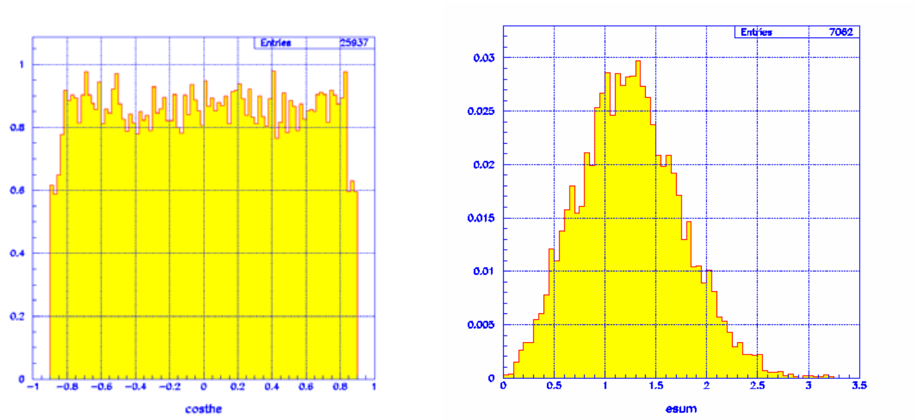

Fig. 3.5-2 The efficiency as a function of $\cos\theta$ and the energy deposition in the BESIII detector simulated by Monte Carlo at 3 GeV

Table 3.5-2. The errors of R measured at BESII and the errors of R predicted at BESIII

Sources of error	BESII	BESIII
Luminosity	2-3 %	1 %
Detective efficiency (acceptance)	3-4 %	1-2 %
Trigger efficiency	0.5 %	0.5 %
Radiative correction	1-2 %	1 %
Hadronization model	2-3 %	1-2 %
Statistical	2.5%	--
Total	6-7%	2-3%

2.3.3.3 Study of Hadron Production Properties

The BEPCII will run in the intermediate energy region (2-4 GeV), which is at the lower boundary of pQCD applicable region. The non-perturbative hadronization mechanism takes important role in the hadronic final states, and in addition resonant structures makes thing even move complex. Physics analysis are perplexed by the poor understanding of the hadronization mechanism and the hadronic spectra. On the other hand, it also offers a new field to study at BEPCII/ BESIII.

The main routine for the study of the strong interaction and the hadronic production processes is to measure various hadronic spectra, which can reveal the strong interaction from different aspects. The following are examples of possible topics.

(1) Inclusive Distribution

The inclusive spectra of final state hadrons are governed by hadronization dynamics, which imposes strict restrictions to hadron production models. The inclusive distributions of charged particle are easy to measure in experiments, and the corresponding one for neutral particles are similar to that of charged one since the strong interaction is charge-independent. In general, the single particle distributions are the function of $(s, p_{//}, p_{\perp})$. There are two questions needed to be answered: (a) how do the distributions change with momentum $(p_{//}, p_{\perp})$ when s is fixed? (b) how do the distributions change with the center of mass energy s? The answer to the first question depends on the type of the initial state and the properties of measured particles in the final state. Feynman supposed the scaling property for the second question, i.e. the single particle distributions are the function of the scaling variable x and the transverse momentum $p_{\perp}$ at large energies. The scaling assumption is a good approximation in high energies, but it has not been tested precisely at intermediate energies. The usually measured distributions are Feynman momentum

x_p and rapidity y. The running strong coupling constant $\alpha(s)$ may be determined by the scaling deviation.

(2) Exclusive Hadron Cross Sections

This is an important measurement similar to that of the branching ratios of J/ψ and $\psi^{'}$ decays. The exclusive cross sections have closer relations with the hadronic dynamics, and it provides an effective way to reduce the systematic error in the forthcoming R measurement at BEPCII/BESIII , since it can improve the hadron production model and the Monte Carlo generator.

(3) Multiplicity Distribution

The charged multiplicity distribution is a basic ingredient which are helpful to understand hadronization mechanism. These measurements need a reliable Monte Carlo simulation and efficiency matrix, which transfer the measured quantity to physical (theoretical) quantity.

(4) Kinematical and Dynamical Correlations

The study of the correlation effects is more useful to extract the dynamical information than that from the single particle spectrum. The correlation function is related to the hadronization mechanism closely, hence, it is a more rigorous test to hadronization model. In order to separate the pseudo-correlation from the true one, experiments can measure the correlation function as below

$$C(x_1, x_2) = C_L(x_1, x_2) + C_S(x_1, x_2),$$

where, x_1 and x_2 are any kinematical observable for two particles in one event, C_L and C_S are the so-called long-distance and short-distance correlation functions respectively.

(5) Topological shape of the Event

Any event produced in one collision has several final particles, and a set of kinematical parameters are needed to describe these particles, and the complicated geometries encountered in multi-hadron event. Usually, these are the event shape quantities, such as sphericity and thrust. QCD gives predictions for sphericity and thrust quantitatively, which are in good agreement with experimental results at high energies, but no test yet at intermediate energies.

(6) Bose-Einstein Correlation (BEC)

In quantum mechanics, the wave function of identical bosons is symmetric for the commute of any two bosons of the same kind. This property leads to a statistic correlation, called Bose-Einstein correlation (BEC). The symmetry leads to an interference term, which contains the space-time information of the hadronic (boson) sources. The manifestation of BEC is that the possibility of finding two identical bosons in a small phase-space is larger than that of two different particles. The Bose-Einstein correlation function and the space-time properties of hadronic source may be inferred by measuring the Bose-Einstein correlation functions. It is expected that the following subjects may be done for charged π (which are the most abundant bosons in the reactions at intermediate energy): (a) two-body correlation and the inflections of multi-body correlation; (b) The multiplicity dependence of BEC; (c) the space-time form of hadronic source; (d) BEC in the resonance decay. This measurement needs a large hadronic sample and excellent power of particle identification.

(7) Possible Fractal Structure of Final State Phase-Space

Events with abnormal high particle density condensed in a small phase-space have been observed in several high energy reactions. The important questions are the following: Do the anomalous fluctuations have their intrinsic dynamics origins? Is the phase-space of the final state isotropic or not? Is the phase-space continuous or fractal? Do the approximate intermittency observed at very high energies also exist at intermediate energies? Can the intermittency be explained by known theories (such as, cascade, BEC, etc.)? The study of this topic has two aspects: (a) Experimental measurement of fractal moments F_q and the Hurst index. For one dimension case, the phase-space variable may be chosen as the rapidity y, or the transverse momentum $p_\perp$, or azimuthal angle ϕ, and the combination of any two of them may be chosen for two-dimensional analysis. (b) The study of its mechanism, whether the asymptotic fractal behavior in the perturbative evolution of partons can be kept after the hadronization process?

(8) Determination of $\alpha_s(s)$

To measure the running coupling constant of the strong interaction and to test and verify the asymptotic freedom of QCD at low energies are still interesting. $R_{QCD}(s;\alpha_s)$ can be expanded as series of $\alpha_s(s)$ in pQCD, therefore, $\alpha_s(s)$ can be obtained directly from the measurement of R. The uncertainty of $\alpha_s(s)$ is about the order of $\Delta\alpha_s(s) \approx \Delta R_{\exp}(s)/R_{\exp}(s)$.

(9) Electro-magnetic form Factors

For the exclusive hadron production, cross section is written as the function of form factor, which embody properties of the vertex of electromagnetic interactions with influence of strong interactions. The following channels,

$\pi^+\pi^-, \pi^+\pi^+\pi^-\pi^-, \pi^+\pi^- K^+ K^-, p\overline{p}$ can be measured to promote the understanding of strong interactions.

Reference

[1] J.Z. Bai et al., Phys. ReV. Lett. 84(2000)594,

J.Z. Bai et al., Phys. ReV. Lett. 88(2002)101802.

[2] H.N. Brown et al., Phys. Rev. Lett. 86(2001)2227

[3] F. Jegerlehner, J. phys. G29(2003)101

K. Melnikov, Int. J. Mod. phys. A16(2001)4591

3.5 Charmornium Physics

In charmornium family, $\psi(2S)$ is in a special position. $\psi(2S)$ can decay into η_c, J/ψ, χ_{cJ} (J=0,1,2), and possibly into $^1P_1$ states. Therefore, by collecting sufficiently large $\psi(2S)$ data sample, one can not only study the property of $\psi(2S)$, η_c, J/ψ, χ_{cJ} (J=0,1,2), but also search for $^1P_1$ states.

The $\psi(2S)$ data sample collected at BEPC/BESI is 4 millions, and at BEPC/BESII 14 millions, with which the BES collaboration has made various studies on $\psi(2S)$, J/ψ and χ_{cJ} (J=0,1,2), and copious results have been reported[1-14]. At BEPCII, one year running will produce 3×10^9 $\psi(2S)$ events, which is a factor of 150 more than that at the BESI and the BESII combined. Statistical error will be improved by at least a factor of 12. In addition, the designed performance of the BESIII detector is much improved with respect to that of BESII, the systematic error is expected to be reduced by a factor of 4 on average for all measurements.

3.5.1 ψ(2S) Decays

1. Hadronic Decays

The BES collaboration has measured branching fractions or upper limits for various hadronic decay channels listed in Table 3.6-1. The statistical errors are in the range of 10% to 30%, and the systematic errors are in similar values. At BEPCII/BESIII, the statistical and systematic errors will be reduced to (1-3)% and (2.5-8)%, respectively, corresponding to a total error of (2.7-8)%. For the upper limits, the sensitivity of BESIII will improve by a factor of at least 100.

Since J/ψ and $\psi(2S)$ decays into light hadrons via ggg, γ^*, or γgg, their partial widths of decays are proportional to $|\psi(0)|^2$, where $\psi(0)$ is the wave function at the origin in the non-relativistic quark model for $c\bar{c}$. Thus, it is reasonable to expect[15] on the basis of the perturbative QCD that, for any hadronic final state h, the ratio Q_h should follow:

$$Q_h \equiv \frac{B(\psi(2S) \to h)}{B(J/\psi \to h)} \cong \frac{B(\psi(2S) \to e^+e^-)}{B(J/\psi \to e^+e^-)} = (14.8 \pm 2.2)\% \qquad (1)$$

where the leptonic branching fractions are taken from PDG2000[15]. This relation is sometimes called PQCD 15% rule. The Q_h values measured at BES for various $\psi(2S)$ hadronic decays based on PDG's value for J/ψ branching fractions are listed in Table 3.6-1.

Most of decay channels, including AP($b_1\pi$), VS(ϕf_0), $B\bar{B}$

($p\bar{p},\Lambda\bar{\Lambda},\Sigma^0\bar{\Sigma}^0,\Xi^-\bar{\Xi}^+,\Delta^{++}\bar{\Delta}^{--},\Sigma^{*-}\bar{\Sigma}^{*+}$) and multi-hadron final states, have relative branching fractions in agreement with PQCD expectations. The intriguing puzzle, reported in 1983 by the Mark II experiment[12], is that the Q_h for $\rho\pi$ and $K^+\bar{K}^{*-}+c.c.$ are one order of magnitude lower than PQCD expectations. This is confirmed by the BES results with much higher sensitivity[7]. The upper limits on the branching fractions of $\psi(2S)\to\rho\pi$ and $\psi(2S)\to K^+\bar{K}^{*-}+c.c.$ are found to be more than a factor of 60 and 20, respectively, lower than the 15% rule predictions. The four $\psi(2S)\to VT$ decay modes($\omega f_2,\rho a_2,\phi f_2^{'},K^{*0}\bar{K}_2^{*0}$) are suppressed also by a factor of at least 3[2]. For the AP decay channel, the BES collaboration observed flavor-SU(3)-violating $K_1(1270)$-$K_1(1400)$ asymmetries with opposite characters for the ψ(2S) and J/ψ [5], which cannot be accommodated by adjustments of the singlet-triplet mixing angle[18]. All these suppressions and anomaly can be further studied with higher accuracy and higher statistics at BEPCII/BESIII.

Table 3.6-1 BESI measured ψ(2S) decay branching fractions and PQCD 15% rule test(# denotes preliminary results; upper limits at C.L.=90%)

	Channel	Br(ψ(2S)) (10^{-4})	Br(J/ψ) (10^{-3})	Q_h (%)
γX	$\gamma\eta$	$0.53\pm0.31\pm0.08$	0.86 ± 0.08	6.2 ± 3.8
	$\gamma\eta'$	$1.54\pm0.31\pm0.20$	4.31 ± 0.30	3.6 ± 0.9
AP	$b_1\pi$	$5.2\pm0.8\pm1.0$	3.0 ± 0.5	17.3 ± 5.1
	$K_1^{\pm}(1270)K^{\mp}$	$10.0\pm1.8\pm2.1$	<3.0	>33.3
	$K_1^{\pm}(1400)K^{\mp}$	<3.1	3.8 ± 1.4	<8.2
VT	ωf_2	<1.7	4.3 ± 0.6	<4.0
	ρa_2	<2.3	10.9 ± 2.2	<2.1
	$\varphi f_2'(1525)$	<4.5	$1.23\pm0.06\pm0.20$	<3.7
	$K^{*0}\bar{K}_2^{*0}+c.c.$	<1.2	6.7 ± 2.6	<1.8
	$\#K^{*0}\bar{K}_2^{*0}+c.c.$	0.798 ± 0.528	6.7 ± 2.6	1.20 ± 0.93
VP	$\#\rho\pi$	<0.29	12.8 ± 1.0	<0.23

	# $K^+\overline{K}^{*-}(892)+c.c.$	<0.23	5.0 $\pm$ 0.4	< 0.46
	# $K^0\overline{K}^{*0}(892)+c.c.$	1.30 $\pm$ 0.34 $\pm$ 0.16	4.2 $\pm$ 0.4	3.1 $\pm$ 1.0
VS	# φf_0	0.63 $\pm$ 0.18	0.32 $\pm$ 0.09	19.6 $\pm$ 7.8
VV	$K^{*0}\overline{K}^{*0}+c.c.$	0.392 $\pm$ 0.103	0.29 $\pm$ 0.04 $\pm$ 0.06	13.6 $\pm$ 4.9
	# ωK^+K^-	1.25 $\pm$ 0.56	0.74 $\pm$ 0.24	16.9 $\pm$ 9.4
	# $\omega p\overline{p}$	0.64 $\pm$ 0.26	1.30 $\pm$ 0.25	5. $\pm$ 2.2
	# $\varphi\pi^+\pi^-$	1.68 $\pm$ 0.32	0.80 $\pm$ 0.12	21.0 $\pm$ 5.1
	# φK^+K^-	0.58 $\pm$ 0.22	0.83 $\pm$ 0.13	7.0 $\pm$ 2.9
	# $\varphi p\overline{p}$	0.082 $\pm$ 0.052	0.045 $\pm$ 0.015	18.1 $\pm$ 12.8
	# $K^*K^-\pi^+ +c.c.$	6.04 $\pm$ 0.90		
	# $\pi^+\pi^-\pi^0 p\overline{p}$	3.49 $\pm$ 0.64	2.3 $\pm$ 0.9	15.2 $\pm$ 6.6
	# $\eta\pi^+\pi^- p\overline{p}$	2.47 $\pm$ 0.96		
	# $\eta p\overline{p}$	<1.8	2.09 $\pm$ 0.18	< 8.6
BB	$p\overline{p}$	2.16 $\pm$ 0.39	2.12 $\pm$ 0.10	10.1 $\pm$ 1.9
	$\Lambda\overline{\Lambda}$	1.81 $\pm$ 0.34	1.30 $\pm$ 0.12	13.9 $\pm$ 2.9
	$\Sigma^0\overline{\Sigma}^0$	1.2 $\pm$ 0.6	1.27 $\pm$ 0.17	9.4 $\pm$ 4.6
	$\Xi^-\overline{\Xi}^+$	0.94 $\pm$ 0.31	0.9 $\pm$ 0.2	10.4 $\pm$ 4.1
	$\Delta^{++}\overline{\Delta}^{--}$	1.28 $\pm$ 0.35	1.10 $\pm$ 0.29	11.6 $\pm$ 4.5
	$\Sigma^{*-}\overline{\Sigma}^{*+}$	1.1 $\pm$ 0.4	1.03 $\pm$ 0.13	11 $\pm$ 4

	$\Xi^{*0}\overline{\Xi}^{*0}$	<0.81		
	$\Omega^{-}\overline{\Omega}^{+}$	<0.73		

2. Radiative Decays

By using the Vector Dominance model, a radiative decay might (or might not) be connected to the corresponding hadronic decay. It is therefore interesting to examine whether suppressions exist for radiative decays too. The BESI has measured the branching fractions of $\gamma\eta, \gamma\eta'$ channels (also listed in Table 3.6-1) and calculates the corresponding $Q_{\gamma\eta}$=6.2% and $Q_{\gamma\eta'}$=3.6%, clearly a suppression by a factor of about 2 and 4, respectively. We will further study these suppressions and extend to more channels, such as $\gamma\pi^0, \gamma f_1, \gamma f_2, \gamma f_2', ...$ etc. at BEPCII/BESIII with higher accuracy and statistics. BEPCII also provides an opportunity to search for glueball candidates such as η(1440), f_J (1710), ξ(2230), etc. via radiative decays.

3.5.2 J/ψ Letponic Decay Width

BESI has determined the most accurate branching fraction of J/ψ leptonic decay

$$B(l^+l^-) = (5.87 \pm 0.04 \pm 0.09)\%^{[3]},$$

via processes of $\psi(2S) \to \pi^+\pi^- J/\psi, J/\psi \to l^+l^-, J/\psi \to anything$.

At BEPCII/BESIII, the statistical error will be negligible and systematic error will be reduced to 0.03%, thus the relative error of $B(l^+l^-)$ will be lower than 0.5%.

3.5.3 χ_{cJ} Physics

BESI has measured many branching fractions of χ_{cJ} decays[6], with much improved accuracies and many of them the first measurements (see Table 3.6-2). From PDG1998[19] to PDG2000 [16], the scenery for χ_{cJ} decays are greatly changed. However, the statistical and systematic errors for χ_{cJ} decay branching fractions are still too large, at the level of (6-20)% and (15-30)% respectively. At BEPCII/BESIII, the statistical errors will be negligible and the systematic errors will be reduced to about (4-8)%.

The widths of χ_{cJ} decaying into light hadrons are theoretically interesting, since the contribution of the color octet component in the $c\bar{c}$ wave function might also be involved, in addition to the ^3P_J color singlet component, according to the NRQCD theory [15]. The widths of χ_{cJ} and χ_{c2} are measured precisely by E760, and the width of χ_{c0} by BESI[6]. At BEPCII/BESIII, the error of χ_{c0} can be reduced by a factor of two.

A careful study of the angular distribution of the radiative decay $\chi_{cJ} \to \gamma J/\psi$ with high statistics at BESIII will provide more information on the transition matrix elements, which are closely related to the $c\bar{c}$ wave functions and interquark forces.

Table 3.6-2 Measured χ_{cJ} width and branching fractions by the BESI.
(upper limits at C.L.=90%)

Channel	BES results	PDG2000
$\chi_{c0} \to \pi^+\pi^-$	$(4.68 \pm 0.26 \pm 0.65) \times 10^{-3}$	$(5.0 \pm 0.7) \times 10^{-3}$
$\chi_{c2} \to \pi^+\pi^-$	$(1.49 \pm 0.14 \pm 0.22) \times 10^{-3}$	$(1.52 \pm 0.25) \times 10^{-3}$
$\chi_{c0} \to K^+K^-$	$(5.68 \pm 0.35 \pm 0.85) \times 10^{-3}$	$(5.9 \pm 0.9) \times 10^{-3}$
$\chi_{c2} \to K^+K^-$	$(0.79 \pm 0.14 \pm 0.13) \times 10^{-3}$	$(8.1 \pm 1.9) \times 10^{-4}$
$\chi_{c0} \to p\bar{p}$	$(1.59 \pm 0.43 \pm 0.53) \times 10^{-4}$	$(2.2 \pm 1.3) \times 10^{-4}$
$\chi_{c1} \to p\bar{p}$	$(4.2 \pm 2.2 \pm 2.8) \times 10^{-5}$	$(8.2 \pm 1.3) \times 10^{-5}$
$\chi_{c2} \to p\bar{p}$	$(5.8 \pm 3.1 \pm 3.2) \times 10^{-5}$	$(9.8 \pm 1.0) \times 10^{-5}$
$\chi_{c0} \to \pi^+\pi^-\pi^+\pi^-$	$(15.4 \pm 0.5 \pm 3.7) \times 10^{-3}$	$(2.0 \pm 0.9) \times 10^{-2}$
$\chi_{c1} \to \pi^+\pi^-\pi^+\pi^-$	$(4.9 \pm 0.4 \pm 1.2) \times 10^{-3}$	$(5.6 \pm 2.6) \times 10^{-3}$
$\chi_{c2} \to \pi^+\pi-\pi^+\pi^-$	$(9.6 \pm 0.5 \pm 2.4) \times 10^{-3}$	$(1.2 \pm 0.5) \times 10^{-2}$
$\chi_{c0} \to \pi^+\pi^-K^+K^-$	$(14.7 \pm 0.7 \pm 3.8) \times 10^{-3}$	$(1.8 \pm 0.6) \times 10^{-2}$
$\chi_{c1} \to \pi^+\pi^-K^+K^-$	$(4.5 \pm 0.4 \pm 1.1) \times 10^{-3}$	$(4.9 \pm 1.2) \times 10^{-3}$
$\chi_{c2} \to \pi^+\pi^-K^+K^-$	$(7.9 \pm 0.6 \pm 2.1) \times 10^{-3}$	$(1.0 \pm 0.4) \times 10^{-2}$
$\chi_{c0} \to \pi^+\pi^-p\bar{p}$	$(1.57 \pm 0.21 \pm 0.54) \times 10^{-3}$	$(1.8 \pm 0.9) \times 10^{-3}$
$\chi_{c1} \to \pi^+\pi^-p\bar{p}$	$(0.49 \pm 0.13 \pm 0.17) \times 10^{-3}$	$(5.4 \pm 2.1) \times 10^{-4}$
$\chi_{c2} \to \pi^+\pi^-p\bar{p}$	$(1.23 \pm 0.20 \pm 0.35) \times 10^{-3}$	$(1.4 \pm 0.6) \times 10^{-3}$
$\chi_{c0} \to 3(\pi^+\pi^-)$	$(11.7 \pm 1.0 \pm 2.3) \times 10^{-3}$	$(1.24 \pm 0.22) \times 10^{-2}$
$\chi_{c1} \to 3(\pi^+\pi^-)$	$(5.8 \pm 0.7 \pm 1.2) \times 10^{-3}$	$(6.3 \pm 1.4) \times 10^{-2}$
$\chi_{c2} \to 3(\pi^+\pi^-)$	$(9.0 \pm 1.0 \pm 2.0) \times 10^{-3}$	$(9.2 \pm 2.2) \times 10^{-3}$
$\chi_{c0} \to K_s^0K_s^0$	$(1.96 \pm 0.28 \pm 0.52) \times 10^{-3}$	
$\chi_{c2} \to K_s^0K_s^0$	$(0.61 \pm 0.17 \pm 0.16) \times 10^{-3}$	
$\chi_{c0} \to \varphi\varphi$	$(0.92 \pm 0.34 \pm 0.38) \times 10^{-3}$	
$\chi_{c2} \to \varphi\varphi$	$(2.00 \pm 0.55 \pm 0.61) \times 10^{-3}$	
$\chi_{c0} \to K^+K^-K^+K^-$	$(2.14 \pm 0.26 \pm 0.40) \times 10^{-3}$	
$\chi_{c1} \to K^+K^-K^+K^-$	$(0.42 \pm 0.15 \pm 0.12) \times 10^{-3}$	
$\chi_{c2} \to K^+K^-K^+K^-$	$(1.48 \pm 0.26 \pm 0.32) \times 10^{-3}$	
$\chi_{c0} \to K_s^0K^+\pi^- + c.c.$	$< 0.71 \times 10^{-3}$	

$\chi_{c1} \to K_s^0 K^+ \pi^- + c.c.$	$(2.46 \pm 0.44 \pm 0.65) \times 10^{-3}$	
$\chi_{c2} \to K_s^0 K^+ \pi^- + c.c.$	$< 1.06 \times 10^{-3}$	
$\Gamma_{\chi_{c0}}$	$14.3 \pm 2.0 \pm 3.0$ MeV	14.9+2.6-2.3MeV

The radiative decay rates of $\chi_{c0}, \chi_{c2} \to 2\gamma$ are also interesting, to which both QCD radiative correction and relativistic correction may be important. The estimated branching ratio is roughly

$$B(\psi(2S) \to \gamma\chi_{c0}) \times B(\chi_{c0} \to 2\gamma) \cong 0.09 \times 4 \times 10^{-4} = 3.6 \times 10^{-5} \tag{2}$$

Due to the limited statistics and poor photon energy resolution, this measurement is not feasible at BEPC/BESI. However, with one year of running at BEPCII, about 40000 signal events of this channel can be collected(assuming an efficiency of 40%) , which will produce a statistic uncertainty no more than 1%.

The χ_{cJ} may decay into light hadrons via gluon intermediate state, e.g., $\chi_{c0} \to 2g \to$hadrons. It is plausible that a pair of glueballs could be favorably produced in its decay process. With higher statistics and better particle ID of BEPCII/BESIII, it is possible to study hadronic decays like

$$\chi_{c0} \to 2(\pi^+\pi^-), \pi^+\pi^-\eta\eta, \pi^+\pi^-\eta\eta', \eta\eta\eta\eta, K\overline{K}\pi K\overline{K}\pi, ... \tag{3}$$

and look for some 0^{++} and 0^{-+} glueballs, e.g.,

$$\begin{aligned} &f_0(1500) \to \pi\pi, \eta\eta, \eta\eta'', && f_0(1400) \to \pi\pi, \\ &f_0(975) \to \pi\pi, K\overline{K}, && \eta(1440) \to K\overline{K}\pi. \end{aligned} \tag{4}$$

3.5.4 $^1P_1$ Search

The R704[23], E760[24] and E705[25] experiments claimed the existence of $^1P_1$ state in 1986, 1992 and 1994, respectively. However, the signal statistics is so low(5, 59 and 42 events respectively in these three experiments) that the existence of the $^1P_1$ state still needs to be confirmed.

Some theoretical calculations taking into account the effect of S-D mixing[21] gives

$$B(\psi(2S) \to {}^1P_1\pi^0) = 2 \times 10^{-4} \tag{6}$$

In addition, $^1P_1 \to \gamma\eta_c$ is expected to be the dominant decay mode. Therefore, we can search for $^1P_1$ via the decay mode

$$\psi(2s) \to \pi^0\, {}^1P_1 \to \gamma\gamma\eta_c \to \gamma\gamma 4K\ . \tag{7}$$

The branching ratio of η_c to 4K is 2.1×10^{-2}, so the total branching ratio of (7) is 2.9×10^{-6}. From 3×10^9 $\psi(2S)$ event, we can obtain 8700 event, which is enough for confirming the existence of $^1\mathrm{P}_1$.

Table 3.6-3 Signal and background channels in $^1\mathrm{P}_1$ search

	$\psi(2S)\to n\gamma+4\,\mathrm{Pr}ong$	$B(10^{-6})$	No. Of MC events
0	$\psi(2S)\to\pi^{0}\,{}^{1}P_1\to\gamma\gamma\eta_c\to\gamma\gamma 4K$	2.90	8700
1	$\psi(2S)\to\gamma\chi_{c1}\to\gamma\gamma J/\psi\to\gamma\gamma\gamma\phi\phi\to\gamma\gamma 4K$	2.29	6870
2	$\psi(2S)\to\gamma\chi_{c2}\to\gamma\gamma J/\psi\to\gamma\gamma\gamma\phi\phi\to\gamma\gamma\gamma 4K$	1.02	3060
3	$\psi(2S)\to\eta J/\psi\to\gamma\gamma\gamma\phi\phi\to\gamma\gamma\gamma 4K$	1.02	3060
4	$\psi(2S)\to\pi^0\pi^0 J/\psi\to 5\gamma\phi\phi\to 5\gamma 4K$	17.26	51780
5	$\psi(2S)\to\pi^0\pi^0 J/\psi\to\pi^0\pi^0\phi K\bar{K}\to 4\gamma 4K$ $\psi(2S)\to\pi^0\pi^0 J/\psi\to\pi^0\pi^0 4K\to 4\gamma 4K$	88 127	645000 (sum of two)

From Table 3.6-3 we can see that most of the background channels have J/ψ resonance. For J/ψ , the branching ratios of 4K+X is less than those of $(\gamma)\pi^+\pi^-\pi^+\pi^-,(\gamma)\pi^+\pi^-K^+K^-,(\gamma)K^\pm\pi^\mp\pi^+\pi^-$. This makes the search much easier through $3\gamma 4K$ than through $3\gamma\pi^+\pi^-\pi^+\pi^-$, $3\gamma\pi^+\pi^-K^+K^-$, $3\gamma K^\pm\pi^\mp\pi^+\pi^-$. In the process, $^1\mathrm{P}_1$ is almost at rest. Therefore the signal event has the following characters that we can use to select the signal and reject the background.

1) $M_{4K}\approx 2980MeV$ (the mass of η_c)

2) $M_{4K,\gamma}\approx 3526MeV$ (the mass of $^1\mathrm{P}_1$)

3) $E_{\gamma 1}\approx 504\,MeV$ ($\gamma 1$ is almost monotonous energy)

4) $\cos\theta_{4K,\gamma 1}\approx -1$

5) $M_{\gamma_2\gamma_3}\approx M_{\pi 0}$

Based on the parameters of BEPCII/BESIII, a full simulation of $3\times 10^9\,\psi(2S)$ events is performed.

After all the selection, the backgrounds is only 1%, as shown in Fig. 3.6-1—3.6-2. We can see that the peaks of $^1P_1$ and η_c can be observed clearly.

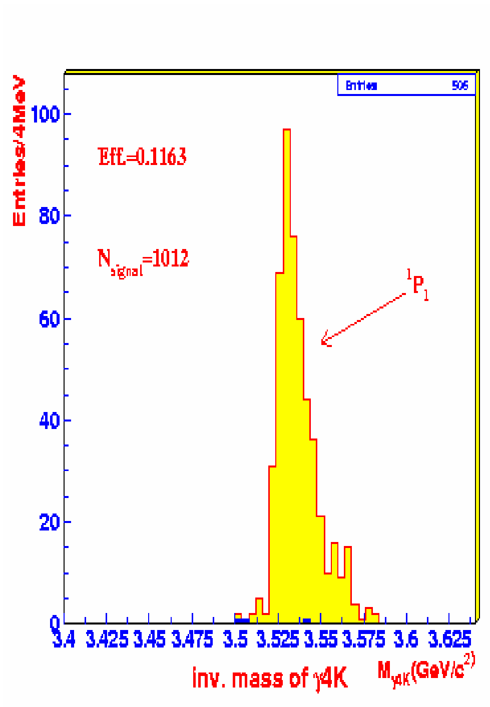

Fig 3.6-1. invariant mass of γ_1 4K（1T）for $^1P_1$ signal

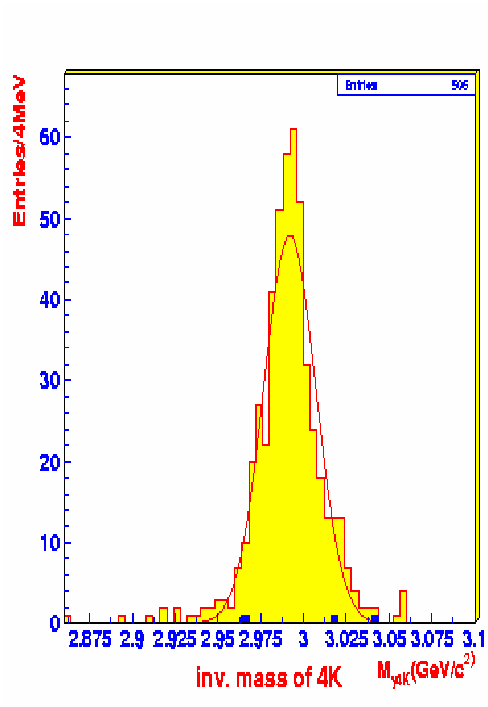

Fig.3.6-2. invariant mass of 4K（1T）for η_c signal

Reference

[1] J.Z.Bai et al., BES Collab., Phys. Rev. Lett. 81 (1998) 3091.

[2] J.Z.Bai et al., BES Collab., Phys. Rev. Lett. 81 (1998) 5080.

[3] J.Z.Bai et al., BES Collab., Phys. Rev. D58 (1998) 092006.

[4] J.Z.Bai et al., BES Collab., Phys. Rev. D58 (1998) 097101.

[5] J.Z.Bai et al., BES Collab., Phys. Rev. Lett. 83 (1999) 1918.

[6] J.Z.Bai et al., BES Collab., Phys. Rev. D60 (1999) 072001.

[7] J.Z.Bai et al., BES Collab., Phys. Rev. D62 (2000) 032002.

[8] J.Z.Bai et al., BES Collab., Phys. Rev. D63 (2001) 032002.

[9] J.Z.Bai et al., BES Collab., Phys. Rev. D65 (2002) 052004.

[10] X.H.Li, representing BES Collab., Nucl. Phys. B (Proc. Suppl.) 75B (1999) 181.

[11] F.Liu, representing BES Collab., Nucl. Phys. A675 (2000) 71c.

[12] X. Y. Shen, representing BES Collab., Recent results from BES, IV Intern. Conf. on Hyperons, Charm and Beuty Hadrons. June 26-30, 2000, Valencia, Spain. Will be published in Nucl. Phys..

[13] Y.S. Zhu representing BES Collab.,Recent results of charmonium physics from BES, Proc. 30th Inter. Conf. on High Energy Physics,Jul.27-Aug.2,2000,Osaka, Japan

[14] Y.S.Zhu, representing BES Collab., Recent results of $\psi(2S)$ decay branching ratios and dacay widths from BES,IX Inter. Conf. on Hadron Spectroscopy, Aug.26-Sep.1,2001,Protvino,Russia.

[15] S.J. Brodsky and M.K. Karliner, Phys. Rev. Lett. 78 (1997) 468,Yu-Qi Chen and Eric Braaten, Phys. Rev. Lett. 80 (1998) 5060; and references therein.

[16] D.E.Groom et al., Particle Data Group, Eur. Phys. J. C15 (2000) 1.

[17] M.E.B. Franklin et al., Mark II Collab., Phys. Rev. Lett. 51 (1983) 963.

[18] Preliminary results from this analysis are discussed in the context of SU(3) symmetry breaking, in M. Suzuki, Phys. Rev. D55 (1997) 2840.

[19] C.Caso et al., Particle Data Group, Euro. Phys. J. C3(1998) 1.

[20] G.T.Bodwin et al., Phys. Rev. D46 (1992) 1914.

[21] C.Z.Yuan, BES97(1997)191.

[22] Edwards et al.Phys.Rev.Lett. 1982,48:70.

[23] C.Baglin et al., Phys. Lett. B171 (1986) 135

[24] T.A.Armstrong et al., Phys. Rev. Lett. 69 (1992) 2337

[25] L. Antoniazzi et al., Phys.Rev. D50 (1994) 4258

[26] Y.P.Kuang et al., Phys. Rev. D37 (1988) 1210

2.3.4 Tau Physics

2.3.4.1 Current Status and Prospects of the τ Lepton Physics

The τ lepton physics has achieved a great progress since its discovery in 1975. Particularly in the last ten years, it starts to become a precision physics, thanks to high statistics data samples and high quality detectors, mainly at high energy e^+e^- colliders running in the ϒ energy range (DORIS and CESR) and at the Z^0 peak (SLC and LEP)[1]. In addition, the BES experiment at BEPC running at the threshold of the τ pair production, measured the mass of the τ lepton precisely[2]. The τ physics study will be continued in the high energy region at the asymmetric e^+e^- colliders of B factories (KEK-B and PEP-II) over the next decade.

While the efforts in τ lepton physics at high energy e^+e^- colliders have been quite successful, there still exist both unique and complementary possibilities at lower energy facilities running close to the threshold of the τ pair production. There are some distinct advantages with respect to high energy machines: the cross section turns on rapidly at the threshold of the τ pair production, reaching a maximum of ~3.6nb at $\sqrt{s}$=4.25GeV; the background is small and experimentally measurable, completely free of c quark background when running below the charm threshold; the nearly monochromatic momentum spectra for two body decays are of benefit for the event selection; the maximum energy of a decay particle is significantly less than the beam energy, easy to reject backgrounds from Bhabha and μ pair, etc. These advantages are of ultimate importance for more precise branching fraction measurements and the Lorentz structure analysis of charged current. BEPCII/BESIII with its high luminosity and a good detector will provide fruitful results for the τ physics.

2.3.4.2 Data Sample at BEPCII

Data taking for τ pairs could be at $\sqrt{s}$=3.557GeV, just near the threshold of the τ pair production, and $\sqrt{s}$=3.67GeV, just below ψ(2S). The expected τ pair yields are shown in Table 3.7-1.

Table 3.7-1 Data taking dedicated for the τ lepton physics

$\sqrt{s}$ (GeV)	$\hat{L}$ ($\times 10^{33}$cm^{-2} s^{-1})	L(fb^{-1})	$\sigma_{\tau\tau}^{(0)}$ (nb)	$N_{\tau\tau}$
3.557	0.9	0.25/3weeks	0.42	1×10^5/3weeks
3.67	1.0	3/1year	2.4	12×10^6/1year

The data sample at $\sqrt{s}$ =3.557GeV, just near the threshold of the τ pair production, could be used for the τ mass measurement while the data sample at $\sqrt{s}$ =3.67GeV, just below ψ(2S), could be used for precise measurements of branching fractions of τ decays and for the Lorentz structure analysis of charged current. BESIII will take data at energy points such as J/ψ, ψ(2S) and ψ(3770) or $\sqrt{s}$ =4.14GeV. For energies above the τ pair production threshold, such as 3.686GeV(ψ'), 3.77GeV(ψ'') and 4.14GeV($D_s^+ D_s^-$), the expected τ pair yields are shown in Table 3.7-2. These data samples are not as pure as those dedicated for the τ lepton physics and may have some complications due to the background from the c quark, but they are still more clean than those taken in the B energy region. Therefore, good physics results can still be obtained with a high statistics at the expense of efficiencies.

Table 3.7-2 Data samples of τ lepton as by-products of charm data taking

$\sqrt{s}$ (GeV)	$\hat{L}$ (10^{33}cm^{-2} s^{-1})	L(fb^{-1}) /year	$\sigma_{\tau\tau}^{(0)}$ (nb)	$N_{\tau\tau}$/year
3.686 (ψ')	1.0	5	4.2(σ_E=1.2MeV)	21×10^6
3.77(ψ'')	1.0	5	2.95	15×10^6
4.14($D_s^+ D_s^-$)	0.6	3	3.56	11×10^6

2.3.4.3 Physics of τ Leptons at BEPCII

From an experimental point of view, the τ lepton holds a special place among the quarks and leptons. It is the only lepton massive enough to decay to hadronic final states, probably the most sensitive lepton to new physics at higher mass scales. The τ lepton constitutes an ideal laboratory to test the Standard Model and search for new physics. The expected subjects of the τ lepton physics at BEPCII are listed as follows:

1. Precise Measurement of the τ Lepton Mass

The currently most precise measurement of the τ mass[2], m_τ =1776.96 $^{+0.18}_{-0.21}$ $^{+0.25}_{-0.17}$ MeV, is from BES, based on a 5pb^{-1} data sample from a scanning near the τ production threshold. The statistical error could be reduced greatly and the systematic error due to uncertainties in the acceptance and reconstruction efficiencies could be improved with 50 times more statistics near the threshold as shown in Table 3.7-1. For the relative beam energy spread of 2.73$E_b\times10^{-4}$[3] at BEPCII, a precision of ±0.1MeV for the τ mass measurement is possible.

2. Measurement of the Upper Limit of the τ Neutrino Mass

The most stringent limit of the τ neutrino mass is 18.2MeV(95%CL)[4]. A total of 12×10^6 τ pairs could be produced with BEPCII running at $\sqrt{s}$ =3.67GeV for one year as shown in Table 3.7-1. The semileptonic decay of $\tau \to l\nu_l\nu_\tau (l = e,\mu)$ can be chosen as tagging channels for the two hadronic channels of $\tau\to KK\pi\nu_\tau$ and $\tau\to 5\pi\nu_\tau$. Both decay channels and the 2-dimensional fit of normalized energy vs invariant mass distribution of the hadronic final states can be used to get a better mass sensitivity. From a Monte Carlo study, the upper limit of the τ neutrino mass at the level of 1 digit (in MeV) is possible[5].

3. Measurement of the Strong Coupling Constant α_s

The τ hadronic decay is related to the strong coupling constant $\alpha_s(m_\tau)$ at m_τ scale, through the ratio of the hadronic decay width of the τ lepton to its leptonic decay width $R_\tau=\frac{\Gamma(\tau \to hadrons + \nu_\tau)}{\Gamma(\tau \to e\nu\bar{\nu})}$. So, $\alpha_s(m_\tau)$ can be obtained from the measurement of R_τ, which can be obtained experimentally from the following two approaches:

$$R_\tau=\frac{\Gamma - \Gamma(\tau \to e\nu\bar{\nu}) - \Gamma(\tau \to \mu\nu\bar{\nu})}{\Gamma(\tau \to e\nu\bar{\nu})},$$

or

$$R_\tau=\frac{1 - Br(\tau \to e\nu\bar{\nu}) - Br(\tau \to \mu\nu\bar{\nu})}{Br(\tau \to e\nu\bar{\nu})}.$$

That means, through the precise measurement of partial widths or branching fractions of the leptonic decays, we can get R_τ, and finally the precise measurement of $\alpha_s(m_\tau)$.

Using the renormalization group equation, one can evolve $\alpha_s(m_\tau)$ at the scale m_τ to $\alpha_s(m_z)$ at the scale of m_Z and compare it with the direct measurement at the Z^0 peak. The error of $\alpha_s(m_\tau)$ must also be evolved using the renormalization group equation, so a modest precision of $\alpha_s(m_\tau)$ results in a very high precision of $\alpha_s(m_z)$. The current experimental value of $\alpha_s(m_\tau)$ is 0.345±0.020, corresponding to $\alpha_s(m_z)$ of 0.1208±0.0025, in excellent agreement with the direct measurement from the hadronic Z^0 decays $\alpha_s(m_z)$=0.119±0.003, but with a better accuracy [6].

4. Investigation of CP/T Violation

It is interesting to search for CP/T violation in the τ sector, proposed by many theoretical physicists. An attempt of precision measurement of the electric dipole moment d_τ^E of the τ lepton is one of the many efforts. The BES experiment has tried to give some information on the CP/T violation through the measurement of the momentum triplet product $\hat{p}_e \cdot (\hat{k}_1 \times \hat{k}_2)$ in the production-decay sequence $e^-(p_1) + e^+(p_2) \to \tau^+\tau^- \to \mu^-(k_1)\overline{\nu_\mu}\nu_\tau + e^+(k_2)\nu_e\overline{\nu_\tau}$, suggested by T.D. Lee. Using the existing data sample collected at $\sqrt{s}$ =4.03GeV, BES has given a result $A \equiv \langle \hat{p}_e \cdot (\hat{k}_1 \times \hat{k}_2) \rangle$= -0.027±0.031 ±0.006 [5]. The precision of this measurements can be improved using a larger data sample of τ leptons.

5. Lorentz Structure Analysis of Charged Current

The current structure of the τ-ν_τ-W vertex can be studied by measuring the lepton energy spectrum in the decay $\tau^- \to \nu_\tau l^- \overline{\nu_l}$. The shape of the lepton energy spectrum, sensitive to non-Standard Model contributions, can be characterized in terms of 4 Michel parameters ρ, η, ξ and δ, written in the τ rest frame as:

$$\frac{1}{\Gamma}\frac{d\Gamma}{dx d\cos\theta} = \frac{x^2}{2} \times \{12(1-x) + \frac{4\rho}{3}(8x-6) + 24\eta\frac{m_l}{m_\tau}\frac{1-x}{x} \pm P_\tau\xi\cos\theta[4(1-x) + \frac{4}{3}\delta(8x-6)]\}$$

where P_τ is the average τ polarization, θ is the angle between the τ spin and the lepton momentum in the τ rest frame, and $x=E_l/E_{max}$ is the lepton energy scaled to the maximum energy $E_{max}=(m_\tau^2 + m_l^2)/2m_\tau$ in the τ rest frame.

The current world average values of 4 Michel parameters ρ, η, ξ and δ are: ρ=0.752±0.0085, η=0.031±0.031, ξ=0.984±0.031 and δ=0.745±0.022[7]. The precision of the measurements of the 4 Michel parameters ρ, η, ξ and δ could be improved, with a larger data sample of τ lepton, especially collected at the threshold of the τ pair production.

6. Search for Rare and Forbidden Decays

Search for rare and forbidden decays, such as that with lepton number violation: τ→e+γ, e+$l+\bar{l}$, …, that with a (pseudo-) goldstone particle: τ→lX (l=e,μ; X=Majoron, familon, flavon, …), and so-called second class current: $\tau^- \to \pi^-\eta\nu_\tau$ are possible.

CLEOII has achieved a limit on the decay of $\tau^- \to \pi^-\eta\nu_\tau$ of 1.4×10^{-4} (95% CL), using a data sample of 3.2×10^6 τ pairs[1,7,8]. The present upper limits on lepton-flavor and lepton-number violating decays of the τ are in the range of 10^{-5} to 10^{-6}. With a τ samples of 10^7 events per year, an improvement of one to two orders of magnitude is possible[6,9].

7. Precise Measurements of Branching Fractions of τ Decays

Accurate global analysis of all τ lepton decay channels, particularly those involving K's and multiple γ's, are possible, using a large data sample of τ lepton as shown in Table 3.7-1 and 3.7-2. These precise measurements will allow the test of universality of charged current of leptons to a new level. It will also provide a precise determination of the vector and axial vector current spectral functions and some useful information to test QCD.

Reference

[1] A.Stahl, Nucl.Phys.B(Proc.Suppl)98(2001)3-11; M.Davier and B.Jean-Marie (eds.), Proceedings of the First Workshop on Tau Lepton Physics (Orsay, France, Sept.24-27, 1990); K.K.Gan (edt.), Proceedings of the Second Workshop on Tau Lepton Physics (Columbus, Ohio, USA, Sept.8-11, 1992); L.Rolandi (edt.), Proceedings of the Third Workshop on Tau Lepton Physics (Montreux, Switzland, Sept.19-22, 1994), Nucl.Phys.B(Proc.Suppl)40(1995); J.G.Smith and W.Toki (eds.), Proceedings of the Fourth Workshop on Tau Lepton Physics (Estes Park, Colorado, USA, Sept.16-19, 1996), Nucl.Phys.B(Proc.Suppl)55C(1997); A.Pich and A.Ruiz (eds.), Proceedings of the Fifth Workshop on Tau Lepton Physics (Santander, Spain, Sept.14-17, 1998), Nucl.Phys.B(Proc.Suppl)76(1999); R.Sobie and M.Roney (eds.), Proceedings of the sixth Workshop on Tau Lepton Physics (Victoria, British Columbia, Canada, Sept.18-21, 2000), Nucl.Phys.B(Proc.Suppl)98(2001)

[2] J.Z.Bai *et al.*, Phys.Rev.Lett.69(1992)3021, J.Z.Bai *et al.*, Phys.Rev. D53(1996)20

[3] Yuan Changzheng et al., "τ-charm physics and restriction to the accelerator and detector design", to be published in High Energy Physics and Nuclear Physics (in Chinese)

[4] ALEPH Collaboration, R.Barate *et al.*, Eur.Phys.J.C2(1998)395

[5] Feasibility Study Report on BEIJING TAU-CHARM FACTORY, IHEP-BTCF Report-03, Oct. 1996, IHEP, CAS, CHINA

[6] A.Pich, Nucl.Phys.B(Proc.Suppl)98(2001)385-396

[7] K.K.Gan, Nucl.Phys.B(Proc.Suppl)98(2001)397-416

[8] CLEO collab., J.Bartelt *et al.*, Phys.Rev.Lett. 76(1996)4119

[9] CLEO collab., Phys.Rev.D61(2000)071101, D57(1998)5903, D55(1997)R3919; Phys.Rev.Lett. 79(1997)1221

2.3.5 Comparison with Other Experiments

Experiments at B-factories (Babar and Belle) will accumulate a large sample of charm mesons before BEPCII, and CESR will start its CLEO-c program by lowering its beam energy to tau-charm region in around 2003-2004. In the following we make a simple comparison of the proposed BEPCII/BESIII with the above projects.

Let's first compare the luminosity and event statistics for both BESIII and CLEO-c in one year, as shown in Table 3.8-1. It can be seen from the table that the luminosity of BEPCII is higher than that of CESR-C by a factor of 1-4 at various energy points, this factor is particularly large at low energies. On top of that, since J/ψ and ψ' are narrow resonance, and the energy spread of BEPCII is smaller than that of CESR-C, the event statistics is a factor of 10 larger, giving us additional advantages. For J/ψ and ψ' physics, such as light hadron spectroscopy, glueball searches, $\rho\pi$ puzzle, searches for $^1P_1$ state, etc., high statistics is clearly advantageous.

Table 3.8-1 Compariosn of the luminosity and event statistics between BEPCII and CESR-C. Here we used 5nb production cross section for the D mesons, instead of 10 nb used by CLEO-c.

Physics Channel	Energy (GeV)	Luminosity ($10^{33}cm^{-2}s^{-1}$)		Events/year (10^9)	
		BEPCII	CLEO	BEPCII	CLEO
J/ψ	3.097	0.6	0.15	10.0	1.0
τ	3.67	1.0	0.30	0.012	---
ψ'	3.686	1.0	0.30	3.0	---
D	3.77	1.0	0.30	0.025	0.03
D_S	4.03	0.6	0.50	0.001	---
D_S	4.14	0.6	0.50	0.002	0.0015

B-factories operate at the center of mass energy of 10.58GeV(r(4S)). Although its luminosity is very high, it has significant backgrounds and hence systematic errors. Some errors can be reduced by using a larger data sample, some are inherent and may not to be reduced. Therefore many measurements of charm physics at B-factories are limited by systematic errors.

On the other hand, physics at the tau-charm energy region are mainly limited by statistics error. Although the BESIII detector is not better than the CLEO in general, the accelerator has higher luminosity and smaller beam energy spread. Monte Carlo studies show that the mass resolution for taged charm mesons is even better than that from CLEO-c. This will be helpful to overcome shortcomes of the BESIII detector so that the overall systematic error will not be worse than that of CLEO-c. Table 3.8-2 lists the comparison of the physics reach of BEPCII with B-factories , CLEO-c on a variety of physcis topics.

Table 3.8-2 The comparison of the physics reach of BEPCII with B-factories , CLEO-c on a variety of physcis topics. The cross section of charmed meson production is taken as 5 nb instead of 10 nb by CLEO-c.

	B-factories	CLEO-c	BEPCII
	$400fb^{-1}$	$3fb^{-1}$	$5fb^{-1}$
$Br(D^0 \to K^-\pi^+)$		<1%	<1%
$Br(D^+ \to K^-\pi^+\pi^+)$	3-5%	<1%	<1%
$Br(D_S^+ \to \varphi\pi^+)$	5-10%	<2%	~2%
f_D	>10%	~2%	~3%
f_{Ds}	6-9%	~2%	~2.5%
V_{cs}	16%	~1%	~1.6%
V_{cd}	7%	~1.5%	~1.8%

Interaction Region, Beam Pipe and Backgrounds

Interaction Region and the Beam Pipe

The design of interaction region is a compromise of many conflicting requirements. In a limited space, such as all the components, the detector, the beam pipe, magnets, beam monitors, vacuum pumps, masks, mechanical supporting structure, etc., have to be accommodated. Another critical issue is that the interaction region design has to guarantee that the beam related backgrounds to the detector is minimized.

A detailed design is close to be completed, Fig.4.1-1 shows the schematics of the interaction region with all magnets and an illustration of synchrotron radiation fans from one of the two beams. Detailed calculation of backgrounds will be discussed in the next section.

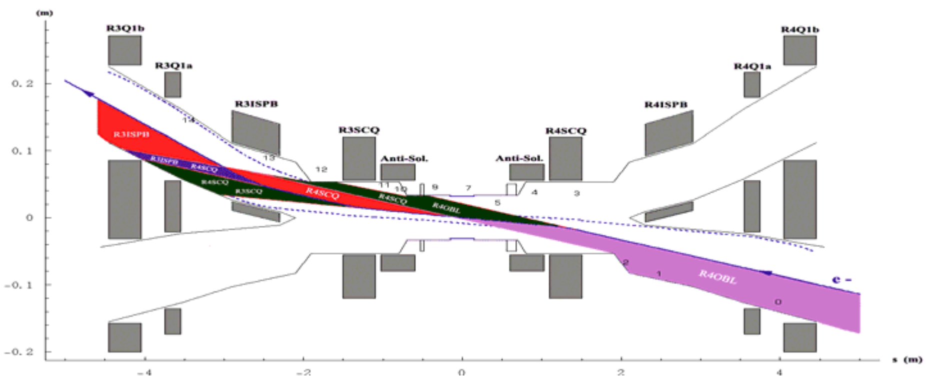

Fig. 4.1-1 General layout of the interaction region and the SR fan from one beam

The interaction region around the beam pipe can be seen in Fig. 4.1-2. The Be beam pipe is 30 cm long with an inner diameter of 6.3 cm. It is welded to an extension section and then connected to the vacuum chamber of the accelerator by a CF63 flange, which is made of copper with an outer diameter of 114mm and thickness of 14mm. A tube type masks made of 2cm tungsten are designed between the accelerator SCQ and the inner wall of the MDC to protect the detectors from the backgrounds.

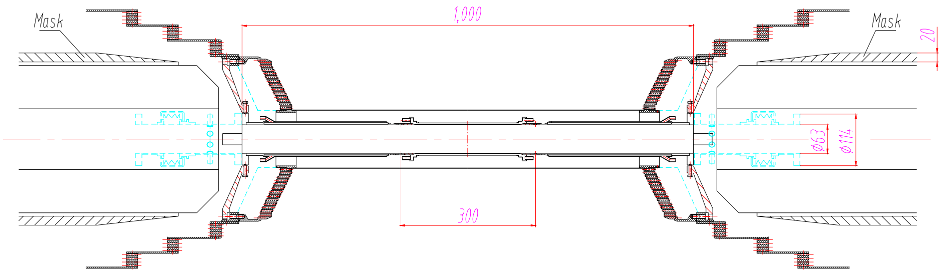

Fig. 4.1-2 The central part of the beam pipe

In point view of physics, the thickness of central beam pipe should be minimized to reduce the multi-scattering, so to improve the particle momentum resolution. At the same time, the beam pipe should be sufficiently cooled to take away heat from synchrotron radiation, lost particles and HOM (High Order Mode) to avoid the damage and prevent its influence to the environment of the MDC due to rising temperature. The working temperature of the central beam pipe should be maintained at 20±2°C. In addition, the inner surface of the central beam pipe should be smooth enough without steps.

Beryllium is selected as the material of the central beam pipe for its small density. Fig 4.1-3 shows the detailed structure of the Be beam pipe.

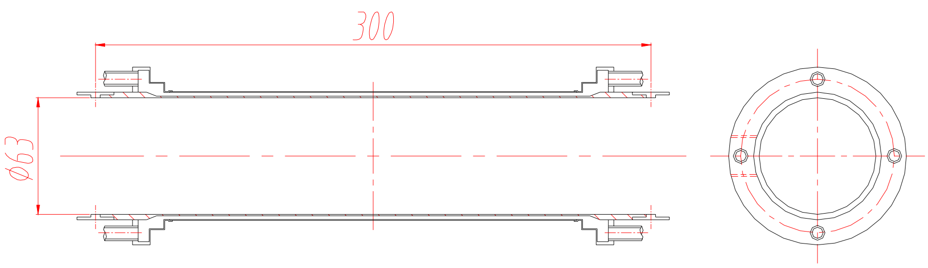

Fig 4.1-3 Detailed structure of the central Be pipe

The Be beam pipe has two layers with 2mm gaps between them. The inner layer diameter is 63mm with a thickness of 0.8mm, while the thickness of the outer layer is 0.5mm. The two layers are welded to a transition copper cavity with four cooling inlet and outlet. One inlet and outlet cooling channel with a width of 20mm is for synchrotron radiation and the rest are for HOM.

In order to have enough safety margin, liquid medium such as water or paraffine will be used as coolant since He gas can not supply enough cooling power.

Both end of the beam pipe are sealed with the enlarged transition copper cavity by laser or EBW, and then welded to the transition copper tube so that it can be easy welded with extending pipe. Fig 4.1-4 shows the detailed structure of the extension of the beam pipe. Copper or aluminum coated with copper is chosen for the extension beam pipe to reduce the scattered SR photons.

The extension pipe is made of copper with an inner diameter of 63mm and thickness of 1.5mm. It has ribs on both sides and welded with two 1.5mm thick half rings of copper to form four 4mm gap cooling channels. Each channel connects to the input or output cooling tube. One end of the tube is welded to a CF flange coated with nickel, the other end is welded to the transition copper tube of the central beam pipe.

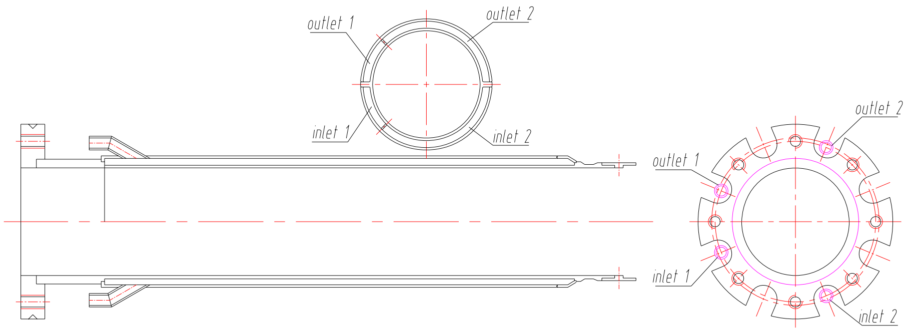

Fig 4.1-4 Detailed structure of the extension beam pipe

Fig 4.1-5 shows the support of the central beam pipe. A ring with thickness of 15mm and inner diameter of 118mm, is connected to the 20mm thick aliminum ring of the MDC, with four entended arms similar to steering wheel to provide enough room for passing through the cooling water tube, gas pipe, signal wires, the cables and enough space for installation and adjustment. Four bolts are designed on the 15mm thick ring to adjust and position the beam pipe.

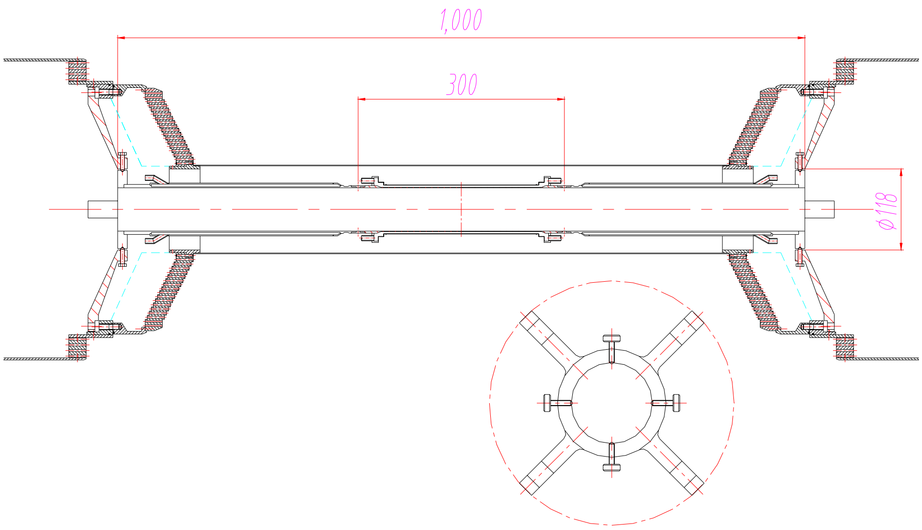

Fig 4.1-5 Support of the central beam pipe

The beam pipe is located in the center of the BESIII with small adjustment space, the structure should be simple and easy for installation, the design must be reliable and easy to repair.

Backgrounds at BEPCII

The problem of beam-related backgrounds is one of the most challenging ones at the BEPCII project. The problem is actually two folds: one is to prevent excessive radiation dose onto the detector so that it is not damaged, the other is to guarantee minimum backgrounds in the detector so that data are not spoiled and physics results are warrant. Table 4.2-1 lists critical safety limits for our detector.

Table 4.2-1 Critical safety limits of radiation dose

Detectors	**Dose Limit**
MDC electronics	1000 rad/year
MDC wires	100 kHz
CsI crystals	500 rad/year

There are three primary sources of backgrounds:

- Synchrotron radiation photons produced by the machine magnets;
- Lost beam particles due to the elastic Coulomb scattering, the inelastic bremsstrahlung and the Touschek effect.
- Lost beam particles due to injection inefficiency.

Some of these backgrounds can be reliably simulated by Monte Carlo programs but some can not. Experiences at the two B-factories are valuable for us, particularly for those not calculable[1]. The generation of synchrotron radiation photons can be simulated by the program SRGEN[2], while the scattering and penetration of photons by SRSIM[2] and EGS[3] respectively. Studies show that these two programs are in agreement within 30%. The background from lost beam particles is simulated by the program Decay Turtle[4], which for the moment includes elastic Coulomb scattering, inelastic bremsstrahlung and Touschek effects. The detector responses to the lost particles are simulated by a GEANT3[5] based program.

In the follows we present our preliminary results from the simulation, further studies are still going on.

Synchrotron Radiation Backgrounds

1. Brief Introduction

Synchrotron Radiation(SR) photons are generated when beam particles undergo the acceleration in magnetic fields of dipoles and quadrupoles. Photons are emitted in the direction near the tangent of the instantaneous trajectories with a total power:

$$dP[KW] = \frac{d\phi}{2\pi} \bullet 88.47 \bullet E_{beam}^{4}[GeV] \bullet I[A] / \rho[m]$$

Where ρ is the local radius of curvature and $d\phi$ the deflecting angle.

The energy spectrum of photons is characterized by the so-called critical energy:

$$U_C[KeV] = 2.2 \bullet E_{beam}^{3}[GeV] / \rho[m].$$

A fraction of photons may unavoidably strike the vacuum chamber walls and protecting masks, scattered or induce fluorescence and ultimately penetrate through the beam pipe into the detector. In the lattice design of the interaction region, attempts are made to keep the SR energy spectrum as soft as possible so that it can be safely absorbed in the IR region. On the other hand, SR background can be substantially reduced if the inner radius of the beam pipe increases. The background is also a steep function of the beam size and can be suppressed if the emittance of the beam is kept small.

In the BEPCII design, the very high beam current must be divided into a large number (93) of bunches, each with a small charge, in order to reduce the single bunch instability. Bunches should be horizontally separated soon after the interaction point to avoid parasitic crossings. This is realized by the use of off-center super-conducting quadrupoles which generate several fans of the synchrotron radiation as seen from

Table 4.2-2 for main parameters of these elements and Fig.4.1-1 for the layout. From the map, we can see that the SR mainly hit downstream of the IP, while we cannot set any masks to intercept them from hitting the beam pipe.

Table 4.2-2 Main parameters of magnets near the interaction region

Element	From IP(m)	Length(m)	K(m^{-2})	Bend(m)(Hori)	Bend(m)(Vert)
SCQ	1.096	0.407	-2.5787		
Q1A	3.550	0.200	1.2450		
Q1B	4.050	0.400	0.6550		
Q2	5.552	0.500	-0.3732		
Q3	9.553	0.500	-0.2376		
Q4	12.554	0.400	0.6536		
OWBL	13.520	0.9322		18.295	10^{30}

For the simulation of SR backgrounds, three programs, SRGEN, SRSIM and EGS are used. SRGEN calculates the synchrotron radiation spectra and power deposition on surfaces of the Interaction Region(IR) by tracing the beam trajectory through magnets. SRSIM simulates the full X-ray scattering down to 1 keV. It includes Compton scattering from bound atomic electrons, Rayleigh scattering, and photoabsorption followed by K and L shell emission. It utilizes appropriate weighting for scattering into small solid angles so that a single-scattering approximation can be made. EGS is similar to SRSIM, but the detector response to SR photons can be simulated. Fig 4.2-1 shows the general procedure of the Synchrotron Radiation simulation.

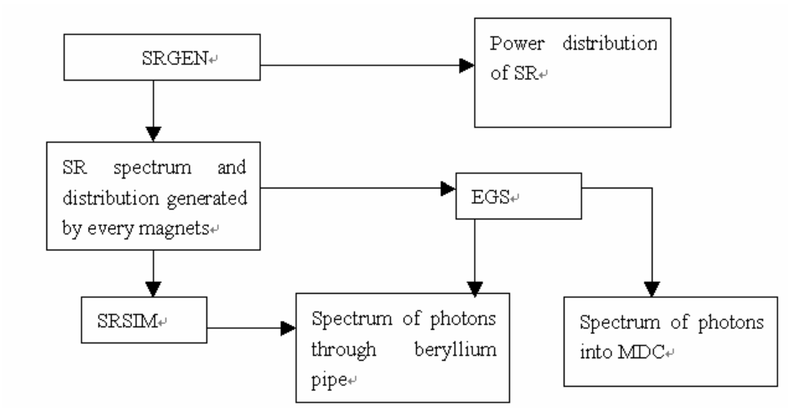

Fig.4.2-1 General procedure of the Synchrotron Radiation simulation

2. Results of the Simulation

The beam energy is set at 1.891 GeV and only one beam with a current of 1A is simulated since the two beams are symmetric. The SR backgrounds are mainly from the super-conducting magnet – SCQ, Q1A, Q1B, Q2, Q3, Q4 and the weak dipole(OWBL).

Fig.4.2-2 shows the power distribution generated by all magnets along the Z direction on the surfaces in the IR. The origin is the IP and +Z is opposite to the beam direction. The vertical coordinate is the power in Watts on surfaces of the vacuum chamber. It can be seen from the figure that most power deposited at the downstream of the beam, and the beam pipe has a limited number of photons.

Table 4.2-3 shows the details of power deposition on each surface. The power on the beam pipe(Surf7) is 0.808W and the power within the pipe(±1.93m including Surf6, Surf7, Surf9 and Surf11) is about 77 W. Although this power level is still small comparing to the HOM power, the collimated nature of SR photons requires a careful design of cooling system. The induced background to the detector will be discussed later.

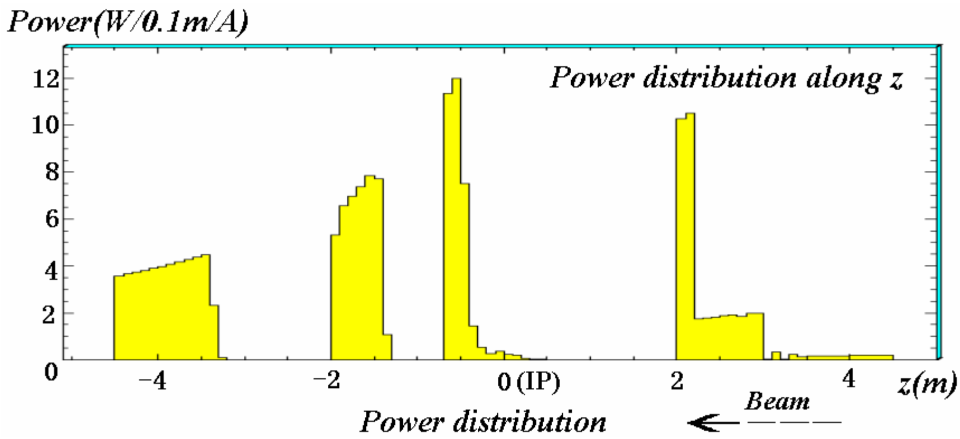

Fig. 4.2-2 Distribution of power generated by all the magnets along the Z axis

Table 4.2-3 The SR power on different surfaces

Surface name	Position(m)	Total power(W)	Power density(W/mm)
Surf0	4.5～3.0	2.7	0.002
Surf1	3.0～2.2	16.5	0.02
Surf2	2.2～2.0	20.9	0.3
Surf6	0.151～0.150	0.12	0.13
Surf7(Be pipe)	0.150～-0.150	0.81	0.003
Surf9	-0.151～-0.7	32.5	0.12
Surf11	-0.8～-2.0	43.1	0.07
Surf14	-3.0～-4.5	46.5	0.06

The calculated SR power on surfaces, particularly on the Be beam pipe, may vary substantially due to the misalignment of magnets, the beam control precision and beam property variations. Table 4.2-4 lists the SR power for various displacement of magnets, of the beam, and the variation of the beam crossing angle. It can be seen from the table that in the worst case of displacement, the SR power increases from 0.8 W to 4.0 W on the Be beampipe, while the change of the beam crossing angle at the IP is more sensitive to the background. When this angle decreases from 11 mrad to 9 mrad(3.3 σ, or about $5.3\,\sigma_X^{'}$), the power on the Be pipe changes from the normal 0.8 W to 11.7 W with the contribution mainly from the weak dipole magnet -- OWBL. Therefore, we should control the beam cross angle at the IP during the operation, so that the background will not exceed the limit.

Table 4.2-4 Variation of SR power due to misalignment of magnets, displacement of the beam, and variation of the crossing angle.

Magnet displacement	**Power on the Be pipe (W)**
SCQ +1mm	4.0
SCQ –1mm	0.06
Q1A +1mm	0.4
Q1A –1mm	2.5
Q1B +1mm	0.4
Q1B –1mm	2.6
Beam displacement	
Horizontal +1mm	0.26
Horizontal -1mm	3.1
Beam crossing angle variations	
-2.0 mrad	11.7
-1.5 mrad	10.2
-1.0 mrad	7.8
-0.5 mrad	4.2
+0.5 mrad	0.04
+1.0 mrad	0.003
+1.5 mrad	0.02

Photons hit the Be beam pipe is especially dangerous. On one hand, Be beam pipe is very fragile due to its limited thickness required by physics, thus may be damaged mechanically by excessive power of SR. On the other hand, SR photons may penetrate through the Be pipe, generating excessive backgrounds in the drift chamber. Too high hit rate in a sense wire of drift chamber may cause severe aging problem or make the track finding impossible. Fig.4.2-3 shows the number of photons on the Be beam pipe in Z direction per second per 0.6 cm. It is good that SR photons are distributed almost uniformly. Fig.4.2-4 shows the energy spectrum of SR photons directly hit on the Be beam pipe, as well as those penetrate through the beam pipe, both SRSIM and EGS simulation results are included. It can be seen from the plot that the Be beam pipe has little attenuation effect for photons with energy above 9 keV. The beam pipe coated with 10μm gold may reduce substantially SR photons in the detector, and hence will be used in the future.

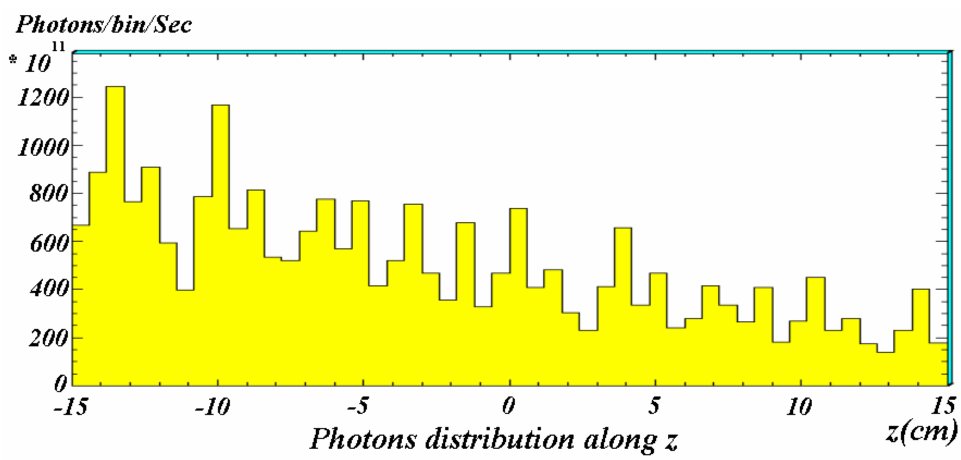

Fig.4.2-3 Photons distribution on the beampipe in Z direction

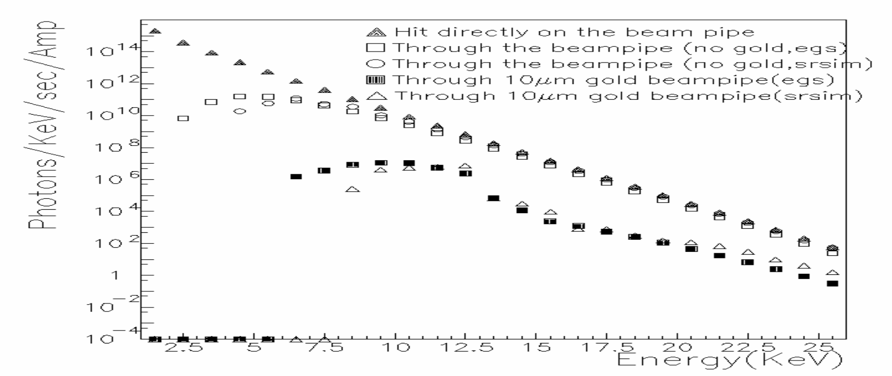

Fig.4.2-4 Spectrum of photons directly hit the beam pipe, through the beam pipe with and without 10μm gold plating(Results of both SRSIM and EGS)

Photons may penetrate through the gold-plated Be pipe and further through the inner wall of MDC, absorbed by the chamber gas and generating signals on sense wires via photoelectric process. Fig 4.2-5 shows the energy spectrum of SR photons in the MDC simulated by a modified EGS code, which takes into account small angle scattering at very low energies[3]. The total number of photons into the drift chamber is $2*10^7$ per second per beam, and the corresponding maximum number of photons through one drift cell is $4*10^6$/s, since SR photons are collimated, as shown in Fig.4.2-6. Calculation shows that the radiation level to the MDC electronics is no more than 100 rad/year, well below the safety limit.

The drift chamber uses a gas mixture of 60%He+40%C_3H_8, whose photon absorption probability is shown in Fig. 4.2-7 and 4.2-8. Assuming each absorbed photon will generate a hit on the nearest sense wire, we obtain the maximum single wire hitting rate no more than 20KHz for two beams, using Fig. 4.2-5 to 4.2-8. A further improvement of a factor of 10 can be obtained by a 20 μm coating of gold on

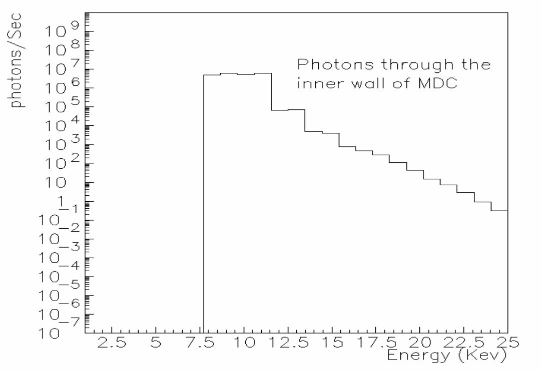

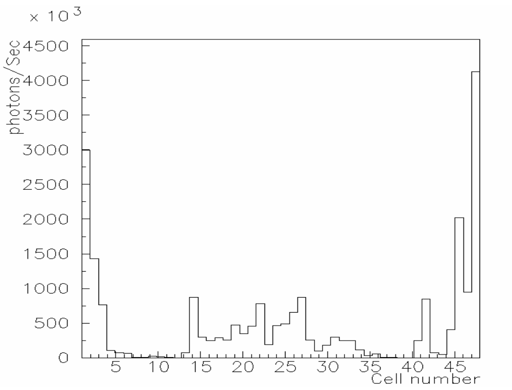

the beampipe instead of 10 μm.

Fig. 4.2-5 Spectrum of photons penetrating through the inner wall of MDC

Fig.4.2-6 Photons in each MDC drift cell of the first layer.

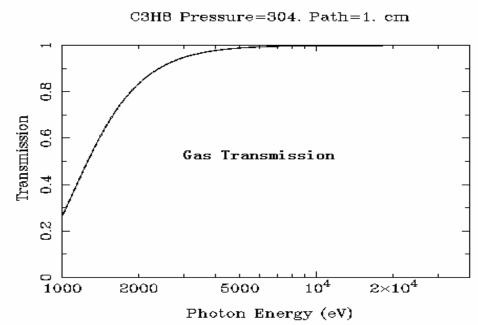

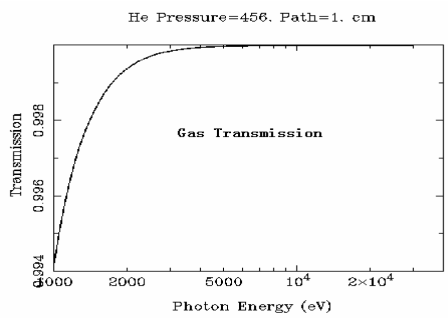

Fig. 4.2-7 Photons transmission in C_3H_8

Fig. 4.2-8 Photons transmission in He

The total power of the scattered photons on the beam pipe is much less than that of direct SR photons. All surfaces hit by the SR fan has a Cu surface, therefore there are only very limited scattered photons on the Be beam pipe. Fig. 4.2-9 shows the spectrum of scattering photons on the beam pipe, through the beam pipe and through the gold plated(10μm) beam pipe. Again, photons penetrating through the gold plated beam pipe are reduced substantially, resulting a negligible background. Fig. 4.2-10 shows the results of the scattering photons on the beam pipe from SRSIM and EGS, which are consistent.

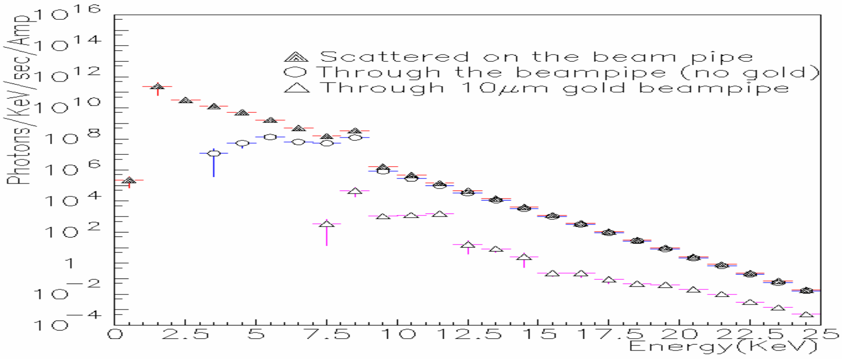

Fig. 4.2-9 Spectrum of scattering photons on the beam pipe, through the beam pipe and through the gold plated(10μm) beam pipe(by SRSIM)

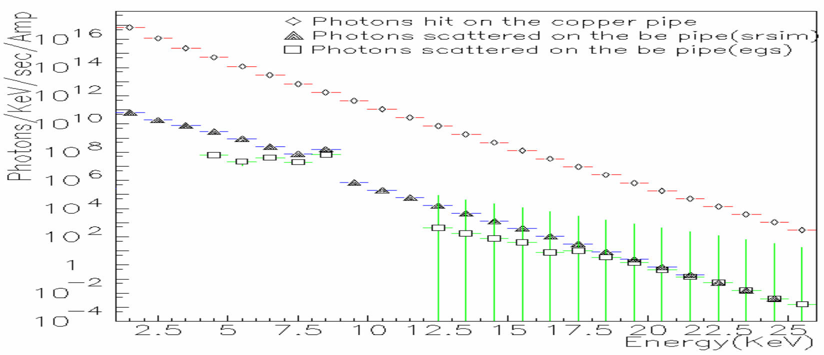

Fig.4.2-10 Spectrum of photons scattered by copper pipe near beryllium pipe

Lost Particles Backgrounds

Beam-gas interactions and Touschek effects can cause lost particles in the vacuum chamber. If lost near the IP, they will probably go into the detector, causing excessive backgrounds harming both the safety and the performance of the detector.

Simulation of the beam-gas interactions and Touschek effects are performed with the program Decay Turtle(with modifications to include beam-gas bremsstrahlung, Coulomb scattering[4] and Touschek effects). Simulation of the detector response is performed with a program based on GEANT3[5].

1. Brief Introduction

a. Beam-Gas Interactions

Particles lost due to bremsstrahlung and Coulomb scattering are simulated separately. Both types of events are generated randomly along the central orbit. The particles are distributed over given ranges of energy transfer $[\varepsilon_{\min}, \varepsilon_{\max}]$ or deflecting angle $[\theta_{\min}, \theta_{\max}]$ according to:

$$\frac{d\sigma}{d\varepsilon} = \frac{1}{\varepsilon} \bullet \left\{ \left[1 + (1-\varepsilon)^2 - \frac{2}{3}(1-\varepsilon) \right] + \frac{(1-\varepsilon)}{9\ln\left(\frac{183}{\sqrt[3]{Z}}\right)} \right\}$$

for bremsstrahlung and

$$\frac{d\sigma}{\theta d\theta} = \frac{1}{\left(\theta^2 + \chi^2\right)^2}$$

for Coulomb scattering, where Z is the atomic number of the target, ε the fraction of energy carried away by the photon, θ the deflecting angle, and $\chi = \alpha\sqrt[3]{Z} m_e / E_{beam}$ a correction factor due to the screening effect of electrons on the atom. The normalizations are done according to:

$$N = \frac{P}{760} \bullet \frac{C}{L_{rad}} \bullet \left\{ \left(\frac{4}{3} + \frac{1}{9\ln\left(\frac{183}{\sqrt[3]{Z}}\right)} \right) \bullet \left[\ln\left(\frac{\varepsilon_{\max}}{\varepsilon_{\min}}\right) - (\varepsilon_{\max} - \varepsilon_{\min}) \right] + \frac{\varepsilon_{\max}^2 - \varepsilon_{\min}^2}{2} \right\}$$

for bremsstrahlung and

$$N = \frac{P}{760} \bullet C \bullet \frac{8\pi N_A}{224} \bullet \left(\frac{Z m_e r_e}{E_{beam}} \right)^2 \bullet \left\{ \frac{1}{\theta_{\min}^2 + \chi^2} - \frac{1}{\theta_{\max}^2 + \chi^2} \right\}$$

for Coulomb scattering, where N_A is Avogadro constant; C is the circumference of the storage ring; Z,P and L_{rad} are the atomic number, the vacuum pressure(in Torr) and the radiation length(in cm) of the residual gas at one atm. respectively. If the residual gas is a molecule made of two atoms, the equation for Coulomb scattering should be multiplied by a factor of 2. For bremsstrahlung, the final state particle keeps its original direction of the motion while for Coulomb scattering, the energy of the particle remains unchanged.

In calculating the deposited energy rates from particles striking near the IP due to bremsstrahlung and Coulomb scattering, we simulate the whole positron ring while the electron ring is almost symmetric with respect to the positron one. Bremsstrahlung scattering produces an electron and a photon whose combined energy is equal to the beam energy. Coulomb scattering gives an off-axis electron with the full beam energy.

b. Touschek Effects [6]

Touschek effects is the scattering of particles in the same bunch due to repulsion forces. Only the single Touschek effects is simulated for simplicity. The beam life

$$\frac{1}{N}\bullet\frac{dN}{dt}=\frac{1}{\tau}=\frac{Nr_e^2c}{8\pi\sigma_x\sigma_y\sigma_z}\bullet\frac{\lambda^3}{\gamma^2}\bullet D(\xi)$$

time due to Touschek effects can be written as the following:

Where, N is the number of particles in one bunch; τ the Touschek beam life time; c the light speed; σ_x, σ_y *and* σ_z the horizontal, vertical and longitudinal rms beam sizes respectively; $\lambda^{-1}=(\Delta E/E)_{RF}=\varepsilon_{RF}/(\gamma m_e c)$; ξ_{RF} the RF acceptance; $\xi=(\varepsilon_{RF}/\gamma\sigma_p)^2$; And $D(\xi)$ being the universal function:

The average effect over the whole ring is:

Where, C is the circumference of the storage ring.

$$D(\xi)=\sqrt{\xi}\bullet\left\{-\frac{3}{2}e^{-\xi}+\frac{\xi}{2}\int_{\xi}^{\infty}\frac{\ln u e^{-u}}{u}du+\frac{1}{2}(3\xi-\xi\ln\xi+2)\int_{\xi}^{\infty}\frac{e^{-u}}{u}du\right\}$$

$$\frac{1}{\tau}=\frac{1}{C}\int\frac{1}{\tau(s)}ds=\left\langle\frac{1}{\tau(s)}\right\rangle$$

$$\Delta N=N\bullet\Delta t\bullet\frac{1}{\tau}=N\bullet\Delta t\bullet\frac{1}{C}\bullet\int\frac{1}{\tau(s)}ds$$

We replace the parameter ξ_{RF} with ΔP, then the number of particles with an energy transfer more than ΔP is:

For energy transfer [εmin, εmax], ΔN is proportional to:

At a certain position of the storage ring, the number of Touschek particles is inversely proportional to the beam size.

$$N_p \propto \frac{1}{\quad} = V$$

$$\delta=\int\frac{D(\xi)}{\varepsilon_{\min}^3}ds-\int\frac{D(\xi)}{\varepsilon_{\max}^3}ds$$

Since D(ξ) doesn’t change too much with ξ, we obtain the following formula:

To calculate tens of series of values – (ΔP, $\delta(\Delta P)$), we can get energy transfer samples with linear approximation. Also, we can calculate series of values - and then get decay position samples according to the series of values $\left(\int_s^C V_{inv}ds, s\right)$

$$\Delta N\propto\int\frac{1}{\sigma_x\sigma_y\sigma_z}ds\bullet\delta$$

The normal factor is expressed as follows:

$$nmf=2\bullet\frac{Nr_e^2c}{8\pi N_sC}\bullet\frac{P_{beam}^3}{\gamma^2}\bullet\int\frac{1}{\sigma_x\sigma_y\sigma_z}ds\bullet\left(\int\frac{D(\xi)}{\varepsilon_{\min}^3}ds-\int\frac{D(\xi)}{\varepsilon_{\max}^3}ds\right)$$

Where, P_{beam} is the beam energy; N_s the number of particles simulated. Since the scattering occurs between two particles in the same bunch, while, we just simulate one particle for one transportation, we get the value – 2 in the front of the formula above.

The main point in the simulation is that we separate the position raleted part – V_{inv} and the energy related part - δ according to the fact that $D(\xi)$ dosen't change too much with ξ.

2. Results of the Simulation

Table 4.2-5 shows the accelerator parameters and vacuum of different parts of the storage ring in the simulation. 224.111m is equivalent to –13.42m, since the circumference of the storage ring is 237.531m.

Table 4.2-5 Accelerator parameters and vacuum in the simulation

Accelerator Parameters in the simulation				
Beam Energy (GeV)	Beam Current (mA)	Emittance - eX (mm.mrad)	Emittance Coupling eY/eX	Energy Spread – σ_e
1.89	900	0.144	1.5%	$5.16 * 10^{-4}$
Vacuum (nTorr of 20% CO + 80% H_2)				
[0.0, 224.111] m	[-13.42, -5.0] m	[-5.0, -2.0] m	[-2.0, +2.0] m	[+2.0, +5.0]m
5.00	0.79	4.20	17.0	4.20

a. Beam-Gas Interactions

Typical trajectories of lost particles due to bremsstrahlung and Coulomb scattering are shown in Fig 4.2-11 and Fig 4.2-12 respectively. For lost electrons due to bremsstrahlung, their energy is lower than the beam energy(the photon takes away part of the energy), so they are over-bent while going through the dipoles and over-focused while going through the quadrupoles, thus finally get lost, part of them in the IR region. For lost electrons due to Coulomb scattering, their angles becomes larger, then their oscillation amplitude becomes larger, thus eventually get lost, possibly in the IR region.

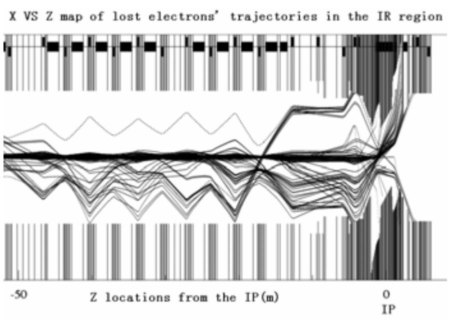

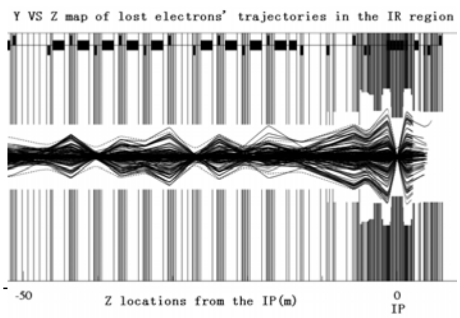

Fig.4.2-11 Typical trajectories for lost electrons due to bremsstrahlung

Fig.4.2-12 Typical trajectories for lost electrons due to Coulomb scattering

Our simulation shows that backgrounds from beam-gas interactions are substantial and masks in the vacuum chamber at various positions to prevent lost particles from hitting the IR region are necessary. Table 4.2-6 shows all eleven proposed masks in the storage ring with their proper apertures, where, eX = 180mm.mrad; eY = 90 mm.mrad

To keep the injection efficiency high, masks far from the IP for preventing backgrounds from the horizontal lost particles are set at 12.5 σ_X, for the positron beam and 12.0 σ_X for the electron one, the one near the IP are set at 13.0σ_X. The energy spread is about 0.5% and the closed-orbit is 0mm. For the vertical dimension, masks are set at 10 σ_Y and the closed-orbits are set at 0mm. Typical trajectories with masks for both bremsstrahlung and Coulomb scattering are shown in Fig. 4.2-13 and 4.2-14.

Table 4.2-6 Proposed 11 masks with their positions and apertures for the positron beam

Name	Mask Type	Characters	Distance upstream the IP(m)	Horizontal Half Aperture (mm)	Vertical Half Aperture (mm)
Befor_R2OQ04	Horizontal Coulomb Scattering	Low Dispersion High BetaX	108.21	$12.5\sqrt{\beta X \times eX} + \lvert DX \rvert 0.5\% \times 1000 = 24.20$	Vacuum Chamber
Middle_R2OQ04	Horizontal Coulomb Scattering	Low Dispersion High BetaX	107.21	$12.5\sqrt{\beta X \times eX} + \lvert DX \rvert 0.5\% \times 1000 = 26.70$	Vacuum Chamber
Middle_R2OQ14	Touschek Effects	High BetaX	73.97	$12.5\sqrt{\beta X \times eX} + \lvert DX \rvert 0.5\% \times 1000 = 22.60$	Vacuum Chamber
Befor_R2OQ16	Vertical Coulomb Scattering	Low Dispersion High BetaY	64.72	Vacuum Chamber	$10.0\sqrt{\beta Y \times eY} = 13.70$
Middle_R3OQ14	Horizontal Coulomb Scattering	Low Dispersion High BetaX	46.68	$12.5\sqrt{\beta X \times eX} + \lvert DX \rvert 0.5\% \times 1000 = 22.60$	Vacuum Chamber
Middle_R3OQ08	Horizontal	High	27.13	$12.5\sqrt{\beta X \times eX} + \lvert DX \rvert 0.45\% \times 1000 = 29.20$	Vacuum

	Lost Particles	Dispersion High BetaX			Chamber
after_R3OQ04_h	Horizontal Lost Particles	Low Dispersion High BetaX	11.67	$12.5\sqrt{\beta X \times eX} + \lvert DX \rvert 0.5\% \times 1000 = 35.40$	Vacuum Chamber
after_R3OQ04_v	Vertical Lost Particles		10.97	Vacuum Chamber	$10.0\sqrt{\beta Y \times eY} = 10.50$
after_R3OQ03_h	Horizontal Lost Particles	Low Dispersion High BetaX	8.20	$12.5\sqrt{\beta X \times eX} + \lvert DX \rvert 0.5\% \times 1000 = 33.80$	Vacuum Chamber
after_R3OQ03_v	Vertical Lost Particles		7.50	Vacuum Chamber	$10.0\sqrt{\beta Y \times eY} = 17.60$
after_R3OQ02	Horizontal Lost Particles	Low Dispersion High BetaX	4.98	$13.0\sqrt{\beta X \times eX} + \lvert DX \rvert 0.5\% \times 1000 = 41.1$	Vacuum Chamber

Note: For electron beam, the horizontal masks except the one – After_R3OQ02 are set at 12.0 σ_X, the others are the same as the positron one.

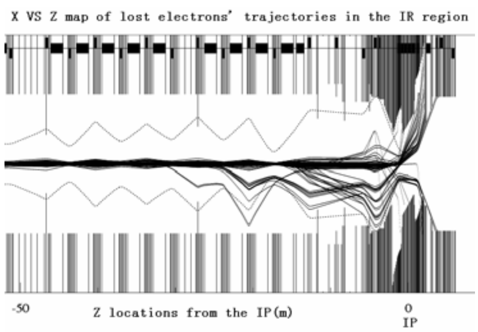

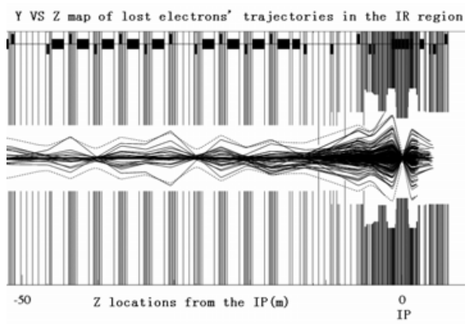

Fig. 4.2-13 Typical trajectories for lost electrons due to bremsstrahlung (with masks)

Fig. 4.2-14 Typical trajectories for lost electrons due to Coulomb scattering (with masks).

These masks can effectively prevent lost particles from reaching the IR. Table 4.2-7 shows the rate of energy deposition of lost particles in different region near the IP. It can be seen from the table that masks can generally reduce backgrounds dramatically and the total background in the region of ±0.8m from the IP is about 353 MeV/μs. Energy deposited to the IR are mainly from the region [-13.42, 0.0] m, so the vacuum of this region is very important for the detector backgrounds.

Table 4.2-7 Rate of energy deposition near the IR region in unit of MeV/μs for one beam

Region	[-5.0m,+5.0m]		[-1.93m,+1.93m]		[-0.8m,+0.8m]	
	No Masking	Masking	No Masking	Masking	No Masking	Masking
Brem	2124	1664	576.0	432.9	310.0	310.0
Brem [-13.42m, +2.0m]		1163		367.2		307.0
Coul	3127	860.9	803.9	247.5	42.57	42.57
Coul [-13.42m, +2.0m]		510.8		195.5		41.27
Total	5251	2525	1380	680.4	352.6	352.6

Detailed Monte Carlo simulations based on GEANT3 have been performed to study effects of the lost-particle-induced showers in the detector. We set a threshold of 500 KeV for TOF hit signal and no threshold for the other detectors. Fig. 4.2 –15 shows an example of such a shower event in the IR region. A tube type masks made of 2cm tungsten between the accelerator SCQ and the inner wall of the MDC is designed to protect sub detectors, especially the MDC and endcap EMC(As shown in Fig.4.2-15). Detailed study of the mask shape is still understudy. Table 4.2-8 and Table 4.2-9 show the simulated results for two beams with and without the tungsten masks respectively:

Table 4.2-8 Single hit rate and energy dose without tungsten masks

	MDC Single Wire Rate (KHz)		EMC Energy Dose (rad/year)		TOF Single hit Rate (KHz)	
	Layer 1	Layer 2	Barrel	Endcap	Barrel	Endcap
Maximum	32.20	19.44	1.39	8.32	6.51	6.67

Average	9.25	6.75	0.25	1.35	4.62	4.38

Table 4.2-9 Single hit rate and energy dose with tungsten masks

	MDC Single Wire Rate (KHz)		EMC Energy Dose (rad/year)		TOF Single hit Rate (KHz)	
	Layer 1	Layer 2	Barrel	Endcap	Barrel	Endcap
Maximum	31.60	18.40	0.77	5.27	3.93	3.14
Average	9.06	6.53	0.14	0.93	2.88	2.23

After the tungsten masking, total energy deposit in the barrel EMC from lost particles is about 5.06 MeV/μs corresponding to a radiation dose of 0.14 rad/year, while those in the endcap EMC is about 9.26 MeV/μs corresponding to a radiation dose of 0.92 rad/year. All of the radiation levels listed above are well within the safety limit.

For the detector performance, the total single rate in the EMC is about 10.5 MHz due to the lost particle background, corrresponding to about 32 crystals fired during each trigger window of 3μs(shaping time 1μs). This background should not substantially affect the EMC performance. For MDC, the maximum single hit rate is 31.60 KHz, marginal for a good performance and further improvements are desired.

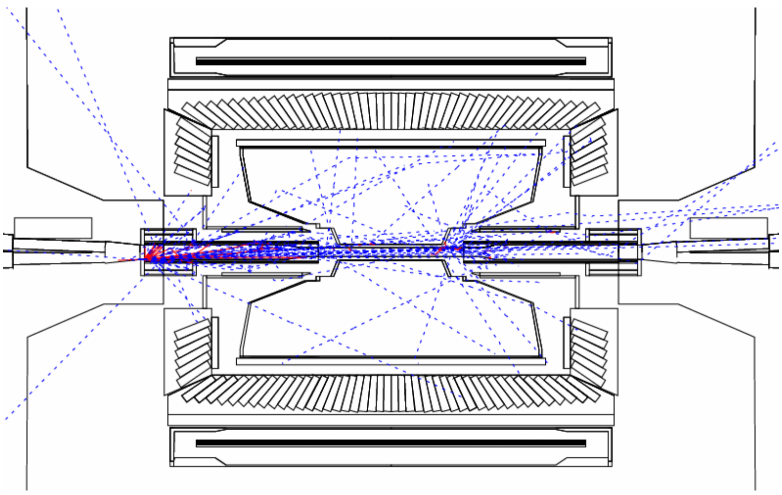

Fig.4.2-15 Shower of a lost particle in the IR region. Also shown are the masks between the MDC and the vacuum chamber. The masks are symmetric with respect to the IP.

b. Touschek Effects

Similar to beam-gas interactions, we simulate the whole ring of the Touschek effects. Fig 4.2-16 shows the typical trajectories of lost electrons due to Touschek effects in the IR region.

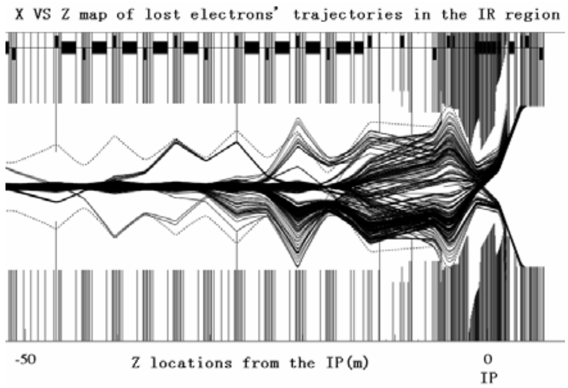

Fig 4.2-16 Typical trajectories of Touschek lost particles in the IR region

Fig 4.2-16 shows the decay points of all the Touschek particles simulated, and Fig 4.2-17 shows the Z distribution of the Touschek lost particles in the IR region hitting the vacuum pipe.

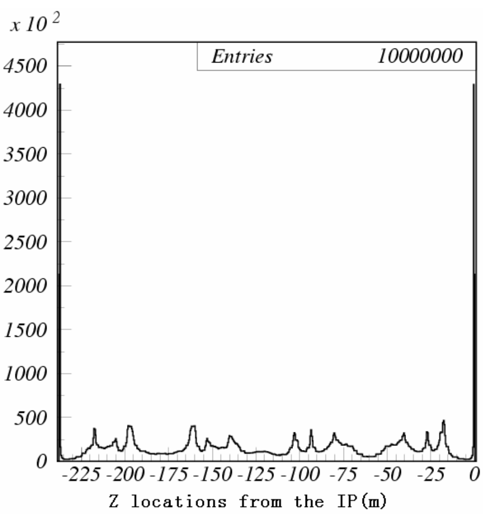

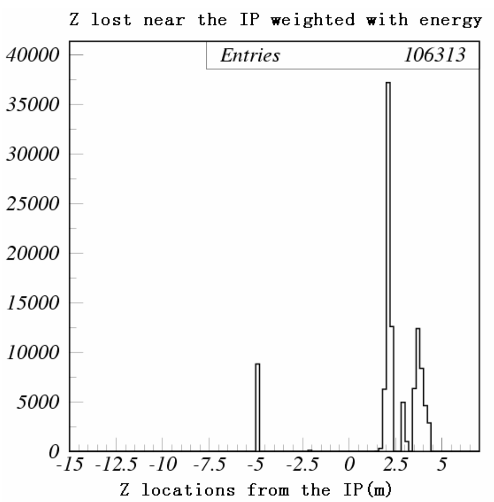

Fig 4.2-16 Decay position of all Touschek Particles

Fig 4.2-17 Z distribution of Touschek lost particles in the IR region

From Fig 4.2-17, we can see that most of the Touschek lost particles in the IR region are 2m away from the IP. Fig 4.2-18 shows the energy fraction vs decay points of the Touschek lost particles in the IR region.

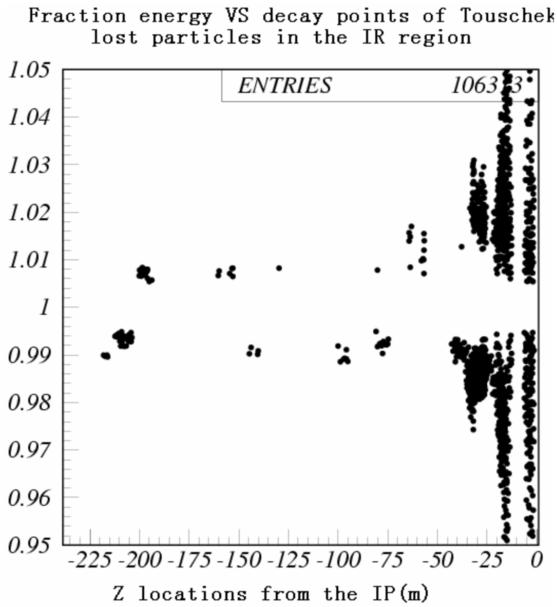

Fig 4.2-18 Enengy fraction VS decay points of Touschek lost particles in the IR region.

The calculated Touschek beam lifetime is 5.4 hours neglecting the influence of the dispersion function on the parameters of the Scattering. The simulated beam lifetime due to Touschek effects is between 3.4 hours and 6.8 hours. From the calculation of the accelerator people, the Touschek beam lifetime is about 9.0 hours. Taking into account the influence of the dispersion function, the calculated Touschek beam lifetime for single scattering is 6.1 hours, in agreement with our simulation.

Table 4.2-10 Single hit rate and energy dose without tungsten masks

	MDC Single Wire Rate (KHz)		EMC Energy Dose (rad/year)		TOF Single hit Rate (KHz)	
	Layer 1	Layer 2	Barrel	Endcap	Barrel	Endcap
Maximum	5.66	4.19	5.98	8.76	6.86	3.56
Average	2.99	2.46	0.28	2.12	4.33	2.33

Table 4.2-11 Single hit rate and energy dose with tungsten masks

	MDC Single Wire Rate (KHz)		EMC Energy Dose (rad/year)		TOF Single hit Rate (KHz)	
	Layer 1	Layer 2	Barrel	Endcap	Barrel	Endcap
Maximum	5.08	4.00	4.67	8.56	6.04	3.69
Average	3.08	2.60	0.24	2.04	3.36	2.04

Touschek effects has larger radiation doses to EMC and TOF than beam-gas interactions.

For the detector performance, the total single rate in the EMC by Touschek effects is about 17.0 MHz corrresponding to a total of about 51 crystals fired during each trigger window. For MDC and TOF, the maximum single hit rate is 5.08 KHz and 6.04 KHz respectively.

Lost Particles Due to Injection Inefficiency

Usually, the injection efficiency is much lower than 100%. For 50% injection efficiency, 67% beam current for reinjection, 18 injections per day and 200 days' run per year, we obtain the results as shown in Table 4.2-12.

Table 4.2-12 Beam parameters and energy deposit

	PEP-II	BEPC	BEPCII
Beam Energy (GeV)	3.1(e^+) , 9.0(e^-)	2.0	1.89
Current of two beams (A)	2.14(e^+) , 0.99(e^-)	0.1	1.82
Charge stored in rings	22.9	0.08	1.43

(μC)			
Energy stored in rings (KJ)	108	0.26	2.75
Fair-share energy loss of a stored beam in the IR (J/m)	100% to 80%	100% to 0.0	100% to 67%
	12.3	1.08	3.8
Fair-share energy loss due to injection inefficiency each time (J/m)	80% to 100%	0.0 to 100%	67% to 100%
	4.1 (75% efficiency)	1.8 (37.5%efficiency)	3.8 (50% efficiency)
Fair-share total energy loss in the IR for one year (KJ/m)	45.7 for 24 injections per day + 116 days' run	4.7 for 8 injections per day + 200 days' run	27.4 for 18 injections per day + 200 days' run

Assuming the lost particles during injections are distributed uniformly over the whole ring, the power to the IR region [-5.0m, +5.0m] is 27.4 * 10 = 274KJ. The injection backgrounds are simulated based on GEANT3 by assuming a uniform distribution in an angle range of [4, 40] mrads ±1m away from the interaction point. For background within 1m from the interaction point, the angular distribution is taken as:

$$N = N_{tot} \bullet \frac{1}{0.99\delta} \bullet \left\{ e^{-(\theta_x - \theta_{\min})/\delta} \right\}$$

Where $\delta = (\theta_{max} - \theta_{min})/\ln 100$, N is the number of particles with angle θ, N_{tot} is the number of all lost particles.

Table 4.2-13 and Table 4.2-14 show the simulated results for two beams with and without the tungsten masks respectively:

Table 4.2-13 Radiation doses to the EMC without tungsten masks

	MDC Single Wire Rate (KHz)		EMC Energy Dose (rad/year)		TOF Single hit Rate (KHz)	
	Layer 1	Layer 2	Barrel	Endcap	Barrel	Endcap
Maximum	--------	--------	45	310	--------	--------

Average	--------	--------	18	73	--------	--------

Table 4.2-14 Radiation doses to the EMC with tungsten masks

	MDC Single Wire Rate (KHz)		EMC Energy Dose (rad/year)		TOF Single hit Rate (KHz)	
	Layer 1	Layer 2	Barrel	Endcap	Barrel	Endcap
Maximum	--------	--------	29	218	--------	--------
Average	--------	--------	13	50	--------	--------

With or without tungsten masks, the radiation doses to the EMC is within the safety limit. Since both lost particles from injection inefficiency and from normal running are included and the simulation conditions are very conservative, the radiation doses for the real cases should be several times smaller than that of the simulation. Hence there should be no problem for the safety of the EMC.

The beam-Abort system is not necessary due to the following reasons:

(1) The abnormal lost particles are mostly stopped by the masks on the storage ring due to their small apertures;

(2) The safety of the BESIII sub-detectors are determined by the integrated doses, occasional cases won't damage them.

Summary

The beam related backgrounds are simulated using well known existing programs. Results show that there are no show-stoppers in the current lattice design and there are no safety problems to our detector.

For synchrotron radiation backgrounds, the simulation shows that SR photons are few enough that detector safety is warrant. They won't affect the proper running of the detector because of their low critical energies (all below 1keV) and powers. During the normal operation, the power on the Be pipe is 0.8*2 = 1.6 W. In the worst case, the power on the Be pipe is no more than 24W. With gold plating, the maximum single wire rate by SR is less than (2-20) KHz, the detector is safe and the current IR design is reasonable.

From the simulation of the lost-particle backgrounds, the safety of the detector is again warrant. The energy deposit to the region[-0.8m,+0.8m] is about 353MeV/μs, mainly from the region [-13.42, 0.0]m. The radiation dose level at EMC is no more than 20 rad/year, well below the safety limit.

From the GEANT3 simulation of the detector response, we obtained the maximum single wire rate of 31.60 + 5.08 = 36.7 KHz for MDC and 3.93 +6.04 = 10.0 KHz for TOF.

During injection, we can turn down the high voltages of the MDC. Assuming fair-share loss along the storage ring of the lost particles, the maximum radiation dose to the EMC for one year is no more than 218 rad, within the safety limit.

Reference

[1] The B_AB_{AR} Technical Design Report, SLAC-R-95-457(1995);
W. Kozanecki and H. Yamamoto, private communication.

[2] S.Henderson, "Synchrotron Radiation Background Simulation with SRGEN/SRSIM " (1995).

[3] W.Nelson, H. Hirayama, and D. Rogers, "The EGS4 Code System," SLAC-PUB-265(1985); A modified code taking into account small angle scatterings was provided by H. Yamamoto.

[4] D.C. Carey, K.L. Brown, and F.C. Iselin, "Decay TURTLE(Trace Unlimited Rays Through Lumped Elements): A Computer Program for Simulating Charged Particle Beam Transport Systems, Including Decay Calculations," SLAC-246(1980). A modified version taking into account the beam-gas bremsstrahlung and Coulomb scattering was provided by W. Kozanecki.

[5] GEANT Detector Description Tool, version 3.21, CERN Program Library W5103, CERN(1994).

[6] J. Le Duff, "Single and Multiple Touschek Effects", P573-586, CERN 95-0

Main Drift Chamber

Physics Design

General Consideration

The BESIII main drift chamber (MDC) is one of the most important sub-detectors. Its main functions are:

1) Precise momentum measurement. To achieve this, special cares should be taken to minimize the effects of multiple Coulomb scattering in the design;

2) Adequate dE/dx resolution for particle identification;

3) Good reconstruction efficiency for short tracks from interaction point;

4) Realization of charged particle trigger at level one;

5) Maximum possible solid angle coverage(～ 90%4 π Sr.) for charged track measurement.

The momentum of a charged particle is determined by the trajectory of the charged particle in a magnetic field. In the BEPCII energy range (between 2-4 GeV), most momenta of the charged particles are below 1 GeV/c, hence, multiple Coulomb scattering will dominate the tracking performance. Therefore the amount of material in the fiducial volume of the drift chamber should be kept minimum.

Argon gas mixture and jet cells are adopted in the drift chambers of BESI and BESII. The single wire position resolution is $250\mu m > \sigma_{xy} > 200\mu m$, the momentum resolution is $\sigma_p / p \approx 1.78\%\sqrt{1+p^2}$ (GeV/c), and the dE/dx resolution is around 8%.

The BES III solenoid is designed to provide an axial magnetic field of about 1.0 Tesla in the tracking volume. Aluminum wires will be used for the field wires, and the helium based gas mixture is used as working gas for reducing the effect of multiple scattering. Rational design parameters of the drift chamber could contribute to the momentum resolution to a lesser extent, compared with multiple scattering. According to the experience from the performance of similar drift chambers built in the world, the single position resolution should be better than $150\mu m$. If the single wire resolution is assumed to be $130\mu m$ for the BESIII drift chamber, the momentum resolution for 1 GeV/c charged particles should be around 0.5%, and the dE/dx resolution could be 6%-7%.

For layer arrangement, enough stereo wire layers are needed to measure the Z dip angles of charged tracks.

To achieve the above performances and meet all the requirements, the design of the drift chamber should take into account the following considerations:

1) In the limited space, as many as possible readout layers should be arranged;

2) The design and manufacture of the drift chamber must ensure good accuracy for wire locations;

3) The end-plates of the drift chamber should adopt a special shape in order to have a large solid angle coverage;

4) The drift cells should be as consistent as possible to obtain good performance, and should have a uniform time-to-distance relation and a uniform dE/dx in the entire cell region. To facilitate the trigger design, a super-layer arrangement will be adopted and the cell arrangement in one super layer should be as symmetrical as possible.

The drift chamber is the innermost sub-detector of the BESIII detector. The inner diameter of the drift chamber is 118 mm for easy assembly of the beam pipe. The physical outer diameter is designed to be 1600 mm to achieve good momentum resolution. The length is 2300 mm with the outmost sense wire layer covers a polar angle of $|\cos\theta| = 0.83$.

MDC is designed to consist of two parts, an inner chamber and an outer chamber. The inner chamber can be replaced if it malfunctions due to radiation damage.

To maximize the polar angle coverage while accommodating the intrusion of the interaction quadruples, the end-plate of the inner chamber is designed to be a tilt shape, while that of the outer chamber has a multi-stepped and tilted shape to reduce the deformation caused by wire tension in large radius. Fig.5.1-1shows the schematic of the drift chamber structure.

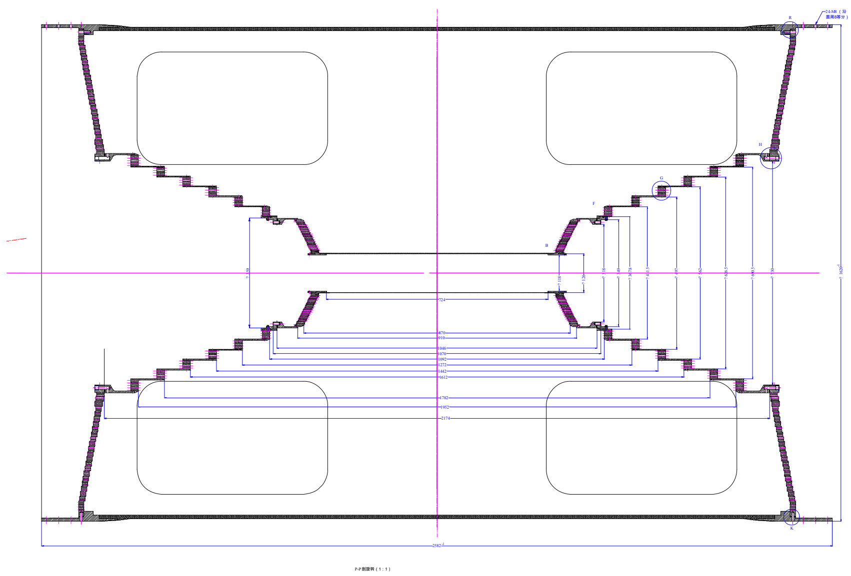

Fig.5.1-1 The drift chamber structure

Design of the Drift Cell

The small cell structure used by BELLE, CLEOIII and KLOE experiments is chosen for the BESIII drift chamber. In this configuration, each cell is nearly square in shape, the sense wire, located in the center, is surrounded by 8 (or 9) field wires as shown in Fig.5.1-2.

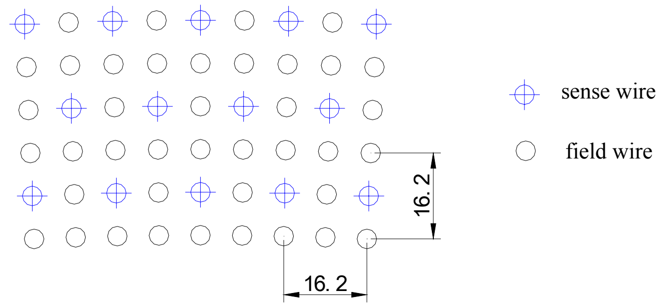

Fig.5.1-2 The cell configuration

To assure gas gain uniformity in every drift cell, the half-height-width of the cell (distance of the sense wire to field wire) is designed to be almost the same. The average half cell width is 6 mm in the inner chamber, 8.1mm in the outer chamber.

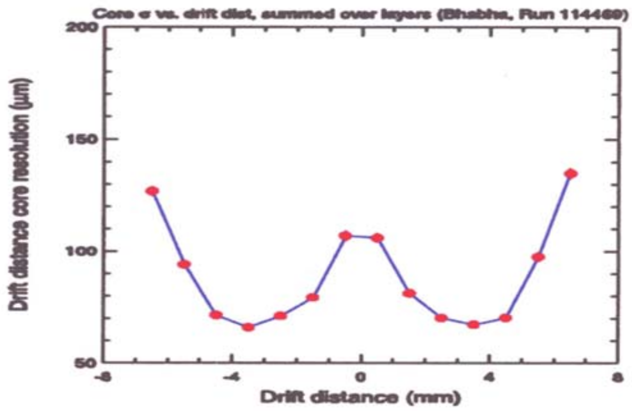

Fig.5.1-3 The position resolution vs drift distance (CLEOIII result)

The drift chamber contains 43 layers of sense wires, every four layers of sense wire constitute one super-layer except the last one. The field wires will be shared between neighboring cells in a super-layer.

The field wire will not be shared by the stereo wire layer and its neighboring axial wire layer, since there is a fall at the center of the stereo wire, which will affect the half–height–width of the cell. Based on experience from other experiments such a design can achieve a $130\mu m$ position resolution as shown in Fig.5.1-3.

All cells in the inner chamber will be symmetrical in 90°, while in the outer chamber they will be symmetrical in 22.5° except in the stepped region, where they are symmetrical in 90° due to the limitation of the mechanical structure. A good symmetry will benefit the trigger and the track reconstructions. The cell dimension parameters for the inner chamber and outer chamber are listed in Table 5.1-1.

Two kinds of wires are selected for the sense and field wires respectively. The sense wire is 25 μm gold-plated tungsten and the field wire is 110 μm gold-plated aluminum. The parameters of wires are listed in Table 5.1-2. The tension of sense wires in the inner chamber is ~17g while that of field wires is 50g-60g. The gravity sag will be controlled to be around 50 μ m.

The tension of wires will be changed with the wire length in the outer chamber. The gravity sag will be controlled to be around 120 μ m.

Table 5.1-1 The cell arrangement of the inner chamber and the outer chamber

layer	R (mm)	Wire N (F+S)	half width (arc *l*,mm)	w/h	偏转单元数	a/2 弧度	Length (mm)	a (mm)	ε (degree)	δ (mm)	σ_z (mm)
F1	73.00	80	5.73		2	0.15708	780	22.83943	1.677	0.8988	
S1	78.85	80	6.20	1.072	2	0.15708	786	24.670	1.798	0.9708	4.142
F2	84.55	88	6.07		2	0.1428	792	24.06544	1.740	0.8606	
S2	90.70	88	6.50	1.070	2	0.1428	798	25.816	1.853	0.9232	4.018
F3	96.65	96	6.35		2	0.1309	804	25.23071	1.797	0.8269	
S3	102.90	96	6.74	1.073	2	0.1309	810	26.86229	1.899	0.8803	3.92
F4	109.20	112	6.11		2	0.1122	816	24.45304	1.716	0.6866	
S4	115.25	112	6.45	1.064	2	0.1122	822	25.80781	1.798	0.7247	4.141
F5	121.35	128	5.94		2.5	0.12272	828	29.70907	2.055	0.9126	
S5	127.20	128	6.23	1.063	2.5	0.12272	834	31.14128	2.138	0.9566	3.482
F6	133.10	144	5.80		2.5	0.10908	840	28.98036	1.976	0.7911	
S6	138.75	144	6.07	1.067	2.5	0.10908	846	30.21056	2.045	0.8247	3.64
F7	144.45	160	5.69		2.5	0.09817	852	28.31715	1.904	0.6956	
S7	150.10	160	5.93	1.067	2.5	0.09817	858	29.42475	1.964	0.7228	3.791
F8	155.50	160	6.17		2.5	0.09817	864	30.48333	2.021	0.7488	
S8	161.60	160	6.40	1.062	2.5	0.09817	870	31.67914	2.085	0.7781	3.57
F8	167.45	160	6.64		2.5	0.09817	870	32.82594	2.161	0.8063	
F9	189.00	152	1				1092				
S9	197.00	152	8.15	1.041			1092				
F10	204.65	152	8.48				1092				
S10	213.00	152	8.82	1.042			1092				
F11	221.55	176	7.90				1282				
S11	229.55	176	8.19	1.044			1282				

F12	237.25	176	8.48				1282				
S12	245.55	176	8.77	1.040			1282				
F13	254.10	200	7.97				1462				
S13	262.15	200	8.23	1.039			1462				
F14	269.95	200	8.48				1462				
S14	278.20	200	8.74	1.047			1462				
F15	286.65	224	8.03				1642				
S15	294.65	224	8.26	1.050			1642				
F16	302.40	224	8.48				1642				
S16	310.60	224	8.71	1.047			1642				
F17	319.05	256	7.82				1822				
S17	326.90	256	8.02	1.035			1822				
F18	334.55	256	8.22				1822				
S18	342.65	256	8.42	1.029			1822				
F19	350.90	280	7.88				1972				
S19	358.75	280	8.06	1.039			1972				
E20	366.40	280	8.24				1972				
S20	374.55	280	8.42	1.047			1972				
F20	382.45	280	8.60				1972				
F21	392.10	320	7.69		5	0.09817	2174	76.86504	2.025	1.8881	
S21	399.75	320	7.85	1.036	5	0.09817	2174	78.3647	2.064	1.9249	3.606
F22	407.25	320	8.01		5	0.09817	2180	79.83496	2.097	1.961	
S22	415.20	320	8.16	1.035	5	0.09817	2180	81.39343	2.138	1.9993	3.482
F23	423.00	320	8.32		5	0.09817	2186	82.9225	2.172	2.0369	
S23	431.20	320	8.48	1.042	5	0.09817	2186	84.530	2.214	2.0763	3.362
F24	439.25	320	8.64		5	0.09817	2192	86.10806	2.250	2.1151	
S24	447.60	320	8.80	1.040	5	0.09817	2192	87.74494	2.292	2.1553	3.248
F25	456.15	352	8.14		5.5	0.09817	2198	89.42104	2.330	2.1965	
S25	464.15	352	8.29	1.045	5.5	0.09817	2198	90.98931	2.370	2.235	3.14
F26	472.00	352	8.43		5.5	0.09817	2204	92.52818	2.404	2.2728	
S26	480.20	352	8.58	1.055	5.5	0.09817	2204	94.13566	2.446	2.3123	3.044
F27	488.25	352	8.72		5.5	0.09817	2210	95.71374	2.480	2.3511	
S27	496.85	352	8.87	1.043	5.5	0.09817	2210	97.39963	2.524	2.3925	2.95
F28	505.25	352	9.01		5.5	0.09817	2216	99.04632	2.559	2.4329	
S28	513.70	352	9.16	1.054	5.5	0.09817	2216	100.7028	2.602	2.4736	2.861
F29	522.65	416	7.87		6	0.09062	2222	94.59847	2.438	2.1447	
S29	530.35	416	7.99	1.051	6	0.09062	2222	95.99216	2.474	2.1763	3.009
F30	537.90	416	8.12		6	0.09062	2228	97.35869	2.502	2.207	
S30	545.95	416	8.24	1.034	6	0.09062	2228	98.81572	2.540	2.2403	2.931
F31	553.85	416	8.36		6	0.09062	2234	100.2456	2.569	2.2727	
S31	562.15	416	8.48	1.032	6	0.09062	2234	101.748	2.608	2.307	2.854

F32	570.30	416	8.60		6	0.09062	2240	103.223	2.638	2.3402	
S32	578.55	416	8.73	1.031	6	0.09062	2240	104.7162	2.677	2.374	2.781
F33	587.25	480	7.67		6.5	0.08508	2246	99.81157	2.545	2.124	
S33	594.75	480	7.78	1.045	6.5	0.08508	2246	101.0863	2.577	2.1515	2.888
F34	602.15	480	7.88		6.5	0.08508	2252	102.344	2.602	2.1783	
S34	609.95	480	7.99	1.030	6.5	0.08508	2252	103.6698	2.636	2.207	2.824
F35	617.65	480	8.09		6.5	0.08508	2258	104.9785	2.662	2.2344	
S35	625.65	480	8.20	1.030	6.5	0.08508	2258	106.3382	2.696	2.2633	2.76
F36	633.55	480	8.31		6.5	0.08508	2264	107.6809	2.723	2.292	
S36	641.65	480	8.41	1.031	6.5	0.08508	2264	109.0576	2.758	2.3212	2.699
F36	649.85	480	8.52		6.5	0.08508	2270	110.4513	2.786	2.351	
F37	658.80	512	8.08				2270				
S37	666.80	512	8.18	1.029			2276				
F38	674.70	512	8.28				2276				
S38	682.85	512	8.38	1.038			2282				
F39	690.85	512	8.48				2282				
S39	699.15	512	8.58	1.040			2288				
F40	707.35	512	8.68				2288				
S40	715.70	512	8.78	1.030			2294				
F41	724.40	576	7.89				2294				
S41	732.10	576	7.98	1.047			2300				
F42	739.65	576	8.07				2300				
S42	747.60	576	8.16	1.032			2306				
F43	755.45	576	8.25				2306				
S43	763.45	576	8.34	1.048			2306				
F43	771.35	576	8.42				2306				
		28680									

Table 5.1-2 The parameters of wires

wire category	Material	Diameter(μ m)	Line density
Sense wire	Gold-plate	25	9.4×10^{-3}
Field wire	Gold-plate	110	28.18×10^{-3}

Wire Layer Arrangement

There are altogether 43 sense wire layers in the drift chamber, 8 layers in the inner chamber and 35 layers in the outer chamber.

The stereo wire layers are necessary to provide longitudinal measurements in the drift chamber. For measuring the tracks with small incident angle, all 8 layers in the inner chamber are stereo, and there are 16 stereo layers and 19 axial layers in the outer chamber. The axial and stereo layers are arranged alternately as shown in Fig.5.1-4.

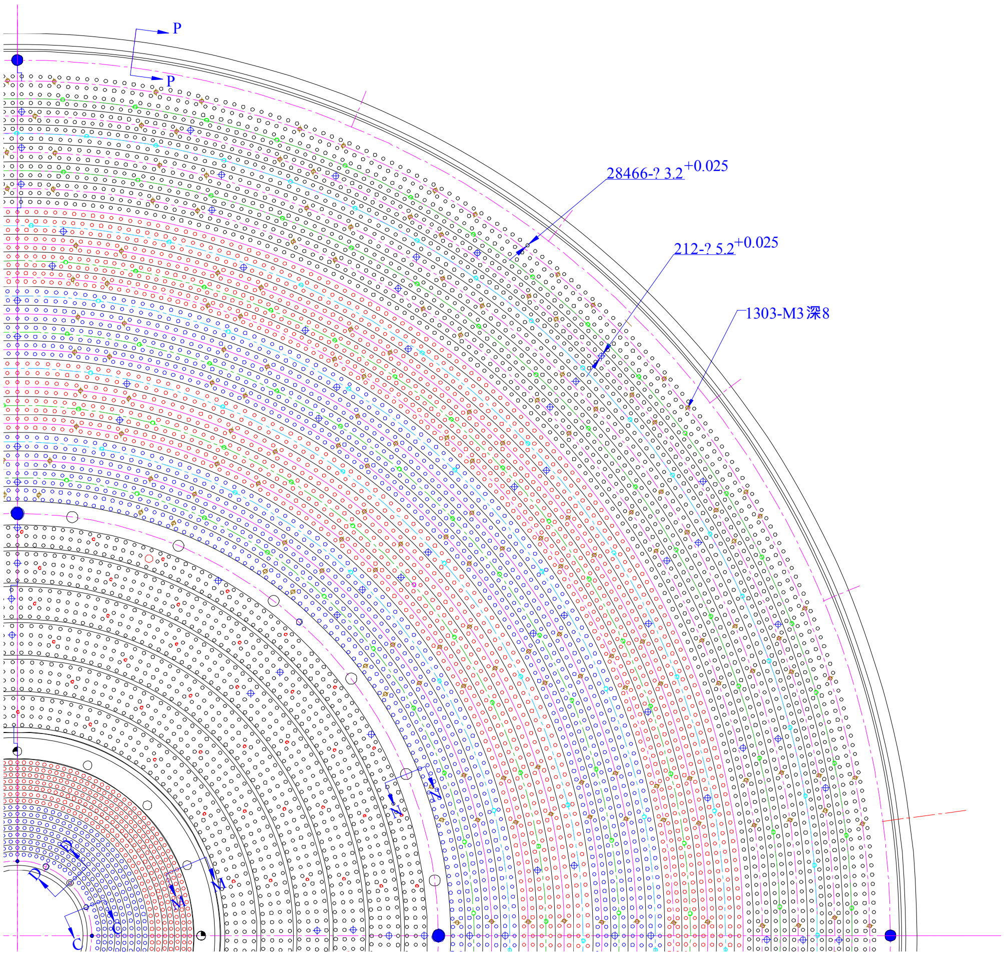

Fig.5.1-4 The layer arrangement

In order to save space and provide the optimum $\gamma-\phi$ pattern recognition, twelve axial layers are located in the stepped range, and every two layers have the same angle segmentation in $\gamma-\phi$ plane. In the tilted plane of the outer chamber, every four layers have the same angle segmentation in $\gamma-\phi$ plane, with no separate stereo field layers in between.

A stereo wire layer will be in a hyperboloid shape, the distance from the central point to the Z axis is the shortest. If the stereo angle is small, the sag ΔR in the center is $\Delta R = D^2/8R_{end}$, here R_{end} is the radius of the wire in the end-plate, D is the displacement of the wire along the circle in one end-plate. The stereo angle is $\varepsilon = tg^{-1}(D/2l)$. The single longitudinal resolution σ_z is approximately $(2l/D)\sigma_X$, where l is the half-length of the wire, σ_z is the single wire resolution. A bigger stereo angle can increase the longitudinal resolution, but at the same time, the sag will be bigger, which may affect the field uniformity. The stereo angle of all stereo wires is designed to be from 1.5 to 3.6 degree and the maximum sag will be less than 3mm. The longitudinal single wire resolution is better than 4.2 mm.

All layers should be arranged to shift with respect to each other in phi direction to prevent a large momentum particle from being always near the wires as it passes through the chamber, since the spatial resolution will be worse near the wires. The first cell of a stereo layer will be started at X-axis, while the axial layer will have to be started at a small angle with respect to the X-axis.

Low Z Working Gas

The helium gas is a low Z working gas with a radiation length of about 50 times longer (≈ 5300 m) than that of argon gas (110m)[1]. However, the ionization of charge particles in pure helium gas is five times lower and the diffusion is larger. Certain quencher needs to be added for stable operation, and a lot of helium based gas mixtures have been tested and simulated[3,4,5,6,7,8,9,10]. The properties of these gas mixtures are summarized in Table 5.1-3.

Table 5.1-3 Properties of some gas mixtures

	Ratio	Radiation	Primary(i.p./*cm*)	Total(i.p./*cm*)	Comment
He/C2H6	50/5	640	22.9	59.9	BELLE
He/iC4H10	90/10	1313	12.7	26.7	KLOE
He/iC4H10	80/20	807	21.2(20.6)	(45.4)	BABAR
He/CO2/iC4H10	83/10/7	960	11.5	29.2	BABAR
He/CH4	90/10	3087	(7.0)	(12.5)	KLOE
He/CH4	80/20	2178	(9.1)	(17.0)	BTCF
He/C3H8	60/40	550	32		CLEOIII

We choose a gas mixture of 60%He-40% propane as the working gas of the BESIII drift chamber, which was also used by the CLEOIII drift chamber. This mixture has a long radiation length (~550m), and a drift velocity saturated at 3.8 $cm/\mu m$ for a relatively low electric field. This is important for the operation of square-cell drift chamber because of the large field non-uniformities inherent from this geometry. The gas gain of this mixture is operated to be 10^4-10^5.

Simulation results based on the Garfield Program for He/propane gas mixture are shown in Fig.5.1-5 to Fig.5.1-8.

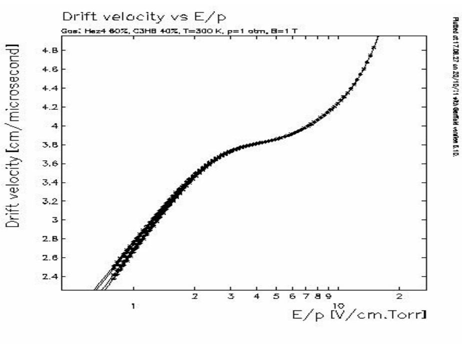

Fig.5.1-5 Drift velocity

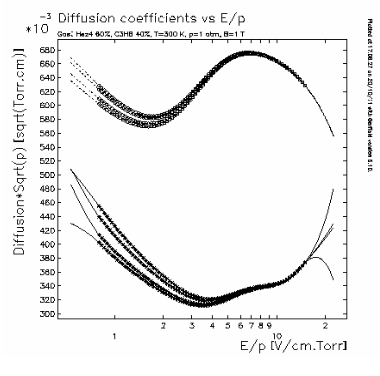

Fig.5.1-6 Diffusion coefficients

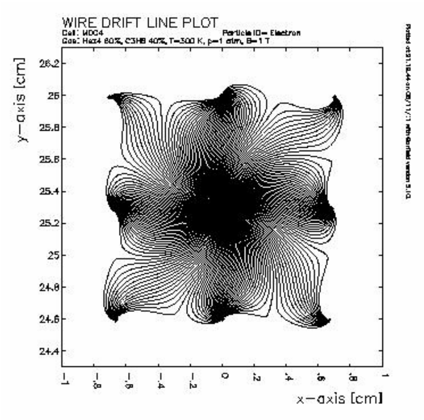

Fig.5.1-7 Positron drift line

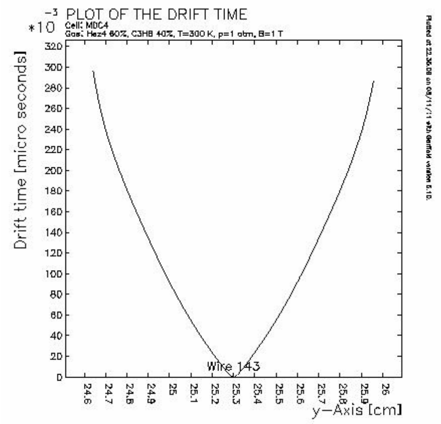

Fig.5.1-8 Drift time vs Drift distance

Low Z Field Wire

Several kinds of light material wires have been proposed and tested. The aluminum wire has a relatively long radiation length and is a good candidate for field wires. CLEOII reported a long-term creeping test for partial tempered 5056-Al field wire[13] (less than 15% tension reduction). Several other experiments like BELLE, BABAR and KLOE have also reported their measurements on the creeping of this kind of wires[3,4,5,6]. Fig. 5.1-9 shows the test result on the creeping effect of 110μm Al wires done in our laboratory.

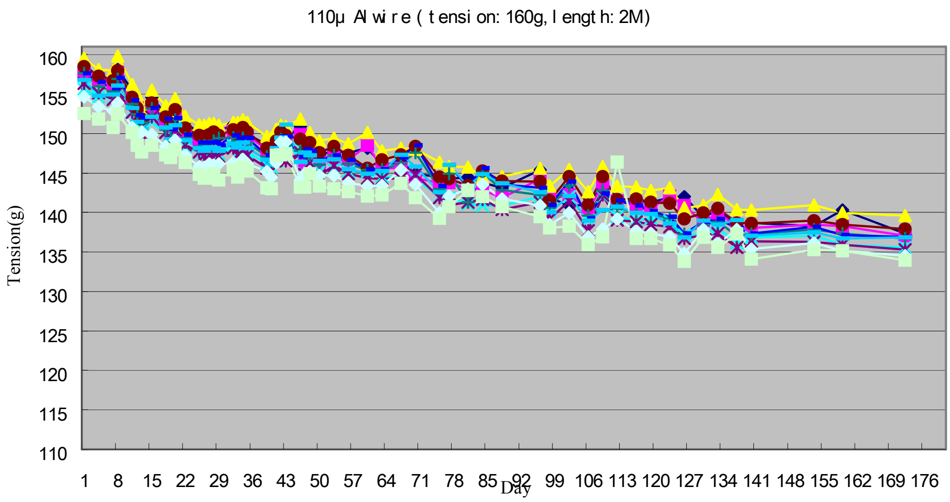

Fig.5.1-9 The creeping result from the Al wire

Feed-through Design

The feed-through is one of the most important components in the drift chamber. The design of the feed-through is based on the feed-through used in the CLEOIII drift chamber. It composes of three parts: the outer part is an insulating bush for high voltage insulation; the middle part is a copper tube for locating an inner tube and a high voltage connector and the inner part is a small tube for wire fixing. The small tube is made of copper for sense wires, and aluminum for field wires. The structure of the feed-through is shown in Fig. 5.1-10. The cramping method will be used to fix the wire in the inner tube.

The precision of the feed-through will directly affect the accuracy of the wire location. The designed radius tolerance of the middle and inner tubes is 0.013 mm, the outer insulating bushing is +0/-0.025 mm, and the concentricity is 0.05 mm.

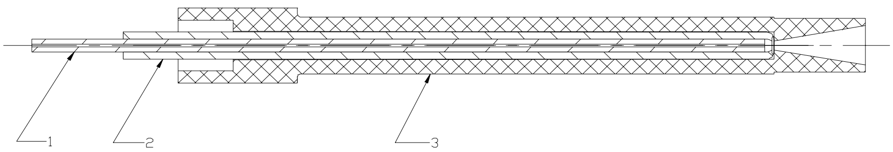

1. Inner tube; 2. Copper tube; 3. Insulating bush.

Fig.5.1-10 The structure of the feed-through

The material of the insulating bush is Vectra A130, a kind of liquid crystal copolyester with 30% glass fiber. It has good mechanical, electrical, and thermal properties. The linear coefficient of expansion is 0.2-2.2×10^{-5}(K-1)(230℃hour), and the dielectric constant is 0.003 at 10^3HZ and 0.016 at 10^6 HZ。

Mechanical Design

Design of the Drift Chamber

1. Inner Chamber

In order to reduce materials inside the particle detecting volume, the inner chamber is designed as an open cylinder, without outer skin as shown in Fig.5.2-1. All wire tension on the inner chamber will be transferred to the inner skin.

It will become a whole chamber after the inner chamber is connected to the outer chamber. However, the deformation caused by wire tension in the inner chamber and the outer chamber will not be the same. It has to be carefully designed on how to hence the connection of these two parts should be carefully designed, and attention should also be paid to the helium gas leakage. The optimum design will be based on the ANSYS simulation.

The endplates of the inner chamber are designed to be stepped structure with a small step size to reduce the deformation and stress in the junctures. The endplates are made of Aluminum (Al-7075) with a thickness of 25 mm. The inner skin of the chamber is made of carbon fiber, 1 mm thick (0.45 X_0). It will be loaded with the wire stress of 100 kilograms.

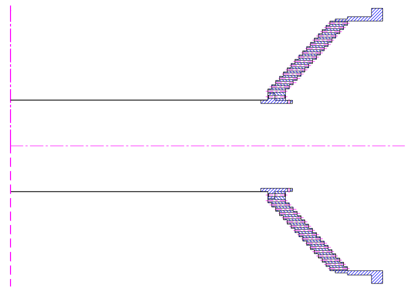

2. Outer Chamber

Fig.5.2-1 The structure of the inner chamber（1/2）

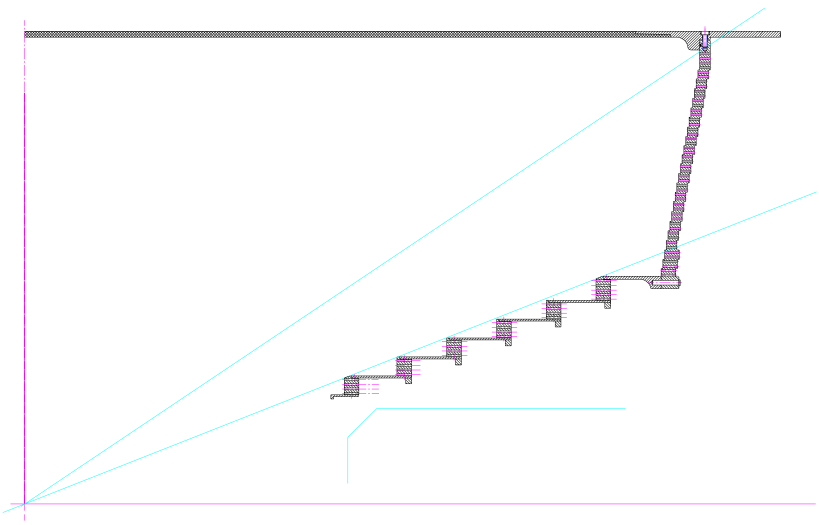

Fig.5.2-2 The structure of the outer chamber（1/4）

The structural design of the outer chamber is shown in Fig.5.2-2. The inner radius of the outer chamber is 198 mm and the outer radius 810 mm. The length of the inner skin is 1180 mm, and that of the outer skin 2350mm. The polar angle for maximum acceptance is $\cos\theta = 0.93$, while tracking with the last sense wire layer has an acceptance of $\cos\theta = 0.83$. The thickness of the outer skin, made of carbon fiber, is 11.0 mm (the TOF detector will be bound on the surface of the outer skin). To facilitate wire stringing(3.5T), 8 windows are cut on the outer skin, and will be covered after stringing is finished. Two extra cylinders are connected onto the sides of the chamber, serving as a support structure.

The endplate of the outer chamber is separated in two parts, one is with a multi-stepped structure, and the other is an inclined plane.

The design of the multi-step part is to guarantee that the chamber has a polar angle of $\cos\theta = 0.93$, and to have enough rooms for machine quadruples and chamber cables.

The stepped endplate is a set of 6 aluminum rings interconnected with aluminum bands via radial screws. Every ring holds 2 sense wire layers. The thickness of the endplate is 25 mm, and the material is aluminum Al-7075. The joint space is limited by half width of the cell (8.1 mm), so the thickness of aluminum bands will be limited to 3 mm. The multi-step endplate is a challenge to

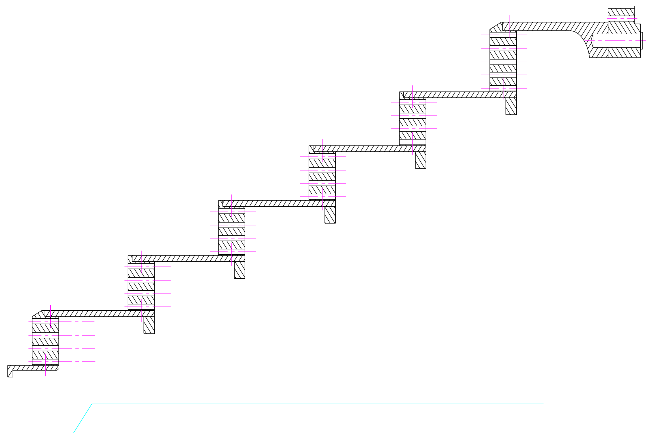

the mechanical manufacture, whose structural design is shown in Fig. 5.2-3.

Fig.5.2-3 The multi-step endplate design

The other part of the endplate is designed to have an inclined plane to reduce the deformation caused by wire tension, as shown in Fig.5.2-4. The inclined plane is machined from a whole aluminum plate and the thickness of the inclined endplate is 18 mm. It will be processed to have some mini steps to guarantee that all feed-throughs are positioned in parallel to the Z axis.

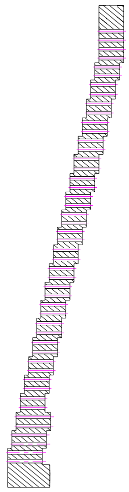

Fig.5.2-4 The structural design of the inclined plane

Analysis of the Chamber Structure

An ANSYS simulation is used for the structure analysis of the drift chamber. A unit plant 42 and a unit shell 51 are used in the ANSYS model. Due to the axial symmetry, the calculation model is a 2 D one with 1/4 of the drift chamber. The inner skin and outer skin are carbon fiber (T700), and all end-plate parts are aluminum (AL7075).

The wire tension effects are on the surface of the AL plate, the wire position is the same as the design chamber position. Points(A) of the inner skin and the outer skin are fully restricted. The load and the restraint of the chambers (inner and outer) are shown in Fig. 5.2-5.

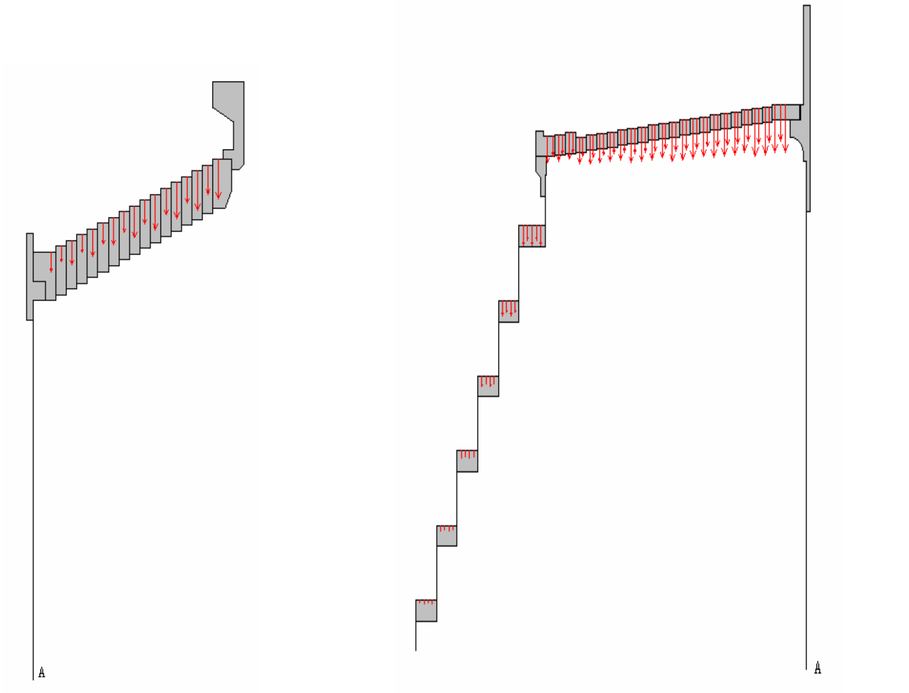

Fig.5.2-5 The load of the chambers and the restraint points

The main deformation area of the inner skin and the outer skin are shown in Fig.5.2-6 and Fig.5.2-7.

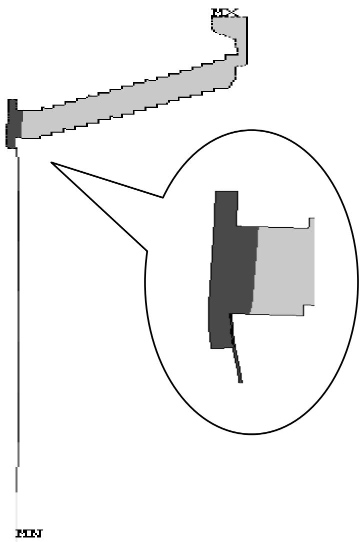

Fig.5.2-6 The schematic drawing of the deformation of the inner skin

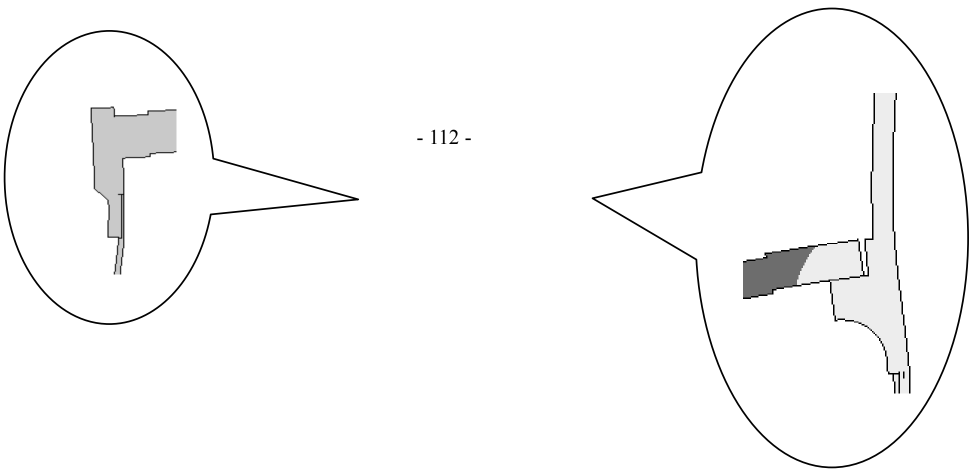

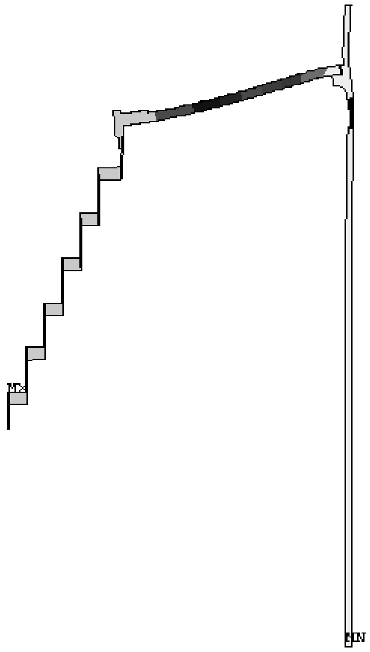

Fig.5.2-7 The schematic drawing of the deformation of the outer skin

1. Analysis of the inner chamber

The shift of the inner skin along the axial is very small, actually less than 30μm. The radial shift and the wire revolving angle, as shown in Fig.5.2-8 are small too.

If the thickness of the inner skin is 0.5mm, the safety coefficient is 19.2925. It does consider the influence after the outer chamber is connected.

The ANSYS result of the inner chamber is shown in Fig.5.2-9.

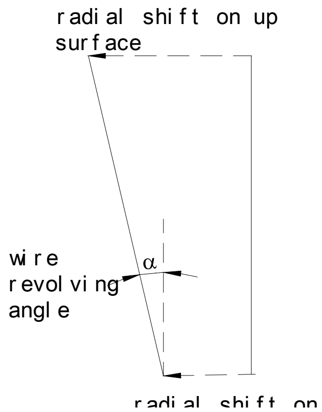

Fig.5.2-8. A wire revolving angle

2. Analysis of the outer chamber

The structure parameters are chosen as the following: the equivalent thickness of the stepped endplate is 20 mm, the equivalent thickness of the inclined endplate is 15.2 mm (because there are holes in the endplates); the equivalent thickness of the outer skin is 11.5mm; and the total wire tension is 3.8T. The influence of the gravity is considered and the restricted points are asymmetrical. The ANSYS result of the outer chamber is shown in Fig.5.2-10.

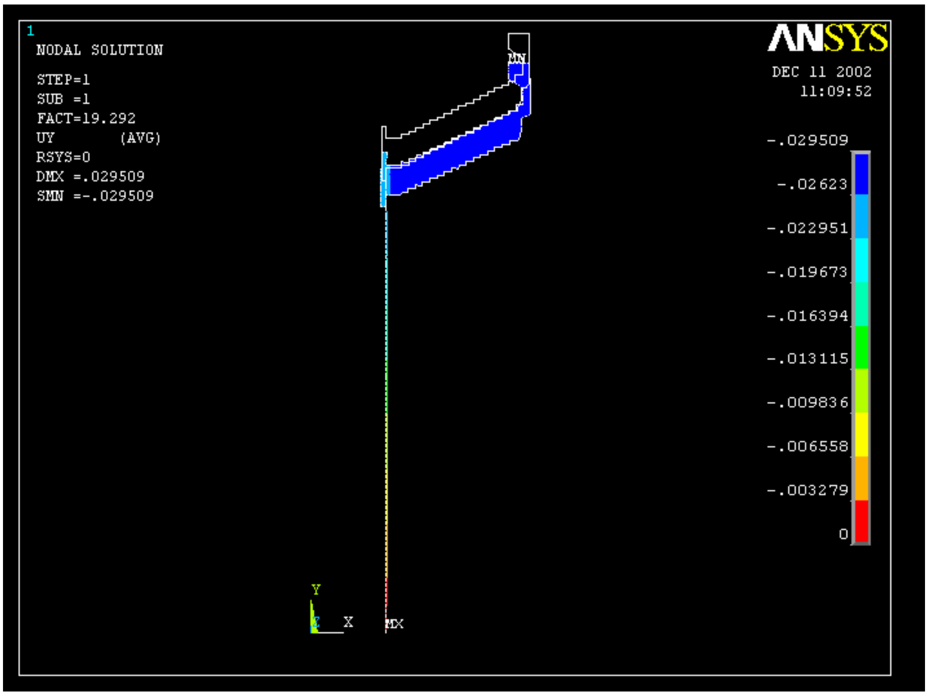

Fig.5.2-9 The ANSYS result of the inner chamber

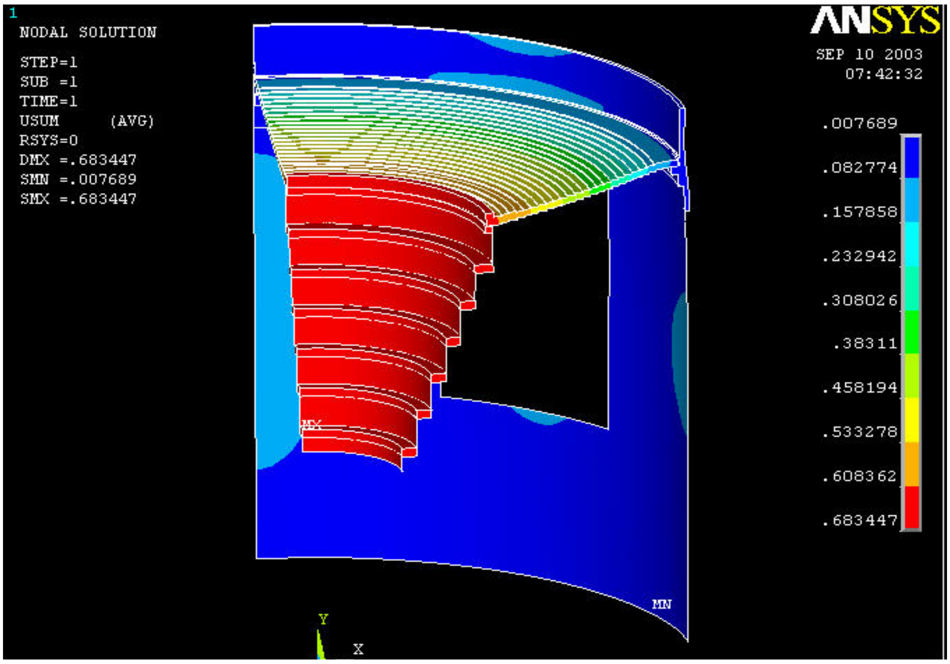

Fig.5.2-10 The ANSYS result of the outer chamber

Drift Chamber Assembling

2.3.1 Installation of the Outer Chamber Endplate

The assembling accuracy of the multiple steps will directly affect the wire position accuracy in the chamber. The tolerance of holes for wires in every ring is 25 μ m. To meet the demand of the single wire position, the tolerances of positions of all wire holes should be below 50 μ m. A method has to be worked out to guarantee the assembling accuracy of multiple steps.

2.3.1 Installation of the Inner Chamber Endplate

The endplate of the inner chamber is processed from a whole aluminum plate, and all wire holes are finished in a digital mechanical center. The hole tolerance could be controlled at 25 μ m. Since there is no outer skin for the inner chamber, two endplates are only jointed with the inner skin. It is a key point to guarantee that two endplates will be paralleled within 200 μ m and the concentricity will be less than 100 μ m .

2.3. ... ber

The parall ... 200 μ m, and their r

Drift C

There will ... total wire tension is ... pre-stress method wi

1.

It is simpl ... the wiring, the inner c ... e the inner chamber t

2. Out

The c ... support to hold the o ... shown in Fig.5.2-9.

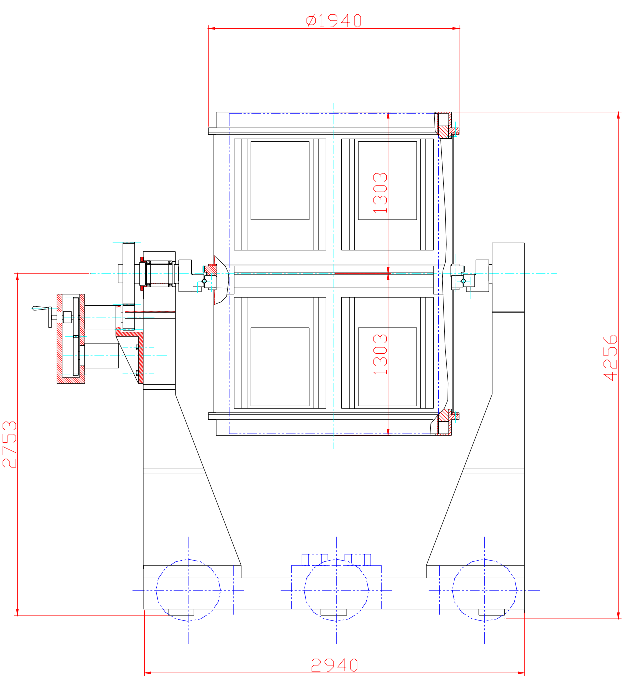

Fig.5.2-9 The wiring machine

The wire in a roll controlled by a step motor is stretched from the up endplate down to the bottom of the chamber. The end of the wire is made to pass through the feed-through by hand (or automatically), and connected to a small magnetic bar, which is sent to the chamber through the hole for wiring. After that the feed-through is inserted into the hole. The wire will go down, with the roll moving, to the expected hole on the bottom endplate. There could be a little position uncertainty in matching the wire with the hole. A small iron stick will be used to guide the bar out from the hole. For a stereo layer wiring, the body of the chamber will be tiled by an angle to guarantee that the holes in the up endplate and the down endplate are aligned in vertical direction.

High Voltage System

A positive high voltage will be connected to the sense wire to form a drift field in the drift cell. The merit of this scheme is that the field wires and the endplate are in the same potential and grounded. The configuration of high voltage connection will become easy and the number of high voltage cables is minimum. The weakness of this scheme is that a capacitor must be used for signal readout, and more noise will be picked up from the capacitor. The BES II drift chamber adopted this signal readout scheme, the noise problem is not serious and the result is acceptable. The principle diagram of the high voltage power supply system is shown in Fig.5.3-1.

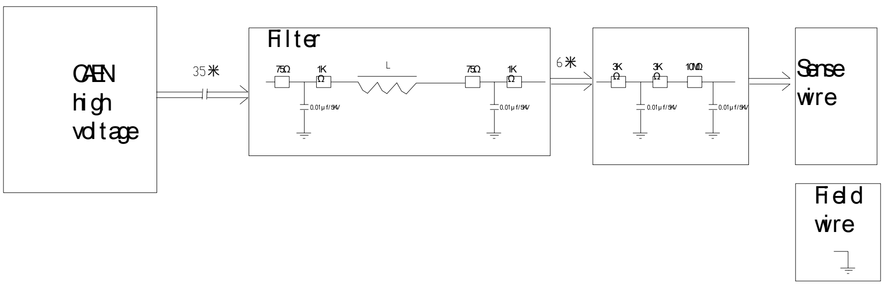

Fig.5.3-1 The principle diagram of the high voltage power supply system

An RC low pass filter is used for each supply at the end plate of the drift chamber before distributed to the chamber wires. This filter is located on the high voltage distribution board that supplies all voltages for one layer. The common side of the filters is tied to the end plate. The filters are designed such that any noise on the power supply lines should contribute less than the equivalent of 1/3 of a primary ionizing particle, in the frequency band of the first stage of the pre-amplifier. The noise reduction through the filter is shown in Fig.5.3-2.

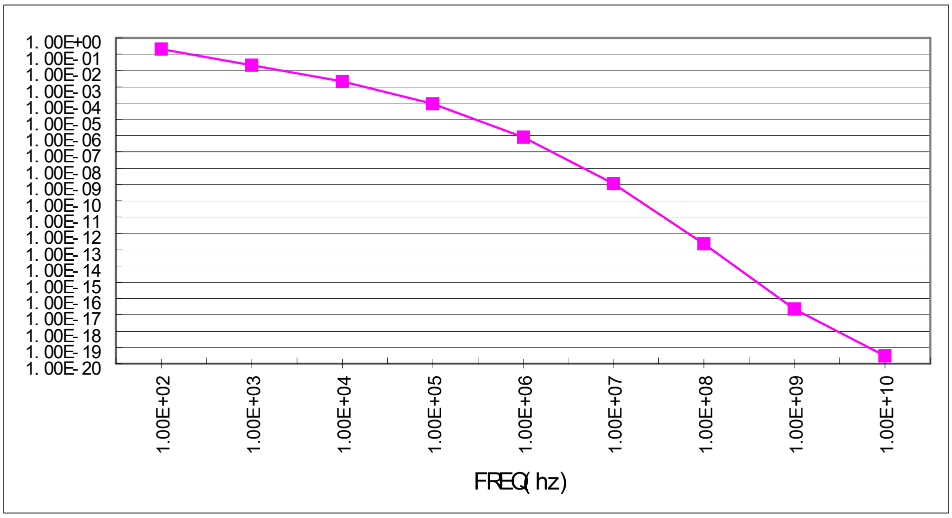

Fig.5.3-2 The noise reduction result through the filter

The HV connector to the feed-through is a key component. It must have a good contact with the feed-through, and be convenient to be replaced. This is an important task on the R & D program.

Electronics Readout

The BESIII drift chamber has a total of 6860 sense wires. The time (T) and electric charge (Q) information of each sense wire will be read out.

Since the single wire spatial resolution is designed to be $\sigma_{xy} \leq 130\mu m$, the time measurement error from electronics readout of 0.5 ns is desirable, assuming a drift velocity of 3.8cm/μs.

The charge deposition could be measured by integrating the signal from sense wire, and the uncertainty should be better than the intrinsic resolution of about 6%. Therefore a charge measurement with a precision of 2% is sufficient to match the chamber resolution. [1,6]

Expected Performance

1. Solid Angle Coverage

As show in Fig.5.1-1 the solid angle coverage is $\cos\theta$=0.93 and in the last sense wire layer is $\cos\theta$=0.83.

2. Single Wire Spatial Resolution

The single wire spatial resolution consists of the following terms:

$$\sigma_x^2 = \sigma_d^2 + \sigma_t^2 + \sigma_i^2$$

where,

σ_d is the contribution from the diffusion, about 60μm in our case,

σ_t is the contribution from the time measurement error of the readout electronics, assuming 40 μm here,

σ_i is the contribution from the statistic distribution of primary ionization electron to the σ_x.

Form experiences of similar chambers, a single wire spatial resolution of $\sigma_x \leqslant 130$ μm can be achieved [1][3].

3. Single Wire Z-direction Resolution

According to the experience formula, $\sigma_z = (2l/D)\sigma_x$, where l is the half length of the wire, D is the displacement of the stereo wire along the circle. There are a total of 28 layers of stereo wires in the chamber, each of the σ_z is listed in Table 5.1-1, where they are all less than 5mm.

4. Momentum Resolution

Transverse momentum resolution consists of contributions from position resolution and multiple scattering:

$$\frac{\sigma_{p_t}}{p_t} = \left(\frac{\sigma_{p_t}}{p_t}\right)^2_{pos} + \left(\frac{\sigma_{p_t}}{p_t}\right)^2_{m.s}$$

$$\left(\frac{\sigma_{pt}}{p_t}\right)_{pos} = \frac{3.3\times 10^2 \times \sigma_x}{B\times L^2} \times p_t \times \sqrt{\frac{720}{n+5}}$$

$$\left(\frac{\sigma_{pt}}{p_t}\right)_{m.s} = \frac{5.7}{B\times L} \times \frac{1}{\beta} \times \sqrt{\frac{L\times P}{X_0 p_t}}$$

Where L (level arm) = 72 cm , B (magnetic field) = 1.0 Tesla , σ_x (spatial resolution) = 0.013 cm , N (number sampling) = 43 and p_t / p ~1 .

Taking the radiation length of gas mixture, X_0, as 550 m[1], and assuming the wire material uniformly distributed in the chamber volume, the total X_0 is =217.76 m. The momentum resolution from the two contributions can be written as:

$$\left(\frac{\sigma_{pt}}{p_t}\right)_{pos} = 0.32\% p_t, \qquad \left(\frac{\sigma_{p_t}}{P_t}\right)_{m.s} = 0.37\% / \beta$$

From the calculation, the multiple scattering is the main contribution to the momentum resolution.

The TRACKERR program was developed by the BABAR drift chamber group to quickly simulate the performances of the chamber. The momentum resolution of the BESIII drift chamber based on simulation using TRACKERR, is $\sigma_{p_t} / p_t = 0.46\%$ at 1 GeV/c, as shown in Fig.5.5-1.The actual momentum resolution of the drift chamber is expected to be 0.5%.

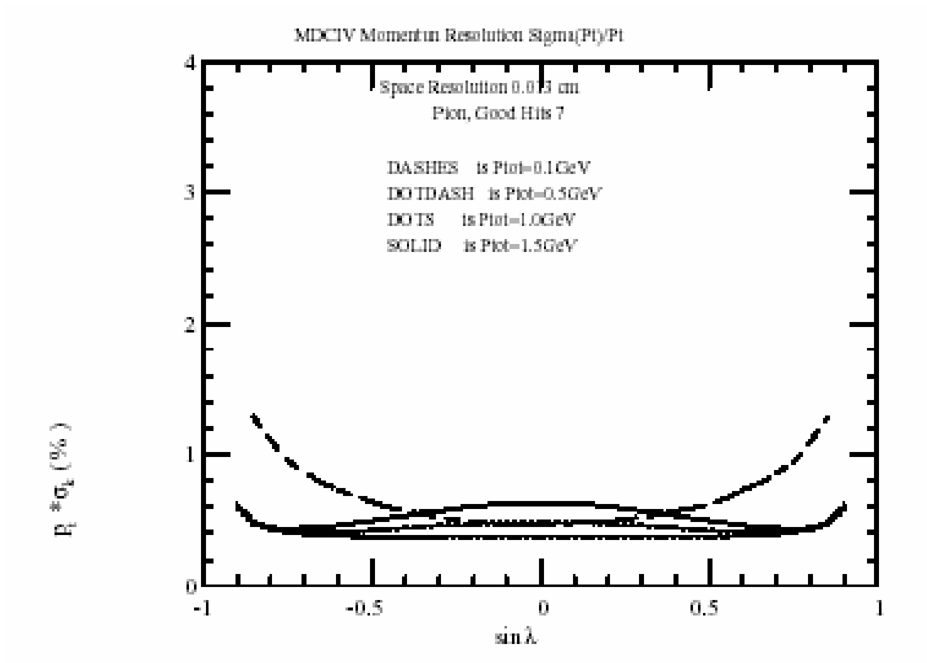

Fig.5.5-1 The momentum resolution from the TRACKERR simulation

The Z resolution of the chamber depends on the wire stereo angle and the number of stereo layers. The Z resolution of the chamber based on the TRACKERR simulation is better than 2 mm, as shown in Fig.5.5-2.

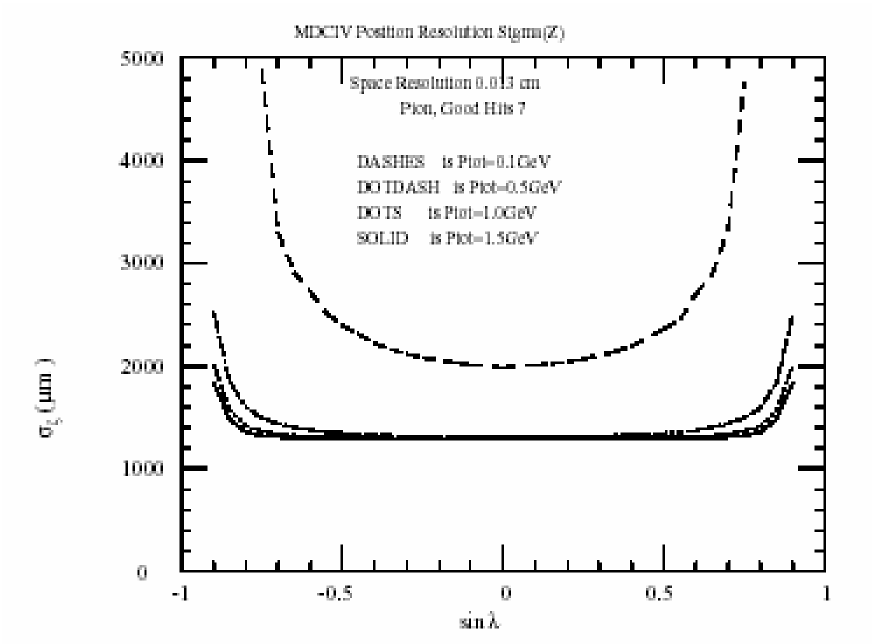

Fig.5.5-2. The Z resolution from the TRACKERR simulation

5. dE/ dX Resolution

The drift chamber is separated in two parts, the inner chamber and the outer chamber. There are 8 sense wire layers in the inner chamber, with the average dimension of the inner chamber being $6\times 6mm^2$, and 39 sense wire layers in the outer chamber, with the average dimension being $8.1\times 8.1mm^2$. The working gas is He (60%)+ C3H8 (40%) mixture.

The single wire ionization signal follows the a Landau distribution, hence there is a long "tail" in the high signal side. The probable energy loss is usually used to represent the ionization energy loss. The results from the calculation are shown in Fig.5.5-3. It can be seen that the distribution for π, K, and p have the similar form, and that the minimal energy loss (~ 1.49 keV) is the same at different momenta. For π particles, the minimal point is at the momentum P～510-550 MeV/c.

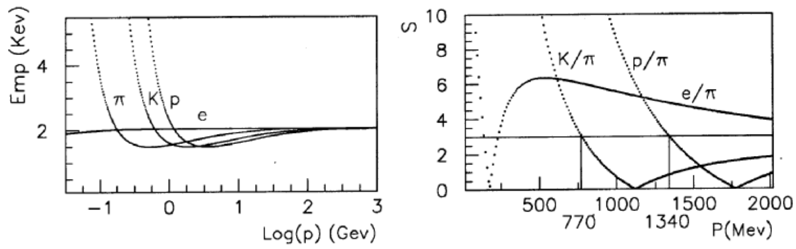

Fig.5.5-3 (a) Calculated probable energy loss E_{mp} as a function of P, in 1.62 cm long samples
(b) The particle identification capability

To estimate the capability of the particle identification of the drift chamber, we defined an identification power:

$$S=\frac{\Delta E}{\sigma_n}=\frac{|\Delta E_i-\Delta E_\pi|}{\sigma_n},(i=e,K,p)$$

where ΔE_i and ΔE_π are the probable energy losses for particle i and π respectively, σ_n is the average energy loss resolution for a sample of N. From the calculation, σ_{43} is 5.7% for the sample length in He/C3H8 (60/40) gas mixture.

3σ_n π/K and π/p separations are at momentum 0.77 GeV/c and 1.34 GeV/c respectively.

The dE/ dx resolution is expected to be 6-7%.

R & D Programs

Following R&D program will be carried out in the next one to two years.

1. Garfield simulation. The distribution of the electric field in a cell, the charge density of a sense wire, the relationship of the drift time and the drift distance, and the wire stability will be studied.

2. Prototypes. A single cell prototype and two multiple-cell prototypes (14mm*14mm, 16.4mm*16.4mm) were made to study the gas characteristics and the cell structure. More

prototypes will be made to study the layer arrangement, the differences between a stereo layer and an axial layer, the connection of the high voltage and pre-amplifier, and the life of the chamber. The beam test will be performed in KEK in 2004.

- The single cell prototype: Results of the gas gain and the electron drift velocity (He/C_3H_8(60/40)) were obtained, as shown in Fig.5.6-1 and 5.6-2.

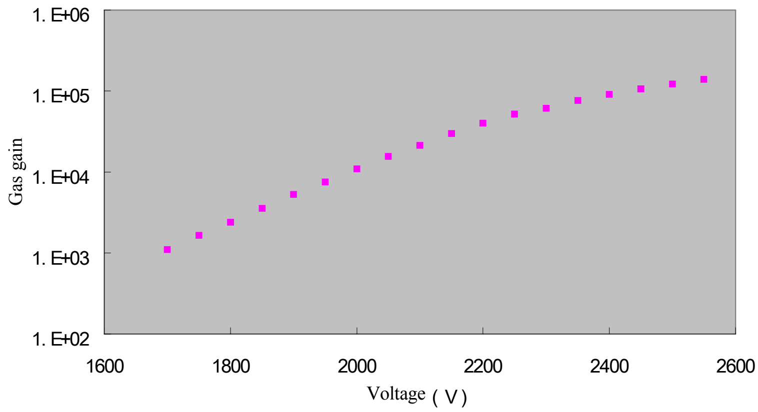

Fig. 5.6-1　The gas gain of one drift cell

Fig.5.6-2　The electron drift velocity with the gas He/C3H8(60/40)

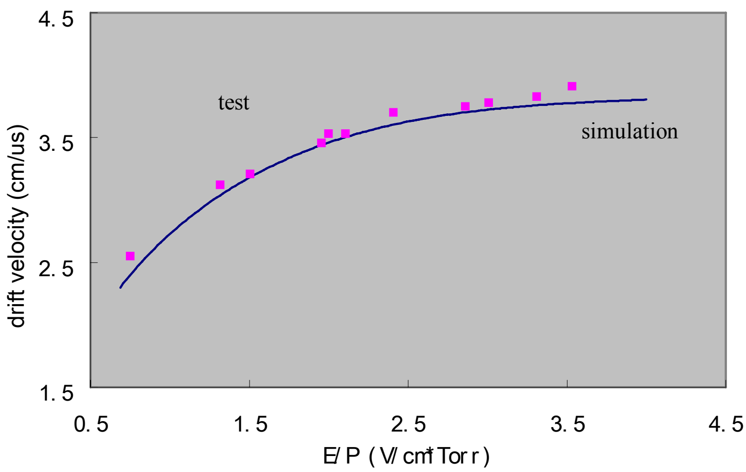

- Multiple-cell: there are two multiple-cell prototypes (the cell size are 16.4*16.4 and 14*14), as shown in Fig.5.6-3 . There are ten sense wire layers in every prototype, five cells in each layer. The single wire special resolution, and drift time with drift distance have been studied; correlation related to the high voltage supply, the temperature, the gas and the threshold have be studied.

The results of the drift velocity, the charge distribution, the relationship of the single wire special resolution are shown in Fig. 5.6-4 to Fig.5.6-6.

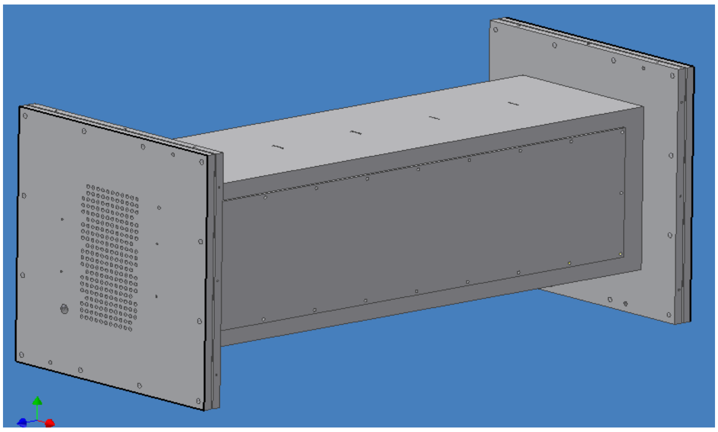

Fig.5.6-3 The Multiple-cell prototype

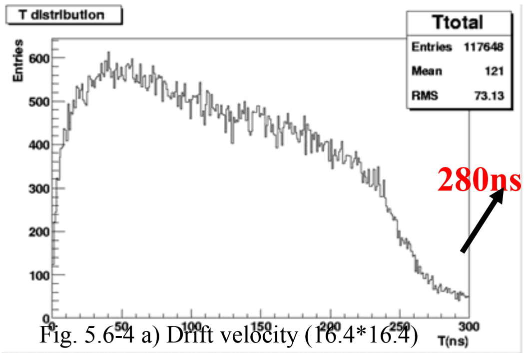

Fig. 5.6-4 a) Drift velocity (16.4*16.4)

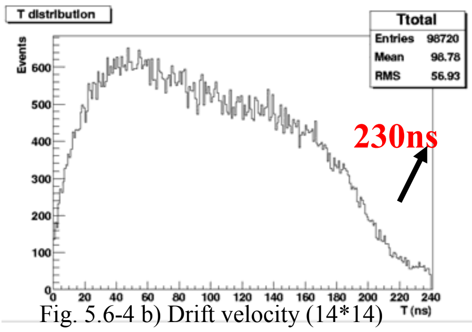

Fig. 5.6-4 b) Drift velocity (14*14)

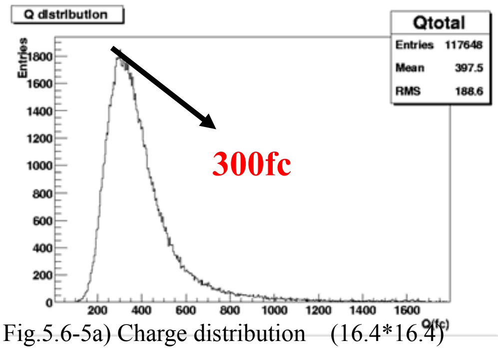

Fig.5.6-5a) Charge distribution (16.4*16.4)

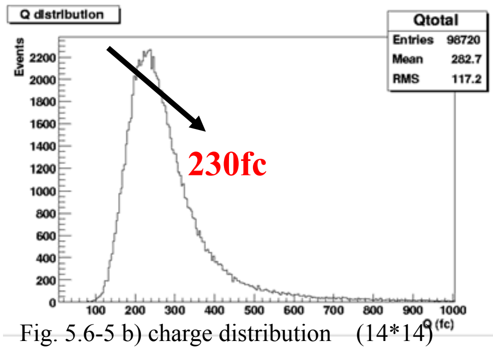

Fig. 5.6-5 b) charge distribution (14*14)

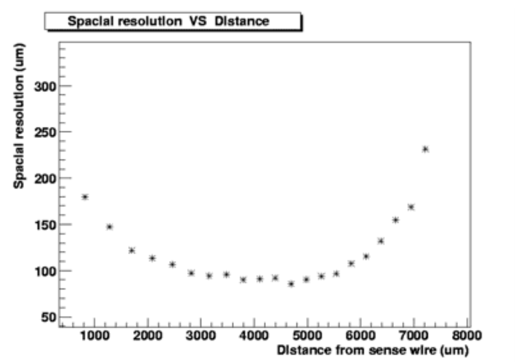

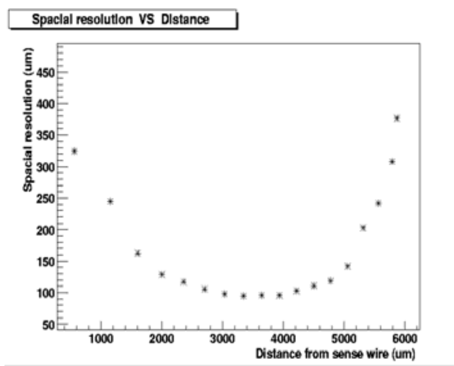

(16.4*16.4) **(14*14)**

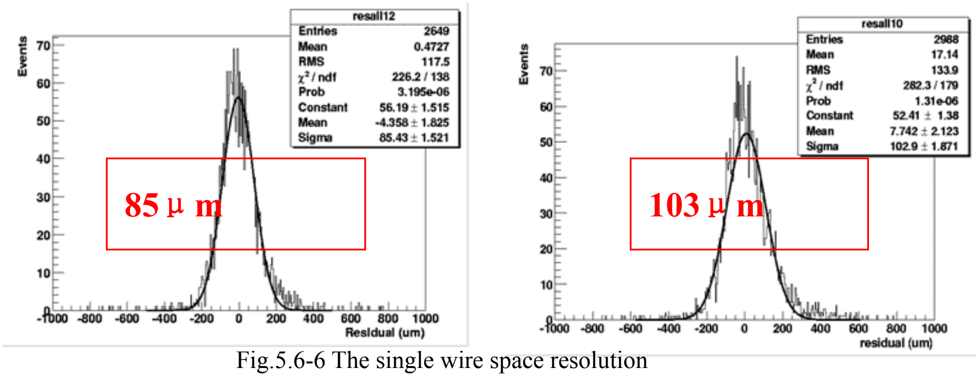

Fig.5.6-6 The single wire space resolution

3. A structural prototype

The manufacture of the multi-stepped structure of the chamber is a challenge for manufactory in China. A structural prototype was made by one of them. The technology of aluminum rings interconnection, and the precision of the assembly among rings and bands, and the precision of holes were studied.

The prototype is a cylindrical structure with three steps, as shown in Fig.5.6-7. The wire holes are copied from the real chamber design, the diameter of the hole is 3.2mm, the position precision of the hole is 0.025mm, and the assembly precision of the bands is less than 0.050mm.

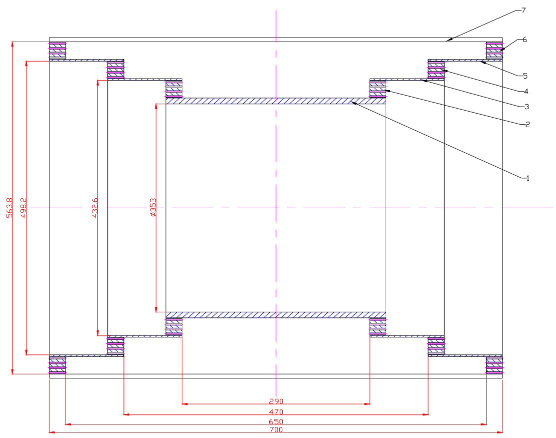

Fig. 5.6-7 The structural prototype

2． Cooperation with the CLEOIII and BELLE experiments is desirable. We will make the best use of the successful technology used by other detectors to design our drift chamber. This is important to reduce the R&D time and to perfect the drift chamber structural design and manufacture.

Reference

[1] IHEP-BTCF Report-03 October,1996

[2] The Analysis of the Construction of MDC III (internal material)

[3] Belle Colla. "Technical Design Report", KEK Report 95-2 (Apr. 1995)

[4] BaBar Colla. "Technical Design Report", SLAC-R-95-457(May 1995)

[5] KLOE Colla. "The KLOE Central Drift Chamber:, LNF-94/028(IR)3.1994

[6] "The CLEO III Detector: Design and Physics Goals" ,www.lns.cornell.edu

[7] "Low Mass Gas Mixtures for Drift Chamber Operation",CERN-PPE/93-51

[8] "Study of Helium-based Drift Chamber Gases", NIM A 374(1996)27-23

[9] "Study of a Drift Chamber Filled with a Helium-Ethane Mixture", NIM A330 (1993) 55-63

[10] "Final Results of an Experimental Study of a Large Area Planar Drift Chamber Filled with a He-based Mixture", NIM A 385(1997) 58-68

[11] " Simulation and Calculation of Performance of the Small Cell Drift Chamber", Nuclear Electronics & Detection Technology,Vol.17 No.4 July 1997

[12] "Study of Performances of a Small Cell Drift Chamber Filled with Helium-methane Gas Mixture", Chen Chang (2000)

[13] D.G. Cassel et al., NIM A252(1986)325

[14] " The Creeping Effect Study of Aluminum Field Wire for High Precision Drift Chamber", Nuclear Electronics & Detection Technology,Vol.19 No.6 July 1999

[15] "Performance Estimation of a High Precision Central Drift Chamber Used to Detect Low

Momentum Particle", Nuclear Electronics & Detection Technology, Vol.22 No.3July 1998

[16] "The Main Drift Chamber for BES Spectrometer", Jimao Ma,1988

[17] "A High Resolution Cylindrical Drift Chamber for the KEK B-factory", KEK Preprint 2000-2, March 22, 2000

[18] " CLEO- c and CESR- c: A New Frontier of Weak and Strong Interactions" CLEO- c Collaboration, CLNS 01/1742

[19] " The CLEO III Detector Status Report", CLEO Collaboration, CBX 96-93, December 1,1996

Particle ID: The Time of Flight (TOF) system

A Time Of Flight (TOF) detector is placed between the MDC and EMC(see Fig.6-1). The solid coverage of the barrel TOF is 0.83, and that of the endcap TOF is from 0.85 to 0.95. TOF is to measure the flight time of charged particles for particle identification (PID) by comparing the measured time against the predicted time obtained from the charged particle track and the momentum given by the MDC. The TOF also provides a fast trigger signal for charged particles identification.

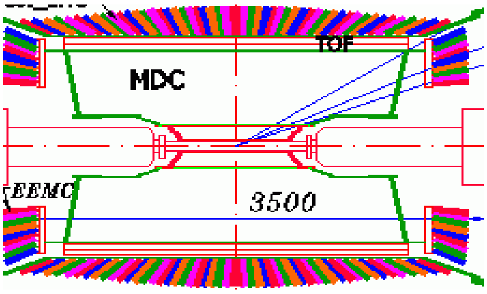

Fig.6-1 BESIII frame

The physics target of TOF is to identify particles and its capability is determined by the flight time difference of particles of different types, which is determined by the flight path. Among all parameters, the time resolution is the key, and it is related to many items as to be discussed in the next section.

Analysis of Time Resolution

The time resolution of TOF have the following contributions:

$$\sigma = \sqrt{\sigma_{TOF}^2 + \sigma_{bunch-time}^2 + \sigma_{bunch-length}^2 + \sigma_{Z-position}^2 + \sigma_{electronics}^2 + \sigma_{expect}^2 + \sigma_{time-walk}^2}$$

1) σ_{TOF} , intrinsic TOF time resolution.

The intrinsic time resolution of TOF is related to the scintillator and the PMT performance via the following formula[1],

$$\sigma_{TOF} = \sqrt{(\frac{1}{2.35})^2 \left\{ \tau_{scin}^2 + \left[\frac{n(n-1)L}{2c} \right]^2 + \tau_{PMT}^2 \right\}} \Big/ \sqrt{N_{pe}}$$

Here, τ_{scin} is the decay time of the scintillator, n the refractive index, L the distance from the hit position to the PMT, τ_{PMT} the time jitter of the PMT for a single pe (photo-electron), and

N_{pe} the number of the pe's detected. N_{pe} depends on the scintillation light output, its attenuation length, and the quantum efficiency of the PMT as given by the following formula:

$$N_{pe} \propto \int N_0(\lambda) L_t e^{-L/L_a} \varepsilon(\lambda) d\lambda$$

where λ is the light wavelength, $N_0\lambda$ is the scintillating light output per unit thickness, L_t is the thickness of particle passing through the scintillator, L_a is the attenulation length of the scintillator, $\varepsilon(\lambda)$ is the quantum efficiency function of the PMT. From this formula and our experiences and that of the Belle, the intrinsic time resolution is expected to be better than or equal to 80ps for a single TOF layer (see section 6.4 and 6.5).

2) $\sigma_{bunch-time}$, from the bunch timing uncertainty.

The time resolution is degraded by the uncertainty of the bunch timing with respect to a global timing marker (e.g. RF clock). There will be 93 beam bunches at the same time and the phase resolution of beam bunches from RF is about 1°, for a RF period of 2ns. Thus the intrinsic bunch timing resolution is about 5ps. A further degradation occurs due to jitters in registering the TOF timing measurements with respect to the global timing marker and in the readout electronics. The bunch timing uncertainty is expected to be about 20ps including jitters due to cables.

3) $\sigma_{bunch-length}$, from the bunch length uncertainty.

Electrons and positions collide in the beam bunch, and their collision time depends on the bunch time and bunch length. According to the design of BEPCII, the bunch length is 1.5cm, i.e., 50ps. Considering the collision of two bunches, the uncertainty will be reduced by a factor of $\sqrt{2}$, which is 35ps.

4) $\sigma_{z-position}$, from the Z-position uncertainty.

The transit time in the scintillator depends on the uncertainty in the Z-position of the particle impact. According to the MDC track reconstruction, the Z-position uncertainty is about 0.5cm, taking into account the refractive index of scintillator of about 1.5, which corresponds to a 25ps timing error.

5) $\sigma_{electonics}$, from electronics of the time measurement.

The electronics of the time measurement of TOF will use the CERN HPTDC chip whose resolution is better than 25ps according to its design.

6) σ_{expect}, from the resolution of expected time of flight in MDC.

The capability of particle identification is determined by the difference of the measured time and expected time. So the resolution of the expected time of flight in MDC, which is determined by the resolution of tracking length and momentum will directly affect Particle ID. The resolution of momentum measurement is better than 0.6% for 1GeV/c tracks, and the tracking length resolution should be several millimeters from our simulation, thus σ_{expect} will be about 30ps.

7) $\sigma_{time-walk}$, from the time walk effect.

The double threshold scheme will be used to suppress the background and reduce the time-walk effect. The high threshold(about 250mV) is to give a trigger and the low threshold(about 50mV) is to measure the time. If the rise time is 3ns and the ADC resolution is 4mV, the time-walk effect is about 10ps, as shown in Fig.6.1-1.

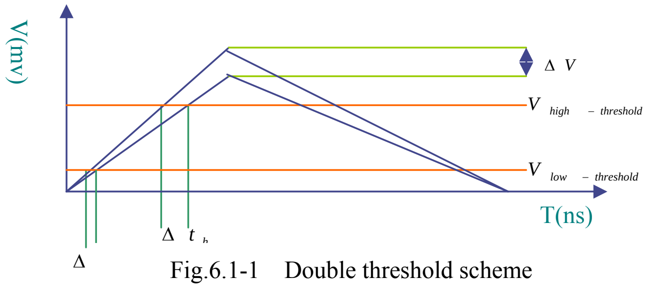

Fig.6.1-1 Double threshold scheme

$$\Delta t_h \approx \frac{\Delta V}{V_{signal}} t_{rise-time},$$

$$\Delta t_l = \frac{V_{low-threshold}}{V_{high-threshold}} \Delta t_h \approx \frac{1}{5} \Delta t_h$$

In total, the double-layer barrel TOF is expected to have an 90ps time resolution, as detailed in Table 6.1-1.

Table 6.1-1 Analysis of TOF time resolution

Item	Barrel time reso.	Endcap time reso.
Intrinsic time reso. of one TOF layer	80~90ps	80ps
Uncertainty from bunch length	15mm，35ps	15mm，35ps
Uncertainty from bunch time	~20ps	~20ps
Uncertainty from Z position	5mm,25ps	10mm,50ps
Uncertainty from electronics	25ps	25ps
Resolution of expected time of flight	30ps	30ps
Time walk	10ps	10ps
Total time reso, one layer of TOF	100~110ps	110~120ps
Total time reso, double layer of TOF	90ps	

The endcap TOF will use the fan-shaped scintillators instrumented with PMTs at inner radius. Though the width of scintillator increases and readout is from only one end, the total scintillator length decreases to about 40cm, hence the intrinsic time resolution can still reach 80ps. Since particle hit position will be not determined as precisely as for the barrel, a 50ps timing uncertainty is expected for an estimated 10mm error. In summary, the endcap TOF is expected to have a time resolution of 110ps.

Capability of Particle ID

The flight time difference of K/π with the same momentum, ΔT, can be estimated from the BESIII dimensions. Compared with the TOF time resolution, an estimate can be made for the K/π separation capability.

If we assume the flight time measurement is a Gaussian distribution, a 2σ separation corresponds to ΔT>3.38σ, and a 3σ separation corresponds to ΔT>5.60σ.

The time resolution is a function of the hitting position on scintillator, which follows the following formula based on our experience:

$$\sigma(x) = \sigma(0) \cdot (1 - 0.3x^2)$$

where $\chi = \cos(\theta)$, θ is the polar angle. σ(0) is the time resolution at the middle of the scintillator.

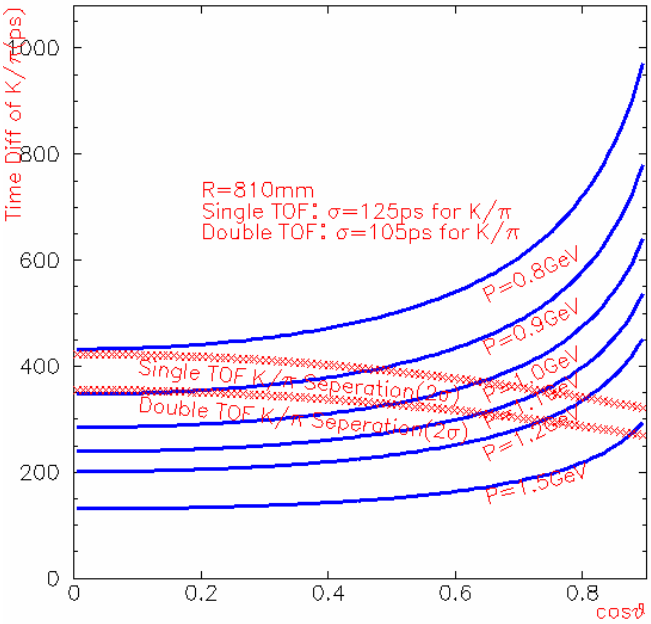

Fig.6.2-1 Kaon and Pion separation capability.

The target of the time resolution of one layer for muons is about 100～110ps. For kaon and pion, it will increase by 20% because of strong interaction as experienced at BESI, BESII and BELLE. For the double TOF, intrinsic time resolutions are reduced by a factor of $\sqrt{2}$, hence $\sigma(0) = 105\,ps$.

Calculated from the above formulae, Fig.6.2-1 give the K/π separation capability for one layer or double TOF. The momentum of 2σ K/π separation can go up to 0.8GeV/c or 0.9GeV/c for single and double TOF respectively.

Experience of BESII and BELLE

The BESII[2] TOF was constructed from 1994 to 1996. Its barrel consists of 48 BC408 scintillation counters of 284cm long, 15.6cm wide and 5cm thick. Each scintillator is connected to a 16cm long fish tail-shaped light guide coupled to a round light guide and mated to a 2" PMT, as shown in Fig.6.3-1. The ratio of the effective area of PMT to scintillator is only 16%. The PMTs used are Hamamatsu R2490-05, with fine-mesh dynodes and a gain of up to $3x10^6$ (0T) at no magnetic field and at a magnetic field of $1x10^6$(0.5T) .

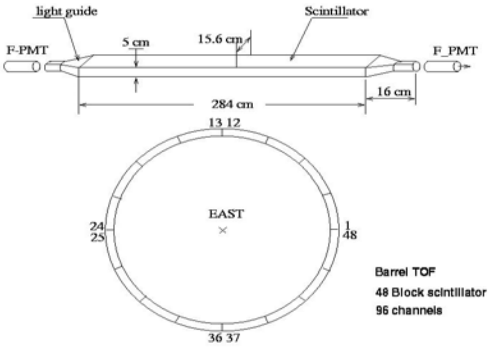

Fig.6.3-1 BESII TOF module

The total time resolution of BESII TOF is 180ps, where the intrinsic time resolution is 135ps while another 125ps error comes mainly from the bunch length of the beam. Because the radius of MDC is large, 115cm, the momentum upper limit for K/π separation is 0.8GeV/c, as shown in Fig. 6.3-2.

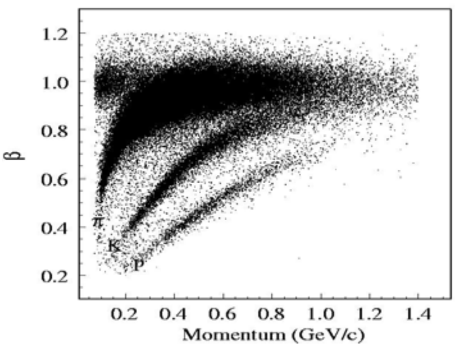

Fig.6.3-2 Velocity versus momentum of different particles in BESII

The Belle ...)

and one layer TOF scintillation counters. Its TOF scintillators are 255cm long, 6cm wide and 4cm thick and connected to PMTs directly. Its ratio of effective area of PMT to scintillator is up to 50%. The PMT, R6680, is specially designed by Hamamatsu with 24 fine-mesh dynode stages. Its gain is up to 3×10^6 in a 1.5T field and its transit time spread is 320ps(r.m.s.). Total time resolution of Belle TOF reaches 100ps with the intrinsic part of 70～80ps.

The major reason for such a large difference is that the BESII TOF has light guides between scintillator and PMT hence small area ratio of PMT to scintillator and less photoelectrons.

Choice of Scintillator and PMT

1. Scintillator: BC408 or BC404?

The scintillator BC404 and BC408 produced by Bicron are both our candidates. Table 6.4-1 lists their performance parameters. BC404 has more light output, faster rise and decay times, but shorter attenuation length. According to our simulation, when scintillator bar is longer, the BC408 is better. More experiment tests will be done.

Table 6.4-1 Properties of BC-404 and BC-408

	BC-404	BC-408
Light Output, % Anthracene	68	64
Rise Time, ns	0.7	0.9
Decay Time, ns	1.8	2.1
Pulse Width, FWHM, ns	2.2	~2.5
Light Attenuation Length, cm	140	210
Wavelength of Max. Emission, nm	408	425
No. Of C Atoms per cm^3, ($\times 10^{22}$)	4.74	4.74
No. Of H Atoms per cm^3, ($\times 10^{22}$)	5.21	5.23
Ratio H:C, Atoms	1.100	1.104
No. Of Electrons per cm^3, ($\times 10^{23}$)	3.37	3.37

Base	Polyvinyltoluene
Density	1.032g/cc
Coefficient of Linear Expansion	7.8×10^{-5}, below 67°C
Atomic Ratio, H/C	~1.1

2. PMT: R5924

To choose a suitable PMT, attention should be paid to parameters such as performance, effective area, gain in magnetic field, cathode quantum efficiency and spectral response. Considering limited detector space, a shorter PMT is preferred. The Hamamatsu R5924 fulfills most of these requirements:

1) Its diameter is 52mm and its cathode diameter is 39mm(See Fig.6.4-1). For a scintillator section of about 50mmx60mm, the effective area ratio is 40%.
2) It has 19 fine-mesh dynode stages and its gain is 1.0×10^7 at 0 Tesla magnetic field, 4.1×10^6 at 0.5 Tesla and 2.5×10^5 at 1 Tesla.
3) It has high quantum efficiency for the light with a wavelength from 300nm to 500nm.
4) It has good timing performance: anode pulse rise time is 2.5 ns, transit time 9.5ns, and transit time spread (FWHM) 0.44ns.
5) Its length is 50mm.

One shortcoming of R5924 is that its gain at 1 Tesla is a little bit too small.

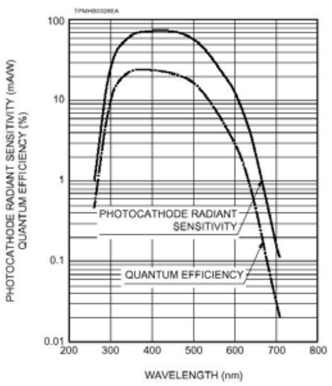

a. Typical Spectral Response

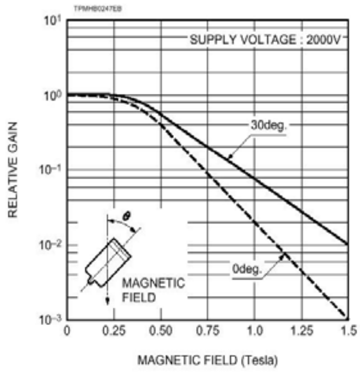

b. Typical Gain in Magnetic Fields

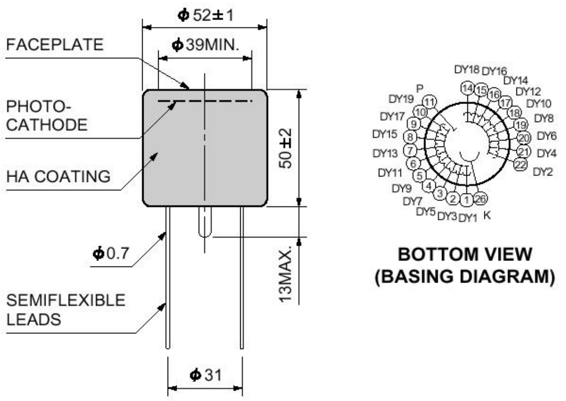

c. Dimensional Outline and Basing Diagram (Unit: mm)

R&D

Beam Test

Electron and pion beam are used to test our TOF modules, the set up is shown in Fig.6.5-1. The orange part is our TOF system and others are for delivering the beam. The T01 and T02 is to give a precise reference time, and the Pb wall is to absorb the background radiation. Scintillator bars are connected directly to the PMT in the dark box. The Cerenkov detector is to give an electron/pion identification. The scintillator S1 and S2 is for trigger, and the wire chamber MWPC is to determine the track position.

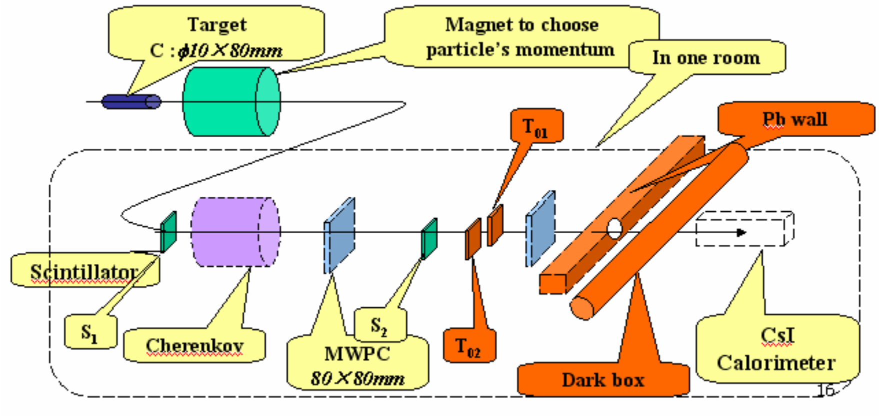

Fig.6.5-1 Illustration of the beam test set up

The experiment has the following tasks:

1) to analyse the time resolution for different schemes
2) to compare BC404 and BC408
3) to select a suitable packing material
4) to evaluate the electronics system
5) to measure the signal amplitude and do Time-Amplitude calibration

Fig. 6.5-2 shows some results of the beam test, (a) is a comparison of time resolution of different scintillator bars(including BC408 of 4, 5, 6cm thick and BC404 of 5cm thick), (b) is a comparison of different threshold, (c) is the attenuation length of different bars.

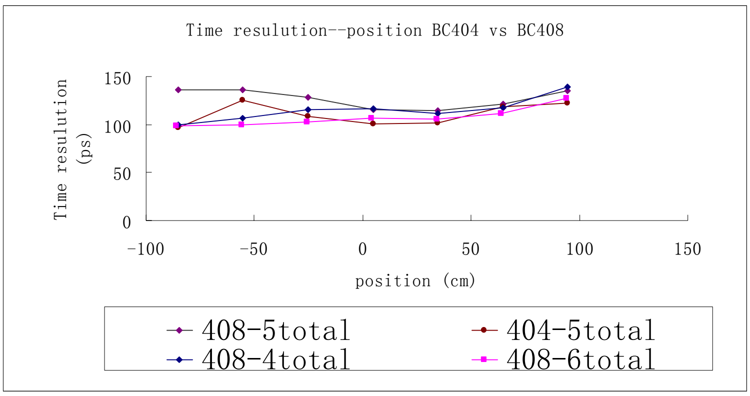

(a)

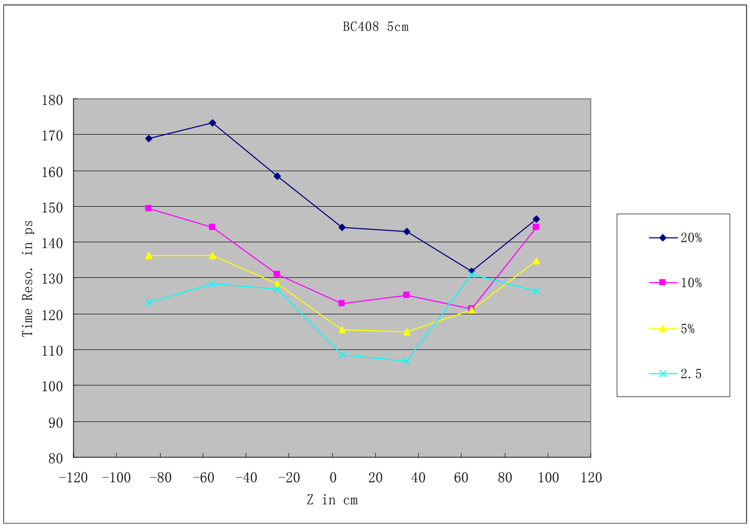

BC408 5cm
Time Reso. in ps
Z in cm
20%
10%
5%
2.5

(b)

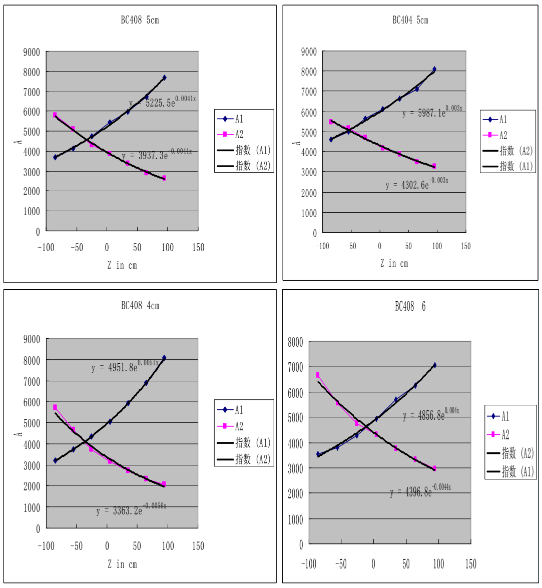

BC408 5cm
BC404 5cm
BC408 4cm
BC408 6
Z in cm
A1
A2
指数 (A1)
指数 (A2)

(c)

Fig.6.5-2 Some results of beam test.

Simulation

The TOF module is simulated based on GEANT4. Most of the physics processes in the TOF are simulated, including the tracking of charged particles, energy deposition, scintillation light production and transport, PMT signal shaping, etc. This simulation program has been used to compare different TOF schemes, like BC404 or BC408, scintillator thickness, threshold value setting, etc. Fig. 6.5-3 shows typical signal from the TOF module.

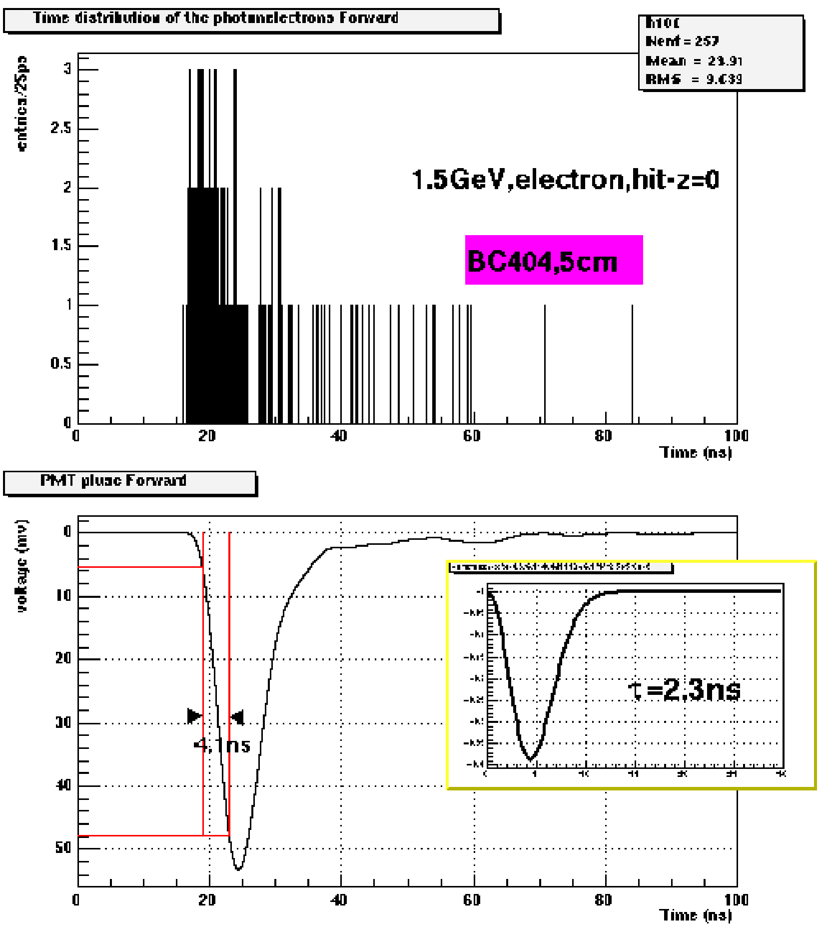

Fig.6.5-3 The signal produced by R5924 when 1.5GeV electron hit BC404. The upper panel is the arriving time spectrum when photons hit the cathode window of PMT. The bottom panel is a typical signal from PMT.

Fig.6.5-4 compares the time resolution with different conditions, like BC404 or BC408, with or without silicon oil.

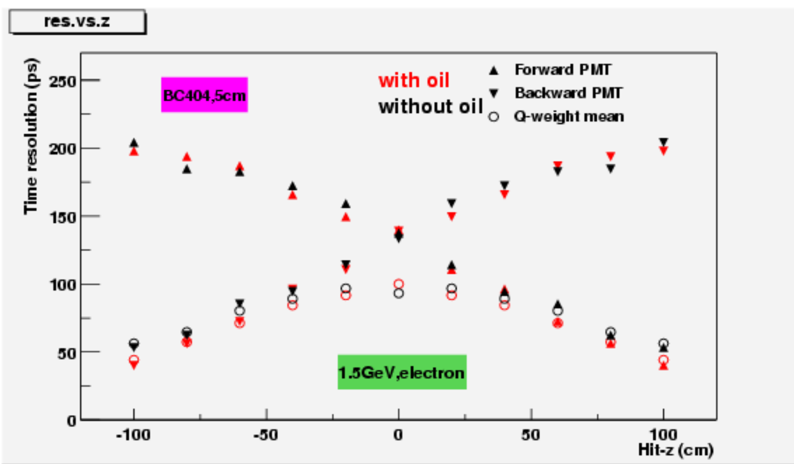

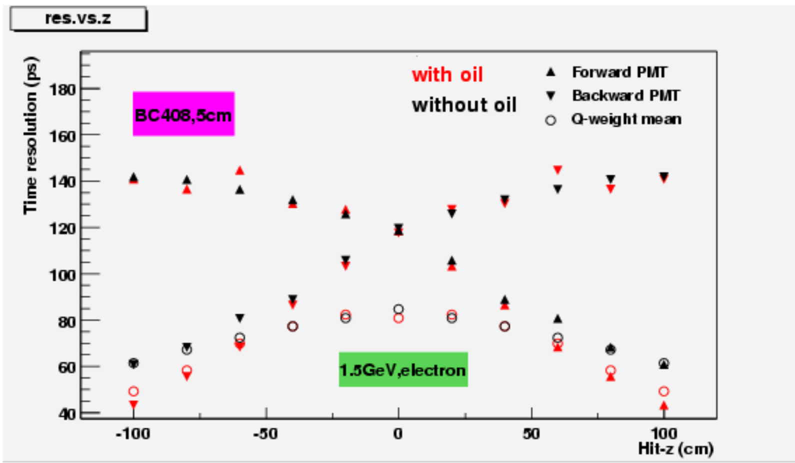

res.vs.z
Time resolution (ps)
BC408,5cm
with oil
without oil
Forward PMT
Backward PMT
Q-weight mean
1.5GeV,electron
Hit-z (cm)

Fig.6.5-4 Time resolution for BC404 and BC408 with or without silicon oil.

Structure and Setup

The barrel TOF will be placed between MDC and EMC. To save space and simplify the setup, TOF will be mounted directly on the MDC. The outer radius of MDC is 810mm and the inner radius of EMC is 930mm. Thus the TOF has 120mm radial space in total, into which two layers of 50mm thick scintillator and mounting hardware must fit with sufficient clearance. The TOF will be 2500mm and 2600mm long including PMT respectively for inner and outer layer. And its solid angle coverage is 82% of 4π after subtracting 2x80mm of the space for PMT. Considering PMT packing constraints, each layer will have 88 scintillator pieces and weight approximately 700kg.

The TOF structural design should meet the following requirements:

1) Scintillator end should match the PMT so as to maximize the effective area ratio.
2) Scintillator should be packed to protect light leak and the connection should be secured.
3) Scintillator and PMT are connected with silicon oil and they should avoid being separated.
4) PMT should be supported independently.
5) The base of PMT should be shorter than 30mm due to the space limit.
6) The maxium radius of TOF should be less than 925mm with a clearance of 5mm to EMC, since the MDC and TOF should be installed inside the EMC after they are wrapped together.
7) The housing of PMT should have a good heat exchange to remove the heat from the voltage divider.

Fig. 6.6-1 shows the assembly of barrel TOF modules. The PMT will be placed in a aluminum alloy housing and the housing will be screwed to the scintillator ends.

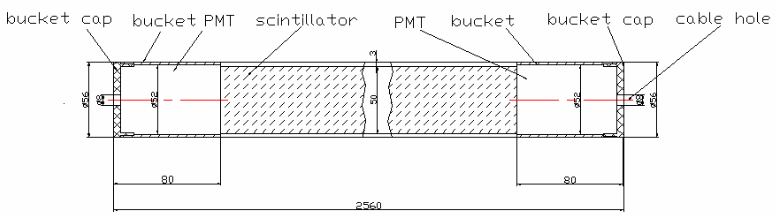

Fig.6.6-1 The assembly of barrel TOF module

The barrel TOF installation sequence is as follows:

1) Encapsulate each piece of scintillator with Al foil and black adhesive tape.

2) Setup inner layer of scintillator: first bind a layer of rubber to the MDC outer skin; then bind scintillator to rubber with adhesive tape.

3) Setup outer layer of scintillator: first bind a layer of rubber to the inner layer of TOF; then bind the second layer of scintillator to rubber.

4) Screw PMT support housings to the scintillator and insert PMTs and screw the housing covers to close it.

The endcap TOF will be placed at both ends of BESIII between the MDC and the endcap EMC, between an inner radius of 410mm and an outer radius 890mm. It consists of 48 pieces of fan-shaped scintillator with a thickness of 50mm. To minimize the impact to the acceptance, the PMT will be connected at the inner end of every scintillator, as shown in Fig.6.6-2.

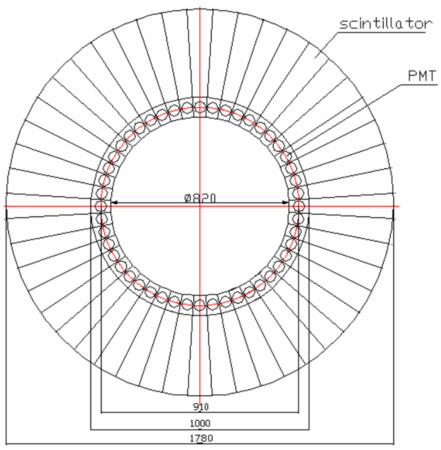

Fig.6.6-2 Endcap TOF structure

Installation of endcap TOF will be simple. Each piece of the scintillator will be mounted on the endcap EMC after it is encapsulated by Al foil and black adhesive tape. At the center there will be a metal ring to support the scintillator. The PMTs will be placed in housings, and the base of the housing will be connected to scintillator by screws, as shown in Fig. 6.6-3.

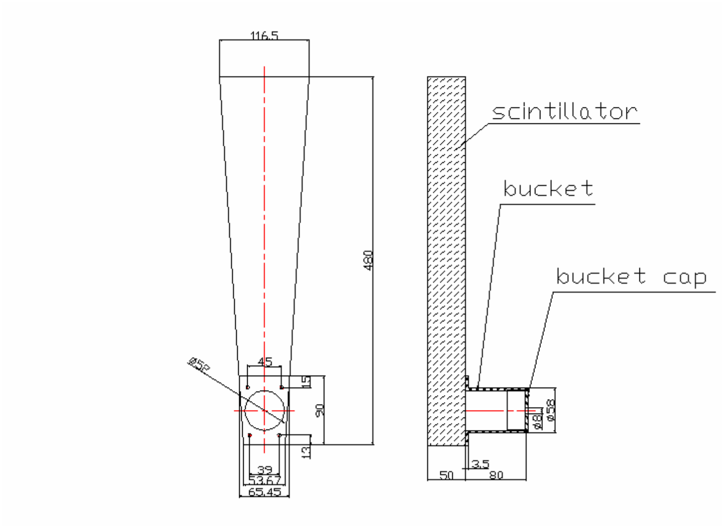

Fig.6.6-3 Installation of the endcap TOF

Monitor System

A monitor system will be employed, which can give a standard signal to monitor the operation and calibrate the TOF time measurement. Fig.6.7-1 is the schematic of such a system.

An N_2-dye laser or xenon lamp can be the light source, both of which can give blue light, consistent with the PMT spectra. From a fiber bundle light is transmitted to every PMT, and also a fiber to an independent PMT to produce a reference signal.

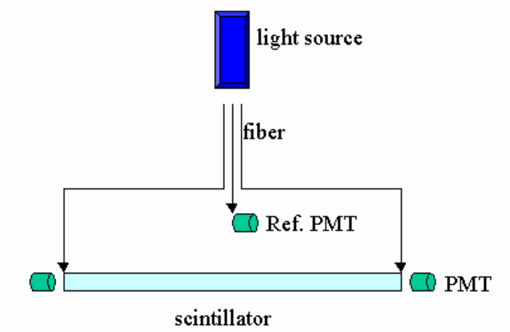

Fig.6.7-1 TOF monitor system

2.1.1.1.1.1 Reference

[1] Chi Peng Cheng, and Hong Wei Zheng, NIM A252(1986), 67-74.

[2] J.Z. Bai et al., BES Collab., NIM A458(2001)627-637.

[3] Kichimi et al., The BELLE TOF system.

Electromagnetic Calorimeter

Introduction

A detector measuring the total energy of particles is called ‘calorimeter’ in high energy physics experiments. The Electro-Magnetic Calorimeter (EMC) plays an important role in the BESIII detector, whose primary function is to measure precisely energies and positions of electrons and photons. Since the radiative decay of J/ψ is considered as one of the best places for glueball production naïvely, a good reconstruction of those decays is required. In the reconstruction of J/ψ radiative decays such as $J/\psi\to\gamma\pi\pi$, $J/\psi\to\gamma KK$, $J/\psi\to\gamma\eta\eta$, a direct photon and photons from π^0 decays should be precisely measured. Photons and π^0 need to be measured in ψ', ψ'', τ and D decays also. Energy spectra of photons in the J/ψ neutral decays and in D decays are shown in Fig.7.1-1 and Fig.7.1-2, respectively. We can see that photons with the energy less than 500 MeV are dominant in those decays. Since the resolutions of energy and position for electrons and photons are proportional to $E^{-1/2}$, high detection efficiency and good resolutions for lower energy photons are very important for the electromagnetic calorimeter of BES III.

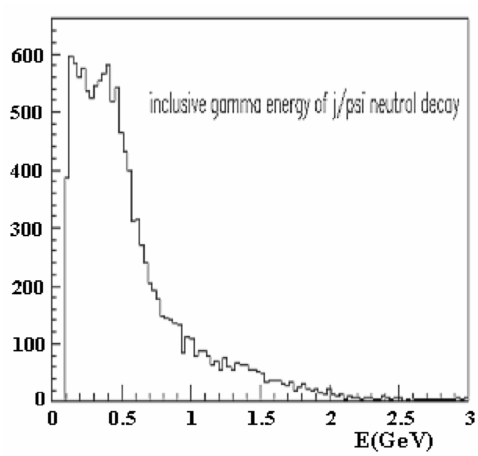

Fig.7.1-1 Energy spectrum of γ’s in the J/ψ neutral decays (BES II data)

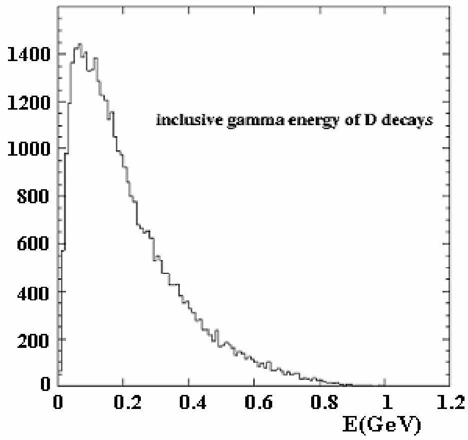

Fig.7.1-2 Energy spectrum of γ's in D decays (BES II data)

Energy spectrum of π0's at the center-of-mass energy of 4.03 GeV for $e^+e^-\rightarrow n\pi^0+X$ is shown in Fig.7.1-3. The results are obtained with the generator Jetset 7.4.1, where π^0's with an energy less than 1.5 GeV are dominant, and the probability with an energy larger than 1.5 GeV is very small. In the laboratory system the minimum opening angle of 2γ's from π^0 decays decreases as the π^0 energy increases. The result is shown in Fig. 7.1-4. The minimum opening angle of 2γ's for 1.5 GeV π^0 is larger than 10 degree.

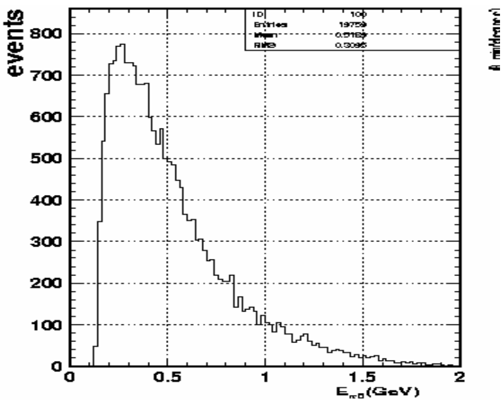

Fig.7.1-3 Energy spectrum of π^0's in the center-of-mass energy of 4.03 GeV for $e^+e^-\rightarrow n\pi^0+X$

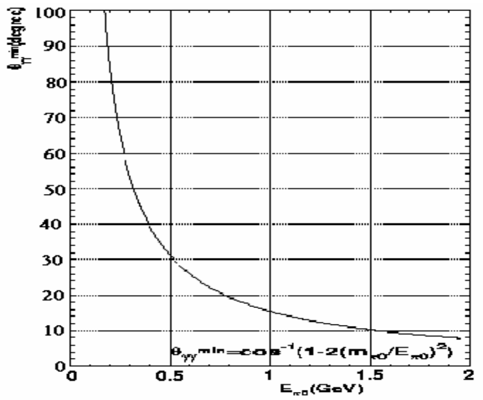

Fig.7.1-4 Energy dependence of minimum opening angle of 2 γ's from π^0 decays in the π^0 laboratory system

The general physics requirements of the BESIII detector leading to the design of the EMC based on CsI(Tl) crystals, with the following expected performance:

(1) The measurable energy range of electron or photon is from 20 MeV to 2 GeV. The energy resolution is about $2.3\%/\sqrt{E(GeV)} \oplus 1\%$, good energy resolution is important especially in the energy region below 500 MeV.

(2) The position resolution for EM shower is $\sigma_{x,y} \le 6\,mm/\sqrt{E(GeV)}$.

(3) A neutral(γ) energy trigger is provided.

(4) A good e/π separation in the energy region above 200 MeV is expected.

(5) Crystals have a fine granularity and signal readout so that overlapping showers can be reconstructed, especially for high energy π^0's.

(6) The electronics noise for each crystal should be less than 220 KeV.

CsI(Tl) Crystal

Crystal Choice

Energy resolution is the most important parameter of an electromagnetic calorimeter. Contributions to the energy resolution can be written as the following:

$$\sigma / E = \sqrt{\sigma_{EC}^2 + \sigma_{\gamma l}^2 + \sigma_{noise}^2 + \sigma_{PD}^2 + \sigma_{CAL}^2},$$

Where σ_{EC} is the intrinsic resolution due to fluctuations of the energy deposition and the photon statistics; σ_{r1} is from the shower leakage including contributions from "dead material" in the inner detectors and the supporting structure; σ_{noise} is from electronic noise including "pile up" at high luminosities; σ_{PD} is from fake signals in photodiodes directly hit by charged particles; and σ_{cal} is from errors of calibration and non-uniformity of the system.

Electromagnetic calorimeters can be divided into two types. One is sampling calorimeter made of heavy metal absorbers and sensitive detectors. The sensitive material usually made of organic scintillators, such as Pb-scintillating fiber sandwich calorimeter [1]. Since the density of the organic scintillator is very low, it absorbs about 10% of the particle energy of a shower, and a small fraction of the energy deposited is converted into scintillation light. The other is total absorption calorimeter [2,3,4,5] such as crystal calorimeter. A fraction of the deposited energy is converted into scintillation light, and the intensity of the light is proportional to the energy of the incident particle. Obviously, the total absorption calorimeters have a direct and truly correspondence between the shower energy and the signal output. In low energy region, the expected energy resolution follows $E^{-1/4}$ for a total absorption calorimeter, while it follows $E^{-1/2}$ for a sampling calorimeter.

Table 7.2-1 Properties of several inorganic crystal scintillators

Crystal	NaI(Tl)	CsI(Tl)	BGO	$PbWO_4$
Density (g/cm ^{3})	3.67	4.51	7.13	8.28
Radiation length (cm)	2.59	1.85	1.12	0.89
Molière radius (cm)	4.8	3.8	2.3	2.0
DE/dx (Mev/cm)(per mip)	4.8	5.6	9.2	13.0
Nucl. Int. length (cm)	41.4	37	21.8	18
Refractive index (480 nm)	1.85	1.79	2.15	2.16
Peak emission λ (nm)	410	560	480	420-560
Relative light output	100	45(PMT) 140(PD)	15	0.01
Light yield temp.coef. (%/^{0}C)	～0	0.3	-1.6	-1.9
Decay time (ns)	230	1000	300	10-50
Hygroscopic	strong	slight	no	no
Referral cost ($/cm ^{3})	2	2.3	7	2.5

In the process of obtaining the final electrical signal from the energy deposition, the light yield and photoelectrical quantum efficiency determine the energy resolution. Table 7.2-1 shows the properties of several inorganic scintillators. It can be seen from the table that CsI(Tl) and NaI(Tl) crystals have higher light output than others, and a better emission spectrum to match with the photodiode. Compared with NaI(Tl) crystals, CsI(Tl) crystals have a smaller radiation length and Moliere radius, therefore shorter length is required and finer granularity can be obtained. The hygroscopicity of NaI(Tl) also makes the construction and operation of the calorimeter difficult. Since the calorimeter is installed in a magnetic field of 1.0 T, the cost of silicon photodiode(PD) readout is about 4 times cheaper than that of the photon multipler tube(PMT) working in high magnetic field, the choice of PD readout is appropriate. The scintillation light emission peak of CsI(Tl) matches perfectly well with photodiodes[6], resulting in a higher signal output than NaI(Tl). Hence we choose the CsI(Tl) crystal for the BESIII calorimeter with a photodiode readout.

Choice of Crystal Dimension

In the measurement of showers, its leakage will affect the energy resolution. Leakage at the back of the calorimeter depends mostly on the length of crystals. The reflection material wrapping the CsI(Tl) crystal has little effect on the energy leakage between crystals. Energy resolution as a function of crystal length is shown in Fig.7.2-1. It can be seen from the figure that the energy resolution improves about 0.5% for every 2cm increase of the crystal length. Hence crystal with a length of 28cm(15X_0) is chosen for the BESIII calorimeter.

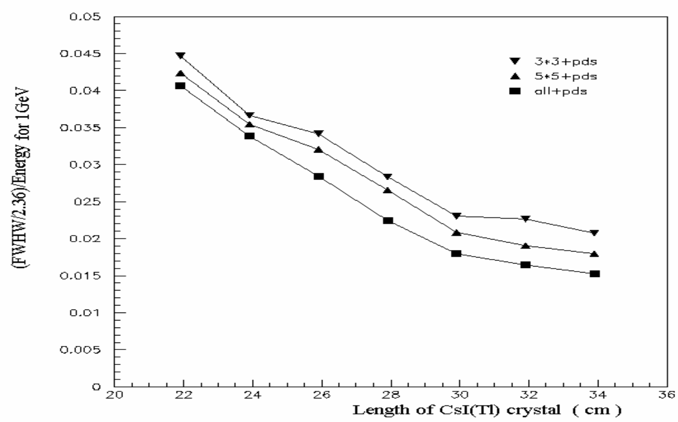

Fig.7.2-1 Energy resolution vs length of CsI(Tl) crystals for three different clustering schemes.

Position resolution depends on the transverse dimension of the shower and the calorimeter segmentation. The transverse dimension of the shower profile scales with the Molière radius R_M, which is about 3.8cm for CsI(Tl) crystal. A finer segmentation and a small R_M are advantageous for a good position resolution, but it does not help to divide the calorimeter much smaller than the shower dimension itself. If the shower is spread over many crystals, the energy resolution could be worse because the leakage of the shower through the gap between crystals increases. The electronics noise will also be higher, because for the same amount of light, the energy is collected with more electronics channels, so with more noise contribution.

Fig.7.2-2 and Fig.7.2-3 show the energy dependence of energy and position resolutions for three crystal sizes, 4×4 cm^2、4.5×4.5 cm^2、5×5 cm^2 in the front face of crystal. It can be seen that energy resolution is better when the cross section is larger, they are 2.29%, 2.23% and 2.07% for 1 GeV photons respectively. But the position resolution is worse when the cross section is larger, they are 4.8mm, 5.5mm and 6mm for 1 GeV photons respectively.

Fig.7.2-4 shows the energy dependences of the detection efficiency for the three different sizes of crystal as mentioned above. The results show that, there are no big differences.

The number of electronics channels in barrel calorimeter is 5380 if the cross section in the front face of crystals is chosen to be 5×5 cm^2. The number of electronics channels increases by 22% or 45% if a cross section of 4.5×4.5 cm^2 or 4×4 cm^2 is chosen.

From the study for optimization, we decided the basic size of CsI(Tl) crystals is 5×5 cm^2 in the front face, 6.5×6.5 cm^2 in the rear face and 28cm in length. One crystal in the zenith of the barrel calorimeter covers an opening angle of about 3°. In our energy region the minimum opening angle of two photons from 1.5GeV π^0 is 10° and it strides over no less than 3.3 crystals. Two photons from the decay of π^0 produced in BES III energy region can be separated from a single photon of the same energy.

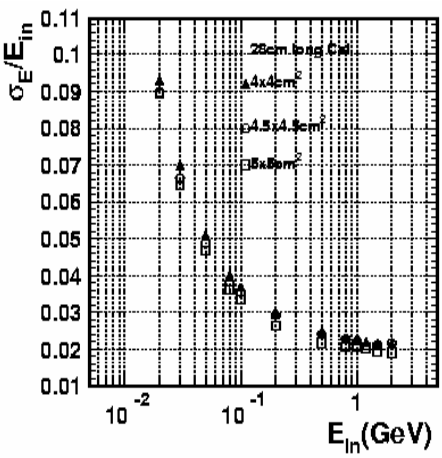

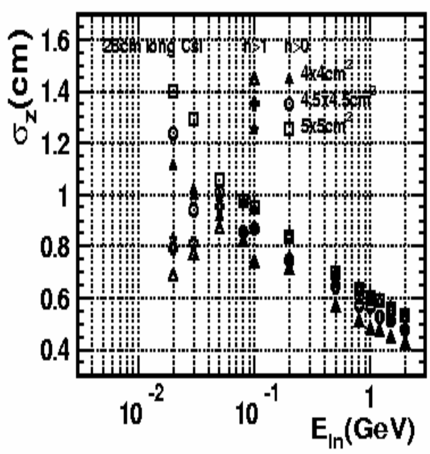

Fig. 7.2-2　　　　　　　　　　Fig.7.2-3

Fig.7.2-2 and 7.2-3: Energy and position resolutions as a function of energy for the 28cm long CsI crystal with the cross section of 4×4cm^2，4.5×4.5cm^2，5×5cm^2 at the front end respectively. Here 0.5 MeV equivalent noise was included.

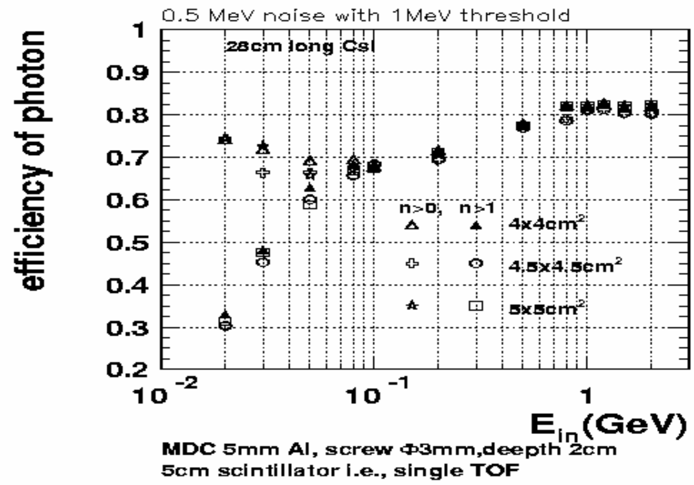

Fig.7.2-4 Detection efficiency as a function of γ energy for CsI crystals with the cross section 4×4cm^2, 4.5×4.5cm^2, and 5×5cm^2 respectively at the front end.

Arrangement of Crystals and Gap between Crystals

Since the collision point of e^+e^- has a standard deviation of 1.5cm in Z direction, in order to avoid the photon escaping through the gap between crystals, each crystal segment points to the interaction point with an appropriate tilt angle in both θ and ϕ directions and the gap between crystals is as small as possible. Fig. 7.2-5 shows relative energy deposition and the energy resolution as a function of impact position for different opening angles θ between the axial direction of crystal and the incident direction of photons. The results were obtained by scanning the central crystal of a 7x7 crystal matrix simulated by GEANT 3.21. The results show that energy depositions and energy resolutions have no significant difference for the different incident angle of photon when the impact point is at the center of the central crystal, but when the impact point is at the edge of the crystal, the difference between them is large and the energy resolution is worst when θ angle is 0°. Hence, each crystal segment in the barrel calorimeter is designed to point to the interaction point with a small tilt angle of 1.5° in the ϕ direction and 1°～3° in the θ direction.

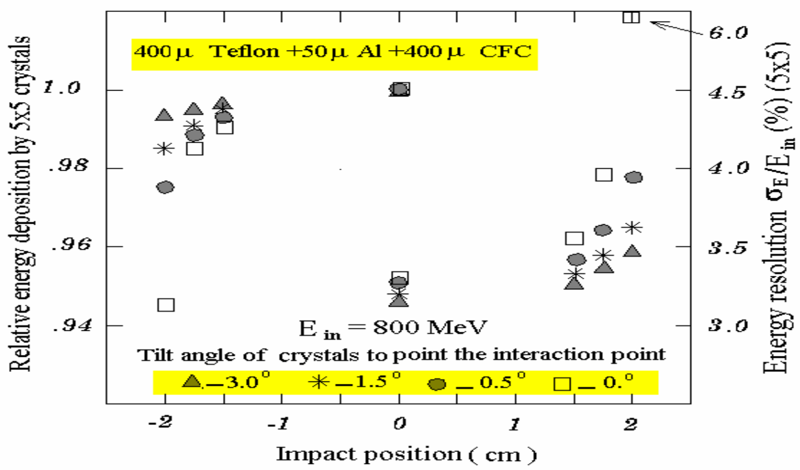

Fig.7.2-5 Relative total energy deposition and energy resolution as a function of impact position. Energy is obtained by the sum of 5×5 crystals. Photons with an energy of 800 MeV scans the central crystal with different incident angles. The compound material layer is 0.4mm Teflon + 0.05mm Al +0.4mm Carbon fiber.

The gap between crystals is determined by the thickness of the reflection material wrapping the crystals and the mechanical support wall, which are made of insensitive material. When the impact point of photon is near the edge of crystal, the effective radiation length decreases, thus energy deposition is lower and energy resolution is worse. Energy resolutions for different thickness of air gap and the compound material are shown in Fig.7.2-6 and Fig.7.2-7, respectively. The results show that the influence of air gap to the energy resolution is small and that of the compound material is large. When the mechanical wall of carbon fiber or 0.5mm Al, besides the indispensable reflection film of 0.4mm Teflon + 0.05mm Al is used between crystals, the energy resolutions increase about 0.2% or 0.4% for 800 MeV photon. Consequently the optimized design of the calorimeter has no mechanical wall between crystals.

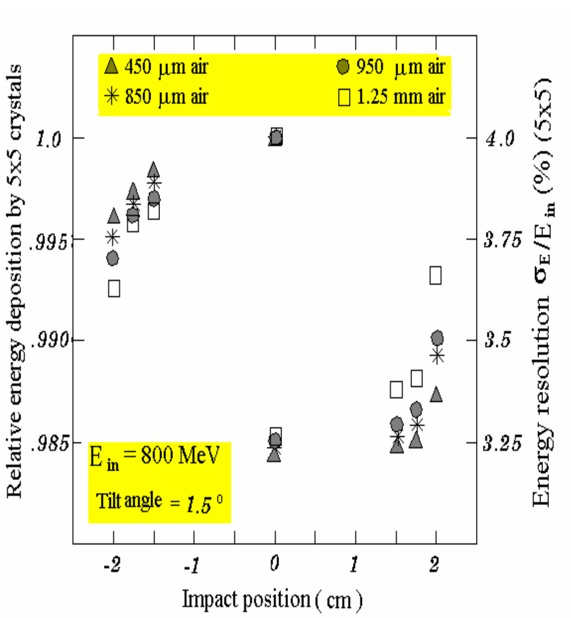

Fig.7.2-6 Relative total energy deposition and energy resolution as a function of impact position for different thickness of air gap. The central crystal is scanned by 800 MeV photons, which point to the center of the crystal front face with a tilt angle of 1.5°

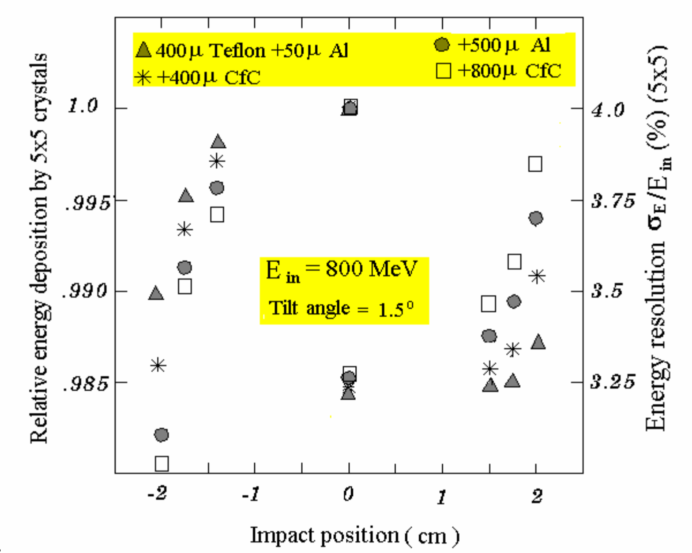

Fig.7.2-7 Relative total energy deposition and energy resolution as a function of impact position for different compound materials

Reflection Material for CsI(Tl) Crystal

The collection efficiency of the scintillation light plays an important role for obtaining good resolutions of the calorimeter. Since CsI(Tl) crystal has the high refraction index (n=1.8), the material meeting the physical and mechanical requirements are thin reflection films. The amount of total reflection generally depends on the medium thickness, the collection efficiency of scintillation light increases with the thickness of the reflection film, as shown in Fig.7.2-8. But thicker reflection film will cause larger gap between crystals and the resolution may become worse near the gap region.

There are three choices for the reflection materials: 200 μm Teflon sheet, 130 μm or 160 μm Tyvek sheet or 106 μm Millipore. Fig.7.2-9 shows the test results of relative light yields of different wrapping schemes. Results show that Millipore and Tyvek have a high reflection performance (see dots 10, 5, 7, and 8 in Fig.7.2-9), while that of Teflon with tiny hole(KEK) is lower (see the dot 4 in Fig.7.2-9). Furthermore, Tyvek has a small atomic number Z and is quite cheap. Hence the double-layer Tyvek with a total thickness of 2×0.13mm is chosen for the reflection material.

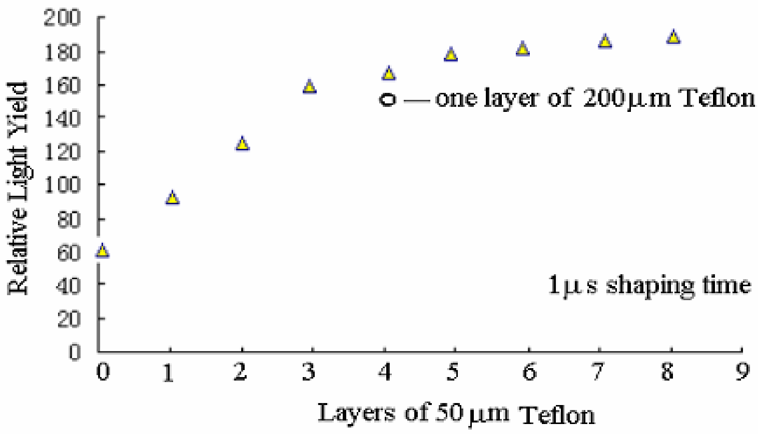

Fig.7.2-8 Relative light output as a function of Teflon thickness

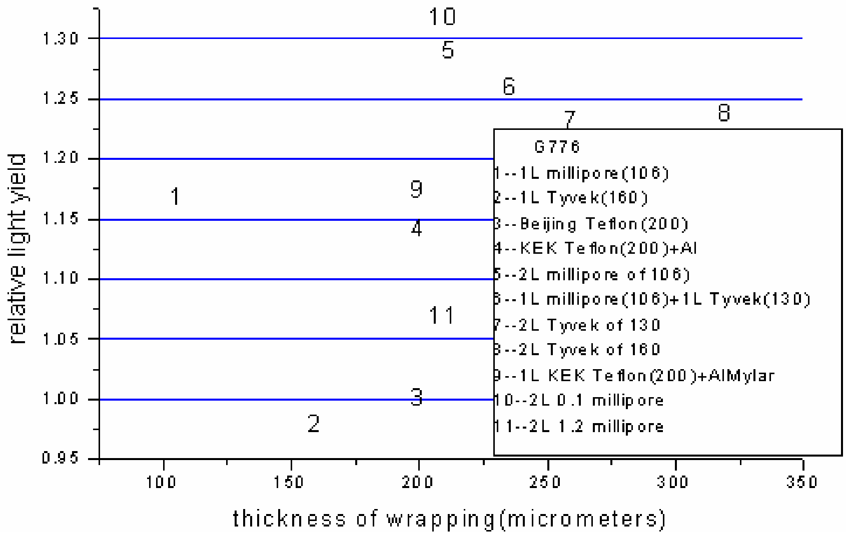

Fig.7.2-9 Comparison of the relative light output (PD readout) for the different material of reflection films wrapping CsI(Tl) crystal.

Non-uniformity of Light Output

The light output from various parts of the crystal is not perfectly uniform. It has the longitudinal and lateral position dependence. The non-uniformity may come from difference light yield caused by variation of dopant concentration. It may also come from the different light collection efficiency determined by the transparency of the crystal and the surface quality for the reflection of the light etc. The uniformity of light collection is different between the measurements by photo-multipliers and by photodiodes. Fig.7.2-10 shows the measurement using ^{60}Co by the PMT and PDs. PDs are coupled to the crystal using silicon oil to achieve a good optical contact, while PMTs are coupled to the crystal with 1mm air gap. The non-uniformity affects the energy linearity which can be corrected by the offline analysis, and the energy resolution. The non-uniformity may be improved by weakening the light output in the region where the light collection efficiency is higher, realized by some technical manipulation, such as locally colored reflection film.

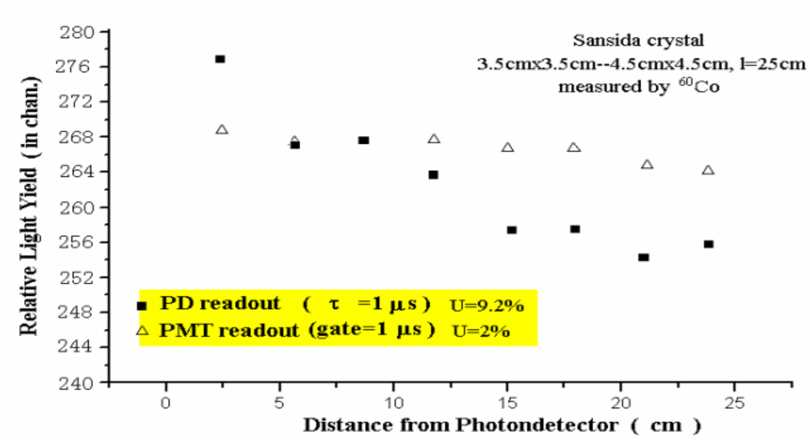

Fig.7.2-10 Comparison between the relative light output of CsI(Tl) measured by PD readout and that by PMT readout.

Light Output and Radiation Hardness of CsI

1. Relative Light Output

The relative light outputs of CsI crystals from different manufacturers are shown in Fig.7.2-11. It can be seen that crystals produced by Shanghai and Beijing (China) are similar, and no significant difference from those produced by Crismatec (France).

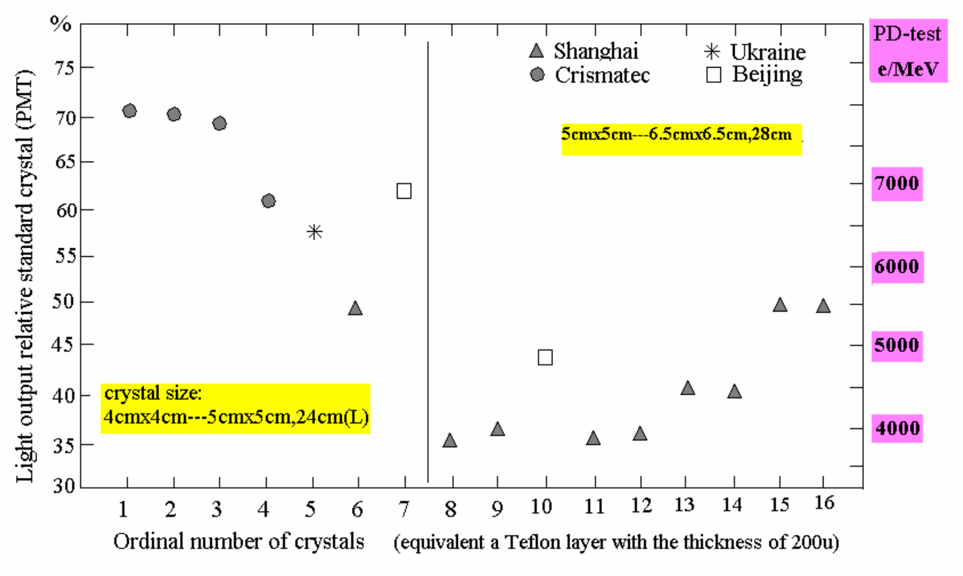

Fig.7.2-11

Fig.7.2-11 Comparison of relative light output of CsI(Tl) from different manufacturers. The left label denotes PMT-readout, and the right label denotes PD-readout (photoelectrons per MeV). The left and right hand of the vertical solid line are the results for different dimensions of crystals.

2. Radiation Hardness

The light output of CsI(Tl) decreased immediately when exposed to the radiation, but some of the loss can be recovered slowly in a few weeks after crystals being removed from the radiation environment. The crystal is known to form color centers by irradiation and it increases the absorption of scintillation light with a certain wave length and influences the light transport inside the crystal. The decrease of the light output by irradiation is related to the radiation dose and the crystal length. With the expected dose of the BESIII calorimeter of about 300 rad/year, the decrease of the light output of CsI(Tl) is required to be less than 10%/Krad in normal operation, and less than 20%/Krad after CsI(Tl) crystals are irradiated for short time by the ^{60}Co γ source with a high radiation dose.

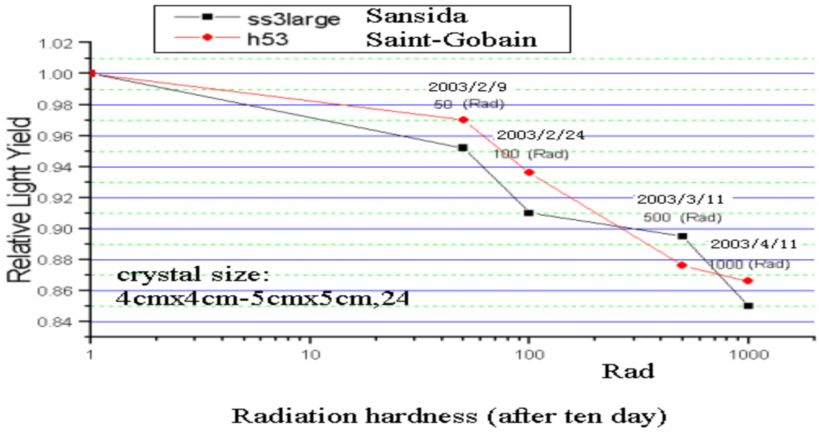

Fig.7.2-12 Radiation hardness of the large CsI(Tl) crystals from different manufacturers

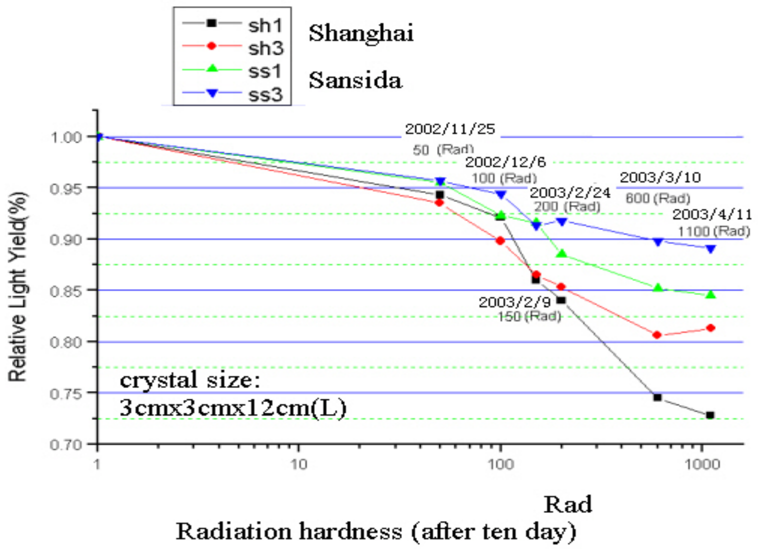

Fig.7.2-13 Radiation hardness of small CsI(Tl) crystals from different manufacturers.

Readout Electronics

Fig.7.3-1 shows the schematics of the readout electronics. To each CsI(Tl) crystal, two silicon PIN photodiodes are coupled, each to be equipped with an independent preamplifier. Two preamplifier outputs are coupled to a shape amplifier by averaging two signals or by choosing one from the two signals. The signal for main amplifier is shaped with a time constant of 1 μs, and then is split into two streams. One is for the trigger of neutral events by summing up many channels, the other is put into Q Module, and is split to feed three amplifiers with gains of 1, 8 and 32. Signals are then digitized by Flash ADCs(FADC) with a sampling period of 50ns. When the synchronous trigger signal of a good event occurs, the peak searching for a time window of 3 μs starts. Three groups of data, each contains the amplitude of the pulse signal and the time mark of the pulse peak, are available and the one with the largest non-saturated digital readout will be used. By using three-range amplifiers, the signal can be measured with 15-bit dynamic range up to 2.5GeV energy. The data are continuously sampled and put into a register array with a length of 6.4 μs .

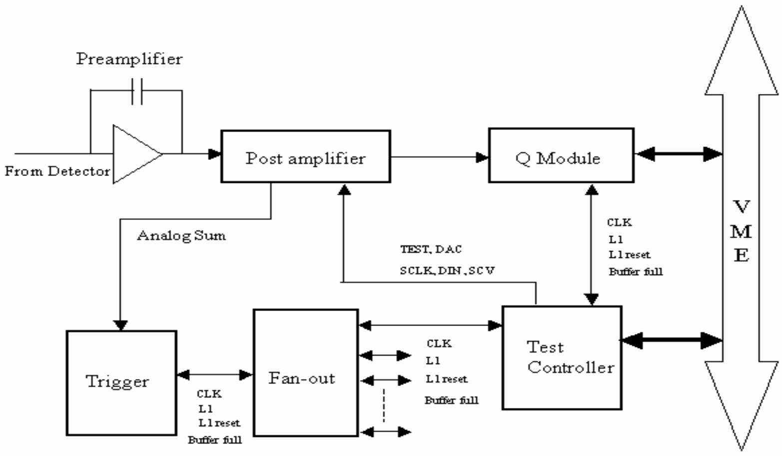

Fig. 7.3-1 Schematics of CsI(Tl) crystal detector readout electronics

The shaping time of the amplifier affects the light yield of CsI(Tl) and the electronics noise. Fig.7.3-2 and Fig.7.3-3 show the results. When the shaping time of 1μs is chosen, the ascending edge and descending edge of the pulse are about 3μs respectively. The electronics noise for one crystal is required to be lower than 220KeV. Besides pure electronics noise, the beam-related background also produces the noise hence the total noise is expected to be about 0.5MeV.

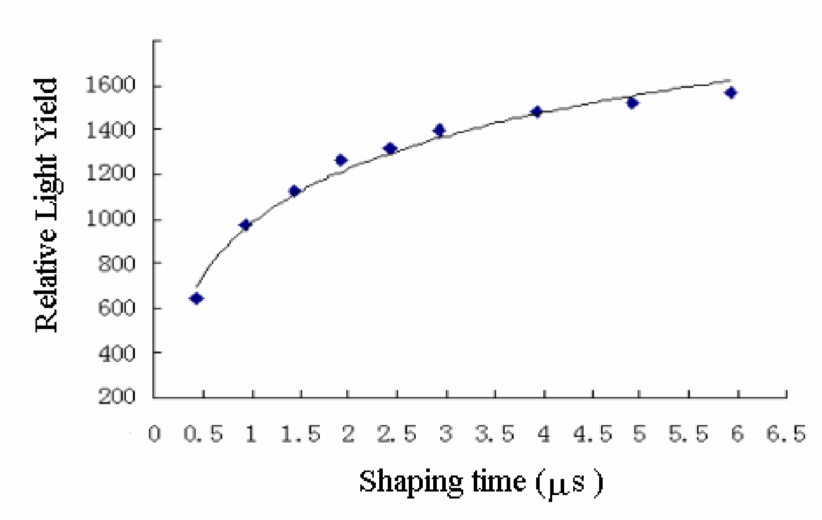

Fig. 7.3-2 Relative light yield as a function of the shaping time.

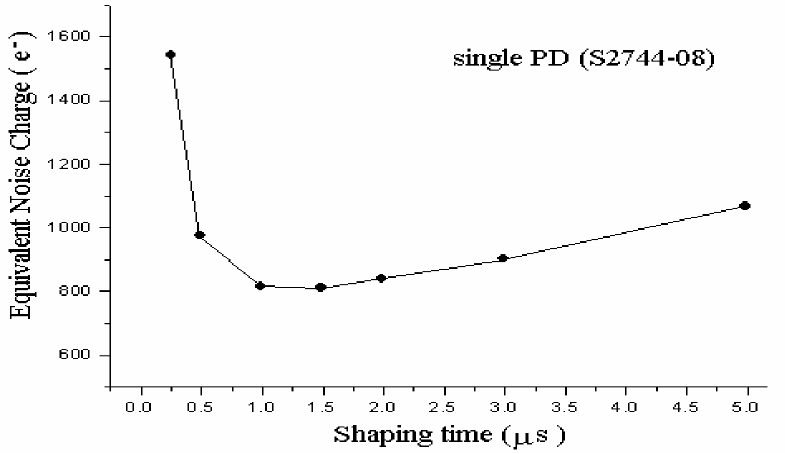

Fig.7.3-3 Noise vs. shaping time for single photodiode (S2744-08)

Expected Performance of the Calorimeter

Energy Resolution

1. Energy Resolution

From the energy resolution aa a function of photon energy as shown in Fig.7.4-1, the dominant effect of energy resolution is the electronic noise in the low energy region, the uncertainty of energy loss in the material in front of the calorimeter and the energy leakage from the rear of the crystals in the high energy region. In the simulation, energy is summed from 5 x 5 CsI(Tl) crystals. Material in front of the calorimeter (MDC and TOF) are taken into account as insensitive material, a 0.5 MeV electronic noise is assumed for each crystal, the fake signal from direct energy deposit in photodiodes is the corresponding deposited energy multiplied by a factor of 50, and a 5% of non-uniformity light output, increased from far to near of PD along the length of crystal, is assumed.

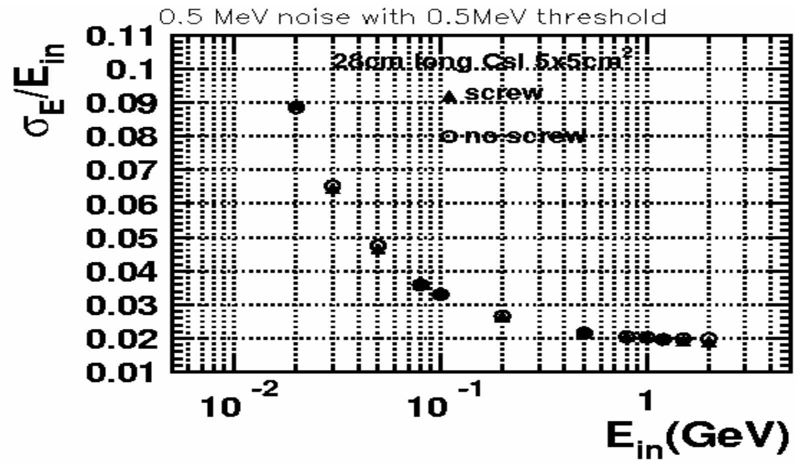

Fig. 7.4-1 The energy resolution of CsI(Tl) calorimeter from GEANT simulation. The electronic noise is 0.5 MeV for each crystal and the factor of fake signal from direct energy deposit in photodiodes is 50.

2. Direct Particle Effect of Photodiode

As a semiconductor detector, the photodiode can produce signals directly when hit by particles leak out from the crystal. Each crystal read out by 2 pieces of photodiode (S2744-08), its sensitive material is 300 μm in thickness and the minimum ionization is about 240 KeV, producing a signal of 66.3K electrons. If the average light output of crystal is 5000 photoelectrons/MeV as shown in Fig.7.2-11, the factor of signal from direct energy deposit in photodiodes equivalent to the energy deposit in CsI(Tl) crystal is 50, hence the equivalent energy of the minimum ionization on photodiode by single charged particle is 11MeV. From GEANT simulation study, the probability of the photodiode to produce fake signal is 2% and 5% when the incident energy is 0.5GeV and 1GeV respectively. Since the probability is small, no big influence on energy resolution is expected.

3. Beam Related Noise

The electronic noise will be at the level of 0.5MeV during the colliding operation based on past experience, and the number of crystals with a random noise higher than 1MeV will be more than 15%. For a sampling window of FADC of 3μs, there will be about one thousand noisy crystals in a good event. More than 90% fake signals can be rejected if we have the time information of real hits for a good event. A rough time information (~0.1μs) will be read out besides the pulse height. In the offline analysis, we can seek the big pulse and use its time as a standard time, to be compared with all other signals. Those with large differences will be identified as fake signal.

To use the FADC sampling information sufficiently, the electronic pedestal before the real pulse, i.e. 4.7μs before the trigger signal, should be subtracted from the data. At lease one sampling point should be taken for the pedestal.

4. Non-uniformity

Assuming the non-uniformity of the light output of crystals increases from far to near of PD at a level of 0, 5%, 10% to 15% respectively, the influences to energy resolution can be simulated by GEANT, as shown in Fig.7.4-2. The energy resolution becomes worse by 0.5% when the non-uniformity is 10% in the energy region lower than 500MeV. Therefore the non-uniformity of the light output along the length of the crystal must be less than 5%.

Position Resolution

A photon will make shower in a crystal and the energy deposit will spread over several crystals. The position of the photon can be defined by the center of the gravity of the shower, $X_{cg} = \sum_i^{all} x_i E_i / \sum_i^{all} E_i$, where x_i and E_i is the position of the center of the crystal and the deposited energy in this crystal respectively.

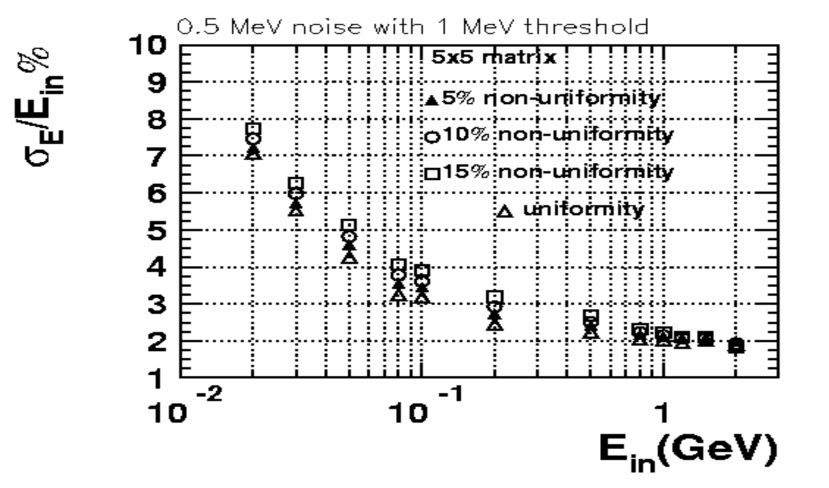

Fig.7.4-2 The influence of non-uniformity of the light output along the length of crystal to the energy resolution

The position resolution is related to the position in the crystal, it's worse at the center than in the edge of the crystal, as shown in Fig.7.4-3. The relationship between the average position resolution and the energy of incident photon is shown in Fig. 7.4-4.

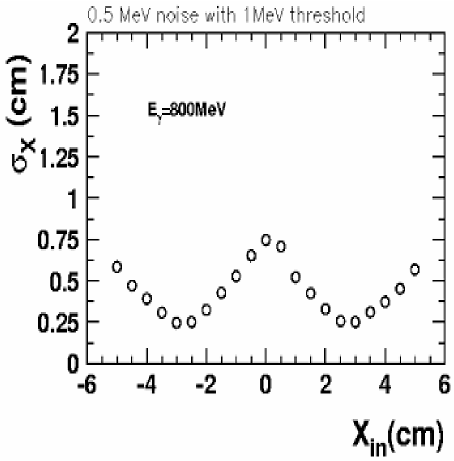

Fig.7.4-3 The position resolution when 800MeV γ scan the crystal

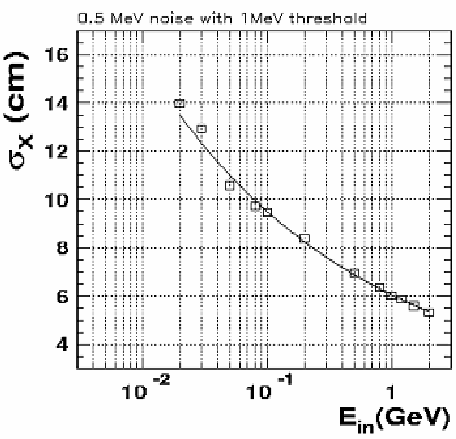

Fig.7.4-4 The position resolution vs incident energy

Detection Efficiency

The detection efficiency is defined as the percentage of events in which the deposited energy is within $\pm 3\sigma_E$ around the energy of incident γ. The detection efficiency is about 90% for high energy showers and it will be lower for low energy showers, depending on the amount of material in front of the Calorimeter.

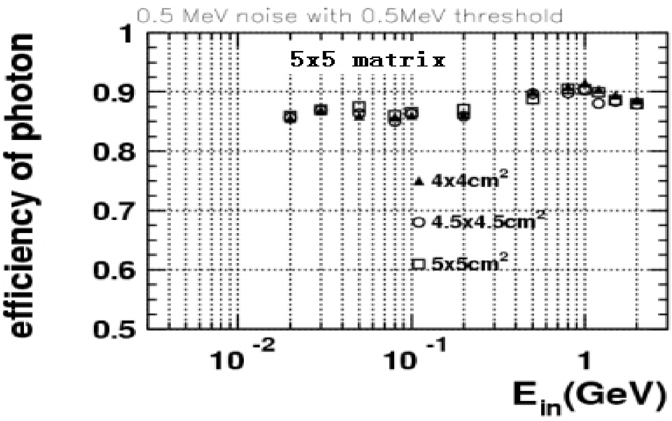

MDC 5mm Al, screw Φ3mm,deepth 2cm
5cm scintillator i.e., single TOF

Fig.7.4-5 The detection efficiency vs the energy of incident γ

Separation of e/π

The power of e/π separation depends on the energy of the charged particles, considering the ionization and nuclear reaction of π in the crystal, especially the π-nucleus action. The minimum ionization energy of π in the crystal is about 160MeV and its strong nuclear action region is about 300MeV. The electron could be mis-identified because of the pollution from π. The e and π has distinct different behavior in the calorimeter when their energy are greater than 300MeV. Both the number of crystals with deposited energy and the total deposited energy of electrons are greater than that of π. In the low energy region, the e/π separation is mainly depended on the dE/dX information from drift chamber. There are two criteria to identify e/π in the high energy region. One is the ratio of energy deposited in 9 crystals to energy deposited in 25 crystals and another is the ratio of the incident energy E_{in} calculated by momentum from MDC of charged particle to the total deposited energy, or say $E_9/E_{25} = \alpha(E_{in})$ and $E_{25}/E_{in} = \beta(E_{in})$, where α,β will be defined by calibration. The distributions of the energy deposited in calorimeter by 1 GeV e and π are shown in Fig.7.4-6. If we identify e by a minimum energy cut at 3σ less than the peak of deposited energy, the ratio of mis-identified p as e vs. energy is shown in Fig.7.4-7.

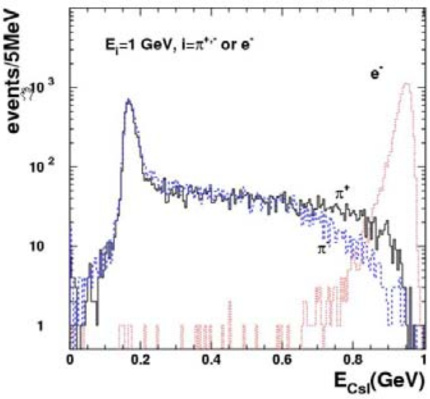

Fig.7.4-6 The distributions of the deposited energy of 1 GeV e and π.

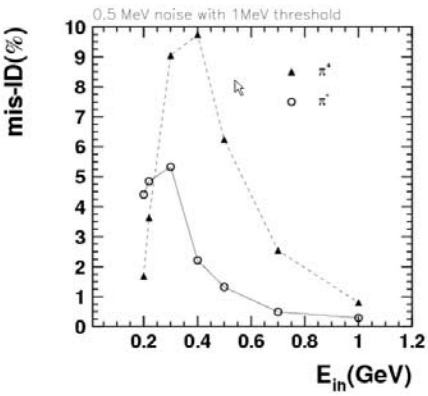

Fig.7.4-7 The percentage of proton mis-identified as e vs. energy

Energy Linearity

The energy non-linearity is mainly caused by the energy leakage through the back of crystals and the energy loss in the “dead material”. Of course, the non-uniformity light output of crystal is another reason. The ratio of energy deposited in crystals to incident energy vs. the incident energy is shown in Fig.7.4-8. There is a bigger variation in the low energy region. The energy non-linearity can be corrected by studying the events ee→γee， ee→γγ and ee→Xπ^0.

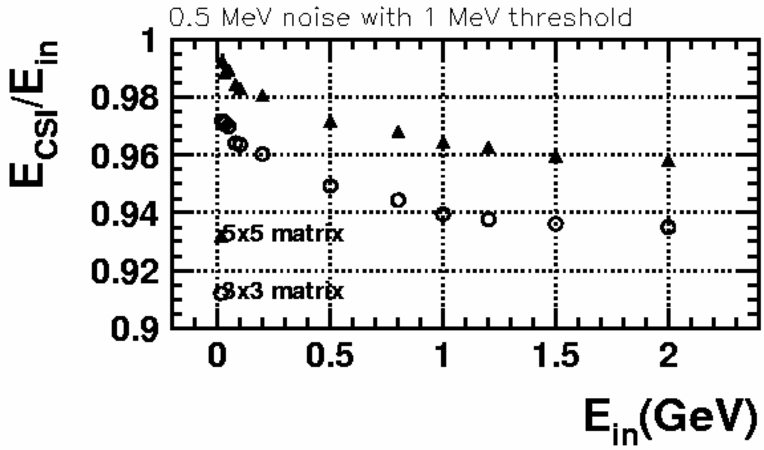

Fig.7.4-8 The ratio of energy deposited in crystals to incident Energy vs. the incident energy

Construction of the EM Calorimeter

The calorimeter is composed of one barrel and two endcap sections as shown in Fig. 7.5-1. The barrel has an inner radius of 94 cm and a length of 275cm, covering the polar angle of 146.5^o - 33.5^o(cosθ～0.83). The endcaps with inner radius of 50cm are placed at $z = \pm 138$ cm from the collision point, covering the polar angle of 32.5^o - 21.3^o(cosθ～0.93). The total acceptance is 93 % of 4π. A small gap of about 5cm between endcaps and the barrel is reserved for mechanical supporting structure, cables and cooling pipes. There are a total of 44 rings of crystals along the z direction in the barrel, each with 120 crystals. All crystals except 2 rings at the center of detector point to Z = ±5cm and all crystals have a small tilt of 1.5^o in the ϕ direction. Each endcap consists of 6 rings and split into two half circles. All crystals point to Z = ±10cm with a tilt of 1.5^o in the ϕ direction. The entire calorimeter have 6272 CsI(Tl) crystals with a total weight of about 24 tons.

The shape and dimension of barrel crystals are illustrated in Fig.7.5-2. To meet the need of pointing to the same point, the section of crystal is a trapezium. Crystals typically have a front face of about 5cm × 5cm and a rear face of about 6.5cm × 6.5cm. The length of all crystals is 28 cm. For easy manufacture, two out of four side faces of crystals are perpendicular to the front and the rear faces. The shape of endcap crystals is more complicated due to varying radius of the rings. Each endcap consists of two half circles and the dimension of the crystal close to the boundary of half circle may be different from the inner ones.

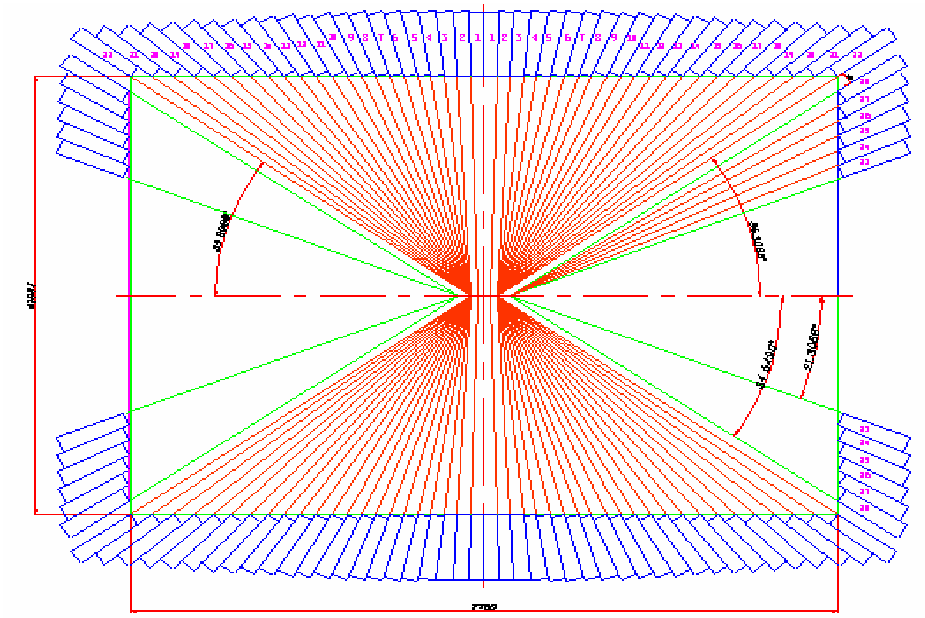

Fig.7.5-1 Configuration of the electromagnetic calorimeter

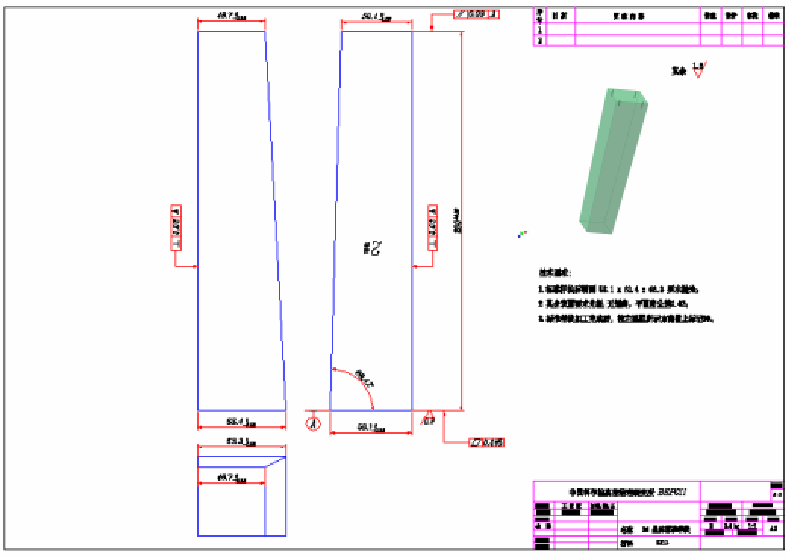

Fig.7.5-2 Definition of the dimension of Cs(Tl) crystal for the barrel

All the serial numbers and dimensions of crystals are given in the Appendix table 1. The collocation of barrel crystal is bilateral symmetry and the dimensions of left 22 rings of crystal are almost the same as that of the right 22 rings. There are 44 serial numbers for barrel crystal corresponding to 44 rings of crystal, 120 crystals for each serial number and a total of 5280 crystals for the barrel.

The collocation of two endcaps is the same. There are 31 types of crystals and a total of 960 crystals for the endcap calorimeter.

Crystal Quality Control

CsI(Tl) crystals from mass production should satisfy a number of requirements: light output, light uniformity, crystal dimension and radiation hardness.

The light output of a crystal is defined as the number of photoelectrons per MeV. When a crystal is wrapped by 2 layers of 130 μm thick Tyvek, coupled to two photodiodes (S2744-08), readout by an amplifier with 1 μs shaping time, the light output should be more than 6000 photoelectrons per MeV. Besides 3 conditions mentioned above, the light output is also related to the size of the surface coupled to the photodiode. The light is not proportional to the area as there is a reflection layer on this face.

Since the light collection efficiency is low and the relative electronic noise is high when coupled to photodiodes, PMT is used for testing of crystals. The measuring equipment is shown in Fig.7.6-1. The crystal is readout by a 2-inch Bialkali photomultiplier, whose output is divided into two, one for discriminator to generate a 1μs ADC gate, and the other for digitization by a charge sensitive ADC after a time delay. Each crystal is tested by measuring the position of 662 keV γ ray photoelectric peak using a ^{137}Cs source, which get through a Φ3mm X 3cm lead collimated hole, at 9 points along the crystal. There is a 0.3mm air gap between the crystal and the PMT. The first point is 2cm away from the rear face and each step is 3cm. The light output of a crystal is defined as the average of the 9 measurements and will be normalized to the light output of a small reference CsI(Tl) crystal with 1 inch in diameter and 1 inch in length.

The average light output is defined as

$$S_{ave} = \frac{1}{9}\sum_{i}^{N=9} S_i$$

where S_i is the light output of the 9 points.

The Non-uniformity of the Light Output is defined as

$$U = \frac{S_{\max} - S_{\min}}{S_{ave}} \le 5\%$$

where $S_{\max}$, $S_{\min}$, S_{ave} is the maximum, minimum and average light output of the 9 points.

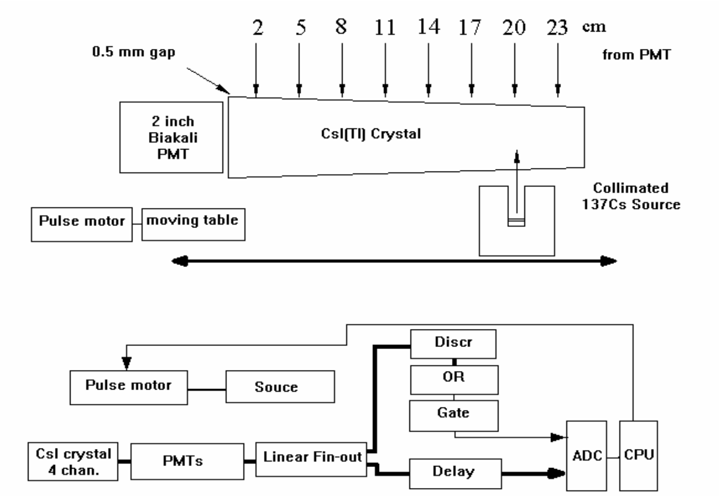

Fig.7.6-1 The setup for measuring the light output and the uniformity

The special supplied sample of 1×1×2cm^3 will be tested for radiation damage during mass production. One sample is needed for every batch of raw material or 100 crystals. The decrease of light output should be less than 20%/Krad after irradiated by ^{60}Co γ ray.

The tolerance of the crystal dimension is defined as +0, -200 μm for all transverse dimensions, ± 1mm for length.

CsI(Tl) Crystal Module and Its Test

The Construction of CsI(Tl) Modules

A CsI(Tl) crystal module consists of one CsI(Tl) crystal and two photodiodes. The five surfaces of the crystal (except the rear surface) are firstly wrapped in a 260μ thick Tyvek sheet, and then wrapped in a 50μ laminated sheet with 25μ aluminum and 25 μ Mylar. The aluminum layer works for shielding against the electronic noise, and the Mylar is used to isolate each crystal electrically from others and also isolate the detector from the support structure. The rear end of the crystal is the window for collecting scintillation light. Two pieces of type S2744-08 photodiodes are glued at the central part of the crystal rear surface via a 3mm thick Lucite with a size of $2.1cm \times 2.5cm$. Epoxy glue is used both for CsI-lucite and Lucite-photodiode joints. Before gluing, the rear surface of the crystal, surfaces of Lucite and photodiodes must be cleaned by special detergent. Except the area for Lucite-photodiode, the rest part of the rear surface is covered by a 500μ thick Tyvek reflection sheet. Four taped holes are drilled on the centerlines of four sides of the rear face by a special technique. An 8 mm thick aluminum base plate with a cut area for photodiodes is fixed to the crystal rear end by four self-tapping screws. An aluminum shield box covering two preamplifiers is fixed to the aluminum base plate with other four screws. The electrical ground of the preamplifier is connected to the shield box and the aluminum shield layer to avoid external noise interference. There is a rectangle hole on the shield box for settling the monitoring light fiber. Through this hole and the prefabricated holes of aluminum base plate and the Tyvek reflection sheet, one end of the fiber with metal sheath contacts the rear surface of the crystal to inject monitoring light.

All processes of the assembly are kept in a dry room with humidity less then 10% and at a constant temperature.

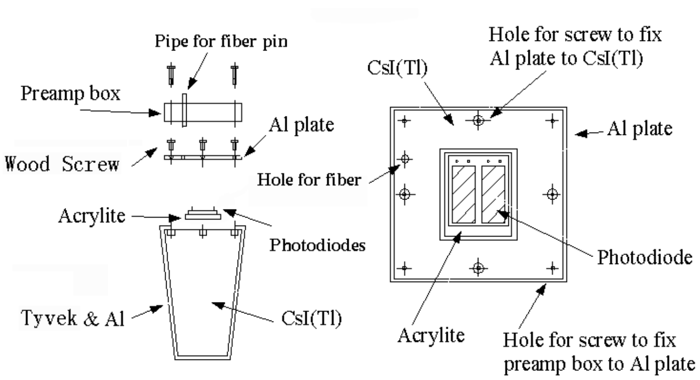

Fig.7.7-1 Assembly of a CsI(Tl) crystal module

Photodiodes

Hamamatsu S2744-08 is selected as the photodiode to be used. Its exterior dimension is 14.2 mm×27 mm. The photosensitive area is 10cm x 20cm and the thickness is 300μm. The general characteristics of the photodiode are as follows:

Photo sensitivity (at λ=540 nm) = 0.36,

Quantum efficiency ~ 80%,

Capacity: 85 pF,

Temperature coefficient: 1.12 times /□,

Dark current: 3 nA,

Typical bias voltage: 70 V.

The following considerations are important for the choice of the photodiode.

(1) For the cost and the reliability, the standard commercial photodiodes should be chosen. They have the following dimensions, 1cm×1cm，1cm×2cm，1.8cm×1.8cm and 2.8cm×2.8cm. Photodiode with a size of 1cm x 2cm is chosen, since it has lowest price-area ratio due to large requests.

(2) The photodiodes are placed on the rear surface of CsI(Tl) crystals, the rest of the surface is covered by a reflector. The number of collected photoelectrons, $N_{e,}$ is roughly proportional to the photodiode area (S_{PD}), hence the energy resolution is $\sim\sqrt{S_{PD}}$, and the electronic noise of one photodiode ENC is proportional to S_{PD}.

(3) Two photodiodes, each equipped with an independent preamplifier are attached to one crystal. Two preamplifier outputs are summed up in a shaping amplifier with a time constant of 1 μs. The crystal can still be readout, if one of the two diodes is dead, so the system has a good safety margin. The signal to noise ratio is proportional to $\sqrt{2}\times S_{PD}$.

(4) The rate of particles hitting the photodiodes from shower leakage is proportional to S_{PD}. The extra signal caused by this effect is proportional to the deposited energy in the photodiode wafer, and it is equivalent to about 50 times of the same energy deposited in CsI(Tl) crystals.

All photodiodes will be burned at 80^0C for 600 hours with 70V bias. After burning, the dark current will be larger, and some of the photodiodes will be rejected. So all photodiodes should be tested and checked as follows:

(1) Test of the capacity with 70V bias,

(2) Measurement of the dark current,

(3) Measurement of the output pulse height spectrum of 241Am source and the noise level, the schematic view of setup is shown in Fig.7.7-2.

(4) Make a record and a label

Charge Sensitive Preamplifiers

The noise level of each photodiode plus one preamplifier is below 800 electrons, and each detector module (including CsI crystal and readout electronics) is below

1100 electrons, which is equivalent to about 200 KeV in the detector.

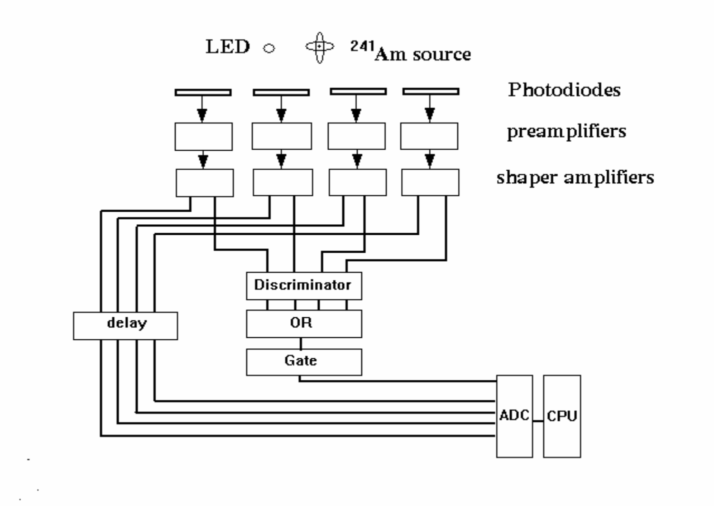

Fig.7.7-2 Test setup for photodiodes and preamplifiers

Photodiodes, crystals and preamplifiers are selected and grouped together, so as to make the gains of all calorimeter modules similar. The test setup is shown in Fig. 7.4-5. By measuring the noise of each photodiode and the 60 KeV X-ray peak position of the 241Am X-ray source, the noise level of the photodiode and the relative gain of each electronic channel can be calibrated.

Light Output Uniformity Test

During fabrication, the size and the light emission property of each crystal are tested by the manufacturer, and will be checked by IHEP. After gluing two photodiodes to one crystal, assembling the preamplifier into shield box, the assembly of a detector module is finished.

Since there are differences in the quantum efficiency of photodiodes, in the gain of preamplifiers and in the light yield of CsI(Tl) crystals, it is necessary to measure all these quantities before assembly and match them to get similar signal amplitude for digitization. After the detector modules are assembled, the differences in their gain should be evaluated by using cosmic-ray muons before installing the crystals into the calorimeter structure. The schematic view of test setup is shown in Fig.7.7-3. When a cosmic-ray muon passes through the crystal being laid horizontally, about 25 MeV is deposited. If the accuracy of the track length of the incident particle in the crystal reaches about $\pm$3mm and a crystal is measured at eight points longitudinally, with a total of about 4000 events, eight distributions of pulse heights per cm path can be obtained, with an energy resolution of about 10% and the accuracy of the pulse height peak of about 2%.

The cosmic-ray test setup could load 40 crystal modules simultaneously for test, and each test takes 48 hours. In addition, this setup also includes random calibration pulser and Xe flash lamp-fiber monitoring system. The former is used to calibrate the electronic noise and pedestal and the latter is used to calibrate the relationship between the light intensities and the energies of cosmic ray muon. The data of the cosmic-ray tests are as the basic data of each crystal module.

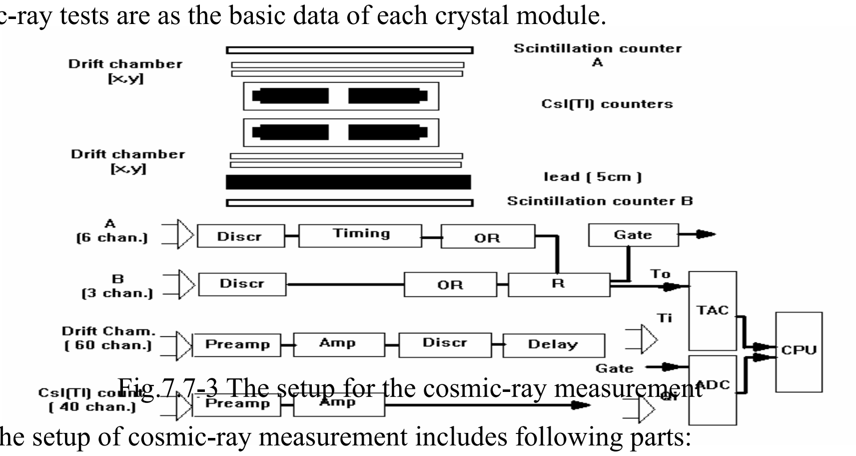

Fig.7.7-3 The setup for the cosmic-ray measurement

The setup of cosmic-ray measurement includes following parts:

(1) The cosmic ray trigger system consists of two scintillation counter arrays, each is about 90 ㎝×90 ㎝, and is made up of three 30 ㎝×90 ㎝ plastic scintillation bars. The upper counters above crystals are read out at both ends to get a starting time with accuracy better than 1ns. The lower counters are read out at one end, only used to make coincidence with upper counters. Above the lower trigger counters, there is a layer of 5cm thick lead for absorbing soft components of cosmic rays.

(2) Two layers of drift chambers are used to measure both the X and Y position with precision of about 0.5mm. Each layer consists of two chambers, and the sensitive area of each chamber is 90 ㎝×90 ㎝ with 60 sense wires.

(3) Between two layers of drift chambers, there are two layers of aluminum boxes on a movable table to hold the CsI(Tl) crystals being tested. Each Al box can house 20 crystals and a total of 40 CsI(Tl) crystals for one measurement.

(4)Electronic and data acquisition system includes data acquisition, data management and graph plot.

Beam Test of a CsI(Tl) Matrix

A beam test of a 6×6 CsI(Tl) crystal matrix is planned to test the system, to obtain first hand experience for calibration, to cross check the results of Monte Carlo simulation, and to finalize the system design. There are two possible choices for beam test sources: one is the experimental single particle beam-line being built at IHEP, Beijing; the other is to cooperate with a foreign lab. The test beam is electron, while a mixed electron and pion beam is also desirable to study e/π separation. The test beam should have a pointing accuracy of less than 2mm, and its energy can be tuned from 30 MeV to 2 GeV, with accuracy of about 1% at high energies.

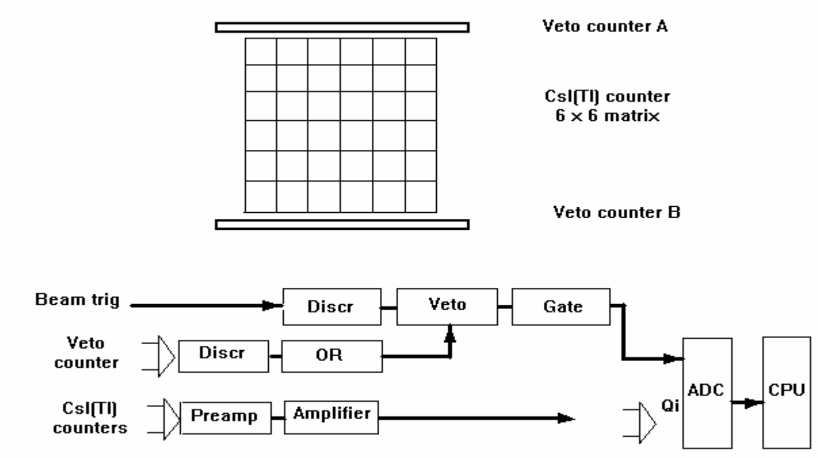

Fig.7.7-4 The schematic diagram for beam test of a CsI(Tl) matrix

Environmental Control and Monitoring

Temperature Control

The heat consumption of two photodiodes for each crystal is about 0.13 W. The local temperature is about 35^0C, which causes a non-uniform temperature distribution between two ends of the crystal. Large temperature gradient will cause a degradation of the energy resolution. In order to control this effect, there are 120 copper water pipes from two cooling ring pipes located at the ends of the calorimeter, each of which is attached to electronic boxes along Φ direction to remove the heat from preamplifiers. The two cooling rings are then connected to the outside heat exchanger by 8 pipes. The temperature of cooling water is kept within $20 \pm 1°C$, to maintain the temperature around the rear ends of crystal about $25°C$.

Temperature Monitoring

There are some photomultipliers of TOF system situated near the inner wall at the two ends of the barrel calorimeter. They are also heat sources need to be cooled, since they could cause non-uniform temperature distribution around the calorimeter, and will increase the luminous non-uniformity of the crystal. In order to limit, control and correct this temperature effect, a temperature monitoring system is necessary. About 600 LTM8802 temperature sensors will be distributed around the calorimeter, and readout by a system composed of Uni-Series Bus(USB) and readout module LTM8301, the temperature can be measured to a precision of $\pm 0.5°C$.

Humidity Control and Monitoring

Owing to the readout electronics at the rear end, CsI crystals cannot be isolated from air. Dry air or nitrogen with humidity less than 5% will be flowed through the volume at a slow rate and slightly overpressure will be used to maintain a dry atmosphere, to prevent degradation of the crystal surfaces. A humidity monitor system is also needed. About 200 sensors are distributed and linked to the slow control system using the same method of the temperature monitor system. The accuracy of the humidity measurement can reach $\pm 3\%$.

Radiation Dose Monitoring

Due to the radiation damage effect of CsI(Tl) crystal (～10% per krad), the radiation dose should be monitored. The typical dose to the calorimeter is around 50～300 rad/year[9], thus a sensitivity level of 0.5 rad is needed for dose measurement. There are about 80 sensors distributed around the calorimeter, particularly around the endcaps.

Calibration and Correction

The light output uniformity and characteristics of each crystal module should be measured and recorded, before installation. During each crystal module installation and after whole calorimeter assembled. Xeon flash lamp calibrations in situ are still needed. Due to temperature variations, radiation damages, drifting of electronics gains, etc, a data base for each crystal module is obtained for a series of corrections. Possible calibration programs in situ are listed in the following:

1. Electronic parameters such as the amplification, the linearity and pedestals can be obtained by the electronics calibration system. The original data of each crystal module can be corrected using these periodical calibration results.

2. Temperature corrections for CsI crystal light yield, which has a temperature coefficient of -0.3%/C^0, can be performed by using the temperature monitoring system.

3. A Xe lamp-fiber system is used to calibrate and monitor the crystal module periodically. The parameters of radiation damage effects could be obtained. This

system can also be used to monitor the effects of beam intensity on the calorimeter etc.

4. Cosmic-ray muons can be used periodically to check and monitor the detector performance and the effects of radiation damage.

5. The ultimate energy calibration will be done using physics events, such as e^+e^-, $\gamma\ e^+e^-$ and neutral particles π^o.

Mechanical Structure

Support Structure of Crystals

The support structure of the crystals should mount the crystals while minimize the dead areas and gaps between the crystals. From the physics point of view, the scheme of suspending the crystals from the support girder is ideal. Since the CsI(Tl) material has good glutinosity and uneasily crumble similar to lead, , it can be drilled and screwed. This scheme can not only meet the physics requirements, but also leads to a simple structure avoiding difficulties of the mechanical manufacture, such as the carbon fiber honeycomb structure of BaBar or thin Aluminum wall structure of Belle. A structure by suspending crystals will greatly decrease the expense of the mechanical support also.

The basic structure of the support frame is the following: each crystal is fixed on a Al base with four wood screws in the rear face of the crystal, the shielding box of electronics is installed in the Al base, and finally the whole cell is fixed on the metal support girder with other four screws and the metal splint.

Several experiments were performed to provide mechanical parameters of crystals and help the comparison between possible schemes.

(1) Pressure test on crystal

The results in table 7.10-1 show that the crystal sample can support the pressure of at least 30kg/cm^2 without deformation. When half of a ring crystals of EMC barrel(60 crystals with the weight of 240kg) press freely on a crystal, the pressure is 1.6kg/cm^2 and far less than the pressure limit to crumble crystals.

Table 7.10-1 Pressure test of CsI Crystal

Sample	Crystal Size	Broken Pressure (N)	Remark
1	Φ16×15	1000	Body changed
2	Φ16×15	1000	Body changed
3	Φ16×15	200	Body changed, appear powder on 5000N

Table 7.10-2 Crystal Sample (Φ 18X15, with hole)

Sample	1	2
Before H (mm)	15.0	14.58
Before ϕ (mm)	17.7	17.8
Before H (mm)	10.6	11.6
Presure P (KN)	3.8	2.1
stress σ (Mpa)	16.39	8.535
strain ε	0.293	0.200
E (MPa)	55.9	42.7

Conclusion: The tensile elastic modulus E of CsI crystal was measured to be E=2.92 Gpa, for CsI crystal sample E=42.7 Mpa.

(2) Destructive test of crystal-screw tension

Different types of screws were tested to find the limit of force before the connection between screw and crystal is broken. The results in table 7.10-3 show that the single wood screw has the largest resisting tensile strength, and the crystal is not destroyed for the single M4 wood screw with a drill depth of 15mm when the shearing strength is 45kg.

(3) Effect of the stress on the light output of crystal

The crystal is laid horizontally with a pressure of 1.2kg/cm^2 on top of the crystal. After the stress is retained for 20 days, the light output decreases about 3%.

Table 7.10-3 Destructive test of crystal-screw tension

Sample	Size	destroy value	Remark
01	M3×8	250 N	pull out
01	M3×12	300 N	pull out
01	M5×15	720 N	pull out
02	M4×10	300 N	pull out
02	M4×15	400 N	pull out
02	M4×15	60 N	pull slanting out
03	M4×10 (wood screw)	600 N	pull out
03	M4×10 (wood screw)	520 N	pull out
03	M4×10 (wood screw)	660 N	pull out
04	M4×20 (wood screw) plastic cover	100 N	pull plastic cover out
05-1	Φ12×50	550 N	crystal adge broken

(4) Test of stress without support

The crystal is horizontally hanged and fixed on a vertical metal bracket with four M4 wood screws and drill depth of 20mm. For a weight of 34kg on the top, the crystal is not destroyed and the far end (i.e. without the screws) of the crystal moves down by 3mm.

The crystal is horizontally hanged through the electronics box as shown in Fig.7.10-8. For a weight of 47kg on the top, the metal bracket of the crystal deforms, the far end of the crystal moves down by about 80mm, but the crystal is not broken. The results show that if a crystal was horizontally hanged and no support underneath, their gravity will put on this crystal and the screws of this crystal would not fall off.

In the whole process of the crystal installation, the hanging operation of crystals is in the perpendicular direction and the screws mainly support the pull in the vertical direction.

Support Structure of Crystal

The mechanical structure of the calorimeter consists of a barrel and two endcaps. They should support all the inner detectors such as TOF and drift chambers, and attached to the main structure (iron yoke) of the detector. Each endcap consists of two half rings, which has to be movable so that inner detector can be accessed. The mechanical structure of the barrel calorimeter is shown in Fig.7.10-1 and Fig.7.10-2. The container of the barrel calorimeter is a slat structure and is divided into 60 (in Φ direction) compartments, each contains two rows of crystals (88 crystals). The 60 stainless steel bars are connected to the two stainless steel end-rings with screws. The inner edge of the stainless steel bars are connected to the stainless steel opening-cut girder and its two sides through two stainless steel reinforce bars are joined with the two adjacent stainless steel bars. Thus the whole support frame is joined together.

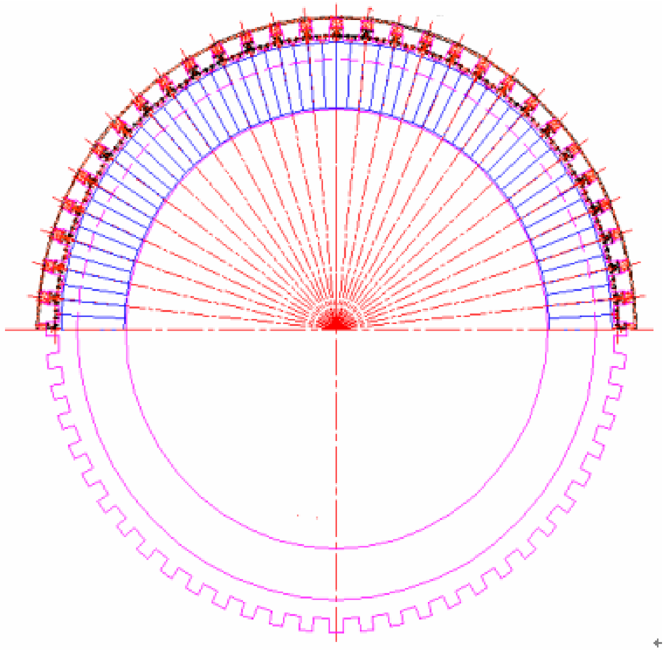

Fig. 7.10-1 Side view of the calorimeter

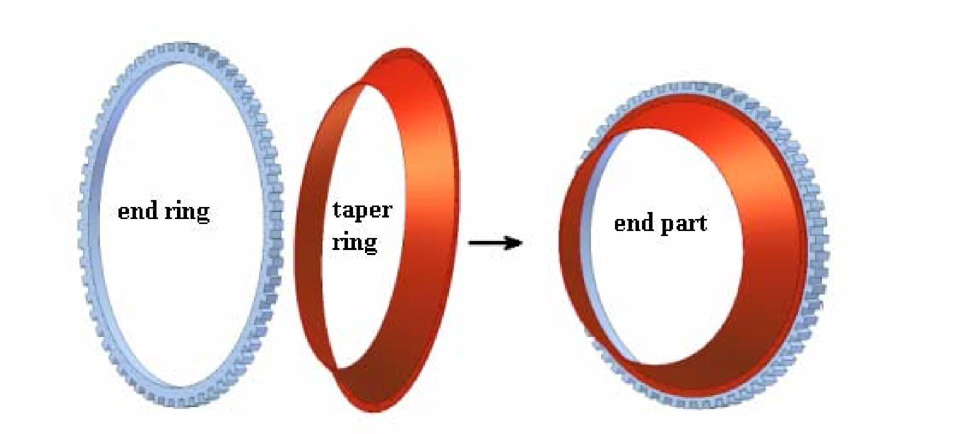

Fig.7.10-2 End of support frame which consists of the end ring and tapered ring

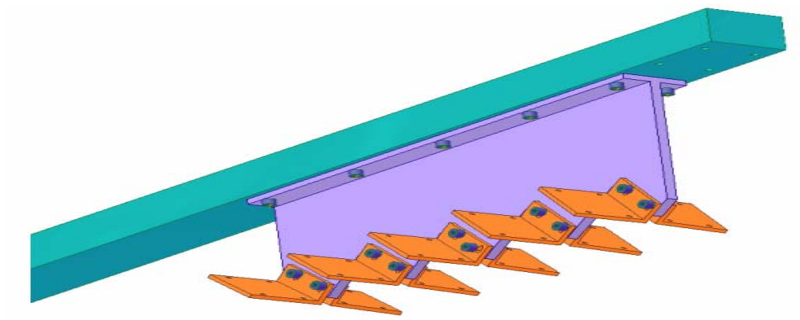

Fig.7.10-3 Stainless steel bar，the opening-cut girder and the splint to suspend crystals

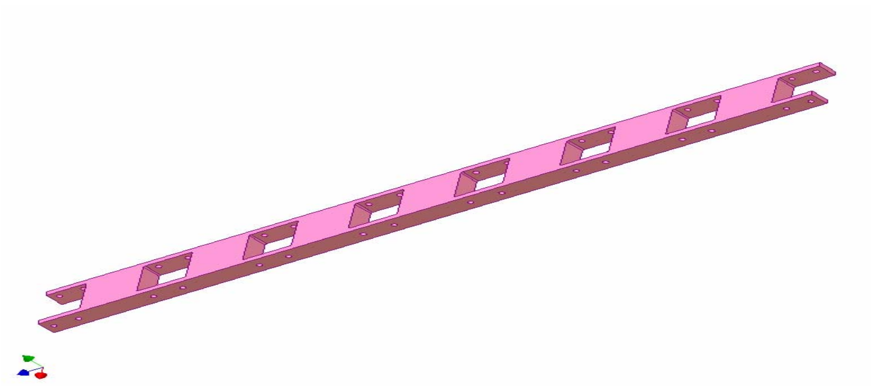

Fig.7.10-4 Stainless steel reinforce bar

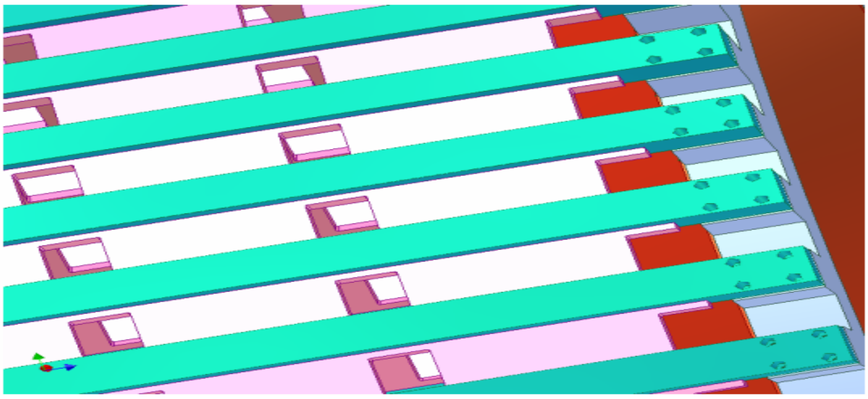

Fig.7.10-5 A part of the support frame of the calorimeter， the stainless steel reinforce bar is located between the stainless steel bars.

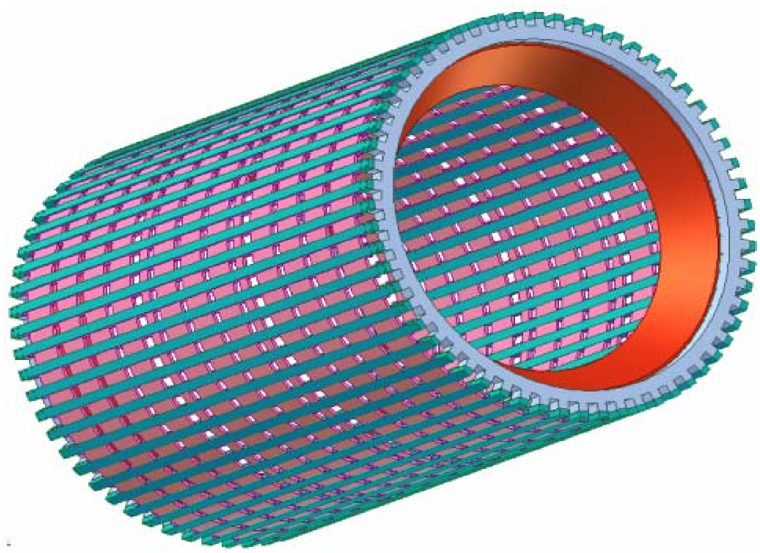

Fig.7.10-6 Barrel support frame without outer wall

The assembly of a crystal and its electronics box, the assembly of the crystal cell and its installation splint are shown in Fig.7.10-7 and Fig.7.10-8, respectively. The assemblies contain the fixation of crystal and Al base, the fixation of electronics box and base-board, and the assembly of the installation splint and electronics box.

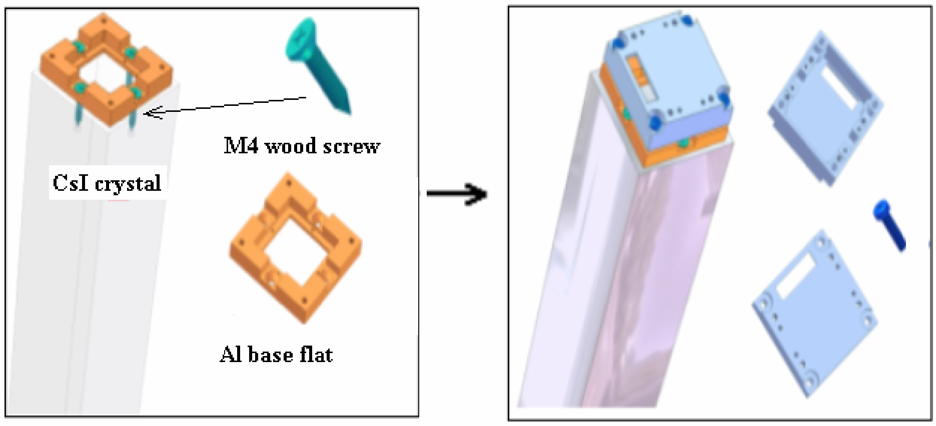

Fig.7.10-7 Assembly of crystal and electronics box

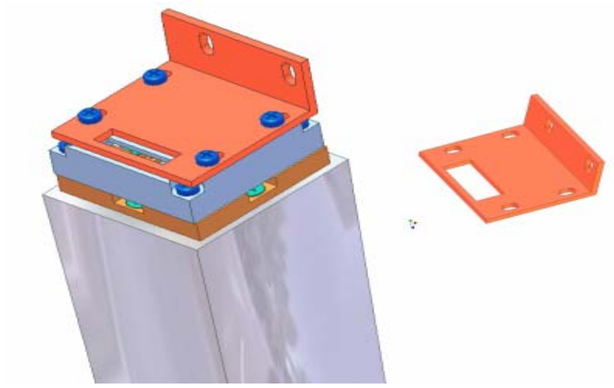

Fig.7.10-8 Assembly of the crystal cell and the splint

Mechanical Analyses of the Support Structure

By calculating the strength and analyzing the stability of the support structure, the structures and sizes of the bearing bar and the reinforce bar are determined and the design of the support structure is optimized. The nonmagnetic stainless steel is chosen for the bearing bars, left and right end-ring, reinforce bars, and outer wall. Al alloy is chosen for the two tapered barrels and the joint parts.

The calculations are made for the following stages in the assembly:

Before the crystals are installed, the strength and rigidity of the bearing bar, left and right end-ring, the tapered barrel and the outer wall, the deformation of the bearing bar and the stripped outer wall are calculated.

In the assembly process, there are four independent sections, each of which contains 15 assembled crystal cells, and each cell consists of two rows of crystals. When 14 crystal assembly cells for each section were installed, the deformation of the support structure of calorimeter and the crystals are calculated, as shown in Fig. 7.10-9. In the direction of gravity the largest deformation is 2.147mm and 1.747mm for crystals and the support structure, respectively. The deformation is larger in the direction of gravity and smaller in the horizontal direction.

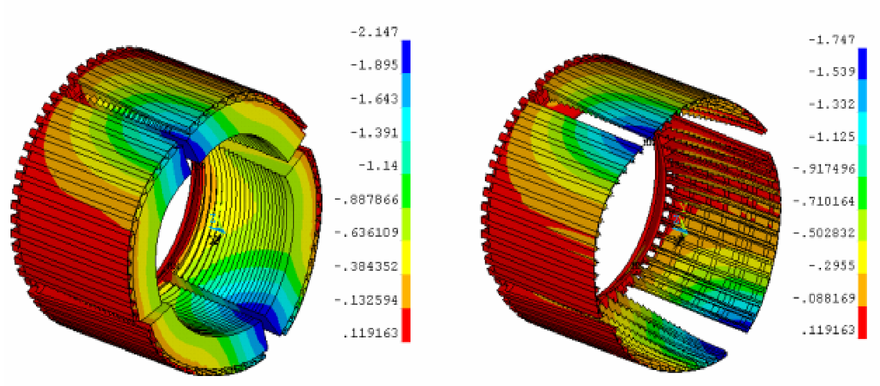

Fig.7.10-9 The deformations of the support structure of calorimeter and the crystals when only one crystal assembly cell for each section has not been installed

When 59 crystal assembly cells have been installed, the deformation of the support structure of calorimeter and the crystals are shown in Fig.7.10-10. In the direction of gravity the largest deformation is 2.143mm and 1.932mm for crystals and the support structure, respectively.

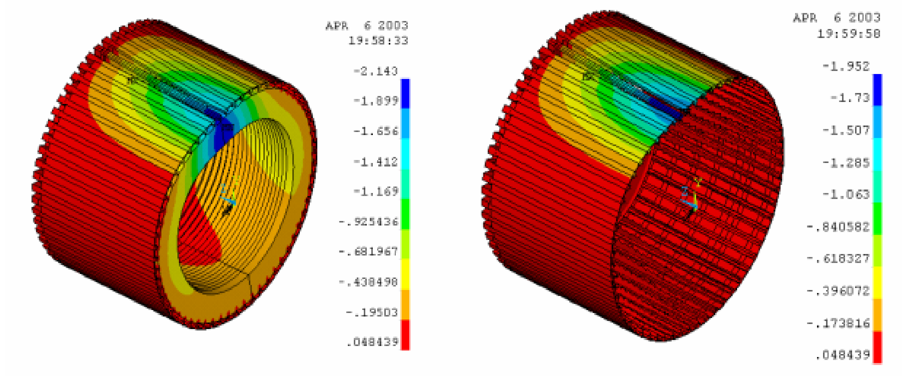

Fig.7.10-10 The deformation of the support structure of calorimeter and the crystals when only one crystal assembly cell on the top has not been installed

When all crystals are installed, the deformation of the support structure of calorimeter and the crystals are shown in Fig.7.10-11. In the direction of gravity the largest deformation is 0.591mm and 0.219mm for crystals and the support structure, respectively.

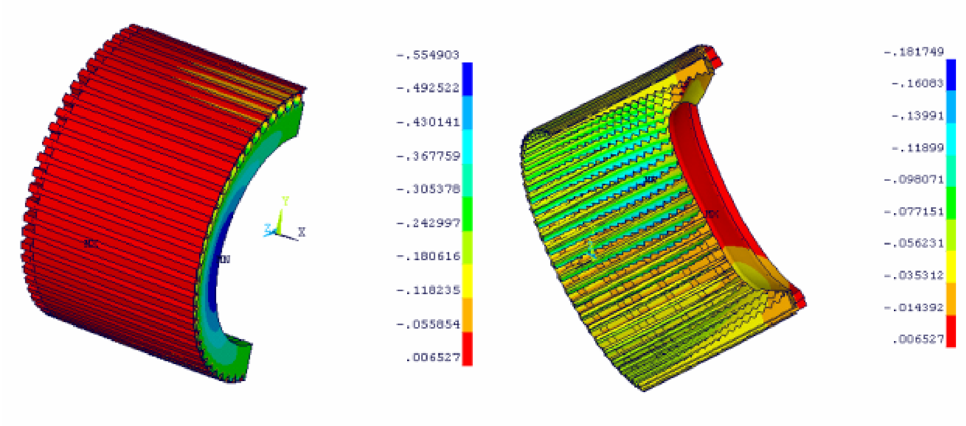

Fig.7.10-11 The deformation of the support structure of calorimeter and the crystals when all crystals have been installed.

Installation of Crystals

Installation of Support Frame

The installation of support frame of crystals consists of the mechanical assembly and the installation of dummy modules. There are 60 dummy modules, whose size is the same as that of two rows of crystals and the precision in Φ direction is 100μm. It limits the position of the inverted crystals when a module is pulled out, and is the support of the crystals. Before the crystals installed, the support frame is full of dummy modules.

Installation of Crystal

The calorimeter structure is supported with a rotational axial frame and a complicated auxiliary facility as shown in Fig.7.11-1. The process to assemble crystals will start at the top horizontal platform. Crystal installation consists of 60 assembly cells. The installation sequence follows Φ1, Φ15, Φ30, Φ45···, so that the stress of the structure is uniform.

The process of the crystal installation is in the following:

(1) Disconnect the two outer wall boards, the two reinforce bars, a bearing bar and a module.

(2) Prepare a cell of 88 crystals with electronics box assembled. Each cell has 44 kinds of crystals, and each crystal is tested by using the fiber-light pulse system.

(3) Insert 88 crystals one by one into the frock mould as shown in Fig.7.11-2 with a high precision of 50μm. The frock mould is one of the 60 orientating modules which consists of crystal orientation slot and the stainless steel bearing bar for the

pedestal fixing. The positions of 88 crystals are confined by the orientation slot, and the up and down position can be adjusted. In principle, there should be no gap between crystals, but an adjustable room of ±2.5mm in the up and down direction is reserved, which corresponds to ±250μm in ϕ direction. When all the 88 crystals are completely installed into the orientation slot, the positions of crystals are fixed.

(4) Install the stainless steel bearing bar and the opening-cut girder. The straight cooling copper pipe has to be installed in each side of the opening-cut girder. The position precision of installation the stainless steel bearing bar is same as that of the support frame. The reinforce frame is installed above the bearing girder. It can avoid the deformation of the bearing bar, and is also the hoisting shelf to hoist and transport this whole wedge shape structure.

(5) Assembly the preamplifier box and the opening-cut girder splint, and fix the crystal cell on the opening-cut girder. The holes on the splint are strip-shape holes, so that the screw can be adjusted to meet the fixed crystal. The splint is connected to the preamplifier box with the screw and a piece of heat strip made of copper net to the cooling copper pipe This connection is electrically insulated so that the grounding of the preamplifier box and the support frame are unattached.

(6) Install the cables of the preamplifier and the fiber, and check again the signal of each crystal cell using the fiber-light pulse system.

(7) The whole assembled wedge structure is hoisted from the frock mould, transported to the top of the support frame and inserted into the position at 12 o'clock, i.e., No. 1 in Φ direction (see 7.11-3). After the wedge structure is installed, the orientation pin on the bearing bar is inserted and fixed to the end-ring. The reinforce bars in the two sides of the bearing bar is then fixed, the hoisting shelf is taken away, and the two outer wall boards are installed.

(8) Fix the 18m long cables rotate the support frame and install the next wedge structure.

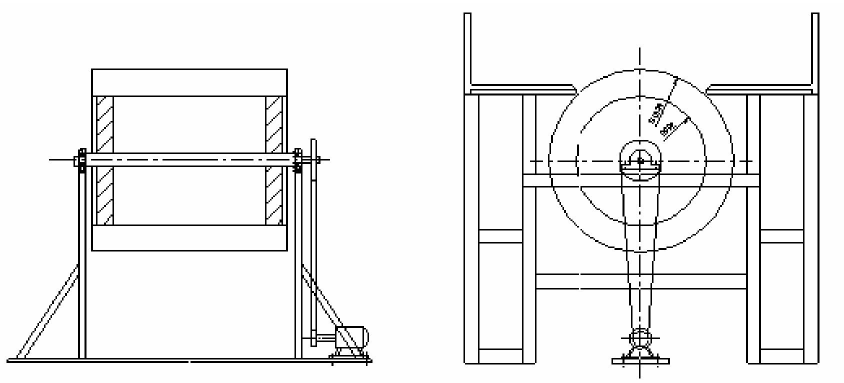

Fig.7.11-1 Calorimeter assembly structure

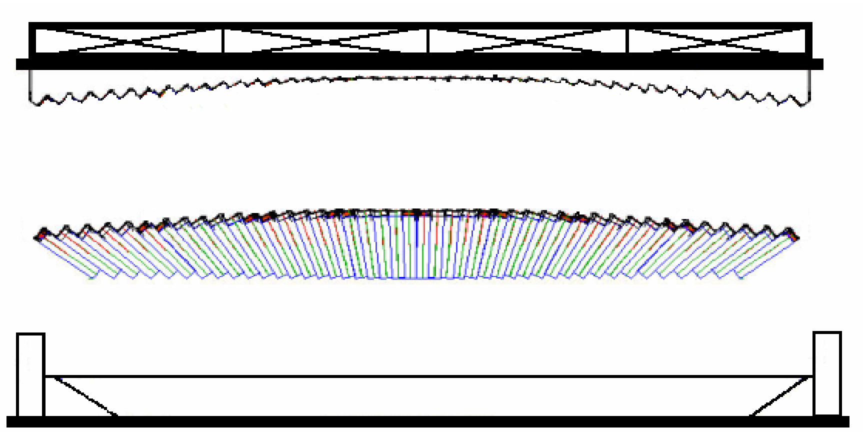

Fig.7.11-2 Sketch of an assembly cell, the three diagrams from bottom to top are the frock mould, the crystal cell, and the bearing bar and the hoisting shelf.

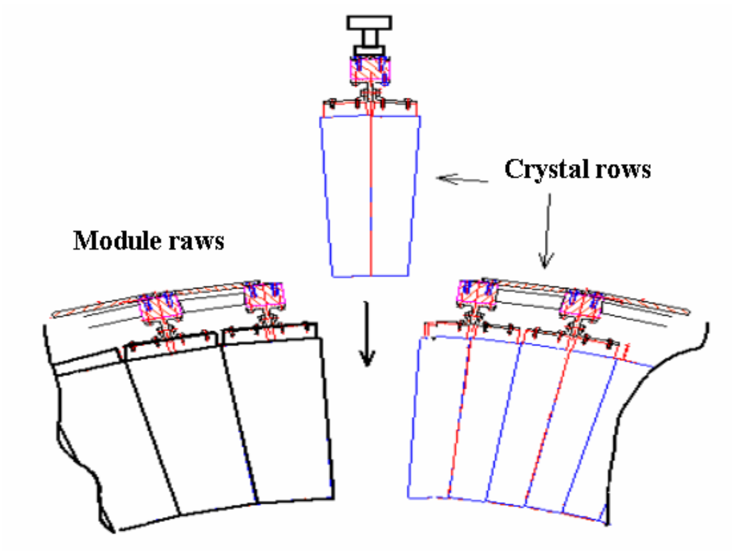

Fig.7.11-3 An assembly cell is inserted into the position at 12 o'clock of the support frame

Support Structure of the Endcap

The endcap calorimeter is composed of east and west endcap. In order to be disassembled easily for fixing inner detectors, each endcap consists of two half rings. When BES III inner detectors need to be repaired, the iron yoke of endcap can be moved away and the endcap calorimeter are movable about 1430mm along the beam direction (east-west direction) and the two half rings are moved separately in the south-north direction. The available space is enough to examine and repair the main drift chamber (MDC). After the repairs are finished, the endcap calorimeter is assembled again and the original precision should be ensured. Since the direction of crystal of endcap calorimeter is close to horizontal direction, the crystals can be piled up and need not to be suspended. The endcap crystals are supported from the rear of crystal. The support structure is quite simple.

Prepare of Working Rooms and Environment

The requirements of working rooms and the corresponding environment are in the following:

(1) Laboratory for measuring crystal performance: ~40m^2 , constant temperature(20±2°C)。

(2) A room to store crystals with an area of ~100m^2, ~60m^2 with constant temperature (20°±2) and dryness（humidity<25%）, and prevented from light.

About 30 shelves with 8 layers are needed to store crystals (2M long, 1.8M high, 0.64M wide).

(3) Room for assembly of crystal cell, testing of PD, cosmic rays measurement, and assembly of barrel and endcap calorimeter (inside big hall):

Area：~100m^2，6M high，movable roof (to offer crane operation); environment：humidity<30%， constant temperature (20$\pm$2°C).

Appendix: Table of Crystal Size

Table1: Crystal size of the barrel calorimeter.

The sizes of No.23～No.44 are the same as No.1～No.22, and the difference is only the interchange of position of H face relative to B face, as shown in Fig.1.

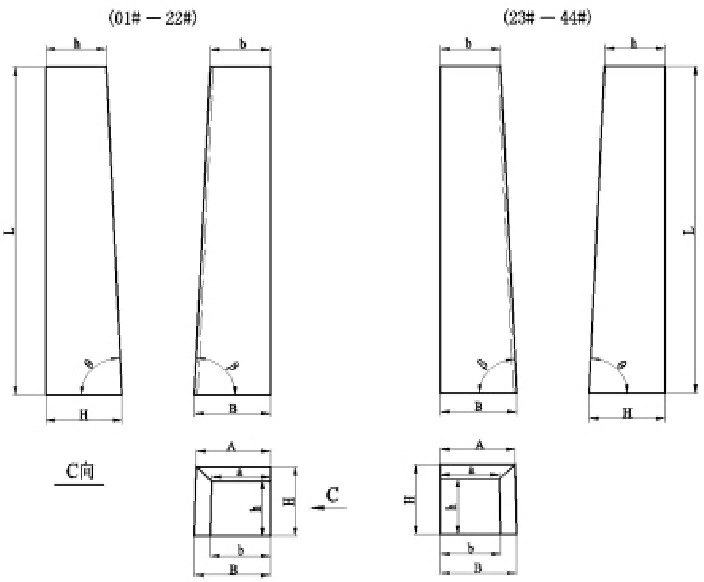

Fig.1 Definitions of size and angle of No.1～No.22 and No.23～No.44 crystal for the barrel.

Table1 Size of crystals for the barrel calorimeter

No.	23 (22)	24 (21)	25 (20)	26 (19)	27 (18)	28 (17)	29 (16)	30 (15)
H(mm)	58.13	58.10	66.79	66.67	66.51	66.31	66.07	65.80
h(mm)	50.40	50.40	51.40	51.40	51.40	51.40	51.40	51.40
θ(deg)	88.419	88.425	86.854	86.878	86.911	86.952	87.000	87.056
B(mm)	63.46	63.53	63.59	63.67	63.71	63.71	63.66	63.57
b(mm)	48.78	48.85	48.93	49.08	49.23	49.37	49.51	49.65
β(deg)	86.999	86.999	87.003	87.017	87.040	87.068	87.107	87.154
A(mm)	63.46	63.45	63.33	63.29	63.14	62.95	62.72	62.46
a(mm)	48.78	48.78	48.78	48.78	48.78	48.78	48.78	48.78
L(mm)	280	280	280	280	280	280	280	280
V(cm3)	853.52	853.52	934.45	935.21	936.01	935.15	933.44	930.90
W(kg)	3.85	3.85	4.21	4.22	4.22	4.22	4.21	4.20
QTY.	240	240	240	240	240	240	240	240
No.	31 (14)	32 (13)	33 (12)	34 (11)	35 (10)	36 (9)	37 (8)	38 (7)
H(mm)	65.50	65.16	64.81	64.43	64.04	63.64	63.23	62.81
h(mm)	51.40	51.40	51.40	51.40	51.40	51.40	51.40	51.40
θ(deg)	87.117	87.187	87.258	87.336	87.415	87.497	87.581	87.666
B(mm)	63.44	63.28	63.09	62.86	62.62	62.35	62.07	61.77
b(mm)	49.78	49.91	50.03	50.14	50.25	50.35	50.45	50.54
β(deg)	87.207	87.266	87.329	87.399	87.470	87.546	87.624	87.703
A(mm)	62.17	61.86	61.52	61.16	60.79	60.41	60.02	59.62
a(mm)	48.78	48.78	48.78	48.78	48.78	48.78	48.78	48.78
L(mm)	280	280	280	280	280	280	280	280
V(cm3)	929.1	925.77	922.42	917.4	913.23	908.24	903.26	898.31
W(kg)	4.19	4.18	4.16	4.14	4.12	4.10	4.07	4.05
QTY.	240	240	240	240	240	240	240	240
No.	39 (6)	40 (5)	41 (4)	42 (3)	43 (2)	44 (1)		
H(mm)	62.40	61.98	61.56	61.15	60.74	59.60		
h(mm)	51.40	51.40	51.40	51.40	51.40	51.86		
θ(deg)	87.750	87.836	87.922	88.006	88.089	88.153		
B(mm)	61.46	61.14	60.81	60.48	60.15	58.58		
b(mm)	50.62	50.70	50.77	50.84	50.90	50.97		
β(deg)	87.783	87.865	87.946	88.028	88.108	88.184		
A(mm)	59.23	58.83	58.43	58.04	57.66	56.06		
a(mm)	48.78	48.78	48.78	48.78	48.78	48.78		
L(mm)	280	280	280	280	280	240		
V(cm3)	893.37	888.45	883.55	877.11	871.44	741.11		
W(kg)	4.03	4.01	3.98	3.96	3.93	3.34		
QTY.	240	240	240	240	240	240		Total 5280

Table2 Sizes of crystals for the endcap calorimeter

table 2-1 symmetrical crystal (total:8)

No.	45#	46#	47#	50#	63#	73#
Name.	A1	A2	A3	B3	D3	F1
A(mm)	61.43	74.82	64.81	56.59	56.67	57.14
a(mm)	51.96	63.31	53.30	47.69	47.42	47.51
B(mm)	64.85	78.97	68.96	60.12	61.12	62.95
b(mm)	54.85	66.82	56.81	50.66	51.14	52.34
C(mm)	65.51	65.51	65.51	66.05	66.52	66.94
c(mm)	55.41	55.41	55.41	55.67	55.67	55.67
α1(deg)	88.51	88.19	88.19	88.47	88.08	87.51
α2(deg)	91.49	91.82	91.82	91.53	91.92	92.49
S(mm2)	4134.53	5034.32	4379.26	3852.99	3915.45	4015.39
s(mm2)	2958.50	3603.68	3049.53	2736.28	2742.04	2777.06
L(mm)	280	280	280	280	280	280
V(cm3)	988.4430	1203.7527	1034.4323	918.0484	927.1845	945.6300
W(kg)	4.4579	5.4289	4.6653	4.1404	4.1816	4.2648
QTY.	160	24	8	64	32	96

No.	74#	75#
Name.	F2	F3
A(mm)	65.44	55.43
a(mm)	54.43	44.42
B(mm)	72.09	62.07
b(mm)	59.96	49.95
C(mm)	66.94	66.94
c(mm)	55.67	55.67
α1(deg)	87.15	87.15
α2(deg)	92.85	92.85
S(mm2)	4597.21	3927.82
s(mm2)	3180.41	2623.66
L(mm)	280	280
V(cm3)	1082.7935	911.0892
W(kg)	4.8834	4.1090
QTY.	24	8

table 2-2 unsymmetrical crystal (total:18)

No.	48#(49#)	51#	52#(53#)	54#	58#	59#(60#)
Name.	B1(B2)	B4	B5(B6)	C1	C5	C6(C7)
A(mm)	56.58	68.97	58.94	62.32	73.64	63.63
a(mm)	47.67	58.14	48.11	52.34	61.86	51.85
B(mm)	60.12	73.22	63.22	66.63	78.77	68.74
b(mm)	50.66	61.72	51.72	55.95	66.17	56.14
C(mm)	66.06	65.04	65.50	64.33	64.33	64.33
c(mm)	55.68	54.82	55.27	54.02	54.02	54.02
D(mm)	68.18	68.18	68.18	66.28	67.26	66.88
d(mm)	57.46	57.46	57.46	55.66	56.48	56.11
α1(deg)	88.47	88.14	88.14	89.80	89.91	89.91
α2(deg)	93.67	94.46	94.46	91.88	92.21	92.21
α3(deg)	89.39	89.25	89.25	91.88	92.21	92.21
α4(deg)	88.47	88.14	88.14	86.45	85.66	85.66
S(mm2)	3913.56	4730.76	4078.08	4207.19	5008.11	4337.41
s(mm2)	2779.38	3361.07	2810.61	2967.06	3533.10	2970.14
L(mm)	280	280	280	280	280	280
V(cm3)	932.4933	1127.4074	958.9288	999.3551	1189.7811	1017.0341
W(kg)	4.2055	5.0846	4.3248	4.5071	5.3659	4.5868
QTY.	64(32)	24	4(4)	32	24	4(4)
No.	61#(62#)	64#	65#(66#)	67#	70#	71#(72#)
Name.	D1(D2)	D4	D5(D6)	E1	E4	E5(E6)
A(mm)	56.64	67.00	56.96	64.03	73.33	63.32
a(mm)	47.39	56.08	46.04	53.42	61.19	51.18
B(mm)	61.12	72.22	62.21	69.66	79.83	69.79
b(mm)	51.14	60.45	50.44	58.12	66.62	56.58
C(mm)	66.53	65.57	66.08	64.52	64.52	64.52
c(mm)	55.69	54.88	55.39	53.82	53.83	53.83
D(mm)	68.97	68.96	68.96	66.72	67.65	67.26
d(mm)	57.72	57.72	57.72	55.66	56.44	56.04
α1(deg)	88.08	87.74	87.74	89.37	89.45	89.45
α2(deg)	94.38	95.16	95.16	92.44	92.79	92.79
α3(deg)	89.46	89.36	89.36	92.44	92.79	92.79
α4(deg)	88.08	87.74	87.74	85.75	84.96	84.96
S(mm2)	3985.20	4675.75	4017.54	4381.55	5052.77	4378.23
s(mm2)	2790.98	3275.74	2724.42	3049.38	3517.52	2955.12
L(mm)	280	280	280	280	280	280
V(cm3)	943.7157	1107.4117	938.0332	1034.7125	1193.3720	1020.1627
W(kg)	4.2562	4.9944	4.2305	4.6666	5.3821	4.6009
QTY.	64(32)	24	4(4)	32	24	4(4)

table 2-3 pentagonal crystal (total:5)

No.	55#(57#)	56#	68#(69#)		
Name.	C2(C4)	C3	E2(E3)		
A(mm)	22.10	33.33	27.82		
a(mm)	18.54	27.99	23.19		
B(mm)	65.81	65.81	66.16		
b(mm)	55.27	55.27	55.19		
C(mm)	62.32	62.32	64.03		
c(mm)	52.34	52.34	53.42		
D(mm)	64.34	65.81	64.53		
d(mm)	54.03	55.27	53.84		
E(mm)	44.57	33.33	41.92		
e(mm)	37.45	27.99	34.99		
α1(deg)	174.35	176.45	173.33		
α2(deg)	90.63	89.90	90.23		
α3(deg)	91.88	91.88	92.44		
α4(deg)	91.88	91.88	92.44		
α5(deg)	91.26	89.90	91.55		
S(mm2)	4240.46	4275.21	4430.10		
s(mm2)	2990.65	2990.92	3083.34		
L(mm)	280	280	280		
V(cm3)	1007.2768	1011.9195	1046.2024		
W(kg)	4.5428	4.5638	4.7184		
QTY.	32(32)	32	32(32)		

References

1. A.Antonelli, et al., Nucl.Instr. and Meth. A354(1995)352
2. The Belle Collaboration, The Belle Detector, KEK Report 1995
3. BarBar Collaboration,The BarBar Technical Design report, SLAC-R-95-475
4. E.Bucher, et al, Nucl.Instr.and Meth. A249(1986)201
5. M.Schneegans,et al ,Nucl. Instr. and Meth. A257(1987)528
6. Photodiodes, HAMAMATSU PHOTONICS
7. BarBar Collaboration, A systematic Study of Radiation Damage to Large Crystals of CsI(Tl) in the BarBar Dector, Calor2002 report
8. A.Satpathy, et al, Nucl.Instr. and Meth. A391(1997)423

Muon Identifier

Physics Requirement

The muon identifier is the outmost subsystem of the BESIII detector. It consists of muon counters and hadron absorbers, as shown in Fig.8.1-1. Its main function is to measure the positions and trajectories of muons produced in e^+e^- annihilation in a multi-layers arrangement. By associating hits in muon counters with charged track reconstructed in inner detector, the muons are identified and their momenta are precisely measured.

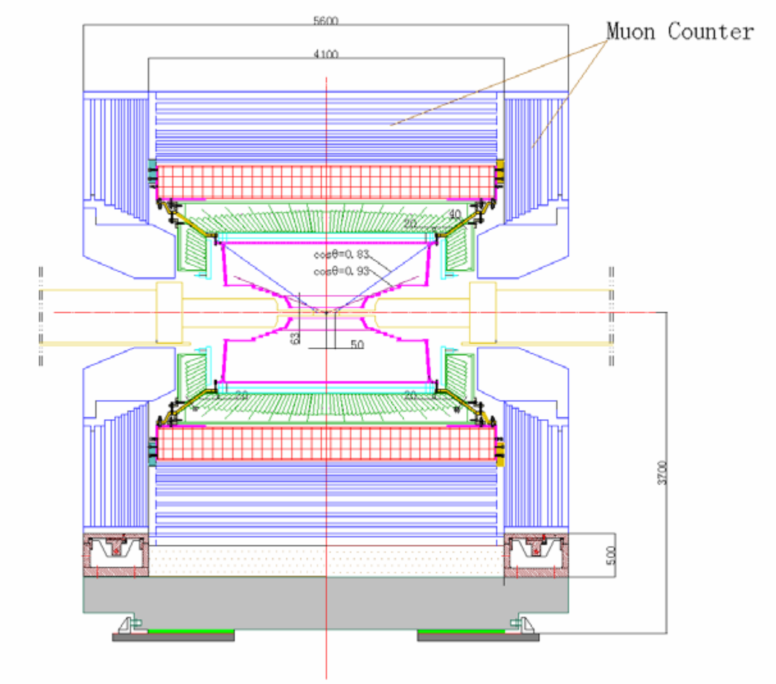

Fig.8.1-1 The BESIII overall structure

For e^+e^- collision physics, the measurement of muons is of great importance. In the discovery of J/ψ, the narrow sharp enhancement of $e^+e^- \to \mu^+\mu^-$ cross section is one of the most important evidences. The energy dependence of $e^+e^- \to \mu^+\mu^-$ cross section has proved that the quantum electrodynamics is correct up to $10^{-16}cm$. The precise measurement of τ mass at BES is also carried out mainly through $e^+e^- \to \tau^+\tau^- \to e\mu + 4\upsilon$.

For some important physics, especially for some rare decay channels measurements, the ability of μ/π identification affects the physical result to a great extent. For instance, the measurement of purely leptonic decay branching fraction, the study of semileptonic decays in charm physics, some rare decay in charm and τ decays such as $D^0 \to \mu^+\mu^-$, rely on the measurement of muons. Many muons are produced in D decays and τ decays, Fig.8.1-2 shows the momentum distribution of muons produced in D decays and τ decays near 2.0 GeV.

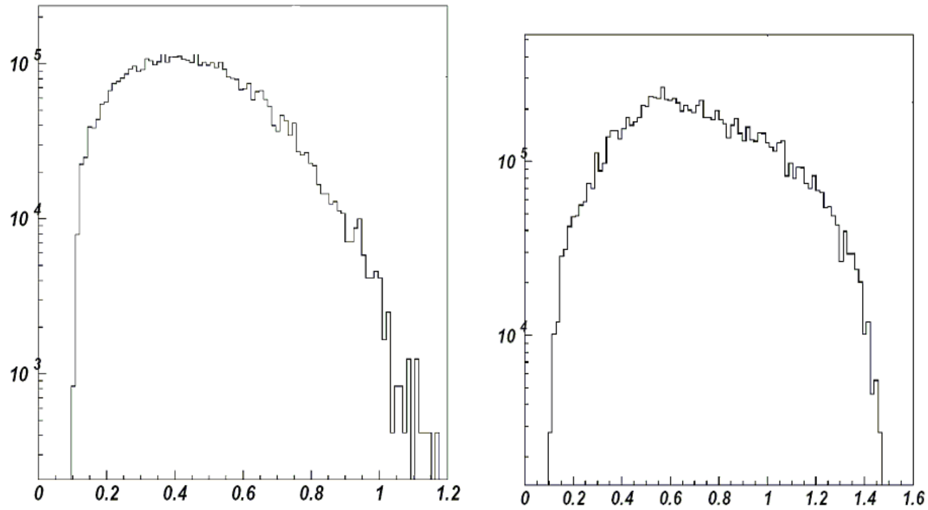

Fig.8.1-2 Momentum distribution of muons produced in D decays(left) and τ decays(right) at Ecm=2x2.0 GeV.

It can be seen that muons produced at the energy relevant to us are mainly in the low momenta range. So the muon identifier should cover a large solid angle, have a high detection efficiency, a low muon cut-off momentum, a suitable position precision and work with a safe gas.

Detector Choice

The resistive plate counter is a new type of detector developed by R. Santonico (Roma) in the early 80's. It has been successfully used in several large scale experiments, such as the BELLE experiment at KEK-B, the BaBar experiment at SLAC, the CMS and ATLAS experiments at LHC that are being built at CERN, the L3 experiment at CERN, the ARGO cosmic ray experiment at Yangbajing in Tibet, etc. As a result, much successful experience on RPC has been accumulated.

RPC is composed of two parallel high resistive plate electrodes with a gap between them for the working gas to pass through. When a particle passes through this gas chamber, an avalanche or a streamer signal is produced. Signal is induced on strips placed outside the gas volume surface to be read out. RPC can be arranged in a multi-layer configuration to allow multi-layer readout simultaneously. The basic structure of RPC is shown in Fig. 8.2-1.

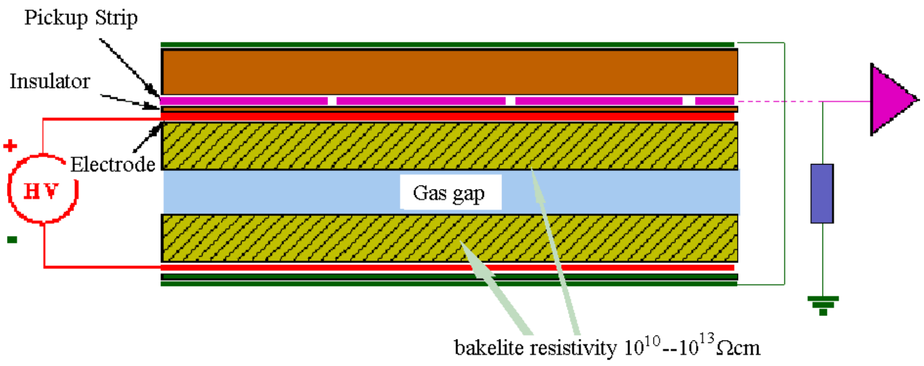

Fig.8.2-1 The sketch map of RPC structure

The material of RPC plate has a very high resistivity (10^{10}—10^{13} Ω •cm) and the RPCs in a groups work independent from each other. The induced signals can be added from several RPCs to increase the detection efficiency. When the counting rate is high, only the avalanche mode can be used for its relative small signal size. The streamer signal is too large that the high voltage drop from discharge will not be recovered on time for high rate application. Fig.8.2-2 shows the streamer signal versus high voltage with different gas mixture. Fig.8.2-3 shows the streamer or avalanche signals at different HV settings. The counting rate of muon identifier in BESIII is expected to be about 150-200Hz/m^2, hence the counting rate will not affect the detection efficiency significantly.

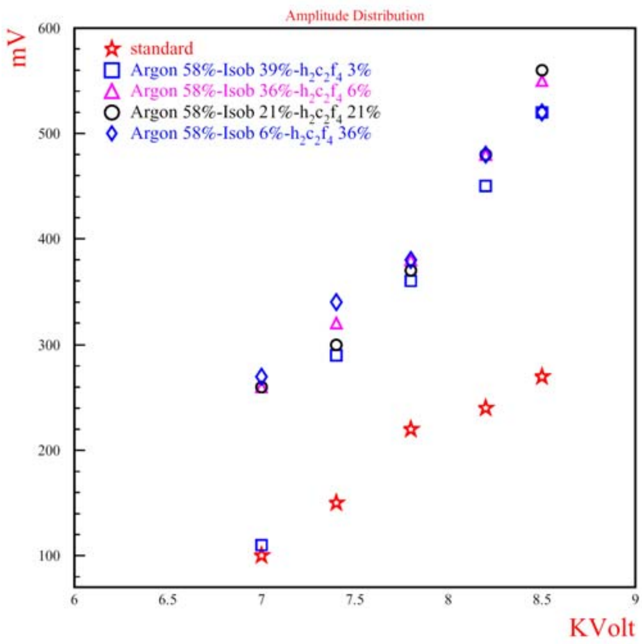

Fig.8.2-2 The streamer signal versus high voltage with different gas mixtures

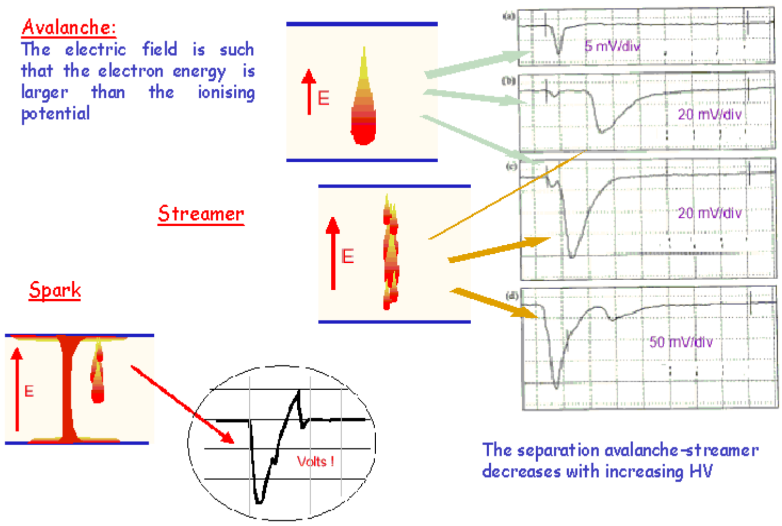

Fig.8.2-3 The comparison of avalanche and streamer signals at different HV settings

RPC has the following characteristics:

1) Simple and solid structure. Compared with other types of gas detectors, the RPC does not have wires and do not use other delicate technology, thus making it relatively easier to fabricate a large sensitive area detector. The Bakelite or glass, the main material used in the resistive plate chamber, are commercial products with a low cost.

2) Superior time and spatial property: Right now, for a large area and single gap RPC, the time resolution can reach about 1ns. So, the time information can be extensively applied for triggering and particle identification. Its position resolution can be designed according to needs. The position resolution of a large area RPC can reach one centimeter.

3) High detection efficiency and small dead space: The muon detection efficiency can reach up to higher than 95%. Since the gas chamber area can be made very large, the structural dead area can be made quite small, typically less than 2%.

4) Flexible signal readout: Since the readout strip is outside of the gas chamber and is independent of the gas chamber, its direction, length, width, etc. can be decided according to the actual needs. For example, the readout can be designed as one dimensional, two-dimensional, or even three-dimensional.

5) Small space occupation: The thickness of a double-layer RPC can be controlled below 32 mm. A single-layer RPC can be made even thinner. It has an obvious advantage in the space limited detecting system.
6) Mature technology: Now the RPC has already been used in many high energy physics experiments and much operation and performance experiences have been accumulated.
7) Good radiation hardness: Since no wires are used, the carbon and other contaminating materials will not be accumulated in small areas as in some wire chambers. So the radiation hardness is superior to that of other detectors that need wire stringing.
8) Easy management and maintenance: The RPC gas room has no sensitive parts, so it will not be easily damaged during operation. Since the area of a single detector is large, the gas and high voltage systems are relatively simple.
9) Big signal: When it works in the streamer mode, the signal can reach hundreds of mV, so no signal amplification is needed. The signal response is fast and the dead time is short.
10) Long lifetime: Problems had happened for the RPCs of BELLE and BaBar, but they were understood up to now. This has offered valuable experience for our operation in the future. The RPCs in L3 have been running for nearly 8 years since 1994, but its efficiency still keeps at the level of 94% — 99%. The counting rate of our BESIII will be smaller than those of BELLE, BaBar and L3. So if we draw experience from them in design, fabrication and operation, the BESIII RPCs should not have serious problem for its lifetime.

The shortcomings of RPC are that a quite high working voltage (about 7-10Kvolt) is needed and that sparks may be easily produced. Unless the surface is well managed, big noise can be produced.

The RPC production technology has been matured. In mass production, the consistency of the RPC performances and the quality control are rather good. Italy is the first country that put forward the idea of developing RPC and boasts the capability for the mass production of RPC. The Institute of High Energy Physics, Beijing University and University of Science and Technology of China have studied RPC and basically mastered the technology. In principle, there will be no major difficulty for establishing a production line of RPC. Once this production line is established, we can supply RPC detectors not only for BESIII muon identifier, but also to other domestic and international laboratories, such as the Yangbajing cosmic ray experiment, the long base line neutrino experiment, etc.

Monte Carlo Simulation

To provide basis for the detector design, we did some Monte Carlo simulation based on Geant 3.21 software package.

In the simulation, the electromagnetic calorimeter is a 15 radiation length CsI crystal array, and the total material of the superconductor and other inner detectors (including the beam pipe, the main drift chamber and TOF) is assumed to be equivalent to 5cm thick iron plate. If we don't require the match between the muon hits and the inner track, the rate of pion contamination to muon is still serious when the muon detection efficiency is to be ensured. But when a requirement is made that for muons only one hit exists within 3σ of extrapolated inner track, the situation becomes much better. If there are more than one hit in a muon layer within a certain distance from the extrapolated inner track, this track is more likely a pion producing secondary particles. The pion contamination to muon can be reduced to a lower level while the muons detection efficiency is ensured. Using the above selection, the muon detection efficiency and pion punch-through rate versus the thickness of the iron absorber is shown in Fig. 8.3-1.

Monte Carlo simulation was performed to study the possible insertion of a few layers of muon counters inside the superconductor coil to improve the μ/π identification at low energy. In fact, muons with momentum below 0.25 GeV are almost completely absorbed in the electromagnetic calorimeter, and that the energy losses of muons and pions in the calorimeter with momentum below 0.3 GeV are basically the same. From Fig. 8.3-1 the muon cut-off momentum is directly proportional to the material it travels through. Therefore if several layers of μ detectors are added inside the superconducting coil, the μ/π separation at 300—350MeV/c can be achieved to a certain extent, but the gain is very limited and it would affect the identification of the μ/π at 400—450MeV/c range. Moreover, the radius of the superconductor coil needs to be increased, hence increase the cost of superconductor magnet.

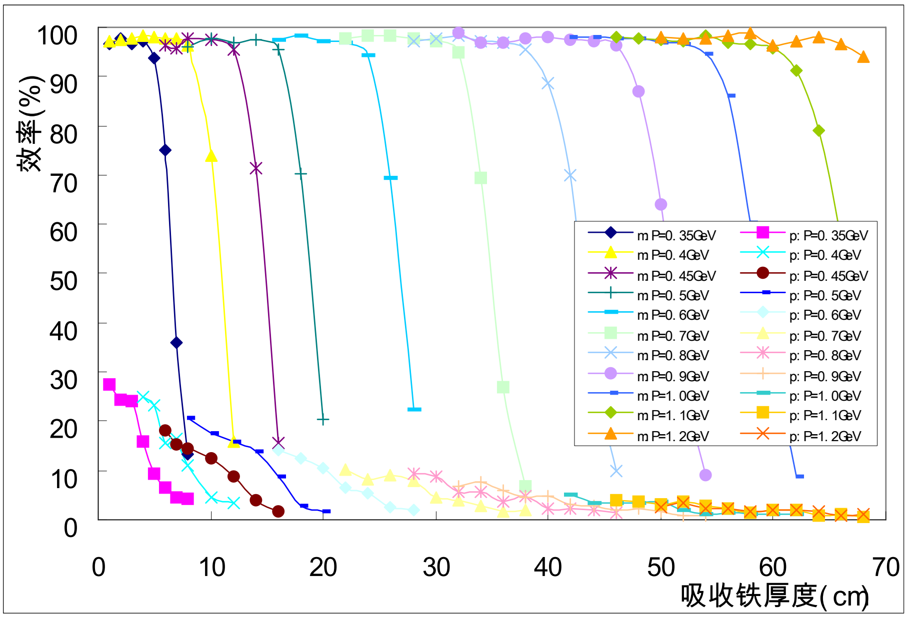

Fig.8.3-1 Muon detection efficiency and pion punch-through versus the thickness of iron

A better position resolution of muon identifier can decrease the pion contamination to muon, but to a very limited degree. Actually if we consider the multiple scattering after the muon passes through iron absorbers, the uncertainty of its position is already large. Fig.8.3-2 is the width of hit position versus the iron thickness passed by muons.

From this figure, it can be seen that the width of the hit location is 4-8cm after multiple scattering, so it does not make any sense for the width of pickup strip to be less than 4cm.

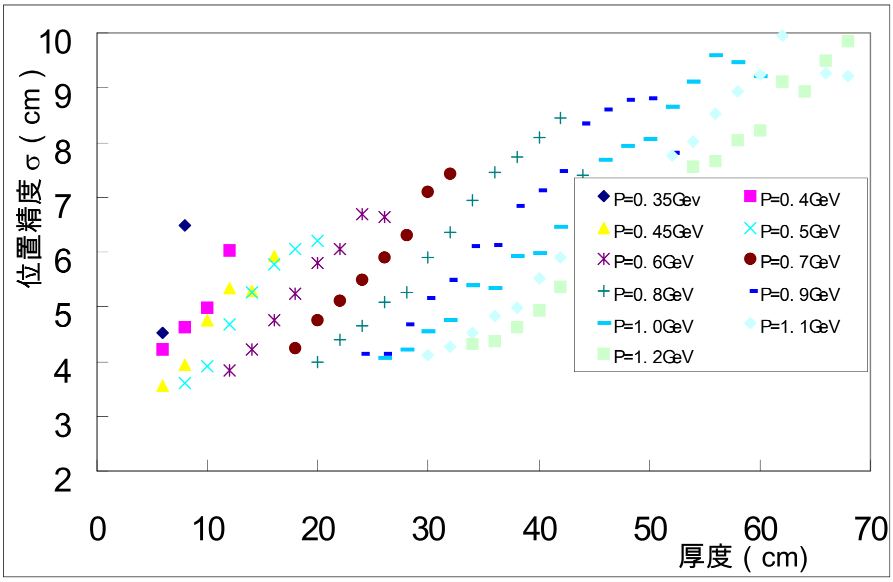

Fig.8.3-2 The width of hit position distribution versus the iron thickness the muons have passed

To lower the cost of electronics, we did some Monte Carlo simulation to study if the readout in a layer should be one or two dimensional. In our simulation, the hit position is required to be within 3σ of extrapolated position of inner track. If there are more than one hit in a layer, and the distance from other hits and the track exceeds 4cm, these hits are regarded as from more than one tracking segment in the muon chamber, hence the track is considered a pion.

For a 9-layer detector, the muon detection efficiency in one- and two-dimensional readout versus the momentum is shown in Fig. 8.3-3. And the pion contamination in one-and two-dimensional readout versus the momentum is shown in Fig.8.3-4.

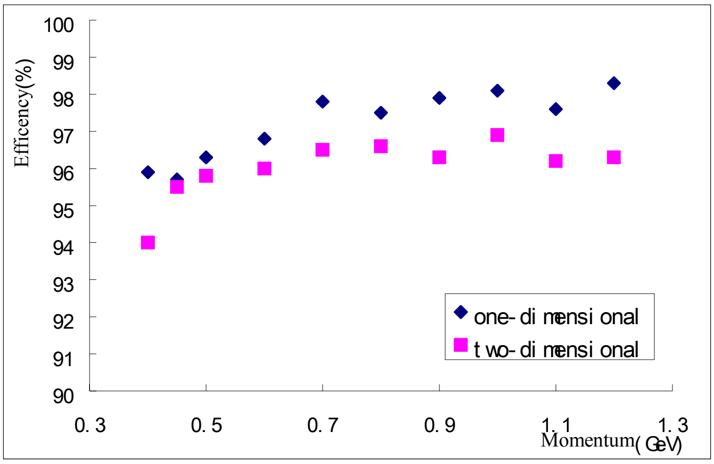

Fig.8.3-3 The μ detection efficiency in one-and two-dimensional readout versus the momentum

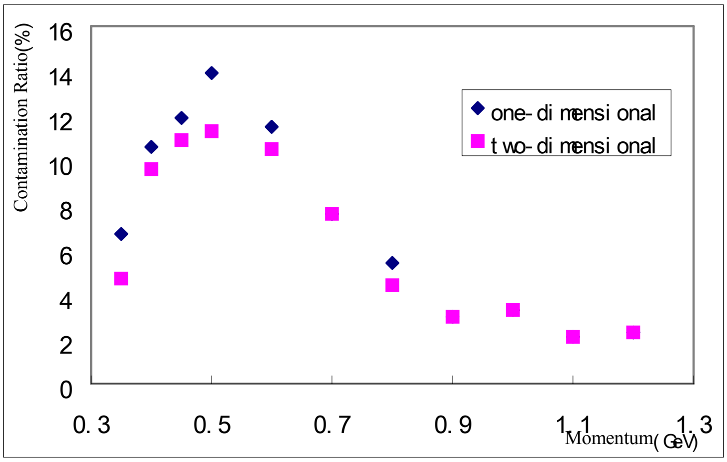

Fig.8.3-4 The π contamination in one-and two-dimensional readout versus the momentum

The simulated results show that using 3σ requirement (1-D readout requires one dimension in 3σ and 2-D readout requires two dimensions be in 3σ), the muon detection efficiency in 1-D readout will be higher than that in 2-D readout. However, the contamination of muon by pion will be high also, but by a very limited amount. In the high momentum range, especially when the momentum exceeds 0.9 GeV, the contamination of muon by pion has almost no difference for these two readout schemes.

Concerning the noise, the two-dimension read-out scheme can reduce the effect of the noise hits, and it is superior to the one-dimension readout. But we can use the time gate to reduce the noise background in the electronics readout. According to MC simulation, even when the noise of RPC reaches 1 KHz/㎡ (the RPC's counting rate of Babar is 0.6-1KHz/㎡) and the electronics gate is 100ns, a total of 2000 ㎡×1000 Hz/㎡×10^{-7}s=1/10 noise signals will be recorded on 2000m^2 RPC for every event, and the odds of it on the track is very small, hence the physics analysis will not be affected. However, one-dimension readout will reduce readout electronics channels by 2/3 and save 50% of pickup strips. At the same time, the adoption of one dimension readout makes it possible for the pickup strip to be put between two layers of RPC, thus making the entire detector thinner.

Overall Structure

For the design of the BESIII muon identifier, the following factors have to be considered: high detection efficiency for muon; large solid angle coverage; lowest possible momentum to be detected; the ability to reject other charged particles and appropriate positioning precision.

It should not be difficult to reach a detection efficiency higher than 95% for muon. To obtain a large solid angle the muon counters are splitted into two parts, the barrel and the end cap. The low momentum reach in detecting muons is determined by the material of the inner sub-detectors. The capability to reject other charged particles while detect muons with a high efficiency are contradictory, especially for low momentum muons. Hence, an appropriate structure must be selected to compromise these two demands. For the position precision, the requirement of physics and the cost have to be balanced. In the following the structures of the barrel and the end cap is introduced.

Barrel

The barrel muon counter is subdivided into 8 pieces in the circular direction. Its inner radius is 1700mm and outer radius 2620mm. Fig.8.4-1 shows the yoke and the RPC arrangement. There are 9 RPC layers radially.

Based on the simulation results, one layer of muon counters between the superconducting coil and the first layer of yoke plate is installed to detect muons at low momentum. Between two iron layers, there is a 40mm gap for the insertion of a RPC. There are altogether 8 layers of absorber with a thickness of 30mm, 30mm, 30mm, 40mm, 40mm, 80mm, 80mm, and 80mm respectively towards outside. The total iron thickness is about 410mm. There is a 15cm protective iron plate at the outside layer.

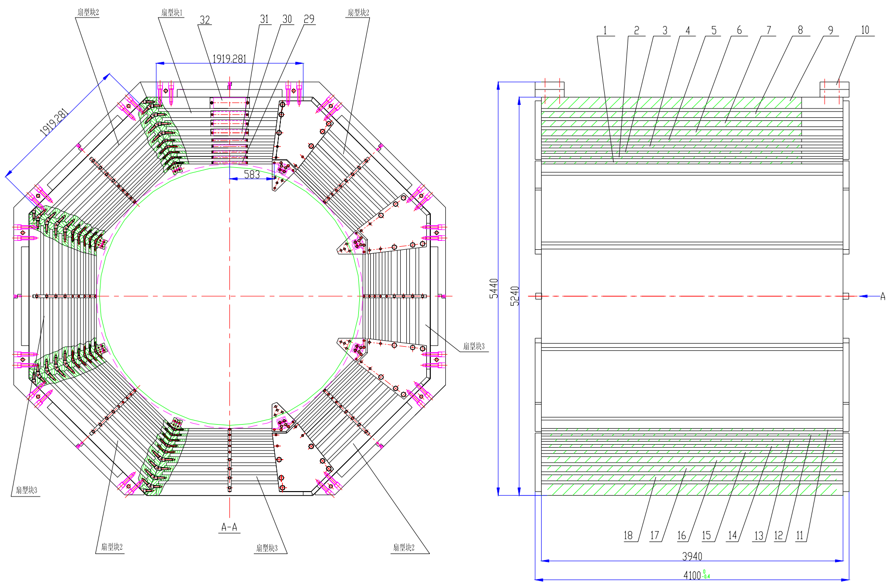

Fig.8.4-1 The barrel yoke and the RPC arrangement

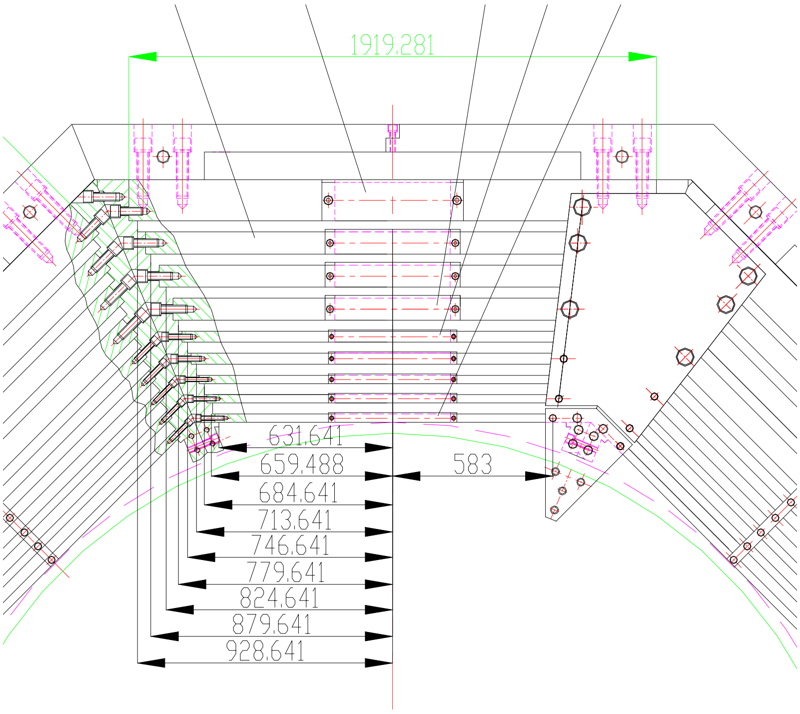

Fig.8.4-2 The size of each layer of the barrel RPC

The width of each layer of RPC in the barrel part is shown in Fig.8.4-2. Since a space of 80mm will be reserved at each end of the barrel for cables of other sub-detectors, and at the same time, a space of 70mm will be reserved at each end to connect the front end electronics readout board, high voltage and gas I/O ports, the RPC is only 3800mm in length. The solid angle coverage of the inner layer of the barrel part can reach 41.5^{o} to 139.5^{o} and that of the outermost layer can reach 53.5^{o} to 126.5^{o}.

The barrel part adopts the rectangle RPCs of different sizes with an alternating arrangement in order to reduce the dead space, as shown in Fig.8.4-3. The double layers of RPC are put into the same aluminum box that is fixed in the gap of the yoke with screws, to guarantee its location precision. The pickup strip is put between two layers of RPC for signals readout which is in Z direction for odd layers, and in Y direction for even layers in order to reduce the effect of noise.

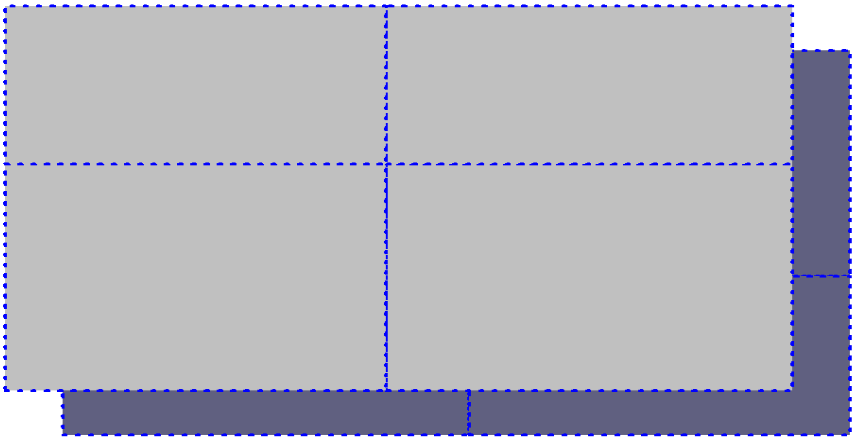

Fig.8.4-3 Barrel RPC of different size with an alternating arrangement

End Cap

The end cap muon identifier has 8 layers of counters and 8 layers of absorber iron as shown in Fig.8.4-4.

There is one layer less of RPC in the endcap due to the space limitation, and the thickness of the end cap iron of each layer towards outside of the detector is 40mm, 40mm, 30mm, 30mm, 30mm, 50mm, 80mm and 80mm, respectively. The total thickness of the iron is 380mm. There is a 5cm protective iron at the outset layer. Like the barrel part, there is a 40mm gap between every two layers of iron for the insertion of the RPC. Inside the first layer of RPC, one 40mm layer of absorber iron is added to close the loop of magnetic field and to improve the uniformity of the magnetic field.

The two end caps are divided into the left and right parts, and separately supported. They have their respective rail to move. When BESIII has a problem in inner detectors, the end cap yoke can be moved apart to reach the inner detectors. As the end cap muon detectors are very heavy, they must be supported individually. The electronics readout scheme is the same as that in the barrel.

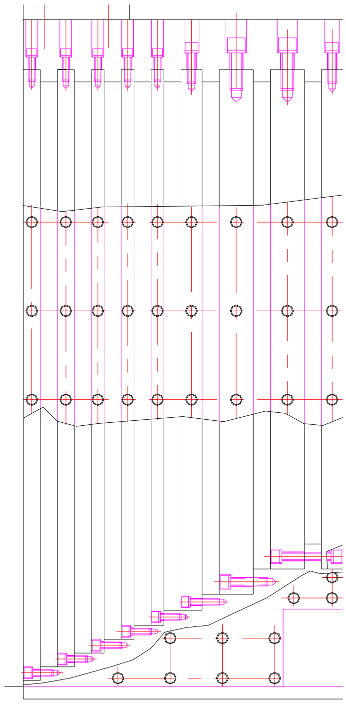

Fig.8.4-4 The end cap yoke and RPC arrangement

The end cap muon in each layer consists of 4 pieces at each end. There is a 20mm iron structure between every two pieces to increase its strength, as shown in Fig.8.4-5. For easy installation of RPC, each piece consists of 4 trapezoids of right angle RPC. The double layers of RPC are put in the same aluminum box, which can be pushed into the gap of the yoke from the left side or the right side, and then fixed in the gap of the yoke, to guarantee its position precision. The odd layer pickup strip uses horizontal direction readout, and the even layer in vertical direction.

The inner radius of overall muon identifier is 1700 mm, the outer radius is 2600 mm and the length is 4100 mm. The width of all the pickup strips is 40 mm. Thus 9 layers of the barrel muon detector need (32+48x3+64+96x4)x8=4992 electronics readout channels and 900 ㎡ RPC. The end cap needs 64×4×2×8= 4096 electronics readout channels and 700 ㎡ RPC. The entire muon identifier needs about 1600 ㎡ RPC and 9088 electronics readout channels.

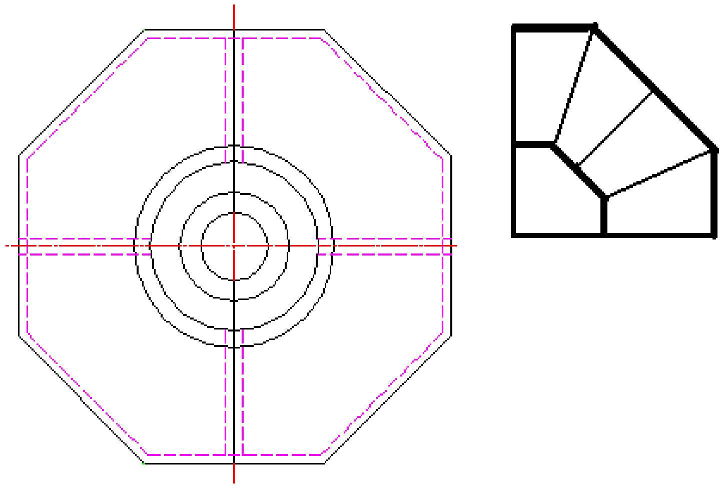

Fig.8.4-5 The structure of the end cap sketch map

RPC Structure

In the RPC design, as mentioned above, the pickup strips is 40 mm wide, the designed position precision for single layer RPC is $40mm/\sqrt{12}=12mm$. The other factor to be considered is the unit area counting rate of the BESIII muon detector. In BESIII, the momenta of particles produced by e^+e^- collision are mostly less than 1 GeV. There are only a few tracks in an event, typically two, but the event rate is around 3 KHz. If one track in every event on average can reach the muon detector (actually less), the muon track rate will be 3 KHz. As the total coverage area of the barrel muon identifier is about 45 ㎡, its counting rate in unit area should be 3000 Hz/45 ㎡≈70 Hz /㎡, which is basically equal to that of the cosmic ray background. The counting rate per unit area in the inner layer of the barrel muon counter should be less than 150-200Hz/㎡, hence there is no need to consider the influence of the counting rate on the detection efficiency. The other factor to be considered is the influence of noise which can be reduced by two means. The first one is to reduce the noise during the RPC design and production. The second one is to use the time gate to reduce the influence of noise. In the RPC design, improving the smoothness of the resistive plate surface can reduce the noise. In the electronics design, the width of the time gate is decided to be 100ns. The event rate of BESIII is estimated to be 3 KHz, so $100 \times 3000 \times 10^{-9}=0.03\%$ of the noise signal will be recorded with the event. The test of RPC shows that the noise rate is less than $1000Hz/m^2$, hence the probability of a noise hit matching with real tracks is very small, and will not affect physics analysis.

To ensure the reliability of the detector, the technique of covering the resistive plate surface with linseed oil should be avoided. Instead, a dense amine membrane pressed on the resistive plate surface will be used to improve the smoothness of the surface. For the equipment cost, the number of high voltage channels should be reduced and the working high voltage should be lowed, hence the noise level will be reduced. For the operation cost, relatively cheap gas should be used.

The resistive plate counter consists of two parallel sheets of 2.0mm Bakelite. The plates are separated by 2.0mm thick circular spacers made of insulating material, making a space for working gas. The places around the gap are sealed with T—shape spacer made of insulating material. After assembly, the RPCs are always be placed vertically or supported by a rigid flat surface to avoid deformation, with the environmental temperature and humidity relatively stable.

The outer surface of the Bakelite is coated with graphite. The surface resistivity is about 10^5—10^6 Ω/□. When the resistive plate is sprayed, the surface where spacers are mounted are covered, as shown in Fig.8.5-1. This is for the reduction of the dark current that may climb on the spacer surface. The surface resistance is chosen so that it will not shield the signal produced when a charged particle crosses RPC, and the resistance is small compared to the resistive plate resistance, thus high voltage can be distributed to the entire resistive plate surface.

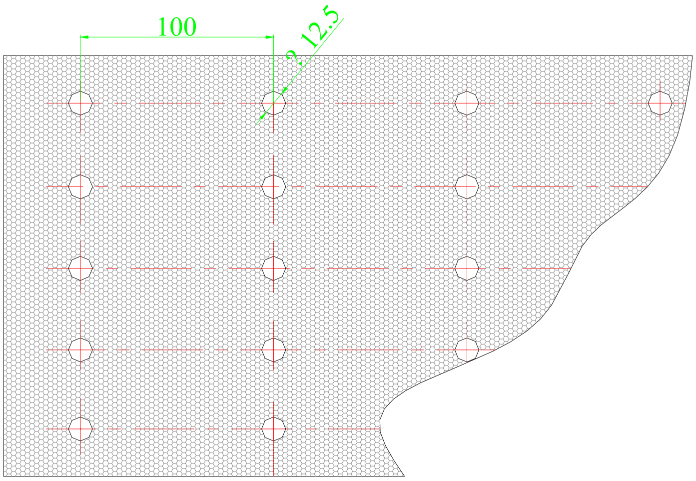

Fig.8.5-1 Sketch map of resistive surface sprayed with graphite

The two layers of RPC and one layer of copper pickup strip constitute a superlayer. The cut-view of an end cap superlayer module is shown in Fig.8.5-2. The cross section of a superlayer module is shown in Fig.8.5-3.

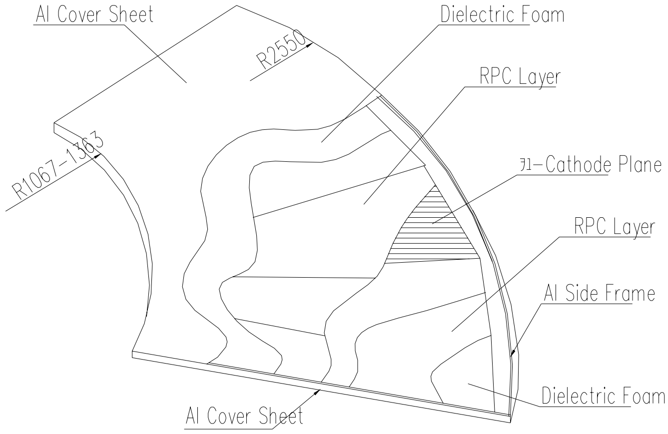

Fig.8.5-2 Cut-view of an endcap superlayer module

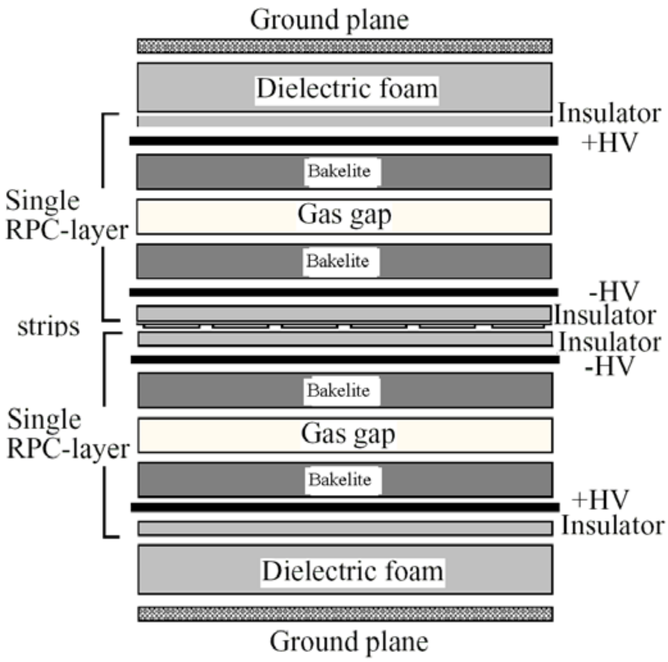

Fig.8.5-3 Cross section of a RPC superlayer module

Two layers of RPC and one readout-plane sandwich are enclosed in an aluminum box with a thickness of about 32 mm. Same as the RPC and pickup strip, RPC and aluminum box is electrically insulated with a double layer of 0.20 mm thick mylar. The geometry of the pickup strips is chosen so that they behaves as a transmission line with a characteristic impedance of about 50 Ω to minimize signal reflections at the junction with the twisted-pair readout cable, and ensure the electronic readout.

Comparing with the one-gap design, the double-gap one provides redundancy, and it can increase the efficiency to more than 98% from 90%—95%. Especially, the interlaced RPCs of Barrel will reduce the dead space, and the superlayer can continue to work even one of the two RPC may develop some problem.

However the double-gap design would increase the superlayer thickness. To ensure the RPCs to fit in the limited gap，it is better to control the superlayer thickness to 32mm.

From the experience of BaBar, Belle and L 3, temperature is one of the factors that affect the RPC lifetime. When the temperature is too higher, the bulk resistivity of the Bakelite will decrease, the dark current will increase and the detection efficiency will decrease. If the Bakelite surface is coated with a layer of linseed oil, the effect will be even worse. Therefore, it is very important to ensure the detector working in a suitable temperature range.

High Voltage System

For the high voltage system of the BESIII muon identifier, we decide to separately apply positive voltage to the anodes and negative voltage to the cathodes. The modules typically operate with a total gap voltage of 8 KV. This approach minimizes the insulated layer thickness, and minimizes the potential to ground. Though this scheme needs two channels of high voltage for one RPC, the total price of such a configuration for each channel, including high voltage, high voltage connector and cables, is cheaper.

From the operation experience of BELLE, BaBar and other experiments, including our own test result, the dark current of RPC is about 1 μA/m², and the working current of each high voltage channel is better not to exceed 100 μA. So each layer of the barrel RPC uses one group of high voltage supply units, one positive and one negative. For the end cap, each end is divided into 3 groups, with 3 layers forming one group. A total of 16 groups of high voltage are needed, include 16 positive and 16 negative.

Since the muon identifier is very difficult to be accessed and repaired after it is installed, a distribution board for the HV supply, with protective resistors on the board to restrict leakage current for each channel is introduced. When the leakage current of a particular RPC increases, the protective resistance can restrict the leakage current, and the other RPCs can still work properly, after re-adjusting the current TRIP value of the HV unit.

Gas System

In choosing the gas mixture, many factors such as safety, environmental protection, price, and detector stability and efficiency should be considered.

According to the experience of BELLE, BaBar and other experiments, argon＋F134A＋isobutane is a good choice. Considering the fact that isobutane is combustible, and the nonflammable limit for isobutane is about 12%, and that the prices of isobutane and F134A are high, the proportion of these two gases should be reduced as much as possible. We will investigate the possible replacement of F134A with carbon dioxide, or adopt the scheme of BELLE, by replacing isobutane with the mixture of n-butane and isobutane. Fig.8.7-1 shows the counting rate versus different gas mixtures, Fig.8.7-2 shows the efficiency versus different gas mixtures and Fig.8.7-3 shows the dark current versus different gas mixtures. From these figures, it is found that increasing argon content or decreasing isobutane content can reduce the working voltage, but shorten the HV working range. Conversely, the range will be lengthened and the working voltage increased.

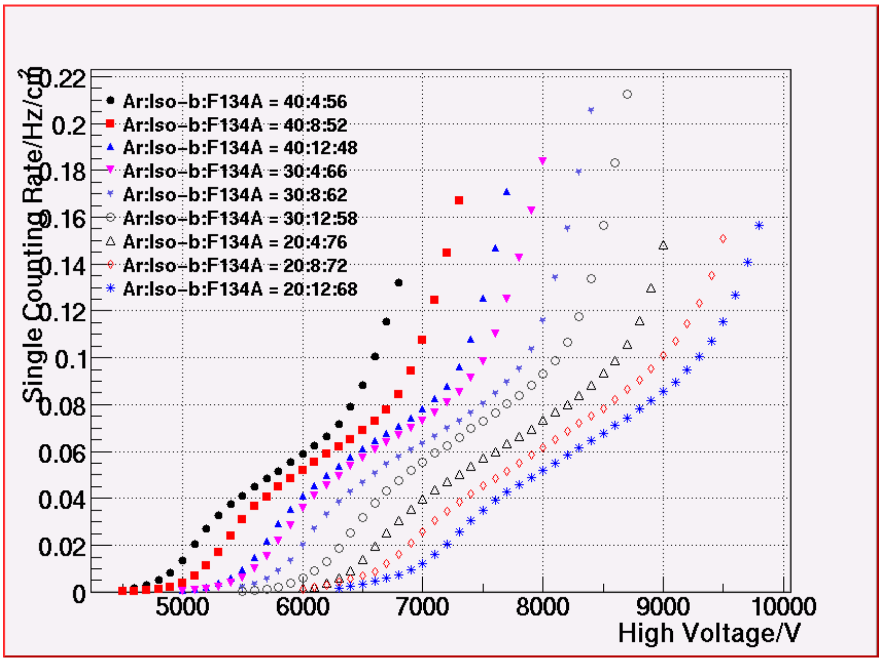

Fig.8.7-1 The counting rate versus different gas mixtures

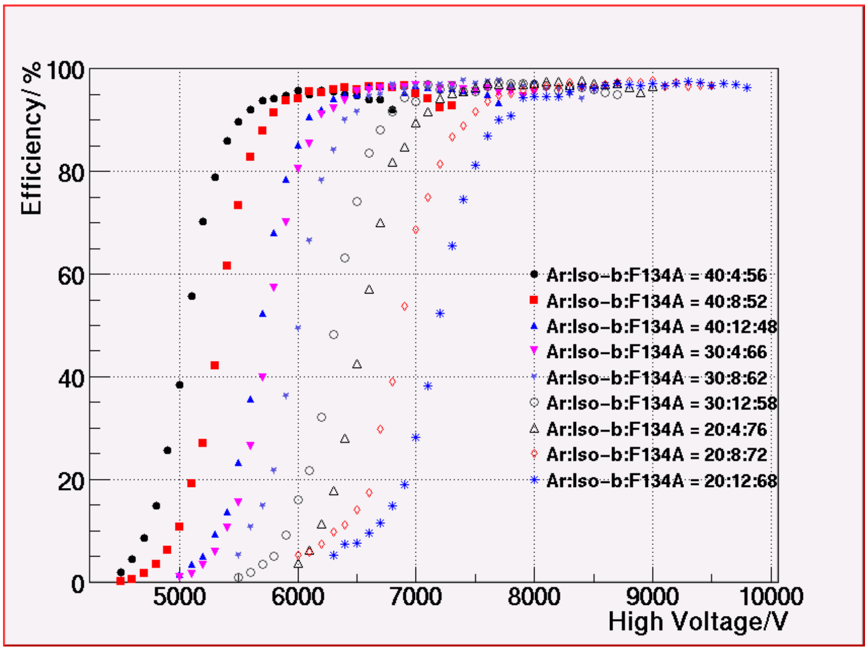

Fig.8.7-2 The detector efficiency versus different gas

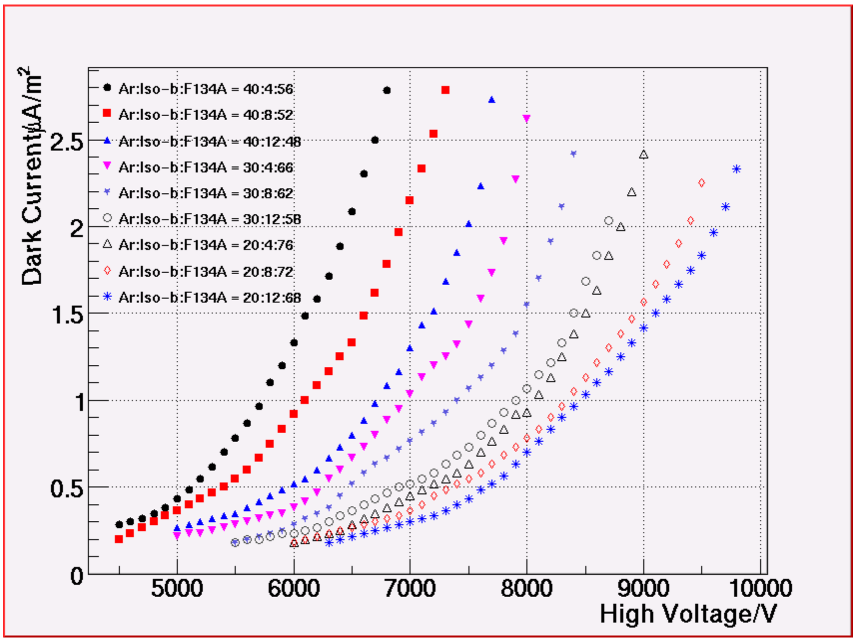

Fig.8.7-3 The dark current versus different gas

Gas is also a major factor that affects detector's lifetime. As the water in F134A and isobutane can increase the dark current and decrease the detection efficiency, they must be de-moisturized before entering the detector. Another factor is the alkenes in isobutene. They can be absorbed on the detector surface, resulting in the increase of the noise and dark current, and the decrease of the detection efficiency.

A gas system for the BESIII muon identifier was designed as shown in Fig.8.7-4. There are two separate tanks of bottles for each type of gas. If one set of bottles is empty, the supply line automatically switches to the other, to guarantee the continuity of gas flow. Gas filters and desiccators are installed in the gas line to reduce the moisture and harmful gas that can affect detector performance. The gas control system adopts the mass flow control system manufactured by MKS company, which have be used by BESII our RPC prototype test. The flow rates can be automatically controlled and monitored by computer and the gas flow is inter-locked with the HV system. The flow rate is controlled to approximately one volume change per day.

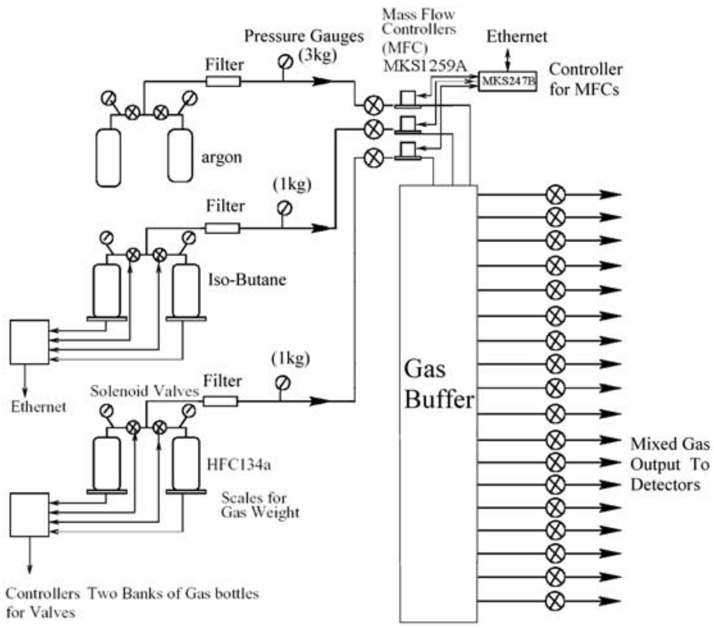

Fig.8.7-4 The sketch map of gas system

The gas distributing system adopts junction row scheme to distribute the gas. Each RPC gas volume use one individual gas pipeline. So that all other PRCs can still work if one pipeline to a RPC is closed due to the leakage.

Expected Performance

The total solid angle coverage of the barrel and end cap is 0.89, with the outermost layer of the barrel reaching 0.75 and the innermost layer 0.60. Its single layer position resolution in Φ direction is 1.2 cm. To reduce the electronics cost, the ϕ and Z position are measured alternatively layer by layer. The minimum momentum of muons that can be detected is about 0.35 GeV. For the muons with the momentum larger than 0.4 GeV, the detection efficiency can reach 95% at various incident angles.

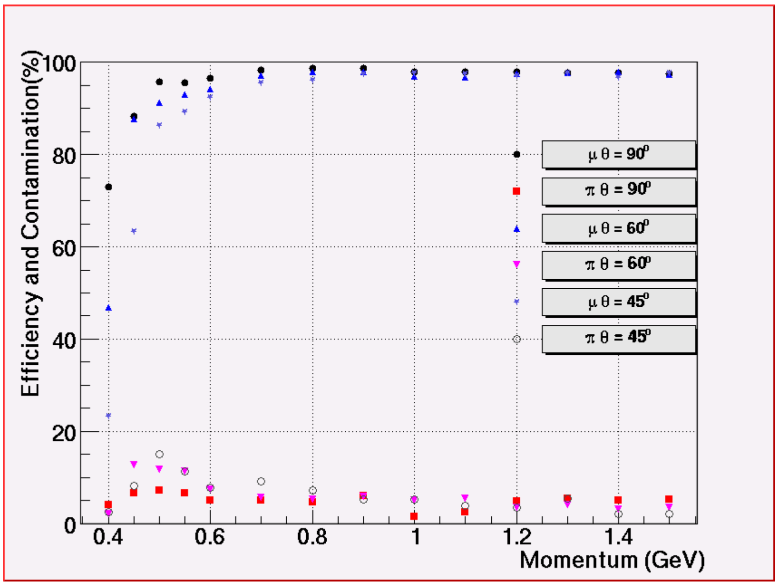

Fig.8.8-1 Muon separation efficiency and contamination from pion versus momentum

Through Monte Carlo simulation, the muon detection efficiency and pion contamination for muons are shown in Fig. 8.8-1. From this figure, muons with a momentum of 0.4-1.2GeV and with different incident polar angles can reach a detection efficiency of more than 95%, and a pion puch-through rate of 10% for a momentum at 0.4-0.6Gev, 4-8% for 0.6-0.9GeV and 4% for more than 0.9GeV. At the incident polar angle of 90 degree and nearby, the pion and muon with the momentum of 0.35GeV can be identified. Due to limited funding and space, the muon identifier cannot have more layers, so K_L cannot be identified with a reasonable efficiency.

Reference

[1] Development of Resistive Plate Counters. R.Santonico Nucl.Instr. And Meth. 187(1981)377

[2] Proceedings of the International Workshop on BESIII Detector, IHEP, Beijing, China, October 13-15,2001

[3] IHEP-BTCF Report-03 October, 1996

[4] Resistive Plate Chamber, G.Iaselli Università di Bari, Italy, 22 Jan. 2002

[5] The CMS Technical Proposal, CERN/LHCC 94-38, 15 December 1994

[6] Aging Basics — Early Developments Since the 1986 Aging Workshop, J.Va'vra, SLAC-PUB-9062 November 2001

[7] The K_L/μ Detector Subsystem for BELLE Experiment at the KEK B-factory, BELLE preprint 99-04, 8 October 1999

[8] Test of Different Gas Mixtures for RPC Detectors, BaBar Note #369 May 8, 1997

[9] Beijing Electron Positron Collider Beijing Spectrometer Study report, Institute of High Energy Physics, Chinese Academy of Sciences, March 10,1989

[10] The collection of Beijing Spectrometer Detector Prefabricated Research Information, Institute of High Energy Physics, Chinese Academy of Sciences, November, 1987

[11] The Simulation Report of Electron Positron Collider, Beijing University Technical Physics Department, Zhengyun YOU, etc., December 14, 2001.

[12] The Preliminary Suggestion of Using RPC to Make μ Detector, Beijing University Technical Physics Department, November 7, 2001

Superconducting Magnet

Overview

The BESIII solenoid magnet is designed to provide an axial magnetic fie1d of about 1.0T with a good field uniformity over the tracking volume. Particle detectors within this volume will measure the trajectories of charged tracks emerging from the co1lisions. Particle momentum is determined from the measured curvature of these tracks in the fie1d. The iron absorber plates of the muon detector provide the magnetic flux return.

Based on the physics requirements, the main drift chamber should have a high momentum resolution which can be improved by reducing the multiple Coulomb scattering and by increasing the magnetic field. On the other hand, if the magnetic field is too high, more low-momentum particle would circle around inside the drift chamber and become difficult to measure. Considering all factors, we selected 1.0T as the field of BESIII solenoid magnet.

The field uniformity within the tracking volume should be better than 5%, and the accuracy of field mapping should be better than 0.1%.

Design of Superconducting Magnet

Basic Parameters and Calculations

Following similar magnets in other HEP laboratories, we decide to adopt a single layer of coil using indirect cooling method, and pure aluminum-stabi1ized NbTi/Cu(1:0.9) superconductor in the BESIII superconducting magnet. The overall length of the magnet is 3.91m, inner diameter 2.75m, outer diameter 3.4m, coil effective length 3.52m@4.2K, and the mean diameter of the coil 2.97m@4.2K.

Suppose the nominal current I=3000A at $B_0 = 1T$, from $B_0 = \mu_0 nI$, we get n≈266 turns in the one meter long coil. Cable width in the axial direction is 3.7mm. Considering the insulator thickness, we get the real number of turns of cables is 902 turns. Since the current will be reduced by the joints inside the winding, we define the nominal current as 3250A.

The energy stored by the solenoid is

$E = (\frac{1}{2} H \cdot B)V = \frac{1}{2} \cdot \frac{B^2}{\mu_0} \cdot S \cdot l = \frac{1}{2} \cdot \frac{B^2}{\mu_0} \cdot \frac{\pi D^2}{4} \cdot l$ = 9.5 MJ. From

$\Phi = B \cdot S \cdot n = B \cdot \frac{\pi D^2}{4} \cdot n$=6063.6WB, $\frac{d\Phi}{dt} = L\frac{dI}{dt}$, $L = \frac{\Phi}{I}$, we get L= 2.1H.

Since the limit of the maximum temperature rise is 70K after a quench, the enthalpy difference of the cable material can be calculated and the height of the cable is determined to be 20mm.

To take into account the hoop stress, an aluminum cylinder using material A5083 is necessary. The thickness of this support cylinder calculated to be 20mm. The total weight of the cold mass is around 4 tons, including the cable, the support cylinder, the end stop ring and the cooling tube.

The yoke consists of barrel yoke, end yoke and pole tip. Nine layers of muon chambers will be interleaved inside the barrel yoke, the first one is located between the outer vacuum vessel and innermost barrel yoke. In the end yoke there are eight layers of muon chambers.

The general parameters of the BESIII detector solenoid are summarized in the table below.

Table 4.9-1 Basic parameters of the BESIII superconducting magnet

Cryostat	
Inner radius	1.375m
Outer radius	1.7m
Length	3.91m
Thickness of Inner vessel	6mm
Thickness of outer vessel	16mm
Thickness of end vessel	32mm
Coil	
Mean diameter	2.97m@4.2K
Length	3.52m@4.2K
Conductor dimension	3.7mm*20mm
Electrical parameters	
Central field	1.0T
Nominal current	3250A
Inductance	2.1H
Stored energy	9.5MJ
Cold mass	4 tons
Radiation thickness	$2.24X_0$
Cool down time	≤7 days
Recovery time	≤1 day

From the nominal current 3250A(@1T,4.5K), we select the cable working current of 6800A(@4T,4.2K). Since the typical critical current density Jc is $2600A/mm^2$(@4T,4.2K) for NbTi conductor(data from the FURUKAWA Ltd.), the area of NbTi is $2.62mm^2$, corresponding to the ratio of NbTi/Cu as 1:0.9, and the area of the superconducting wire section is 4.97mm^2. The final size of the superconducting conductor is 1.26 x 4.2 mm^2, with a cross section view as shown in Fig. 9.2-1.

The conductor dimension is key-stoned in order to realize the flat shape after pre-bending, with a thickness difference of 60 micron at narrow and wide ends. For the winding procedure for this kind of magnet, we select the bobbin-less technique. During the fabrication, great attention should be paid to the tightness between the cable and the supporting wall, ground insulation and joints.

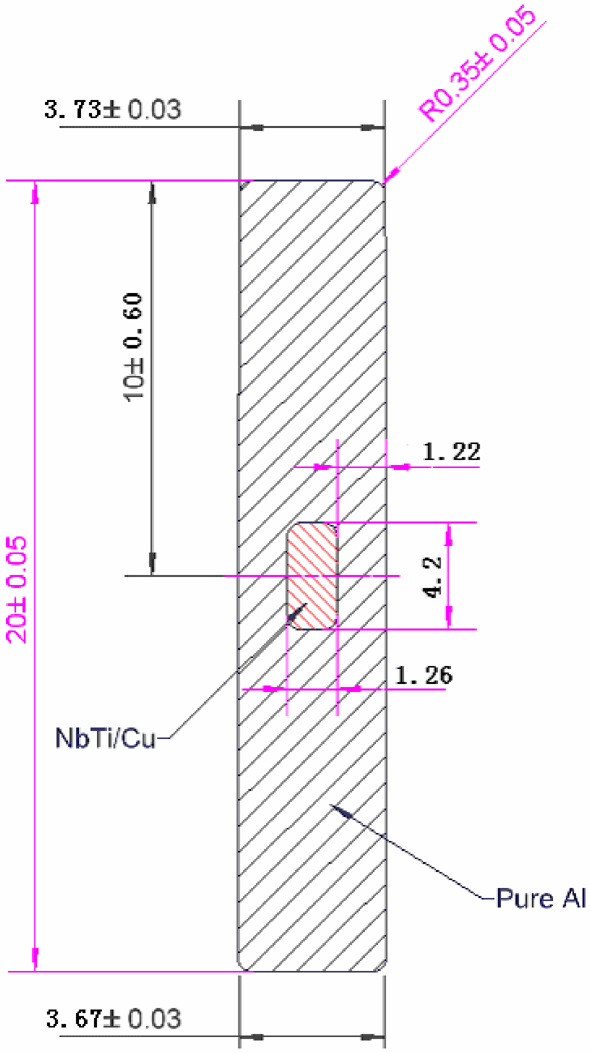

Fig.9.2-1 Cross section view of superconducting cable

Magnetic Field Analysis

There are two main parameters, one is the uniformity in the tracking volume, and the other is the fringe field along the beam axis outside the detector. We investigated various iron configurations. The latest version for iron configuration is: the thickness of end yoke plates layer 1~9 is 40, 40, 30, 30, 30, 50, 80, 80, 50mm, the barrel yoke layer 1~9 is 30, 30, 30, 40, 40, 80, 80, 80, 150mm, with pole tips at each side.

The field distribution presented in the following figure shows that the uniformity in the tracking volume is around 2%. This value will reach up to 13% by taking into account the effect of anti-solenoid. The fringe field remains 54 gauss at a distance of 3.5m from the interaction point. It will decrease sharply to less than 50 gauss by adding some iron material in the gap between the barrel yoke and end yoke. To reduce the fringe field near the ISPB and Q1 magnet, some iron shield structure have been studied.

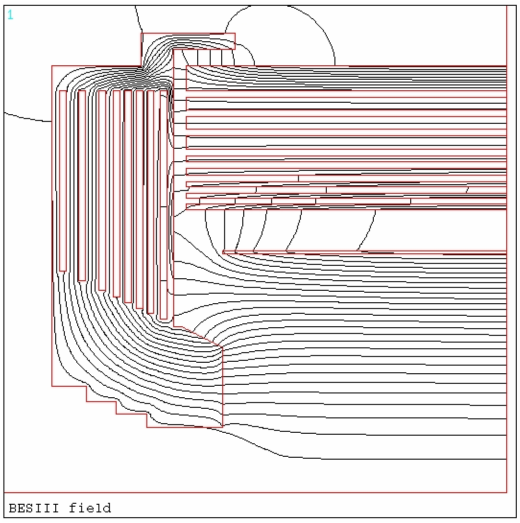

Fig.9.2-2 Flux of magnetic field

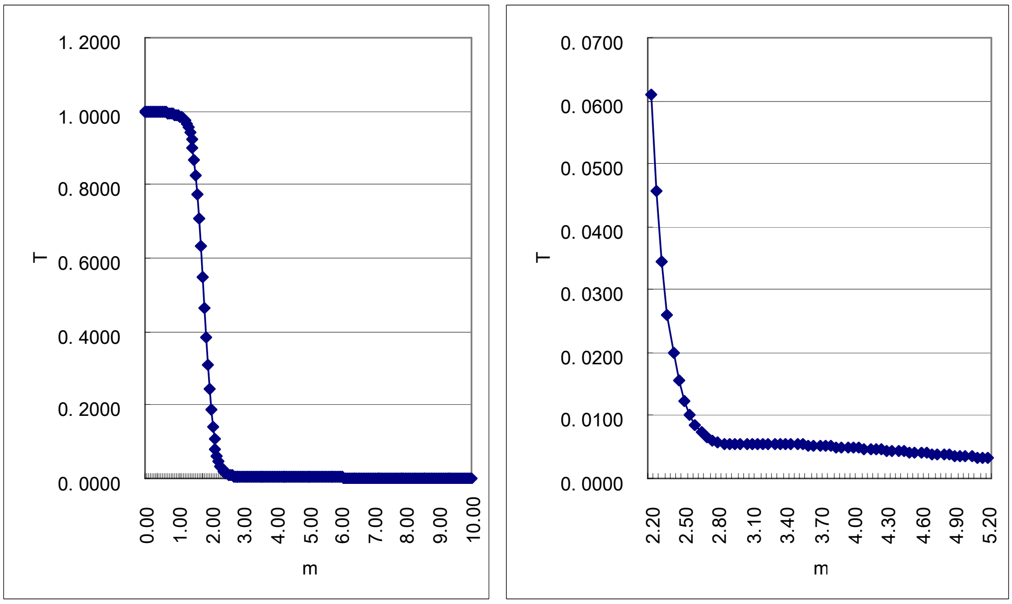

Fig.9.2-3 Bz as a function of Z along the beam axis

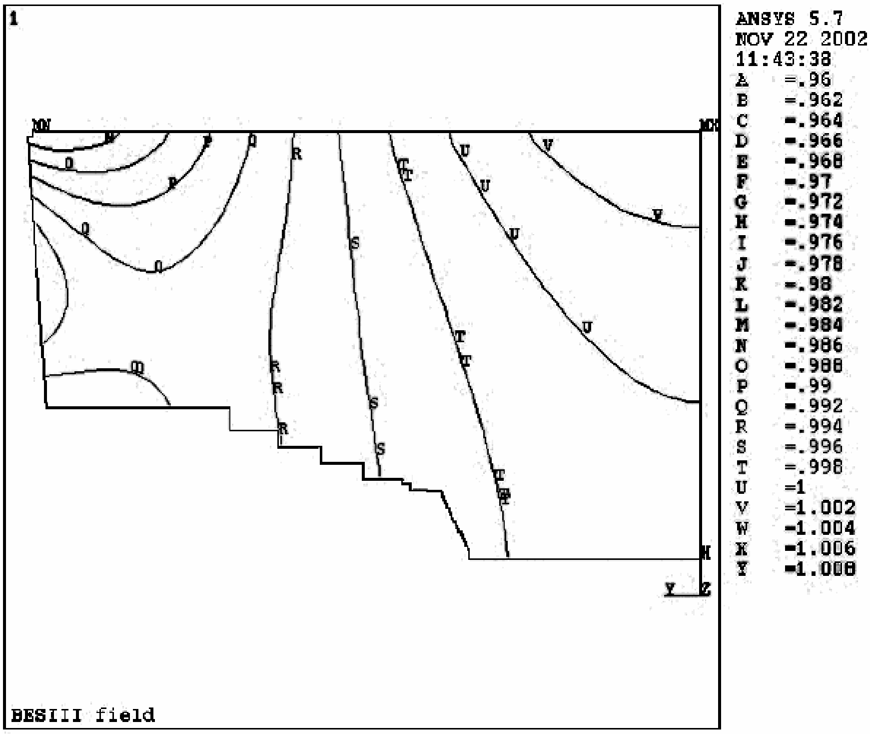

Fig.9.2-4 The field uniformity in the tracking area

Other Analysis of Coil

The results of FEA reveals that the stress in the coil increases from the end position to the middle, the maximum hoop stress in the coil is 19 MPa, and the maximum axial stress is 3.3 MPa.

The ampere heat of the joints inside the coil is about 2.54mW when using 99.993% purity aluminum as the stabilizer. In order to detect a quench, usually the voltage between the two ends of the coil is monitored. Here is the relationship of the voltage and the length of the quenched area.

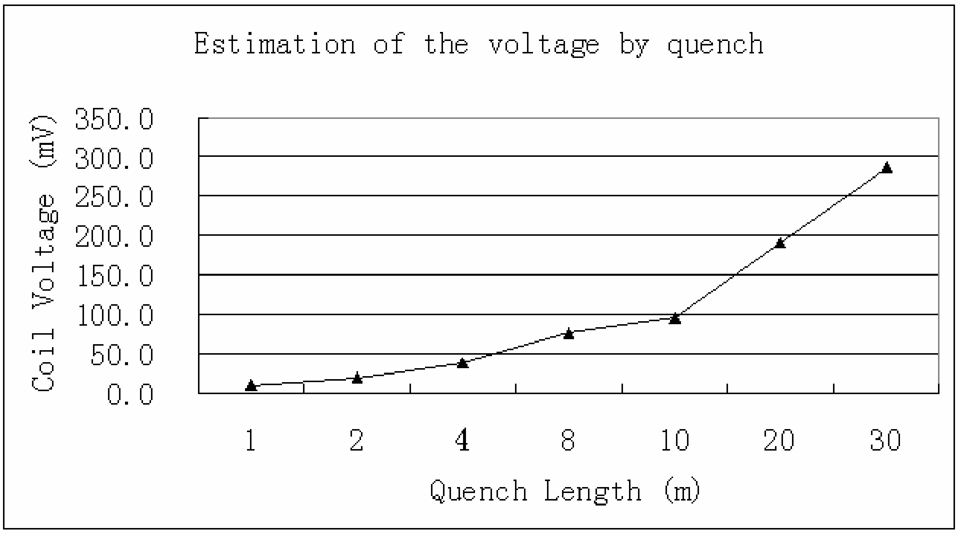

Fig.9.2-5 Voltage versus length of quench area in the coil

Vacuum Vessel

Design of Vacuum Vessel

The coil is suspended in the cryostat. In order to ensure that coil has a long term stability at 4.2K, we must take into account, factors such as gravity, electromagnetic force, thermal stress, etc. In/out channels should be designed at one end of the cryostat for power-leads and tracing tubes, and then thermal leakage should be minimized.

The cryostat includes the inner cylinder, the outer cylinder and the endplates. According to the design guide of the pressure vessel and cryogenic vessel, the buckling stability and the mechanical strength is calculated by using theoretical and FEA. The stainless steel SUS304 can be selected as the material, the thickness of the inner vessel is 6mm，the outer vessel 16mm, and the endplates 32mm. The fabrication process includes roll, weld, assembly, pressurize and leak hunting. The maximum stress 34.8Mpa and maximum distortion 0.18mm will be at the center of inner vessel.

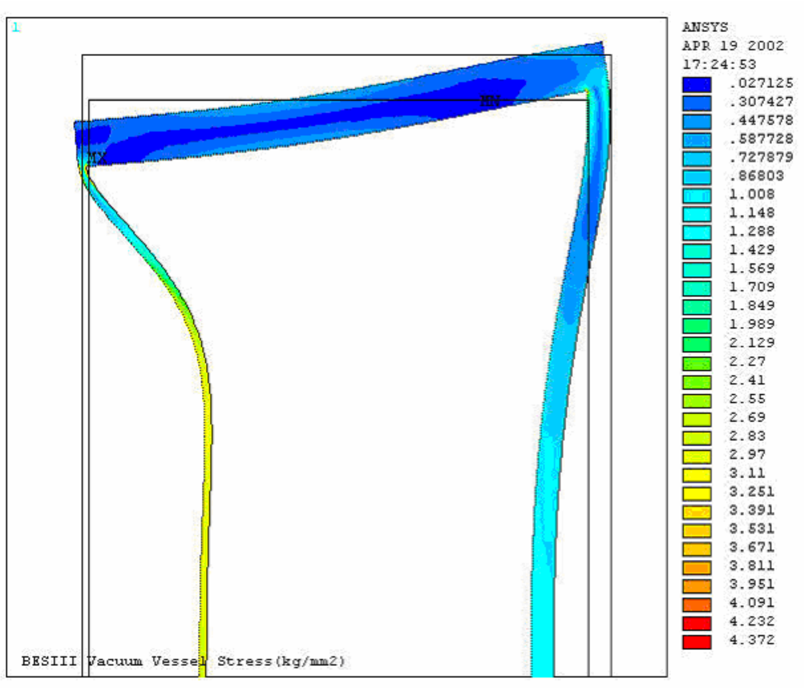

Fig.9.3-1 Stress and deformation of the near end plate（2D 1/2 Model）

Coil Support

The coil support system has to ensure a precise and rigid suspension of the cold mass inside the vacuum vessel. The loads to be supported are the self-weight of the cold mass and the magnetic forces due to the decentering of misalignment of the coil with respect to the return yoke. The design also takes into account the contraction of the coil during cool down and its deformation under magnetic forces, with enough strengths and smallest heat conduct. The support system consists of a set of rods made of GFRP. There are a total of 24 radial and axial rods, half at each end.

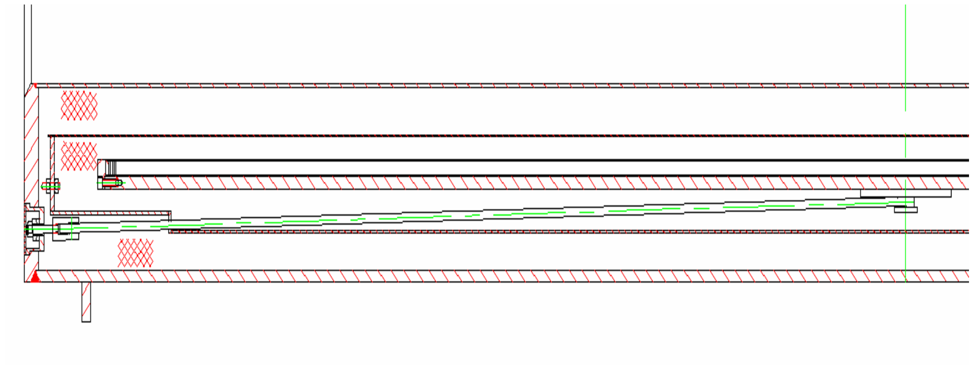

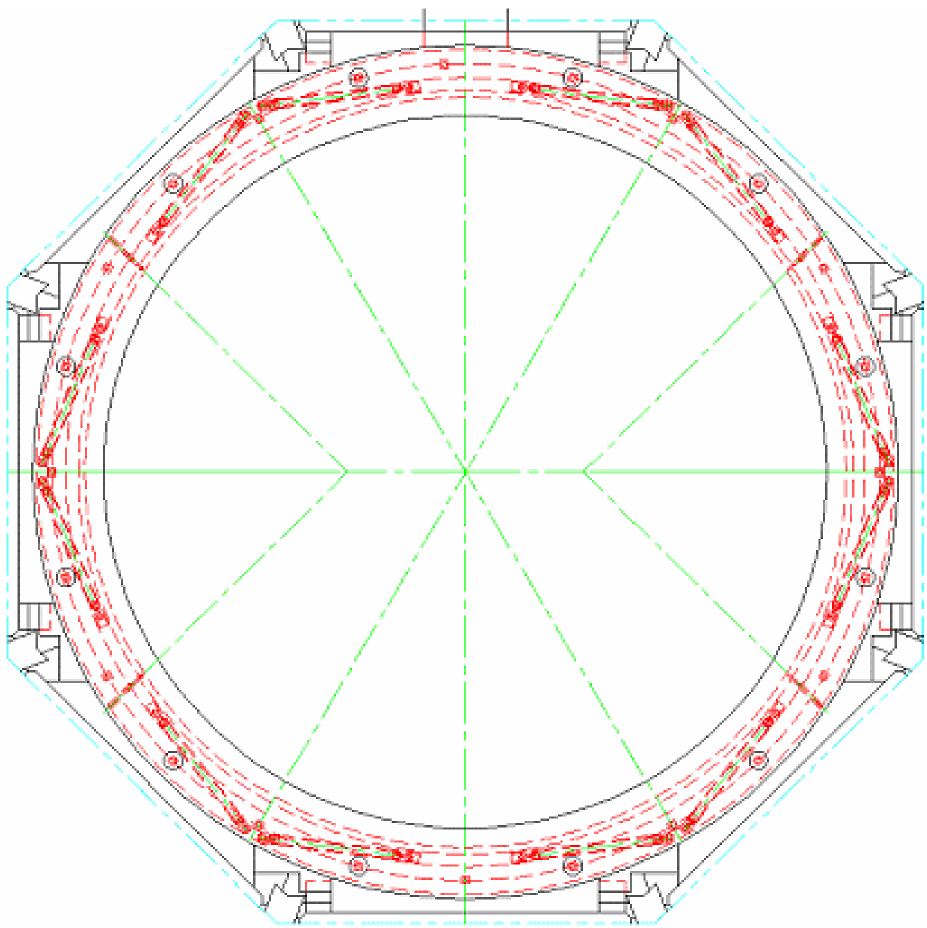

Fig.9.3-2 The coil axial/radial support rods

Magnet Weight & Radiation Thickness

Table 9.3-1 and 9.3-2 list the weight and material thickness of magnet components.

Table 9.3-1 Weight of the BESIII superconducting solenoid magnet

Parts	Weight(kg)
Coil	3735
Cryostat	8113
Shield	938
MLI	200
Support rods	83
Cooling pipe	113
Chimney/Service port	2298
Total	*15480*

Table 9.3-2 Material thickness of the BESIII superconducting magnet

Material	Thickness	Radiation length		Material
	X, mm	X_0, mm	X/X_0	Ratio
SC cable, NbTi/Cu	4.2	14.3	0.29	13.13%
Stablizer, Al	15.8	88.9	0.18	7.95%
Support cylinder, Al	20	88.9	0.22	10.06%
LN_2 radiation inner shields, Al	4.5	88.9	0.05	2.26%
LN_2 radiation outer shields, Al	4.5	88.9	0.05	2.26%
MLI, Fiber glass	44.4	286	0.16	6.94%
Glass/polyimide/epoxy	2	286	0.01	0.31%
Inner vacuum vessel st. steel	6	17.7	0.34	15.16%
Outer vacuum vessel st. steel	16	17.7	0.90	40.42%
Quench propagator strip, Al	1	88.9	0.01	0.50%
Lhe/LN_2 cooling tube, Al	2	88.9	0.02	1.01%
Total, X_{tot}			2.24	100%

Cryogenic System

The cryogenic system for the superconducting magnet consists of a helium refrigerator/liquefier, liquid and gas transfer lines, liquid and gas storage, and a nitrogen system. The major components include: the compressors, oil removal systems, cold box and control system.

The concentric wave pipes connect coil cryogenic system and helium refrigeration system, and the whole system is measured and controlled by computer.

Heat Load

The system heat load is mainly caused by cryostat, chimney, current leads, radiation, support rods, valves, pipe joints, and sensor wires, as listed in Table 9.4-1.

Table 9.4-1 Heat load estimation

Items of Heat Load	77 K	4.5 K
Caused by the support rods in cryostat	26.527 W	1.038 W
Caused by the radiation in cryostat	73.801 W	3.236 W
Caused by the current leads	——	7.920 W + 0.421 g/s
Caused by the radiation in chimney & SP	10.025 W	0.407 W
Caused by the support rods in chimney & SP	3.900 W	0.022 W
Caused by the bayonet and valves in SP	46.000 W	13.000 W
Caused by the measuring wires	5.311 W	0.831 W
Total	165.5 W	26.46 W + 0.421g/s
Adopted heat load（×1.5）	248 W	39.7 W + 0.63 g/s

Helium and Nitrogen Pipes

From the estimation on heat load with a margin factor of 1.5，the mass flow rates of nitrogen and helium is determined to be 1.94 g/s (~ 8.64 L/h) for nitrogen and 10g/s for helium whose inlet pressure is 0.285MPa and temperature is below 5.5K. Based on the mass flow, the inner diameters of nitrogen and helium pipes are also decided to be 14mm for nitrogen and 16mm for helium. Taking into account the quench mode, the inner diameter of helium pipe in the coil cryostat is increased to 25mm. In this case, the maximal pressure drop in nitrogen pipe is expected to be 0.12MPa and the pressure drop will be 3500Pa during the normal operation. Concerning the helium pipe, the maximal pressure drop is 0.26MPa, and the normal pressure drop 2900Pa, and the quench pressure drop 4100Pa. Diameter and height of the valve box are 1500mm and 2100 mm respectively.

The system control and flow chart is shown in Fig.9.4-1, and main dimensions of the valve box and chimney are shown in Fig.9.4-2.

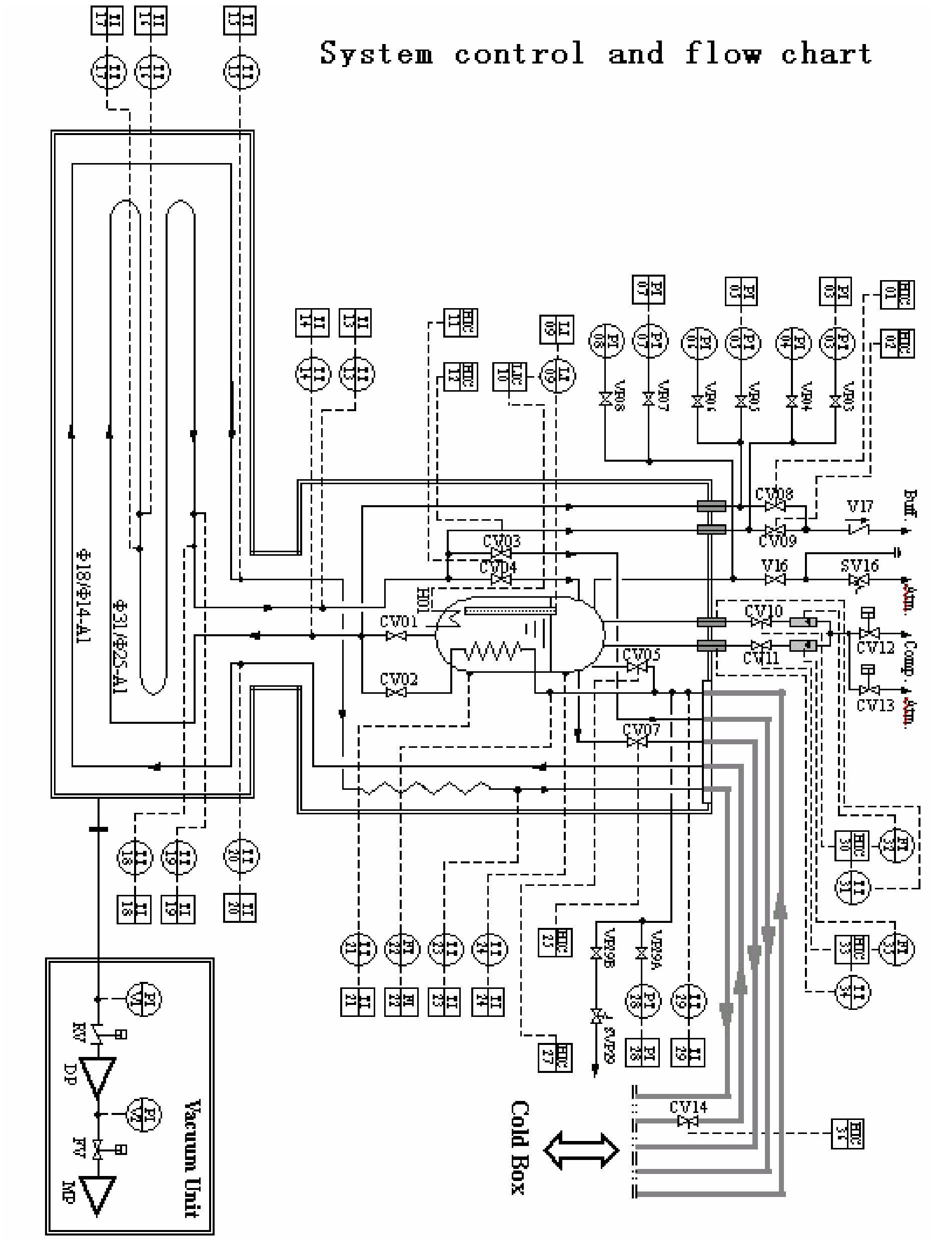

Fig. 9.4-1 System control and flow chart

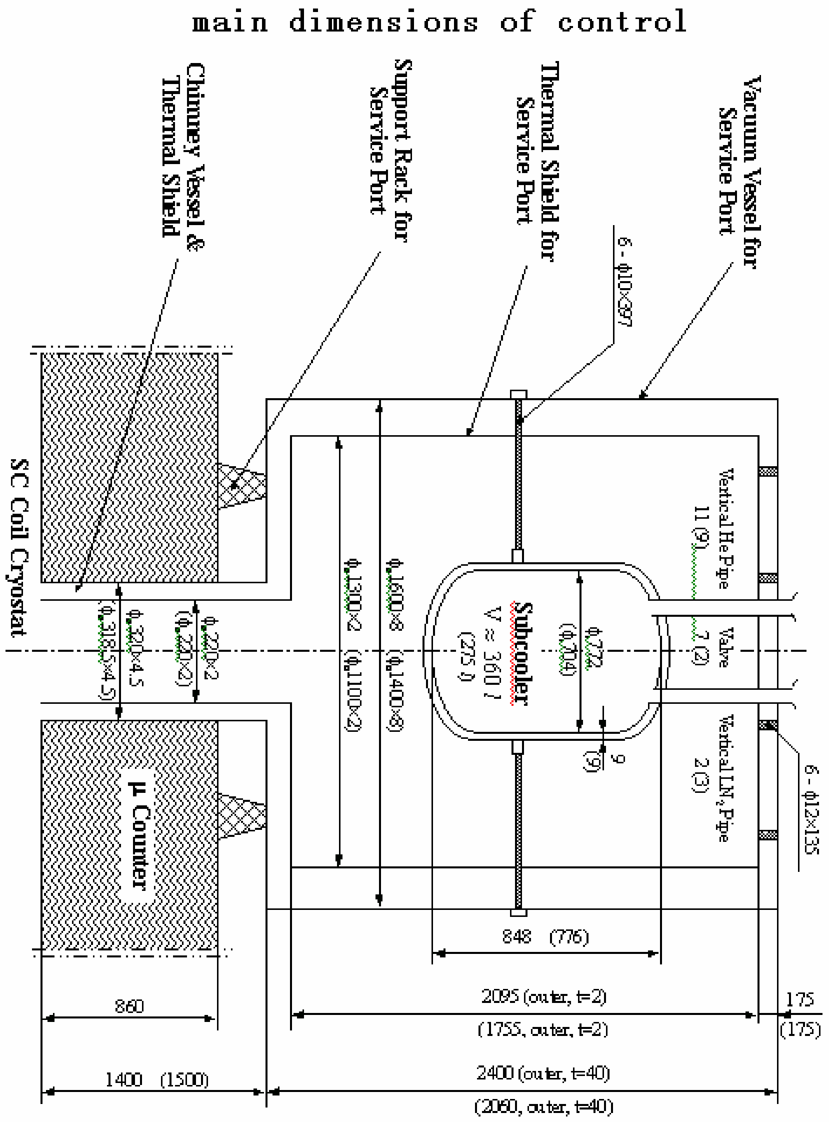

Fig.9.4-2 Main dimensions of the valve box and chimney

Operation Modes of the Cryogenic System

There are nine operation modes designed for BESIII cryogenic system: gas changing mode, cool down mode I, cool down mode II, normal operation mode, quench mode, quench recover mode, refrigerator failure mode, warm-up mode and shut down mode. The detailed operation of the system for each mode is presented in the table below.

Table 9.4-2 Operation Modes of the Cryogenic System

Control Scheme of the Cryogenic System of BESIII for Nine Operation Modes

Valves	Before Start	Changing* or Charging	Cooldown I	Cooldown II	Normal (η)	Quench (from η)	Recovery (from Quen.)	CP works ab. (from η)	TB Works ab. (from η)	Warmup (from η)	Shutting Down
CV01	100% C	→	→	→	→	→	→	② 100% O	② 100% O ④ 100% C (after TBs start)	→	→
CV02	100% O	→	③ 100%C, 5%/s ④ CAS. TIC TI18	①60%O, 1% ②50%O, 1% 30%O, 1%/s after V04 FO	① FIC22 SV=12g/s	① 100% C	② 30% O, 0.5%/s	② 100% O 5%/s	④30% O, 1%/s (after TBs start)	①MAN, MV=C ②30%O, 1%/s ⑤ CAS. TIC TI18	① 100% O
CV03	100% C	③ 10% O, 1%/s	① 100% O, 5%/s	100%C, 5%/s TICB <20K	→	① 100% C	① 100% O, 1%/s	① 100% C	① 100% O	③30%O, 1%/s ④100%O, 1%/s	① 100% C
CV04	100% O	③ 100% C, 1%/s	→	15%O, 1%/s TICB <25K 100%O, 0.5% TICB <20K	→	① 100% C	→	① 100% O	① 100% C, 5%/s	③70%O, 1%/s ④100%C, 1%/s	① 100% O
CV05	100% C	② 15% O, 1%/s	→	①30%O, 1% ②35%O, 1% 20%O, 1%/s after V04 FO	→	①CAS-MAN 30% O, 5%/s	→	① 100% O 1%/s	③ 100% C ⑤ 20% O, 1%/s	①M100%C,1% ②PIC07, .35atg ④15%O, 1%/s	① 100% C
CV07	100% C	① 100% O, 1%/s	→	CAS. PIC07 SV=0.12atg after V04 FO	→	→	→	① 100% C	→	① 100% O	① 100% C
CV08	100% C	⑤ 20% O* ⑥ 100% C*	→	→	→	① 100% O	① 100% C	① 100% O	→	→	→
CV09	PIC03 SV=10.5atg	⑤ 20% O, 5%/s	① 100% C, 5%/s	→	① PIC03 SV=1.0atg	① 100% O	① 100% C	① 100% O	→	① AUT-MAN 100% C	PIC03 SV=10.5atg
CV10	100% C	④ 15% O, 5%/s	① 100% C, 5%/s	③ FIC32, SV=50SLPM	CAS. TIC31 SV=190K	① FIC32, =150SLPM	① FIC32, SV=50SLPM	① FIC32, =100SLPM	① FIC32, =100SLPM ④100%C(aTBs)	① 100% C in turn	→
CV11	100% C	④ 15% O, 5%/s	① 100% C, 5%/s	③ FIC35, SV=50SLPM	CAS. TIC34 SV=190K	① FIC35, =150SLPM	① FIC35, SV=50SLPM	① FIC35, =100SLPM	① FIC35, =100SLPM ④100%C(aTBs)	① 100% C in turn	→
CV12	100% C	④ 100% O	② 100% C	③ 100% O	100% C when flow is low	→	→	100% C when flow is low	→	① 100% O in turn	① 100% C
CV13	100% C	⑤ 100% O* ⑥ 100% C*	→	→	100% O when flow is low	→	→	100% O when flow is low	→	① 100% C in turn	→
CV14	100% C	→	⑥10% O, 1% (TBs start)	① TIC23	→	→	→	→	→	④ 100% C	→

Note: TICB is the temperature of the return flow just flowing into the Cold Box

Power Supply and Quench Protection

The power supply for the solenoid is a DC stabilized current supply with low voltage and high current, and should be adjusted slowly and evenly. In order to have a steady field, the supply should have a very small ripple.

Quench protecting equipment should be installed, which consists of magnet sensors, instrumentation modules, line breakers and dump resistor.

For safety reasons two breakers which open both polarities of the power supply are used to quickly separate the magnet from the power supply for easy checking of the insulation and protect the power supply against the high voltage developed during the energy dump.

The power supply is designed to be 10V，4000A, with a current ripple $\leqslant 1\times10^{-4}$ p-p，voltage ripple <=5×10^{-3}p-p，and current stability <=1×10^{-4} within 8 hours. Current is sent from power supply room to the connection between coil and chimney along a pair of copper drainage.

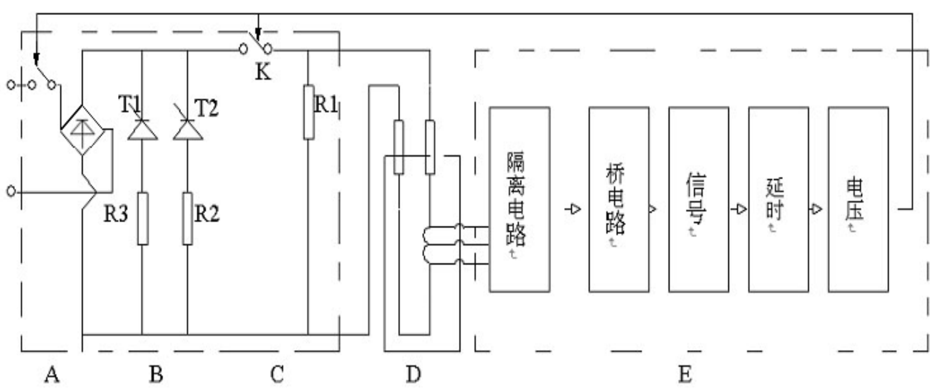

Fig.9.5-1 Circuit of power supply and quench protection

In addition, a substantial amount of instrumentation is required to monitor the operational status of the magnet and to provide diagnostic data. The following table gives a list of diagnostics and instrumentation required.

Table 9.5-1 Diagnostic instrumentation in the BESIII solenoid

Element	Coil	Radiation shield	Support rods	Valve box & Chimney
Voltage taps	7			8
Heater	2			
Temperature sensors				
Pt(300K-4.2K)	2	14		
Cernox	8			
Strain gauge(pair of Φ,z)	6		48	
Position sensor(z)	2			
Hall sensor				2
Total	27	14	48	10

The Pt and Cernox sensors are used to measure temperatures from LHe to R.T. Strain gauges are installed to measure stress of suspension rods. Heaters are used for quench test. In addition, vacuum gauge should be installed near the vacuum pump port. The total is about 100 sensors and 400 lead wires.

Vacuum System

In order to ensure thermal insulation of coil, the vacuum should be kept at 10^{-6}~10^{-7}mbar by using molecular and machinery pumps.

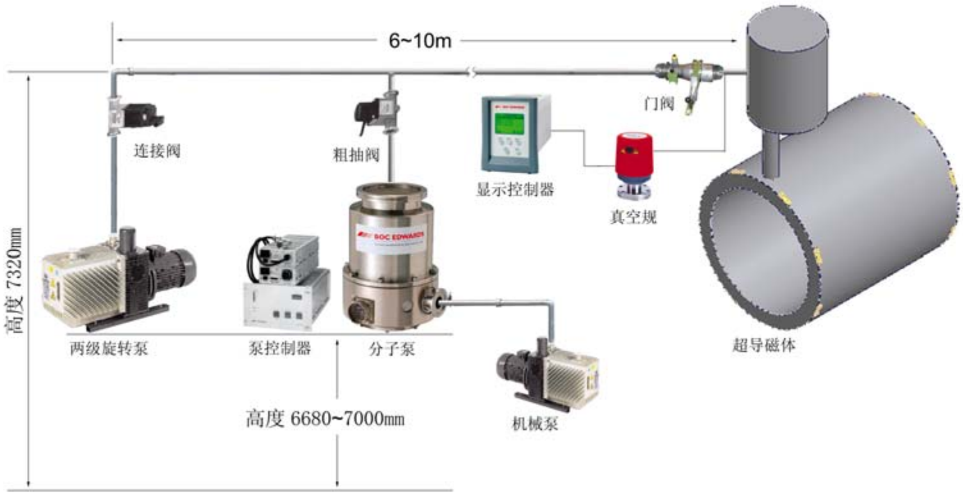

Fig.9.6-1 Vacuum system of the BESIII SC magnet

Field Mapping

A field-mapping device should be developed to measure the magnetic field precisely. From the mapping results, all the field data are used as basic parameters to determine particle momentum, and data along the Z axis are used as parameters for beam debugging.

The field mapping system will measure the field distribution in a volume of 2.6m in diameter and 3.5m in length. The total error of measurement should be less then 0.1%.

Field mapping system consists of a real-time control system with sensors, probes, etc., for three coordinates and a multi-channels data acquisition system. Sensors and probes provide magnetic field strength, position, and temperature, information to be collected by DAQ system. Driving system can be stepped in three-dimension using non-magnetic material with sufficient position precision, and controlled by computer. The characteristics of the mapping device are shown below.

Table 9.7-1 Characteristics of the mapping device

Design field	1.0T
Size	Length 3.2m, diameter 2.6m
Measuring accuracy	≤0.1%
Positioning accuracy	Axial<1mm, Radial<1mm, Angle<0.1°
Step	In volume Φ1.6m×2.4m: axial 5cm,radial 5cm,5° Other: axial 10cm,radial 10cm,10°
Mode	6 modes

Time	Two months

2.3.5.1 Reference

[1] 北京谱仪研制报告，中国科学院高能物理所，1989 年 3 月

[2] Feasibility Study Report on Beijing Tau-Charm Factory, IHEP-BTCF Report-03, October,1996

[3] Y. Doi et al., A 3T Superconducting Magnet for the AMY Detector, NIM,1989

[4] A. Yamamoto et al., Performance of the TOPAZ Thin Superconducting Solenoid Wound with Internal Winding Methods, Japanese Journal of Applied Physics, 1986

[5] H. Kichimi et al., A Field Mapping Device for the TOPAZ Magnet, NIM,1986

[6] A. Yamamoto et al., Quench Characteristics and Operational Stability of the TOPAZ Thin Superconducting Solenoid, Japanese Journal of Applied Physics, 1986

[7] The European Physical Journal C, Review of Particle Physics, Volume 3,1998

[8] 机械设计手册，第 1 卷，徐灏，机械工业出版社，1991 年 9 月

[9] “JIS 铁钢”第一卷，日本规格协会著，共立出版株式会社，1985 年 4 月

[10] “Formulas for stress and Strain”, Raymond J. Roark, Warren C. Young，Mc GRAW-HILL BOOK COMPANY，1986 年

[11] “Buckling of thin-walled circular cylinders”, NASA SP-8007

[12] “压力容器”，野原石松著，共立出版株式会社，1981 年 9 月

[13] “CMS-The Magnet Project Technical Design Report”, CERN/LHCC, 97-10，May 1997

[14] “The Belle Detector”,The Belle Collaboration,November 2000

[15] “Monographs on cryogenics superconducting magnets”, Martin N.Wilson, 1983

10 Electronics

Drift Chamber Electronics

Design Goals

The BESIII MDC (Main Drift Chamber) electronics system is designed to process the output signals from 6796 sense wires of MDC. The main tasks for the MDC electronics are the following:

① To measure the drift time of ionized electrons produced by charged particles towards anode wires (sense wires) to provide position information of particles passing through the chamber, so as to determine the momentum of charged particles.

② To measure the charge collected by anode wires (sense wire) to determine the energy loss of particles per unit length, dE/dx, so as to identify particles.

③ To provide the hit information to the trigger system, which will be used as one of the trigger conditions for L1.

1. Specifications Required for Charge Measurement

The main design specifications for charge measurement include charge resolution, dynamic range and integral nonlinearity etc.

(1) Charge Resolution

According to the selected gases and working parameters designed for the MDC, the resolution of the most probable energy loss, dE/dx, for minimum ionizing particles is designed to be

$$\sigma_e = 6\%$$

This resolution consists of two portions, the contribution from chamber itself and the one from electronics.

The inherent energy resolution of the chamber is a major contribution to the system. The contribution from electronics to the system is required to be no more than 15% of that of the chamber in order to be negligible, hence it can be easily calculated to be

$$\sigma_{ee} = 0.9\%$$

The BESIII MDC is designed to be the stepped cylindrical shape with a small cell configuration. The chamber has a total of 43 layers of sense wires, therefore 43 samples of energy loss can be obtained for a track which passes through all the layers of the chamber. The energy losses of particles in the chamber usually has a long Landau tail at the higher end of the distribution. During offline processing, the energy losses at the higher end will be truncated at a certain percentage, for example, at 70%.

Let σ_{ENC} denote the resolution for each electronics channel, σ_{ee} the resolution contribution from electronics system and take 70% truncation into account, we have

$$\frac{\sigma_{ENC}}{\sqrt{43 \times 0.7}} \leq \sigma_{ee} = 0.9\%$$

hence

$\sigma_{ENC} \cong 5\%$

According to the design parameters of the chamber, the estimated most probable charge for the minimum ionizing particles is about 100 fc. So, the charge resolution of a single electronics channel will be:

$$\sigma_{ENC} = 100\, fc \times 5\% = 5\, fc$$

(2) Dynamic Range

When the electronics system and the chamber are assembled together, the equivalent input noise of the electronics will be dominated by the output noise of sense wires. Since the contribution of the sense wire noise is much larger than that of electronics channel itself, the lower range to be measured is taken to be 15fc.

Taking into account the experience from BESII MDC dE/dx measurement, the upper range is defined to be 1800 fc.

(3) Integral Non-linearity

Within the full scale range (15fc-1800fc)，the integral non-linearity is required to be INL ≤2 %. If necessary, a quadratic correction can be applied to deliver a better linearity.

2. Specifications for Time Measurement

(1) Time Resolution

As mentioned above, tracks of particles are reconstructed by measuring the drift times towards the sense wires. According to the chamber design, the wire positioning error is required to be

$$\sigma_p \leq 130\,\mu m$$

This error mainly consists of two portions: One is from the single wire spatial resolution σ_{dp} of the chamber, which is mainly caused by diffusion effect of the ionized electrons during the drift process. According to the chamber design, it will be:

$$\sigma_{dp} \leqslant 125\mu m$$

The other one is from the single channel electronics error σ_{ep}. Therefore we have

$$(125\mu m)^2 + \sigma_{ep}{}^2 \le (130\mu m)^2$$

thus

$$\sigma_{ep} \le 35.7\mu m$$

since the drift velocity of electrons is about 30μm/ns for the selected gas and electric field, the time resolution σ_t of a single electronics channel is then required to be:

$$\sigma_t \le 1.2ns$$

In order to further reduce the effect of electronics on position resolution, the design goal for the time resolution of a single electronics channel is set to be

$$\sigma_t \le 0.5ns$$

In this case, the contribution of electronics to a single wire spatial resolution is about ～5%.

The time measurement error of electronics mentioned above is mainly caused by three factors:

① The length of e- and e+ bunches along the Z direction (beam direction). Since the beam length in Z direction is designed to be σz = 1.5 cm， so the collision time uncertainty caused by beam length is

$$\sigma_{t1} = \frac{1.5cm}{\sqrt{2} \times c} = 35ps$$

where c is the velocity of light. For the time measurement of drift chamber, this error can be neglected.

② The time-walker effect. This is caused by amplitude variation for the leading edge discrimination at a low threshold. Since the output signal of the drift chamber has a large dynamic range, this leading time variation is estimated to be around 1ns. However this time-walker effect can be partially corrected using the measured charge value for corresponding channel.

③ The time measurement error σt3 of the TDC. This is a main contribution to the time resolution of electronics. Using the CERN HPTDC chip, which can deliver a time measurement error less than 0.5ns. As a key component to design a time measurement circuit, it is believable that the time resolution with 0.5ns-1ns mentioned above should be a reasonable design value.

(2) Range

The range of the time measurement depends on the drift time of ionized electrons in the small cell. When a particle hits directly on a sense wire, the drift time will be 0; When a particle just passes through the edge of a vertical angle of a small cell, there is a longest drift time ～350ns(see the next section). In order to leave some leeway, the time measurement range can be taken as 0-400ns.

(3) Integral Non-linearity

Within the full scale range，the integral non-linearity with a value INL ≤0.5 % is required. If it is necessary, the quadratic correction can be made by the master controller to give a better result.

Design Considerations

BEPCII collider will run with multi-bunches. The collision cycle is 8ns. The trigger latency for L1 is 6.4us which is much longer than the collision period. Therefore, the design of electronics system must use pipeline technique, and the data acquisition and storage must be taken with a very high speed, so as not to lose any good events.

The luminosity of BEPCII will reach $1\times10^{33}/cm^2/s$. The data amounts to be processed by electronics system will be very large, hence the circuit design must adopt the multi-stage parallel processing technique, in order to effectively reduce the dead time.

The conceptual diagram of a small cell is shown in Fig.10.1-1. According to the design parameters of the chamber, the drift velocity of the ionized electrons in the gas is 30μm. The drift distance depends on the incident position and the direction of the particle produced from the e^+e^- collision. Obviously, the maximum drift distance is about a half of a diagonal, typically $1/2 \times (14^2+14^2)^{1/2} = 9.9$mm. When the diffusion and the non-uniformity of electric field are not taken into account, the maximum drift time of electrons in the chamber is

$$t_{max}=9.9\text{mm}/30\mu\text{m} = 330\text{ns}$$

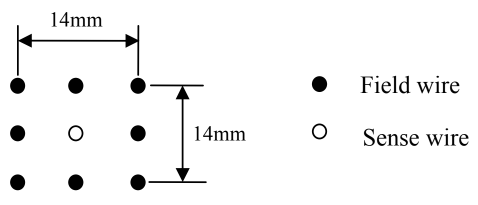

Fig.10.1-1 Conceptual diagram of a small cell

Since the cell size of the outer layer is a little bit larger and the electromagnetic field will have some influence on the drift direction of ionized electrons, the drift trajectory of electrons in a cell will not be a straight line. So, the maximum drift time is taken to be

$$t_{max} = 400\text{ns}$$

When a single ionized electron arrives at a region very close to an anode wire, a 1/t current waveform due to the strong electric field is formed on the anode wire due to the avalanche process. This current can be expressed as

$$i(t) = k \times \frac{1}{\frac{t}{t_0} + 1}$$

where k is a constant related to the working conditions of the chamber; t_0(≈1.5ns) is a characteristic time constant of the chamber. The waveform of i(t) is shown in Fig.10.1-2.

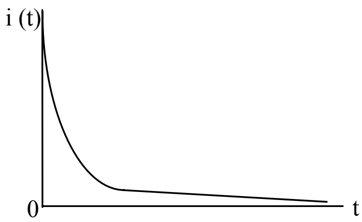

Fig.10.1-2 Output waveform of a single ionized electron on sense wire

The long tail of the waveform is caused by the slow movement of the positive ions towards field wires. From the formula given above, we can easily calculate that the required time, for which the current falls down to 1% of the peak current, is roughly 250 ns. The actual output waveform from a sense wire is a pile-up of a number of such 1/t waveforms formed by a single ionized electron. A simulation of the output waveforms of the MDC has been performed by using the Garfield program, and a typical result is shown in Fig.10.1-3. In the figure, the peaks of the current waveform are just the results of pile-up of a number of 1/t waveforms.

The width t_w of an actual output waveform depends on the incident position and angle of the particle. The observation shows that this width can roughly be expressed as follows:

$$t_w = t_{d\_max} - t_{d\_min} + 250 \quad (\text{ns})$$

where, t_{d_max} is the maximum drift time of an ionized electron at the position most far away from the sense wire in the cell; t_{d_min} is the minimum drift time of an ionized electron at the position nearest to the sense wire in the cell.

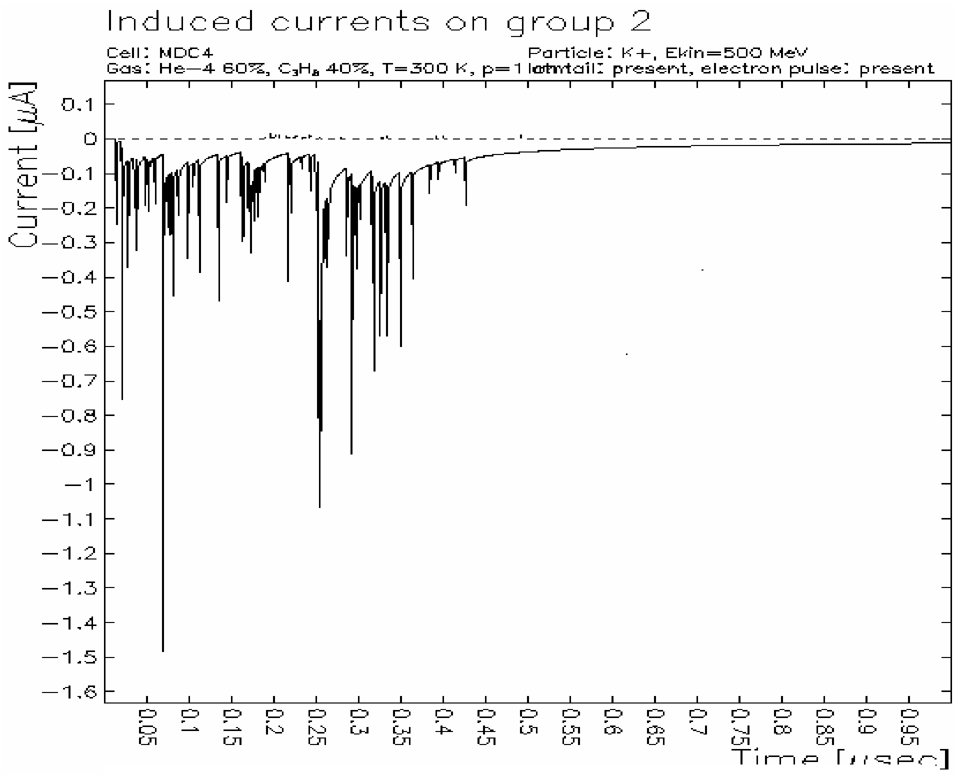

Fig.10.1-3 Simulation result to a sense wire signal of BESIII MDC

Obviously, when a particle passes through the diagonal of a cell, as shown by the arrow ① in Fig.10.1-4, the output signal has a maximum width:

$$t_{wmax} = 400\text{-}0\text{+}250 = 650\text{ns}$$

This value is consistent with our simulation results.

When a particle passes through the inside cell with an angle of 45^0 as shown by the arrow ① in Fig.10.1-4, only a few ionized electrons are produced in a cell, and these ionized electrons will arrive at the sense wire almost at the same time. So the output signal, in this case, will have a minimum width:

$$t_{wmin} = 400\text{-}400\text{+}250 = 250\text{ns}$$

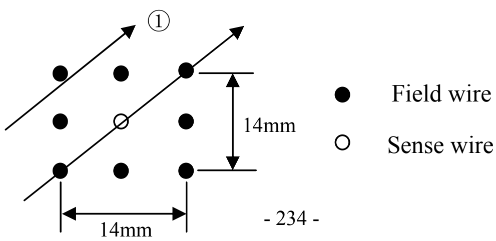

Fig.10.1-4 Conceptual diagram showing particle incident

Obviously, when a particle passes through the cell with any other angle, the width of the signal will have a value between 250ns and 650ns, assuming that the ionized electrons have an uniform distribution along the track.

The considerations mentioned above are the important basis for designing the electronics system.

Preliminary Design Scheme

A principle block diagram of the MDC electronics system is shown in Fig.10.1-5. In view of the functionality, basically the system consists of 7 different functional circuitries as the followings:

① Preamplifier；

② 《Post amplification + Shaping + Discrimination》circuitry；

③ Charge measurement circuitry；

④ Time measurement circuitry；

⑤ Threshold voltage circuitry；

⑥ JTAG control circuitry;

⑦ Calibration and system control circuitry；

⑧ Read out control circuitry;

⑨ Fan-out circuit.

It is important how to configure circuitries to form modules for obtaining an optimized system structure. The princeple idea is to have as less as possible the number of different parts including modules and cables in order to simplify the system design, enhance the system reliability and save the cost.

Based on these considerations, we prefer to integrate the 《post amplification + shaping + discrimination》circuitry, charge measurement circuitry, time measurement circuitry and the threshold voltage circuitry in a single 9U VME module as shown inside the dotted line block in Fig.10.1-5. We call this board as the MQT module. To integrate so many functional circuitries with high performance in a single board, we need to resolve many technical problems, which is a serious challenge.

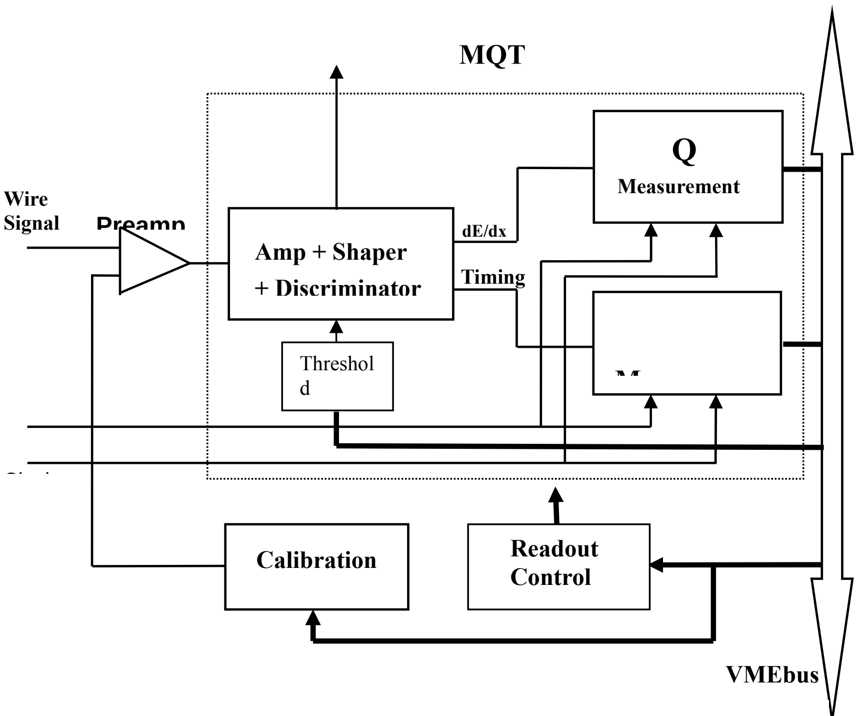

Fig.10.1-5 Simplified block diagram of the MDC electronics

According to the design scheme mentioned above, the hardware architecture of the MDC electronics mainly consists of the following 4 parts:

① Preamplifiers；

② MQT modules；

③ Calibration and system control circuit；

④ Read out control modules;

⑤ Fan-out modules.

In the following we discuss in detail each part of the system.

1. Preamplifier

The energy losses of particles in the chamber obey the landau distribution, the signal size in the low energy end of the distribution is very small (～μA). Therefore, the output signals from sense wires must be pre-amplified properly, to be suitable for further processing by subsequent circuitry. In order to reduce the effects of distributed parameters of connecting cables and to increase the signal/noise ratio, the amplification should be very close to the output end of sense wire. The main points for the circuit design can be briefly described as follows:

① Since both the charge and time measurements are required for each signal, a trans-impedance type preamplifier must be used so as to preserve the time information carried by the signal's rising edge. The bandwidth is designed to be between 70MHz—80MHz in order to avoid a significant degradation of the rising time of wire signals.

② The characteristic impedance of the sense wire is about 390Ω, which should be well matched to the input impedance of the preamplifier to avoid the signal reflection. The cross talk between sense wires is effectively reduced for a small cell design, and the simulation shows a 2% cross talk for a 14mm×14mm cell. Therefore, within the allowed error range the compensation network for the input of the preamplifier is not necessary.

③ All the sense wires, especially those of inner layers, are very close to the collision point. Therefore it is very important to design the preamplifier with low noise pickup from beams.

④ The power dissipation should be controlled at a low level, for example no more than 30mW per channel.

⑤ The differential output (driving 50Ω load) should be adopted in order to drive long cables (～18m).

⑥ The calibration pulses, which will be generated by a programmable stepping voltage, are injected to the input of each channels via a small capacitor.

⑦ Each card of preamplifiers will cover 8 channels, adopting a PCB with 4 layers. The size of the card is estimated to be about 6×7.6cm for inner layers, and 5×10.5cm for outer layers. The cards for outer layers will be directly mounted on the endplate of the chamber and connected to the feed-through via a wire of about 10cm. For wires of inner layers, the preamplifier cards have to be mounted some where away from the endplate due to space limitation, and the input of preamplifier card will be connected to feed-through via a cable of about 0.5-1m. For these preamplifiers the input noise could be a little bit larger.

The schematic diagram for a single preamplifier channel will adopt the similar design used for BESII MDC's. Their long-term operation (more than ten years) actually has a good performance, and table 10.1-1 shows the main specifications of the BESII MDC preamplifier.

Table 10.1-1.　Main specifications of BESII MDC preamplifier

Gain	12 k ohm (±12mv/μA)
Band width	70 MHz
Rise time	5 ns
Input impedance	30 ohm
Noise	50 Na
Output impedance	47 ohm
Output mode	Differential, driving 50 ohm
Power dissipation	30 mW @6V

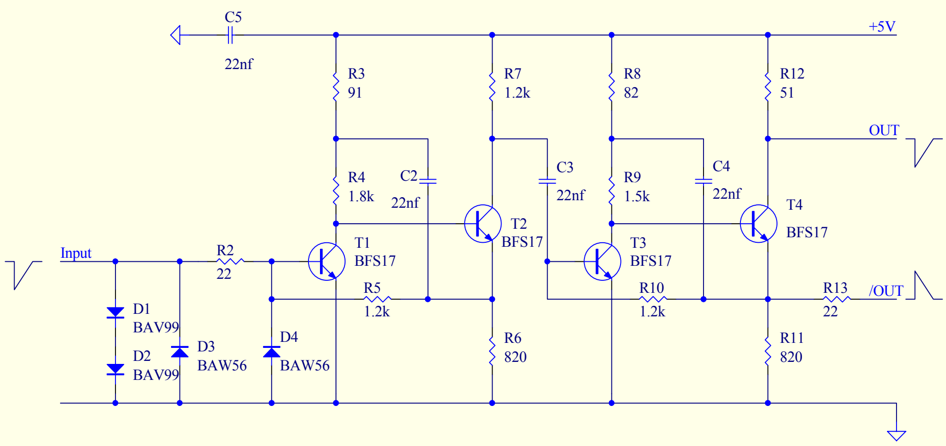

Fig. 10.1-6 Schematic of a single channel preamplifier

Recently we have integrated a single channel preamplifier on a small daughter board with a size of 2.6×0.9cm, Fig.10.1-6 shows its schematic diagram. The test shows that the performance of the daughter board is very similar to that shown in table 10.1-1. Eight daughter boards will be plugged into a mother board to form a preamplifier card with other components.

2. MQT Module

As mentioned above, this module is mainly composed of four parts. In addition, part of the calibration circuitry is also covered in this module.

(1) <Post Amplification + Shaping + Discrimination> Circuitry

The MQT module receives the analog differential output signal from the preamplifier. Via a cable of about 18 meters long. Fig.10.1-7 shows its block diagram.

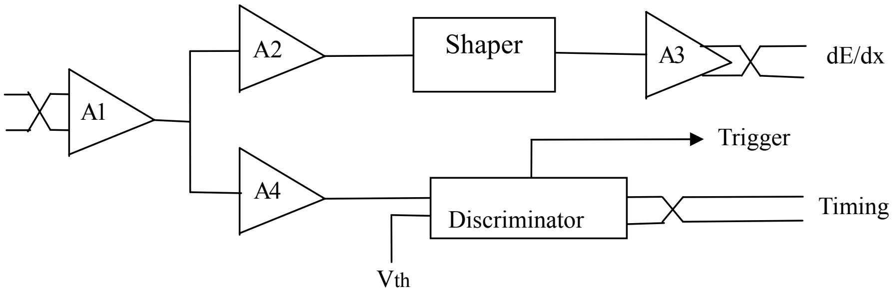

Fig 10.1-7 Block diagram of <post amp + shaper + discriminator

The main functions of this circuitry are as follows:

① To split the signal from the preamplifier into two branches, one for charge measurement, and one for time measurement.

② The signal in the time branch is further amplified and then sent to a fast discriminator at a low threshold to deliver a timing pulse, whose leading edge corresponding to the arrival time of the signal. This timing pulse is used as hit signal in the subsequent time measurement circuitry.

A stable threshold voltage is required for the low threshold discrimination. See the section below for the generation of this voltage.

As it is well known, the output signal of the drift chamber usually has a large dynamic range. Due to the time walk caused by amplitude variation, the leading edge discrimination will cause a significant timing uncertainty, estimated to be around 1ns. This error can be corrected offline by using measured charge of the same channel, and lowering the threshold is an effective measure to reduce it. However the reduction of threshold is limited by the system noise. Therefore, reducing the equivalent input noise of the preamplifier is very important for getting high timing precision. We expect that the threshold could be set at a level of about three to five times the amplitude of a single electron.

③ The signal in charge branch is shaped to satisfy the requirement of charge measurement, in a way depending on technical schemes to be used for the acquisition of the charge.

There are several ways to implement charge measurement. According to the BESIII working environment and characteristics of MDC output signal, taking into account the experience of the similar system in other laboratories, the numerical integral method based on the FADC (pipeline ADC) is adopted. The basic principle of this method is to successively digitize the input analog signal with a FADC, and then to integrate the digitized data. The integral result represents the area of the input signal, therefore the charge carried by the signal.

As mentioned above, the output waveform of sense wire is a pile-up of a number of 1/t waveform. When a numerical integral method is used for acquiring the charge, it is necessary to smooth the waveform so as to reduce the sampling rate of FADC. It is noticeable that the signal rate of a single sense wire is quite high, and the generation of signal is random in time. Once a pile-up with two or more signals occurs, it will be hard to separate one signal from another. Therefore, The circuitry must be designed according to the allowed pile-up probability, which means the width of shaped signal must be restricted within a certain limit.

The average signal rate (fired rate) for a single wire of BESIII MDC is estimated to be about 30k/sec. Using the Poisson probability distribution formula

$$P(N, \Delta t) = \frac{(\bar{n}\Delta t)^N}{N!} e^{-\bar{n}\Delta t}$$

where $\bar{n}$ is the average signal rate, P(N, Δt) is the probability of N signals which appear within interval Δt. Using this formula, we can easily calculate the probability of appearance of two or more signals within a time interval Δt , as shown in table 10.1-2.

It can be seen from the table, when Δt = 2μs, the piple-up probability is ～6%. This value is a little bit too high. When Δt = 1μs, the piple-up probability is reduced to ～3.0%. When the interval Δt is further decreased to less than 1μs, although the pile-up probability can be reduced somewhat further, but it will be hard to shape the signal smooth enough. Therefore, the interval 1μs is a reasonable choice, and the numerical integral width is set to be 1μs. Within this limit, the pile-up probability will be no more than 3%, which is acceptable. The starting point for integral should be set at t = tϕ, which is the collision instant.

Table 10.1-2 pipe-up probability within different interval Δt

Interval Δt（μs）	Pipe-up probability
2.0	5.8 %
1.5	4.4 %
1.0	2.9 %
0.9	2.7 %
0.8	2.4 %
0.7	2.1 %
0.6	1.8 %

As mentioned above, when particles pass through a drift cell, the output signal of sense wire will have the relationship “drift time + signal width” ≤650ns. In order to cover fully the output signal of the sense wire within the integral width, the shaping should satisfy

“Drift time + shaped signal width” ≤1μs

Simulation with the Garfield program shows that the measurement precision is good enough with 10bit FADC running at 40MHz sampling rate.

After buffering, the shaped signal will be sent to a charge measurement circuitry with AC coupling. The purpose to use AC coupling is to keep a stable baseline level for the input of FADC.

(2) Charge Measurement Circuitry

As described above, the charge measurement will adopt the scheme based on FADC and digital pipeline, and the charge value will be extracted through a numerical integral. Fig.10.1-8 shows the conceptual diagram for charge measurement with a numerical integral method. The input signal (Vin) is digitized by a FADC (based on a pipeline architecture ADC) to deliver a series of digitized data D_0, D_1,

D_2 ······ D_n. Let

$$Q = k\sum_{i=1}^{N}\frac{D_i + D_{i-1}}{2}\times T\ ,$$

the value Q is proportional to the charge carried by the input signal. In this formula, T is the sampling clock cycle, k is a factor which can be given through a calibration algorithm. With this scheme, the circuit will be rather simple, and it is also easy to design a fast digital pipeline.

The sampling clock for the 40MHz FADC will be provided by the trigger system, which is synchronized to the machine collision cycle.

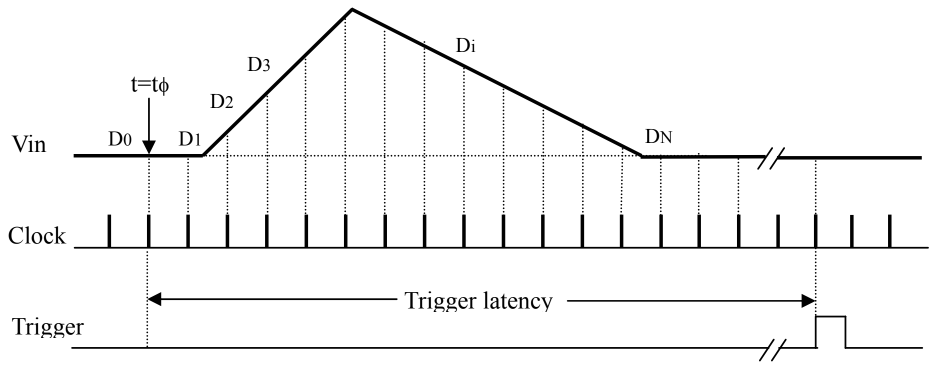

Fig.10.1-8 The conceptual diagram for numerical integral based on FADC

Fig.10.1-9 is a simplified block diagram for charge measurement. The analog processing circuitry receives the dE/dx signal from the shaping circuitry and make some necessary processing, such as trimming the gain, shifting the DC level, enhancing the drive capability, and filtering out the RF noise etc, in order to match the signal with the input characteristic of FADC chip. The FADC digitizes the signal with 40MHz clock, meanwhile the digitized data are written into the digital pipeline with the same clock. The length of digital pipeline should be more than

$$L = \frac{Trigger\_latency}{clock\_period} + 1 = \frac{6.4us}{25ns} + 1 = 257 \quad \text{(cells)}$$

In this case, there will be no lost of good event. In above formula, the reason for plus 1 is to get a datum just prior to t=tϕ instant, which is actually the pedestal value in normal case. If no active trigger L1, data moved sequentially into the last cell of the pipeline are discarded without entering the subsequent circuitry. In this case, the data in pipeline is updated constantly.

Once the trigger L1 signal is present, the data in the pipeline will be taken for processing. Under the control logic, the circuitry will sequentially perform the following operations:

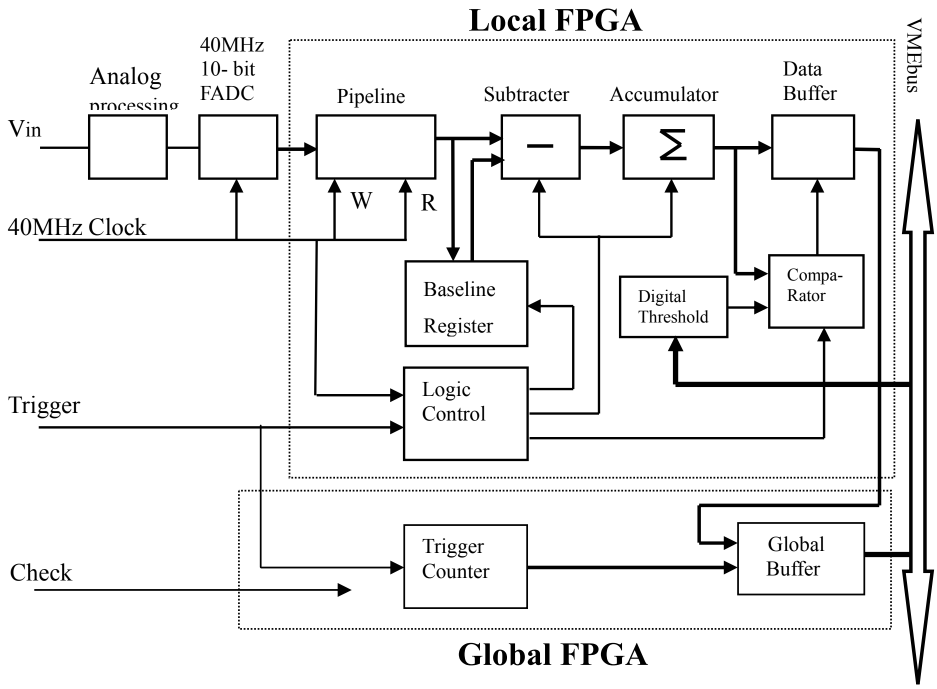

Fig.10.1-9 Simplified block diagram for charge measurement

① the first datum taken out from the pipeline will be stored into the baseline register. This datum is treated as the pedestal value.

② The subtracter receives the data from the pipeline one by one in the following 40 readouts , and subtract respectively the pedestal from the accepted data. The difference of values obtained will be sent to the accumulator one by one. Note that the integral width of 1 μ s corresponds to 40 readouts from the pipeline.

③ The accumulator sums up the 40 readout data from the subtracter, the summed data will then be compared with the programmable threshold stored in the digital threshold register. If the compared result is “0”(equal to or less than the threshold), the summed data will be thrown away; if it is "1"(greater than the threshold) , the summed data will be written into the data buffer. This written data represent the area of the input signal, therefore the charge carried by the signal.

④ Following the operation ③, data in each channel buffer, if any, will be transferred to a global buffer synchronized to the clock one by one, waiting for read out by VME master controller. Details about the global buffer will be discussed in the next section

⑤ After finishing the processes mentioned above, the subtracter will stop to receive the data from the pipeline until next trigger is active, and then the procedures ①-④ will be repeated again.

During the 1 μs period of data transfer from the pipeline to the subtracter. Active trigger signals will be masked by the trigger system. Otherwise, the control logic will be too complicated. Therefore the 1 μs interval is the system dead time.

All the logic functions described above will be implemented within a piece of FPGA as shown in the upper dotted block of Fig.10.1-9. This FPGA is called local FPGA which will deal with four or eight channels. All the functions of the FPGA are programmed with Verilog HDL language.

In addition, there is a trigger counter with eight bits in the circuit board. For each active trigger, the counter will increment by 1. The output of the counter after increment for each trigger will be, as a header flag, written into the global buffer, indicating that the data block following the header flag is an event associated to the current trigger (the data format will be discussed in next section).

The global buffer and the trigger counter will also be implemented with a piece of FPGA. This FPGA is called global FPGA as shown in the lower dotted line block of Fig.10.1-9.

From the above discussions we can conclude that the FADC conversion, subtraction of pedestal, charge extraction, zero data suppression and data readout by VME, etc., all can be implemented simultaneously, greatly enhancing the parallel processing capability at the board level.

(3) Time Measurement Circuitry

The MDC time measurement circuitry is to measure the time interval between the tϕ signal, at which a collision occurs, and the starting point (first electron arrival time) of the output signal of the sense wire. This interval actually includes three different sub-intervals as follows:

① The flight time by the particle created at t = tϕ from the collision point to a certain drift cell. This time interval depends on the flight direction of the particle and the geometric position of the cell.

② The drift time towards the sense wire by the ionized electron mostly close to the sense wire. This is the time we want to measure, since it is directly related to the track reconstruction.

③ The time to transfer the wire signal from avalanche point to the input of preamplifier along the wire.

The time measured by the time measurement circuitry is a sum of the above three parts , and contributions from the part ① and part ③ will be corrected by offline analysis.

Recently, the CERN micro-electronics group developed a High Performance TDC chip, called HPTDC, which is widely used by several detectors at LHC. The main specifications of this chip are listed in the following:

☐ Almost dead time free.

☐ 32 channels/chip.

☐ External clock (synchronized to beam crossing): 40MHz.

☐ Programmable time resolution:

250ps RMS for low resolution mode;

70ps RMS for medium resolution mode;

35ps RMS for high resolution mode;

20ps RMS for very high resolution mode (8 channels/chip in this case)

☐ Double pulse resolution: 5ns (typical); 10ns (guaranteed).

☐ Separate leading edge or trailing edge measurement; or simultaneous measurement of the leading edge and the pulse width (this working mode is not true for very high resolution mode)

☐ Built-in Zero suppression and address assembly.

☐ Low cost. ～RMB 20Yuan per channel.

It is obvious that the HPTDC has a very good performance/price ratio. We plan to use it in its low resolution mode as the key device for the BESIII MDC time measurement.

In order to measure the arrival time of the hit signal with respect to tϕ , an external 40MHz clock, which should be exactly synchronized to the collision time, and the trigger L-1 signal should be provided to the HPTDC. There is a coarse time counter and a fine time counter in the chip, which also contains a PLL (Phase Locked Loop) and a DLL (Delay Locked Loop). The PLL takes care of the performing clock multiplication from the external 40MHz to 40MHz, 160MHz or 320MHz. According to the precision requirement, the coarse counter can use one of the above three clocks to record an integer number of clock pulses between $t\phi$ and hit. The DLL divides the period of a clock, on which the coarse counter works, into a number of equal small interval, i.e. it is equivalent to turn the clock into a high frequency clock which is used as the working clock for the fine counter to measure the mantissa time which is less than a coarse clock period. Combining both results from the coarse and the fine counter, a complete measurement result t_{dr} is given. In order to get the drift time td with respect to $t\phi$, the count number of the coarse counter at $t = t\phi$ should be subtracted from the result t_{dr}. Fig.10.1-10 shows how to do this.

We can see from Fig.10.1-10 there are two counters, one coarse time counter and one trigger counter. At initialization, the coarse time counter and the trigger counter are set at preset_1 and preset_2 respectively, and the two preset values have the relation

Preset_1 – preset_2 = trigger latency

The two counters work on the same coarse clock. At $t = t\phi$, an interesting collision happens. After a time interval of the trigger latency, the output value of the trigger counter must be equal to one of the coarse time counter at $t = t\phi$. So the $t\phi$ can be easily found. From this point on, we can open a search window with a width equal to or greater than the maximum drift time. The drift time to be measured must be covered within this window. Subtracting the current trigger counter value from the searched drift time, the result must be the real drift time with respect to the $t\phi$.

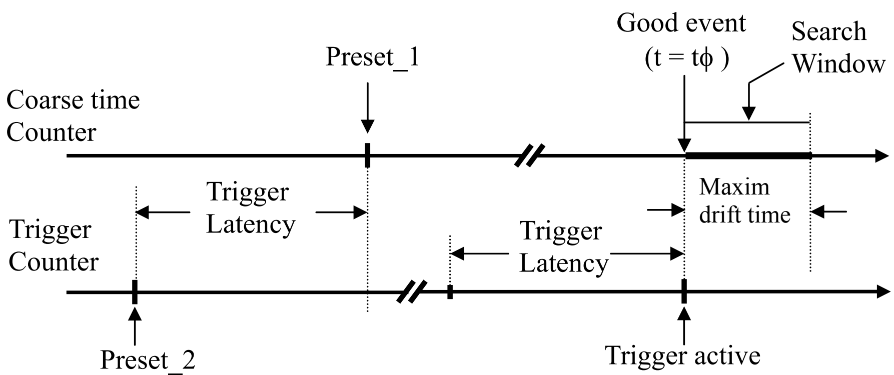

Fig 10.1-10 HPTDC time extraction concept diagram

It is worthwhile to note that the trigger system works on a clock of 40 MHz.

During a single clock, there are three bunches involved. The trigger system can not tell at which bunch crossing the interesting collision happened. So it only treats the leading edge of a corresponding clock as the $t\phi$. The deviation of 1 or 2 bunch cycles from the real $t\phi$ can be corrected by offline analysis.

A JTAG controller is required for the initialization and the test of HPTDC chip. At present the TDC board is designed according to the 9U VME64x standard. This board receives 32 differential signals from preamplifiers, and it covers mainly three parts, the “post amplification + shaper + discrimination”, the charge measurement and the time measurement. This board is called MQT board. On this board the charge extraction and time measurement will be performed simultaneously. In addition, a threshold voltage circuitry, which is used to provide a threshold to discriminators, will also be accommodated in this board.

The HPTDC chip will complete the zero suppression and address assembly internally, and a header and trailer flag will be given to form a standard data format.

An important question is how the VME master controller reads out the charge and the time data from the MQT module with limited time overhead. The present consideration for this question is as follows.

As mentioned in the section for the charge measurement, a global buffer is set up in the MQT board for storing the charge data, as well as the time data. In order to speed up the data readout, we will use the VME CBLT (Chained BLock Transfer) readout mode, and the data width will be arranged as 64 bits(D64). The data format in the global buffer is shown in Fig.10.1-11.

D63•••••••••••••••• D32	D31•••••••••••••• D0
Event1 header	
T1	T2
T3	T4
T5	Q1
Q2	Q3
Q4	Invalid data
Event1 trailer	
Event2 header	
T1	T2
T3	T4
T-error information	Q1
Q2	Q3
Event2 trailer	

Fig.10.1-11 Data readout concept diagram

In this Fig there are two typical events, each has a header and a trailer. Between the header and the trailer there are T(time) data and Q(charge) data. The data field width is 32 bits, and contains every two T data or Q data are combined to form a 64 bit data. Each event header also a corresponding trigger number.

The global buffer with a width of 64bits is composed of FIFO. Its depth could be around 2k. This buffer will be completely implemented in the Global FPGA as shown in Fig.10.1-9.

If for some reasons, the data in the global buffer can not be read out in time, an overflow will occur. In this case the FPGA will deliver an overflow flag to the trigger system, which will then stop sending out subsequent trigger signals until the overflow status is back to normal.

(4) Threshold Voltage Circuitry

There are many ways to provide the threshold voltage to discrimination circuit. One is to design a global threshold voltage generator and distribute the threshold voltage to all MQT modules. In this way there is a good consistency among all voltages, but too many cables to MQT modules, and possibly pick up noises is these cables.

Another way is to use a DAC in each MQT module to provide a threshold on-board directly. This threshold can be programmed via VME operation, and it is good for the stability, reliability and resistance to pick-up noises. In particular it is flexible to have different thresholds for different sense wires. The consistency of the voltage among different modules are controlled by a 10-12 bit DAC.

3. Calibration and System Working Mode Control Circuit

This circuitry is used to calibrate the electronics system and to set up the system's working mode. It mainly consists of three parts:

Timing sequence and system working mode control circuit. Its main function is to set the system to the online data acquisition mode or calibration mode.

On data acquisition mode, the circuit receives control signals from the trigger system including the trigger L1, 40MHz clock, reset and check signal.

On calibration mode, it will block signals from the trigger system and the circuit itself will generate the emulated trigger signals, 40MHz clock, reset, check and start signal. The start signal, will be sent to the preamplifier via the MQT module for creating a calibration pulse. The circuit will be a VME 6U module.

② Programmable DC voltage source. This circuit is designed to generate a DC voltage by simply programming a DAC chip in each MQT module. The output voltage of the DAC is sent to the preamplifier card for providing a DC voltage for the chopper circuit on the card.

③ Calibration pulse generation circuit. This circuit is simply, as mentioned above, a chopper circuit on the preamplifier card. When the start signal arrives, the chopper circuit will immediately deliver a step voltage, which is coupled via a small capacitor to the input terminal of preamplifier. The input signal is then a pulse, containing both the charge and timing information programmed by software.

4. Readout Control Circuit

This is a VME 9U module to be plugged into the same crate of MQT modules. The function of this module is as follows:

To receive the trigger signal and fan it out to all MQT modules in the crate.

To alert the crate master controller—PowerPC that a batch of data in MQT modules are ready to be readout. In responding to this interrupt signal, the PowerPC will readout the data from MQT modules is CBLT mode.

5. Fan Out Circuit.

This circuit is used to fan out all logic signals from the calibration module, i.e. the clock, trigger, reset, check and start signal. The fanout process is taken in two types of modules, fanout-I and fanout-II. The fanout-I module, located in the same crate of the calibration module, will only fan out signals from calibration module. The fanout-II module located in the same crate of MQT modules, will receive the clock, reset, check and start signals from the fanout-I module, and then fan them out to MQT modules.

System Framework

Fig 10.1-12 shows the system framework, which consists of one 6U VME64x crate and 16 9U VME64x crates.

The 6U crate containing calibration and Fanout-1 modules will be located at the top of BESIII detector.

The 9U VME64x crates will be installed at the north and south side of the detector respectively. Each crate contains 15 to 16 pieces of MQT modules, one readout control module and one Fanout-II module.

The preamplifier cards amount to 853 pieces. Every 4 cards fit to a MQT module. The cable between them is 18 meters long with 14 individually shielded twist pairs.

In order to isolate the ground of the MDC electronics from that of the trigger system, the timing signal from the MQT module will be sent to the trigger system via on optical fiber. Other signals such as the 40MHz clock, trigger, reset and check signal will be sent to MDC electronics from the trigger system via optical fiber too.

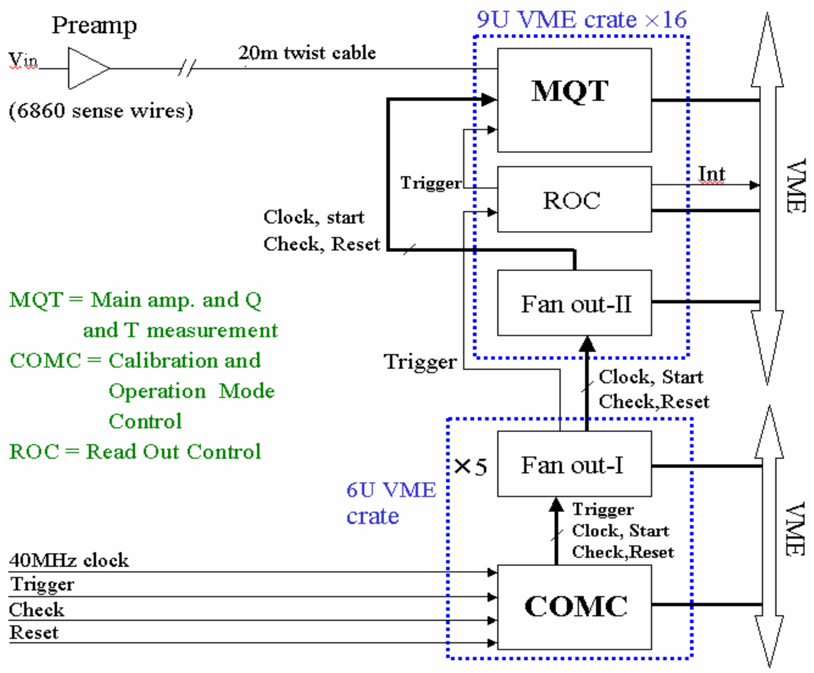

Fig 10.1-12 MDC electronics System framework

Calorimeter Electronics

Introduction

The main purpose of electromagnetic calorimeter read out electronics is the charge measurement to determine the energy deposited in the CsI crystals.

The traditional charge measurement method adopted in the read out electronics is to integrate the output current from the detector. The voltage peak of the signal waveform, after amplification and shaping of the integrated signal, is proportional to the detector output charge, which can then be measured through the peak voltage.

Electromagnetic calorimeter electronics adopts digital pipeline method to hold the data in compliance with the 6.4μs L1 trigger latency, so that no good events will be lost before the L1 trigger. Data read out follows the VME bus standard.

There are 3 operation modes, collision mode, calibration mode, all can be selected using VME commands.

1. Collision Mode

This mode corresponds to the data acquisition of the spectrometer when the collider is in operation. A 20MHz clock and a L1 trigger signal are all provided by the trigger system, and synchronized with the collision time.

2. Calibration Mode

We can check the electronics system and get the correction constants with this mode. The test controller provides the 20MHz clock, trigger signal, and a series of charge value with good linearity to test the linearity of each channel. The VME master calculates the linear correction constants from the data obtained in this mode.

3. Gain Adjustment Mode

The analog "sum" of 8 channels is sent to the trigger system to reduce the number of cables between the calorimeter and the trigger system, and simplify the whole BES system. We must adjust the gain of each channel before they are added together to insure the gain uniformity of each channel, including the contributions from CsI crystals and PIN diodes. The test controller generates serial clock and serial data to adjust the gain according to the VME master commands. The serial decode circuit in the post amplifier module implements decode and gain adjustment task with the serial clock and data.

Operation Principal and System Configuration

1. System Operation Condition and Specification

System clock	20MHz
L1 trigger latency	6.4μs
Single channel event rate	≤1KHz
Range of charge	0.5fc~1500fc
Equivalent noise charge (energy)	0.16fc (200KeV)
Number of channel	6272
Integral nonlinearity	1% (before correction)
Cross talk	0.3%
Dynamic range	15bit
Information to trigger	Analog "sum" of 8 channels
Gain adjustable on line	≤20% non-uniformity

2. System Block Diagram

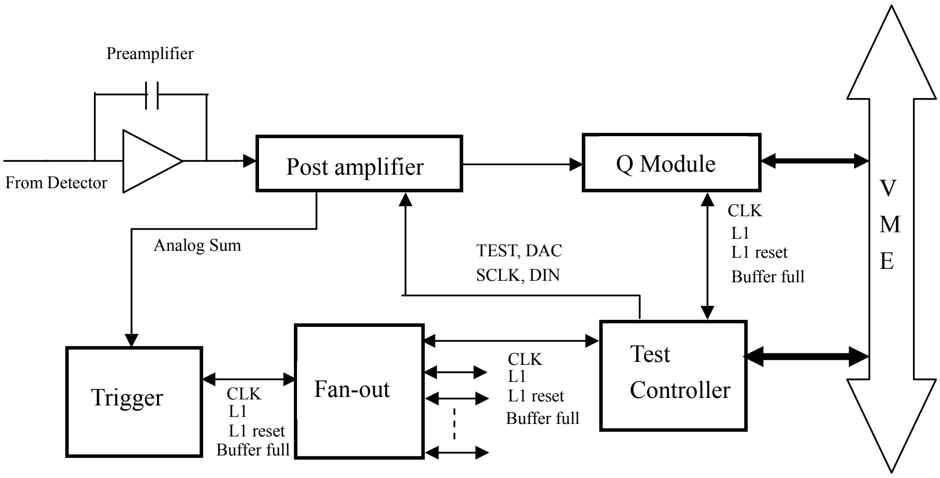

Fig.10.2-1 Block diagram of the electronics electromagnetic calorimeter

Fig. 10.2-1 shows the block diagram of the electronics of electromagnetic calorimeter, which is divided into 3 main parts: Preamplifier, Post amplifier, Q module and Test Controller.

(1) Preamplifier

There are 6272 CsI crystals in the electromagnetic calorimeter. Two S2744-08 photo diodes are mounted on each crystal. Two charge sensitive preamplifiers are mounted on the backs of the photo diodes respectively. They are fixed on the crystal with an aluminum shielding box. The low voltages of the preamplifier and the bias voltage of the photo-diode are all supplied by the post amplifier. The preamplifier and the post amplifier are connected via a 20 wire twisted cable.

(2) Post Amplifier

The post amplifier makes semi-gauss shaping to reduce the noise and pile up rate. A gain adjustment circuit is placed in the post amplifier to insure the precision of “analogue sum” for the trigger system. The post amplifier output signal is sent to the Q module with a 34 wire twisted cable.

(3) Q module and Test Controller

The digitization is implemented by a 10bit FADC of 20MHz. Multi-range digitization method is adopted to get 15bit dynamic range. The voltage signal to be measured is sent to three amplifiers A, B, and C simultaneously. The gain ratio of the three amplifiers is 1:8:32. The three outputs from A, B, and C are digitized at the same time. The unsaturated lowest range datum is chosen and a 2-bit range code is added to the datum. The digitization, pipeline, and peak finding are all implemented by hardware.

The Q module is a 9U VME module with 32 channels. The module has data processing and data transferring functions besides the digitization.

The VME master may choose one of the 3 operation modes through the test controller and Q module. The clock and control signals required by the system are provided by the test controller, or through the test controller. Test controller is a VME module, one in each crate.

3. Operation Principal

(1) Preamplifier

There are 6272 CsI crystals in the electromagnetic calorimeter. 2 PIN photo diodes and 2 preamplifiers are mounted on each crystal. The preamplifier is a low noise charge sensitive amplifier.

A calibration circuit is placed at each preamplifier input. One leg of the calibration capacitor is connected at the preamplifier input. Another leg can be connected to DAC output or to the ground by switch control. When the calibration capacitor is connected to the DAC, the capacitor is charged to the charge of Q=VC, where V is the output voltage of DAC, and C is the capacitance of the calibration capacitor. When the capacitor is connected to the ground the capacitor with the charge of Q=VC is discharged through the preamplifier and ground to calibrate the system. The calibration circuit can be used to check the electronics system, calibrate the gain, and correct the nonlinearity of each electronics channel.

Specifications of preamplifier:

Gain	1mV/fc
Equivalent input noise charge	0.16fc (when input capacitance is 80pf)
Dynamic range	0.5fc to 1500fc
Output decay time	50μs
Maximum linear output	2V

The falling edge of the charge sensitive amplifier decays slowly. The signals may pile up at certain counting rate. Suppose the counting rate of the input signal is $\overline{n}$, the input charge is Q, the average output voltage of the piled up signal is $\overline{V_0}$, we have:

$$\overline{V_0} = \overline{n}\int_0^{\infty} \frac{Q}{C_f} \cdot e^{-\frac{t}{\tau_f}} dt = \overline{n} \cdot \frac{Q}{C_f} \cdot \tau_f$$

Take:

$\overline{n} = 10^3$, $C_f = 1$pf, $\tau_f = 50\mu$s, $Q_{max} = 1500$fc (the worst case)

We get:

$\overline{V_0} = 0.08$V

The effects of the 0.08V pile up voltage to the dynamic range of the amplifier can be ignored.

Since the decay time constant of CsI crystals is 1μs, much smaller than the decay time constant of the charge sensitive amplifier τ_f, the "ballistic deficit" effect is negligible, and it cannot affect the energy resolution. The outputs of the 2 preamplifier which is differential, the low power supply voltage, the PIN diode bias voltage and calibration signals are all connected to the post amplifier with a 20 wire twisted cable.

(2) Post Amplifier

Fig.10.2-2 shows the block diagram of the post amplifier:

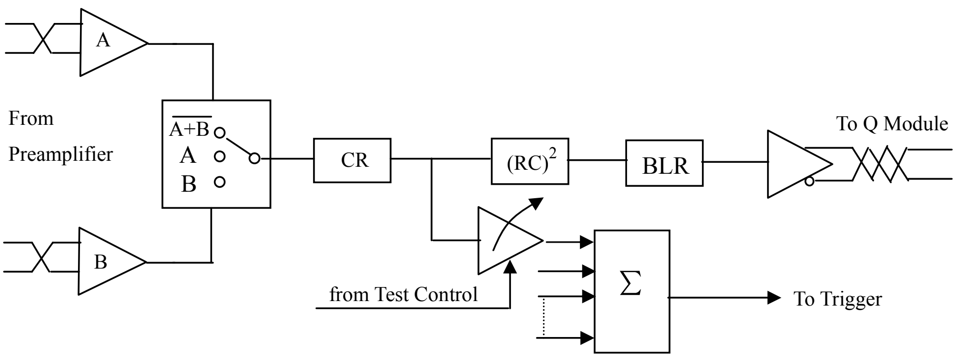

Fig.10.2-2 Block diagram of post amplifier

The shaping circuit of CR-$(RC)^2$ with pole-zero cancellation is adopted to increase the signal to noise ratio and reduce the pile up rate. The time constant of the shaping circuit is 1μs.

Since the charge is proportional to the peak voltage of the signal and the ADC sampling rate is 20MHz, it is required that the peak width of the signal should be wide enough to insure that the ADC sampling can “catch” the peak. If we define the “peak” as the part of the signal waveform near peak, where the voltage difference should not exceeds 0.1%, the peak width is 126ns. Hence for the time constant of the shaping circuit of 1μs, two or three ADC samples can be obtained at the signal peak for the 20MHz sampling rate.

The main functions of the post amplifier are:

A: Receives the differential signal from the preamplifiers. The differential receivers with high common mode rejection ratio are adopted for the signals from the two preamplifiers A and B. Three choices can be made by the post amplifier with jumpers: A, B, or the average of A and B. The signal to noise ratio can be improved if the average of A and B is chosen. Choice A or B can be selected, and the gain is almost the same, if one of them fails and the other still works.

B: Further amplifies the signal, makes CR-(RC)2 shaping to increase the signal to noise ratio and insure the peak sampling precision.

C: provides the preamplifier power supply voltage, PIN diode bias voltage and online calibration signals.

D: Adjusts the gain of each channel to the trigger, including gain of CsI crystal and PIN diodes, with a three lines serial bus to guarantee the gain uniformity. The serial data has 17 bits, the first 5 bits are the module address, the middle 4 bits are the channel address and the final 8 bits are the data for the channel gain. The gain adjustment is implemented with the digital potentiometer MAX5400. The VME master must set the gain and check the gain, every time the system is powered up, since there is no data storage function inside MAX5400. The fast signals after CR stage of 8 channels are gain adjusted, amplified, summed and converted to a pare of differential signal for trigger system.

E: The signal after CR-(RC)2 shaping, amplifying and base line restoring is sent to Q module with single end to differential signal converter.

(3) Charge Measurement

A. Multi Range Digitization

The electromagnetic calorimeter requires that the maximum energy to be measured for a single crystal is 2GeV, while the minimum energy is 0.6MeV. The digitization range must not be less than 15 bits to ensure enough dynamic range and accuracy. We use three 10-bit FADC to digitize the post amplifier output signal with 3 different ranges as shown in Fig. 10.2-3, since 15-bit 20MHz FADC is not available. The unsaturated lowest range datum is chosen as the final result.

Table 10.2-1

Range	Gain	Full Scale	Min. Energy	Digital Res.	CsI Res.	Res. Increa.
High	×0.25	2.5GeV	0.625GeV	1.4×10^{-3}	2.1×10^{-2}	0.2%
Middle	×1	0.625GeV	0.078GeV	2.3×10^{-3}	2.9×10^{-2}	0.3%
Low	×8	0.078GeV	20MeV	1.1×10^{-3}	3.7×10^{-2}	0.04%
			0.6MeV	3.5×10^{-2}	7.3×10^{-2}	11%

The digitization resolution and the CsI crystal resolution in the above table are for the minimal energy of each range. They are the worst case in the range. It indicates that the 3 different ranges can cover the dynamic range required by physics. The digital resolution is much less than the CsI crystal resolution itself when the energy is higher than 20MeV. The effect to the total resolution can be ignored. The total resolution is only increased by 11% if the energy falls to 0.6MeV.

B. Obtain the Charge Value

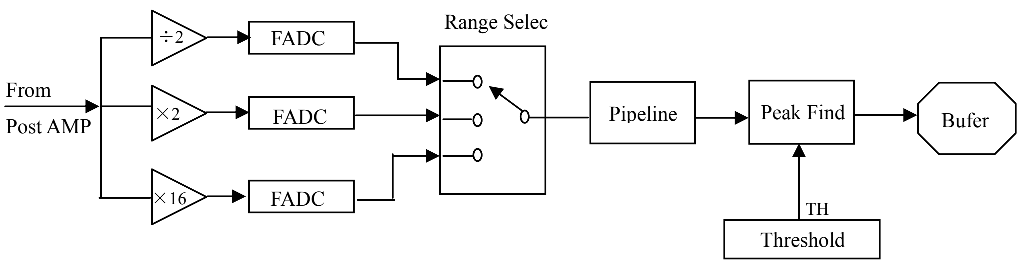

Fig.10.2-3 Schematic of 3 ranges digitization

The detector output signal is shaped to a semi-gauss waveform after preamplifier and post amplifier. The peak is proportional to the energy deposit in the detector. Three different gain amplifiers with 3 different ranges amplify the output signal of the post amplifier. They are sampled by three 10-bit FADC with 20 MHz sampling rate. The lowest range unsaturated value among the 3 sampled data is selected and a 2-bit range code is added to the datum. The 12-bit data are passed through a digital pipeline to obtain proper delay time. The total delay time of the pipeline is chosen as 4.9μs, which is 1.5μs less than the 6.4μs trigger latency. The time interval between the waveform peak and the L1 trigger signal is 1.5μs since the peaking time of the shaping circuit for a 1μs decay time input current signal is 3μs. The waveform peak is in the middle of the 3μs peak finding time window to guarantee the correct peak finding procedure. The peak value should be compared with the threshold stored in the threshold register. The signal is too small and should not be kept if the low range peak is smaller than the threshold. The 10-bit peak value, its 2-bit range code and additional 6-bit peaking time are stored in the buffer to be read out.

C. Data Buffer

A dual port RAM is used for data buffer. The writing address of the dual port RAM is the same as the writing pointer of the trigger number FIFO, and the reading address of the dual port RAM is the same as the reading pointer of the trigger number FIFO, to ensure that the reading and writing of every event is exactly synchronized with the reading and writing of the trigger number. The data below the threshold are still stored in the dual port buffer, but there is a flag bit with each datum, “0” means the datum is below threshold, “1” means the datum is no less than threshold.

D. VME Interface

Power PC reads out the data through VME crates. There are 32 channels on each module for a 9U VME module.

The token method is implemented to read out the data from the 32 channel buffers. The data are read out if the channel receives token and the data are above the threshold. The token is passed to the next channel if the data are below the threshold.

The CBLT protocol is adopted to read out the data in a VME crate.

(4) Test Controller

The main functions of the test controller are:

A: Fans out the 20MHz clock, L1 and L1 reset signal from trigger system in the collision operation mode.

B: Generates 20MHz clock and L1 signals required by the charge measurement in the calibration mode. Sets 16bit DAC data and generates test pulses for injecting charge according to VME commands.

C: Generates the necessary gain adjustment signals: serial clock and serial data, in the gain adjustment mode. The serial datum is 17bit wide. The first 9 bits are the address codes, and the following 8 bits are the gain codes. The number of the clock pulses sent by the test controller to adjust the gain is 17 and the baud rate is 500Hz.

When it is not in the gain adjust mode, the test controller does not generate the serial clock and serial data, so there is no interferences to the post amplifier.

D: A flag signal can be obtained from each Q module to indicate if the unread event number is greater than a preset value "N". These signals of a crate are wire-ORed to form a single flag signal, sent to the test controller. The test controller requests interrupt for a N-event CBLT read out procedure if this flag signal is active.

Fig. 10.2-4 shows the block diagram of the test controller.

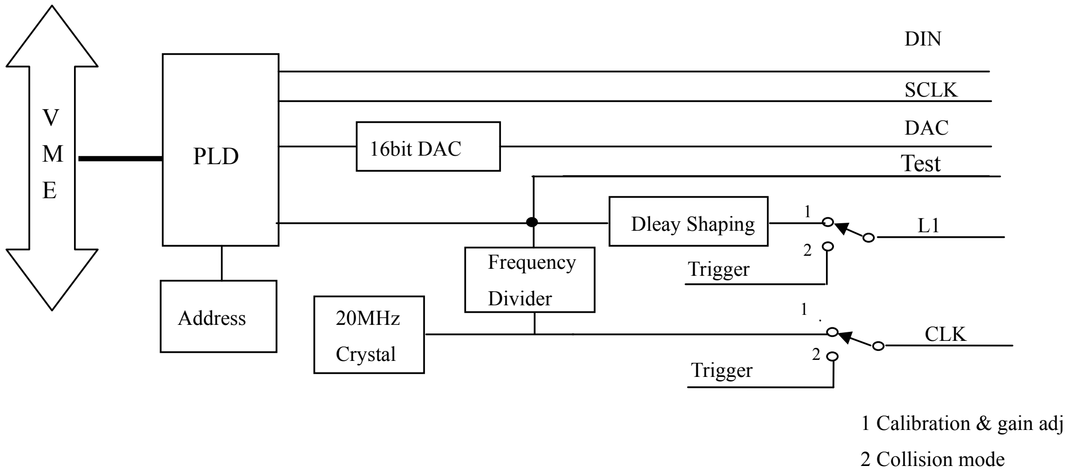

Fig.10.2-4 Block diagram of the test controller

(5) Fan Out

The trigger system only gives one 20MHz signal, one L1 signal and one L1 reset signal to each sub-system. These signals should be fanned out to all the readout channels. There are 3 levels of fan out. The first level is system fan out, the signals from the trigger system are fanned out to 16 test controllers in their respective VME crates via a special VME module. The second level fan out happens in the crate, implemented by the test controller of the crate. It fans out and sends theses signals to the 16 Q modules via user defined bus in the same crate. The fan out inside the Q module for the 32 channels is implemented by the module itself.

4. System Configuration

The charge sensitive amplifier converts the output charge of the detector to voltage signal. It is amplified, semi-gauss shaped by the post amplifier, and sent to Q module for digitization. The VME standard is used for digitization parts. There are one master (Power PC), 16 Q modules (512 channels altogether) and one test controller in a crate. The VME master sends out the results of digitization.

The VME master can make gain adjustment, electronics calibration besides the normal data acquisition.

The electronics of the electromagnetic calorimeter are divided into 3 main parts: preamplifier, post amplifier and charge measurement. Two preamplifiers are mounted on a crystal, and connected with the post amplifier by a 20 wire shielded cable. The post amplifier is built in a single width NIM module, with 16 post amplifiers in one module. The NIM crates with the post amplifier modules and the VME crates with

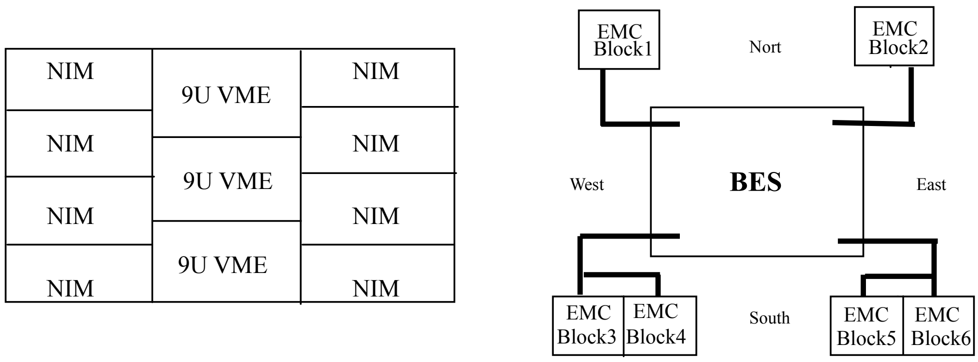

Fig.10.2-5 Schematic arrangements of crates and EMC blocks

the charge measurement modules are assembled in the 19" racks. The charge measurement circuit is assembled on a single width 9U VME module, which covers a total of 32 channels. One rack with charge measurement modules (including 3 VME crates, 1536 channels at most) and 2 racks with post amplifier modules (4 NIM crates in each rack, 786 channels each rack at most) form an "EMC Block", as shown in Fig. 10.2-5. There are 6 "EMC Block" around the spectrometer.

The charge-energy conversion ratio is 0.8fc/MeV. Fig.10.2-6 shows that the dynamic range of digitization is larger than that required by physics, so that required physics precision and range is guaranteed. The noise level is between the lowest physics interest and the smallest digitization bit. Therefore, The digital resolution will be affect the noise measurement, and the noise will not affect the charge measurement precision seriously.

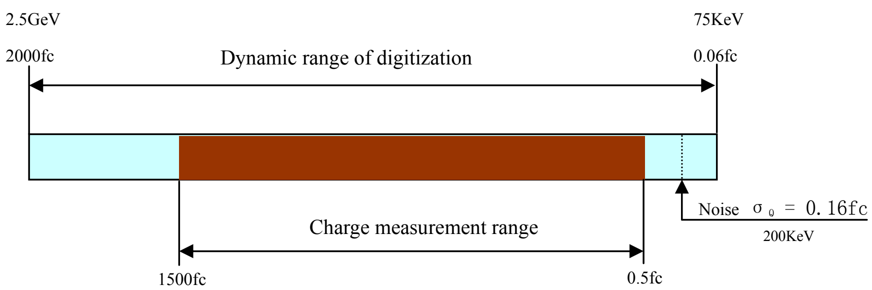

Fig.10.2-6 Dynamic range of charge measurement

Power dissipation is a design concern, particularly for preamplifiers. Table 10.2-2 lists the power dissipation of each channel.

Table 10.2-2 Power dissipation of each channel

Single channel power dissipation 4000 mw		
Preamplifier	Post amplifier	Charge measurement
120 mw	2000 mw	1870 mw

.

TOF Electronics

The primary task of the TOF electronics is to measure the flight time of charged particles, referred as the “time measurement”. In order to correct the timing error caused by the “time-walk” effect, the total charge from scintillators should also be measured, referred as the “charge measurement”. Therefore the three essential functions of TOF electronics are as follows:

① Time measurement

② Charge measurement

③ Fast timing signals for trigger.

Pre-Amplifier

Since the gain of PMT in a magnetic field of 1T is about 2.5×10^5. The signal amplitude is then about 50mV, and it will decrease further after a long cable(15-20 meters). The attenuation depends on the frequency characteristics of the cable.

Generally, if the diameter of coaxial cable is 6-7mm, and the bandwidth of signal is 200MHz, the attenuation of signal will be 2.8dB. If the diameter is 2.9mm, the attenuation will be up to 8dB. Hence, a high-performance pre-amplifier is a good choice. The basic design considerations about the pre-amplifier are as follows.

1. Good Bandwidth

In order to achieve a no-distortion amplification for the PMT signal with 4ns rising time, the pre-amplifier must have a good high-frequency performance. The requirement is that –3dB bandwidth should not be less than 150MHz, the rising time of the amplifier should be around 2.3ns, and the effect to the rising edge of the signal should be less than 0.65ns.

2. Dual-linear Amplifying

Dual-linear amplifying is to have a higher gain for small signal in order to obtain large enough signal amplitude and good signal to noise radio (SNR); While have a gain of only a factor of one or two for large signals in order to guarantee the output signal in the linear range of the amplifier. Therefore, the dynamic range of the pre-amplifier can be broadened, and the long dead time due to signal over loading and long recovering time can be avoided. The inflexion of dual-linear amplifying is set according to the simulation result of the PMT output signal.

3. Fully Differential Amplifying

Fully Differential Amplifying is a new type of amplifier with differential input and output. It can improve SNR and the dynamic range of signals, and its differential input and output signals can suppress the noise and disturbance from long distance transmission.

Scheme of Pre-amplifier

The CDF experiment developed a new type of pre-amplifier[?] which is composed of discrete components with advantages of high gain and high bandwidth, however its reliability, long term stability and consistency could be a concern. With the development of integrated amplifier in recent years, it is possible to realize a high gain, high bandwidth pre-amplifier with integrated circuit. In our design, a scheme of two-level structure is adopted. The first level is for dual-linear amplifying and the second one is fully differential amplifying with fixed gain. Dual-linear amplifying will be tested with two techniques, one is discrete components, and the other is the current feedback (CF) integrated structure with a single chip.

1. Dual-linear Amplifying (discrete components) + Fully

Differential Amplifying

The basic idea of the dual-linear amplifier based on discrete components is shown in Fig 10.3-1. Its first level dual-linear amplifying circuit is based on the idea of the CDF system. The second level is composed of a single chip, a fully differential amplifier with a gain of two. The output level is a fully differential amplifier. Because the output of PMT is differential, we can build a complementary differential PMT signal with its anode signal and the last dynode signal, which has the same amplitude and opposite polarity as the anode signal. The difference between our design and common TOF pre-amplifiers is that our pre-amplifier adds one time gain to the signal, and at the same time, it can restrict output noise of the detector and improve SNR. Fig 10.3-2 and Fig 10.3-3 shows the dual-linear input and output wave of the pulse response of the amplifier based on the spice simulation.

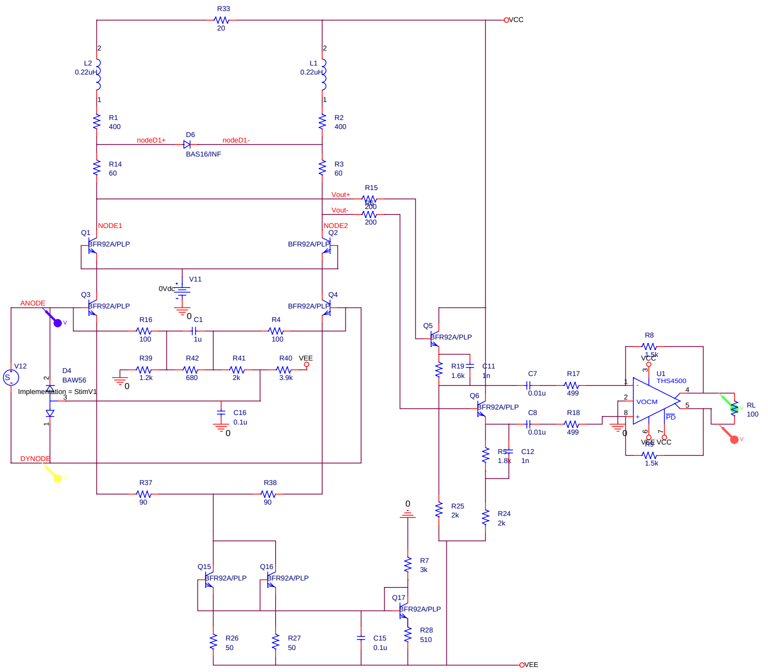

Fig 10.3-1 Schematic of dual-linear amplifier based on discrete components

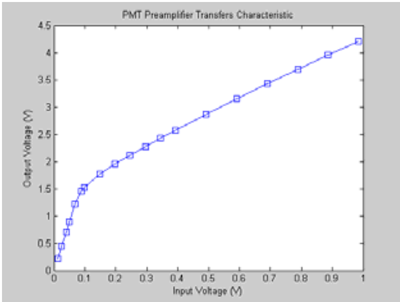

Fig 10.3-2 Simulation of input and output waves

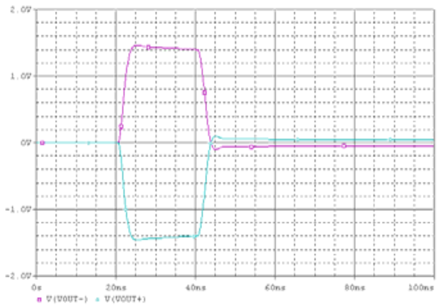

Fig 10.3-3 Simulation of pulse response

2. Dual-linear Amplifying (CF integrated amplifier) + Fully Differential Amplifier

Fig 10.3-4 shows the schematic of dual-linear amplifier based on the CF amplifier. Unlike the voltage feedback amplifier, the product of bandwidth and voltage gain of CF amplifier is not a constant, and it can have a higher bandwidth with a higher voltage gain. The key in this scheme is the selection of an amplifier with high frequency and high gain. Obviously, the circuit in Fig 10.3-4 is simpler than the one in Fig 10.3-1. Considering the low impendence at the negative input of CF amplifier, there is a big different on the impendence of the two inputs. So, we cannot obtain a differential input with the CF amplifier, and only use the single anode signal.

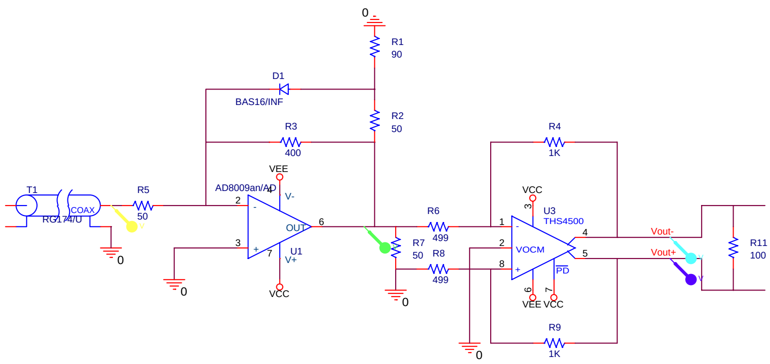

Fig 10.3-4 Schematic of the dual-linear amplifying based on CF amplifier

Fig 10.3-5 and Fig 10.3-6 shows the result from spice simulation for the dual-linear amplifying circuit based on the CF amplifier. From the simulation, we can find that there is no big difference in the performance of these two circuits. So, the finial scheme will be decided based on the real circuit test.

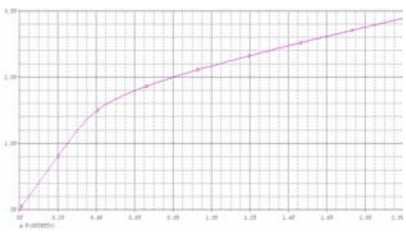

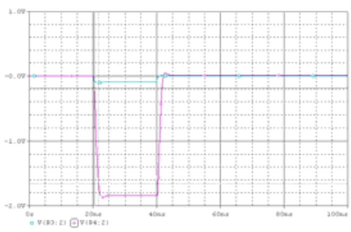

Fig 10.3-5 Simulation of input and output wave

Fig 10.3-6 Simulation of pulse response

3. Single Level CF Amplifier

As the spare scheme, we still consider the design of an amplifier with a fixed gain similar to that of the BELLE experiment. In our design, the gain will be improved by a factor of three to fifteen, which is the main difficulty of this scheme. High-performance CF amplifier plays an important role in this scheme. Two-level structure with CF and fully differential amplifier has to be used if it is too difficult in this scheme.

Basic Parameters of Pre-amplifier

Basic parameters considered now are as follows.

Voltage gain:	15
Signal bandwidth:	>150MHz
Rising time:	2ns
Output signal:	differential or single
Dynamic range of output signal:	0-2V (single)
	0-4V (differential)
Power:	± 6V

TOF Front-end Electronics

The Front-End Electronics (FEE) of the TOF system is made of three parts, including the time measurement circuit, the charge measurement circuit and the mean timer. Mean timer is used to provide a fast timing signal for trigger system. A simplified block diagram of a single channel of the TOF front-end electronics is shown in Fig. 10.3-7. A total of 16 channels are to be assembled in a 9U VME module.

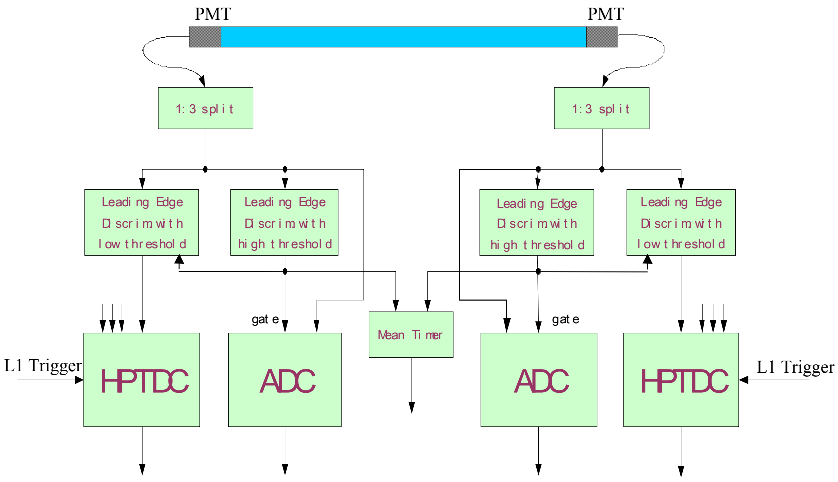

Fig. 10.3-7 A block diagram of Front-End Electronics (FEE)

Fast signals from PMT have the characteristics as shown in Table 10.3-1. Each PMT signal will be split into three. Two of them are sent to the discriminators with two different threshold levels: The low level (LL) threshold discriminators and the high level (HL) threshold discriminator. The former is used to provide the best possible timing information to be sent to a multi-hit TDC, while the later provides a gate signal for charge measurement and to be combined with the other end of the scintillator bar to form a mean timer for trigger system. The choice of the threshold level is a trade-off between the efficiency and the background rate. Both thresholds will be set via DAC circuits. The third one is sent to ADC for the charge measurement, which is used to correct the intrinsic time skewing of a fixed threshold discriminator (so called “time walk”). To achieve the design goal of 25ps, a high performance TDC chip called HPTDC[2] will be used for the time measurement. For the charge measurement, two options are under consideration: One is the traditional current integral ADC, and the other is the waveform digitalizer. All of them will be described below. Full analysis of different options is still in progress and each of them will be completed before the final decision to be made.

Table 10.3-1 Characteristics of signals from PMT

Rising Time	~ 4ns
Falling Time	~ 8ns
Pulse Width	~12ns
Pulse Amplitude	0~ -4V
Mean Event Rate/PMT	4K/s
PMT signal cable	~ 20 meters

10.3.2.1 Double Threshold Techniques

As showed in Fig. 10.3-7, discriminators with two different thresholds will be used for TOF FEE in order to achieve the accurate timing and reduce the signal rate due to backgrounds. The selection of high-speed comparator will be a key point, while a number of comparators currently available can satisfy our requirements, such as MAX9693, MAX9601 of MAXIM[3], AD96687 of Analog Device[4], SPT9693 and SPT9689 of SPT[5], etc. A number of tests for these chips will be performed before the final decision is made.

10.3.2.2 Time Measurement

1. HPTDC

As mentioned above, we plan to use HPTDC chip designed by microelectronics group of CERN for the time measurement in order to achieve a time resolution of 25ps. CERN HPTDC is a high performance multi-hit and multi-channel TDC chip with a programmable resolution of ~25ps–800ps, implemented in a 0.25μm CMOS technology.

A total of 32 channels are available with up to 100ps of bin size in the lower resolution mode, and only 8 TDC channels are available with 25ps of bin size in the highest resolution mode, since four low-resolution channels are used to perform a fine time interpolation.

Unlike the traditional Start-Stop type of TDC, HPTDC is a data driven multi-channel TDC[6]. The architecture of HPTDC is divided into two main functional units: A timing unit and a digital data processing and buffering unit, as shown in Fig. 10.3-8.

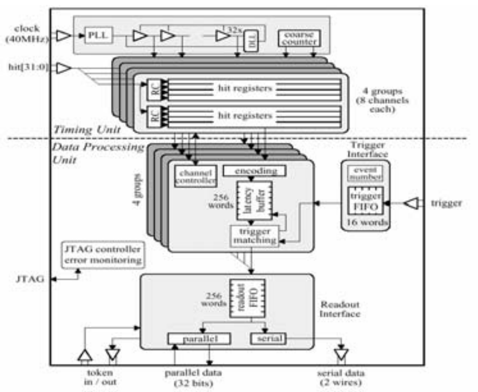

Fig. 10.3-8 The architecture of the HPTDC chip

❶ The Timing Unit:

The timing unit performs time digitization based on a clock synchronous counter (called "coarse" counter) and two types of interpolators. An on-chip PLL is used for clock multiplication up to 320MHz from an external 40MHz clock synchronized with the accelerator cavity's RF clock. A 32 elements Delay Locked Loop (DLL) performs time interpolation down to about 100ps. For the highest resolution mode, a fine time interpolation down to 24.5ps can be reached by using four samples of DLL generated by an adjustable on-chip *RC* delay line. Only 8 TDC channels can be used in this mode due to this fine time interpolation. With two kinds of interpolation, one clock period can be divided into 128 clock phases. In contrast to the coarse counter, the store of clock states with the interpolation mechanism is called the count of "fine" counter.

When a TOF hit signal comes, the current count of the coarse counter and the clock state recorded by the fine counter, as a time tag of the hit signal, are stored in the channel buffer with 25ps binning. When a L1 trigger signal comes, the current count of the coarse counter, as the time tag of trigger, is stored in the trigger FIFO with a 25ns binning.

❷ The Digital Data Processing and Buffering Unit:

The digital data processing unit encodes and stores the data previously digitized in four buffers with a depth of 256 words. Upon receiving the trigger-matching signal, data filtering is performed and only those related to the triggered event are forwarded to a readout FIFO, where it waits to be readout.

Trigger-matching is a time match between a trigger time tag and the time measurement themselves. To perform an exact trigger matching, the basic time measurement must be aligned with the positive trigger signal taking into account the actual latency of the trigger decision. The effective trigger latency in number of clock cycles equals to the distance between the coarse count offset and the trigger count offset. When no counter roll-over is used(roll-over = FFF hex), the relationship is simply:

$$\text{Latency} = [(\text{Coarse\_Count\_Offset}) - (\text{Trigger\_Count\_Offset})]\text{Modulus}(2^{12})$$

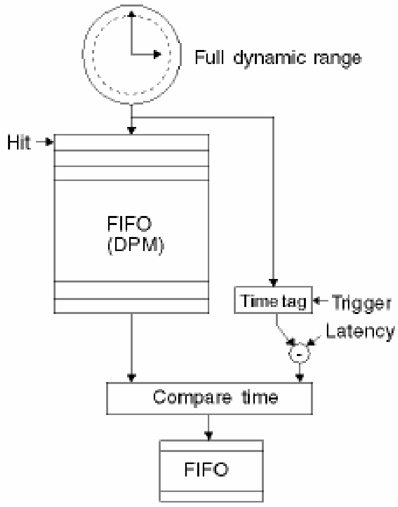

Fig. 10.3-9 Data drive TDC

As a data driven TDC, HPTDC only stores the time tag in the L1 buffer (FIFOs) when a hit has been detected. The hit time tag in the buffer is compared with the L1 trigger time tag, as shown in Fig. 10.3-9. Hits located inside a given time window are extracted as the trigger matching hit(See Fig. 10.3-10) and will be stored in the readout FIFO. Taking into account the total flight time for different particles and the detector size, the time window for the L1 trigger will be about 60 ns. The technical specifications of the HPTDC are listed in Table 10.3-2.

Table 10.3-2 Technical specifications of HPTDC

Number of channels	8 (Very high resolution mode) 32 (lower resolution mode
Clock frequency	40 MHz / 160 MHz/ 320 MHz
Time bin size	25 ps
Time resolution:	19 ps RMS *
Dynamic range	12 + 7 + 2 = 21 bit
Double pulse resolution	5 ns (if two hit registers free).

Max. recommended hit rate	8 MHz per channel
Event buffer size	4× 256
Read-out buffer size	256
Trigger buffer size	16
Power supply	2.25 ~ 2.75 V
Icc	Typical: 100 mA; Max: 200 mA
Temperature range	-40ºC~80ºC
Hit inputs	LVDS or LV TTL (3.3 V)

*: After the off line correction.

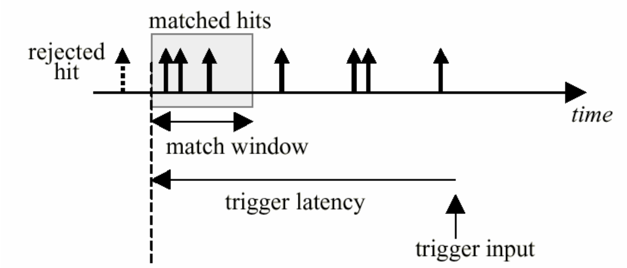

Fig. 10.3-10 Window based trigger matching

2. Two Options for Time Measurement with HPTDC

It is known that the HPTDC 1.2 has the following non-linearity problems:

- **INL from 40 MHz logic:**

The INL in the high resolution and the very high resolution have a fixed pattern of non-linearity caused by cross talks from the logic circuit of the chip running at 40MHz.

- **DNL at bin27:**

The DNL in the high resolution mode has a clear non-linearity in the timing bin27 plus multiples of 32.

Due to these non-linearity problems, the time resolution(RMS) of HPTDC 1.2 is about 69.8ps in the very high resolution mode as shown in Fig. 10.3-11 and table 10.3-3 according to the HPTDC manual (version 2.1) [2]. We expect the non-linearity problem will be solved in HPTDC 2.0 at the end of 2002. However, to ensure the 25ps resolution of TOF, two options are considered for the time measurement: HPTDC with or without a time stretcher.

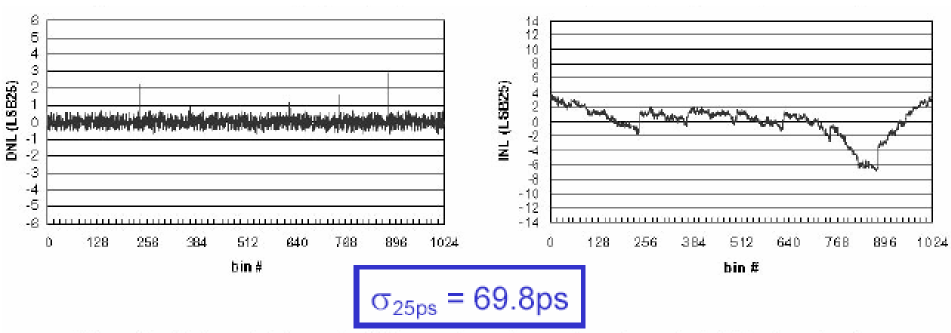

Fig. 10.3-11 DNL & INL graphs (25ps mode)

Table 10.3-3 Effective HPTDC resolution based on cable delay measurements

2.1.1.1.1.2 Mode	2.1.1.1.1.3 Resolution
Low resolution	0.34 bin (265 ps)
Medium resolution	0.44 bin (86 ps)
High resolution	0.65 bin (64 ps)
High resolution DLL tap adjust INL table correction	0.35 bin (34 ps)
Very high resolution	2.4 bin (58 ps)
Very high resolution DLL tap adjust INL table correction	0.72 bin (17 ps)

HPTDC without the time stretcher will be our first choice. As an alternative method, HPTDC with the time stretcher will be adopted in the case of no significant improvement of non-linearity in the final version of HPTDC, since HPTDC has the ability to simultaneously measure leading and trailing edges. An evaluation board of HPTDC with a time stretcher board from KEK has been started, and a new evaluation board with a monolithic integrated time stretch chip (MTS1) developed at KEK and at Hawaii university[7] will be started later. The prototype of MTS1 will be submitted soon and test will start around the end of 2002 [8]. The following is a brief list of MTS1's technical parameters:

▪ Process: Agilent 0.5 μm CMOS, 3 metal, single poly, linear Capacitor

- 8 Channels: 8 LVDS inputs & 16 LVDS outputs (2x 8 channels)
- Programmable Stretch factor: 1:1 to 1:20 (1:4 will be used in BESIII)
- Ping-Pong Mode
- RF clock: LVDS pair (up to 100MHz)
- Package: 84-pin TQFP

10.3.2.3 Charge Measurement

There are two schemes considered for the charge measurement: one is the current integral pulse amplitude measurement, and other is the pulse waveform digitization.

In principle, if the pulse into the FADC is well captured, accurate pulse amplitude and leading edge information can be obtained from the waveform. With the waveform recording at a very high sampling rate, such as 1 GSPS, the shape of each PMT pulse can be well measured, including rise and fall times, as well as any structure caused by pulse pile-up. Some commercial FADC chips are good enough in speed, but the cost and power consumption is too high for hundreds of TOF channels.

The Analog Transient Waveform Digitizer (ATWD) chip developed at LBNL lab[9] is a possible choice to be used to capture the PMT signal pulse. ATWD addresses the problem of capturing fast transient waveform of modest duration with miserly power consumption. It meets the speed, cost and power requirements of the BESIII TOF system.

Pulse amplitude measurement is a more traditional way for the charge measurement by integrating the current from the PMT. It has been successfully used in most of the current TOF FEE system.

Option 1: Pulse Waveform Digitization

❶ ATWD

As mentioned above, we plan to use the very high sampling rate(~1GPSP) waveform recorder to capture the PMT output signal. ATWD is a monolithic ADC chip with 10 bits resolution. It can simultaneously capture four channels of independent signals at a sampling speed from 300 MHz to 2GHz. The sampling action is generated internally without the need for external high-speed clocks, thus it permits extremely high sampling speeds while allowing engineers to design the board with a conservative board-level clock frequency (e.g. 40 MHz). The PMT waveform is captured at a high sampling rate and held temporarily as analog data in an array of storage capacitors within the ATWD. The sampling action of the ATWD is triggered by the discriminator at the high level threshold, and PMT signals will be delayed a few ns to ensure that baseline appears prior to the PMT pulse. The analog data are digitized subsequently with a 10-bit common-ramp parallel Wilkinson ADC, permitting the direct conversion on-chip of the captured analog signal. The ATWD v3 properties are summarized in Table 10.3-4.

Table 10.3-4 Properties of ATWD v3 chip.

number of input channels	4
number of samples/channel:	128
sampling rate	0.3 to 2 GHz, controllable by analog current
sample span	64 to 422 ns, depending on sample rate
Input bandwidth	> 300 MHz
Noise/maximum signal	0.001
Input signal range	0.2 to 3.0 V
Power dissipation	rate dependent, typically < 100 mW
ADC type	common-ramp 128 Wilkinson 10-bit

❷ Dead Time and Dual-ATWD "Ping Pang" Mode

The signal processing of ATWD can be divided into a sampling phase and a digitization phase. The sampling of the ATWD is triggered by a pulse from the discriminator at the high level threshold, and the analog data stored in an array of capacitors are digitized subsequently after the waveform is captured. Digitization and readout of the entire 128-sample waveform requires about 15μs for one channel and about 60μs for 4 channels at 40 MHz clock for the 10-bit range. If we arrange two PMTs from the two end of the same scintillator bar into the same ATWD chip, the dead time due to digitization per chip will be 30 μs. For the single channel hit rate of about 4KHz, the dead time is more than 10%.

Dead time may be brought to an insignificant level by employing two ATWDs, which can be alternately selected to maximize readiness. The board circuitry for each PMT output signal includes two ATWD channels, located in two ATWD chips individually. They alternately acquire waveforms in a "ping-pong" mode as shown in Fig. 10.3-12. The dead time only happens when three pulses occurs in the period of 30 μs. Such a probability follows the Poisson distribution, and can be calculated with the following formula [10]:

$$P(3,\Delta t)=\frac{(\bar{n}\Delta t)^3}{3!}e^{-\bar{n}\Delta t} \ = \ 2.56\times10^{-4}$$

where, $\bar{n}$ is the mean hit rate of single PMT(4KHz), and Δt the time interval(30 μs). It can be seen that this probability is negligibly small.

An evaluation board of ATWDs with "ping pang" mode is under development for testing.

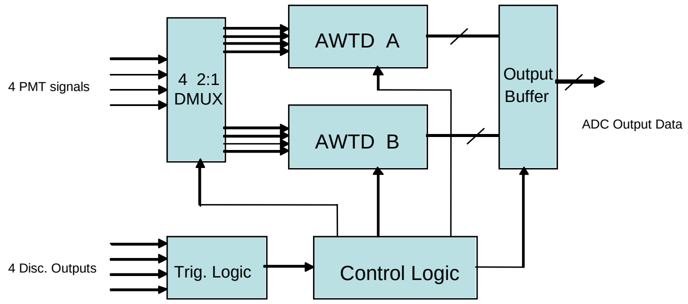

Fig. 10.3-12 A block diagram of "Ping Pang" mode

Option 2: Pulse Amplitude Measurement

Conceptually，this scheme is quite simple. Every time when the signal goes above the high level threshold of discriminators, a Q-V conversion by an integrator will happen, and the pulse amplitude will be measured by a 12 bits ADC. This digitized value is then stored for 3.2μs in a pipeline FIFO, waiting for being matched with the trigger signal. A simplified block diagram of one channel of pulse amplitude measurement is shown in Figure 10.3-13. It is similar to the scheme used by the BELLE TOF electronics [11].

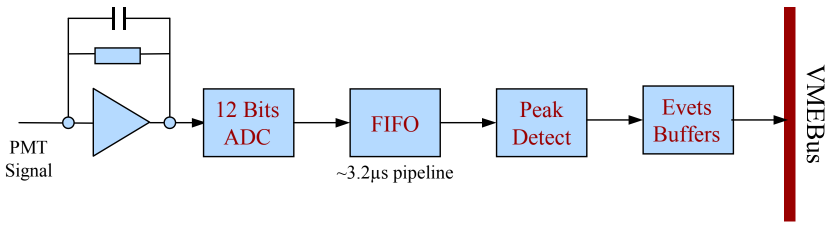

Fig.10.3-13 A simplified block diagram of one channel

One of the most attractive features of the scheme that digitizes continually is the possibility of providing a "pre-sample" of the baseline value just before the arrival of signal pulse. Not only will this aid in determining when pile-up may be affecting the time measurement of a given pulse, it may actually provide useful data in correcting for this effect.

An active plan of prototyping and testing has been undertaken to verify which circuit gives the best timing correction, within the confines of cost and the other system performance criterion listed in Table 10.3-5.

Reference Time for TOF Measurement

In order to derive a Time of Flight, the beam collision time in each event should be known precisely. For the BESII experiments, button type of beam sensors close to the interaction point was used to determine the beam crossing time, with a period of 5μs. However, the same scheme may not be practical at BESIII because of the very short crossing period of 8ns. Instead, we plan to use the RF clock from the superconducting cavity of the accelerator, which is precisely synchronized with the beam collision time.

A reference clock of approximately 25ns period will be generated from the RF signal of 500 MHz since a precise 40 MHz reference clock is needed for HPTDC as a reference time (t_0). The clock jitter should be less than 20ps, similar to that of the BELLE TOF system.

The phase/timing precision of the 40MHz reference clock is crucial. To achieve the designed goal of 90ps time resolution of the TOF system, the following design strategies will be adopted for the reference clock system.

- use PLL technique to generate 40MHz clock and clean up the input clock.
- use an optical transfer system with 80m Phase Stabilized Optical Fiber (PSOF).
- use low skew & low jitter clock driver for clock distribution.

A block diagram of the 40MHz reference clock circuit is shown in Fig.10.3-14. In this scheme, the 40MHz clock signal is generated from the RF signal of the SC cavity, transmitted to TOF electronics room with an 80 meters long optical fiber, and then fan out to all TOF FEE modules in the TOF electronics room. Another slightly different scheme transmit the RF clock to TOF electronics room with an 80 meters long optical fiber first, and then the 40 MHz clock is generated from this RF signal and broadcast to all of TOF FEE modules as shown in Fig. 10.3-15. The different of the two schemes is the frequency of clock signal transmitted in the optical fiber. The former is 40MHz, and the later is ~500MHz. It may be easy to transmit the clock signal with the lower frequency from the view of circuit design, but it is possible that PSOF can not work well in the lower frequency, such as 40MHz.

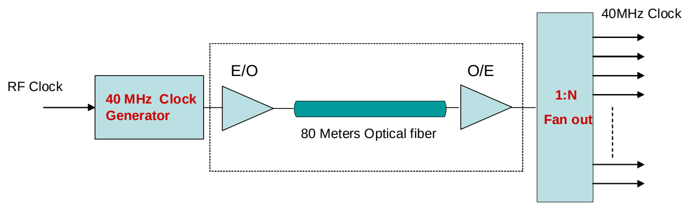

Fig. 10.3-14 Block diagram of reference clock system (Scheme A)

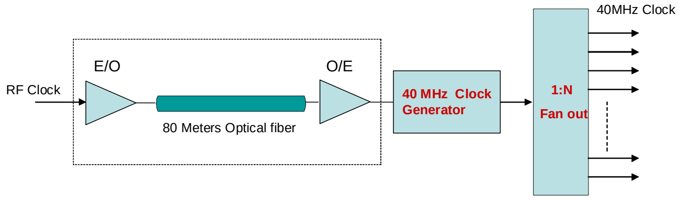

Fig. 10.3-15 Block diagram of reference clock system (Scheme B)

1. PLL

We plan to use a monolithic integrated PLL for 40MHz clock generation. In this way, the 40 MHz clock can be directly generated with only one PLL chip, such as SY89421V[12] of MICREL. With a ~500MHz input clock, it can output a ~40MHz clock with 10ps RMS (typical) as shown in Fig. 10.3-16.

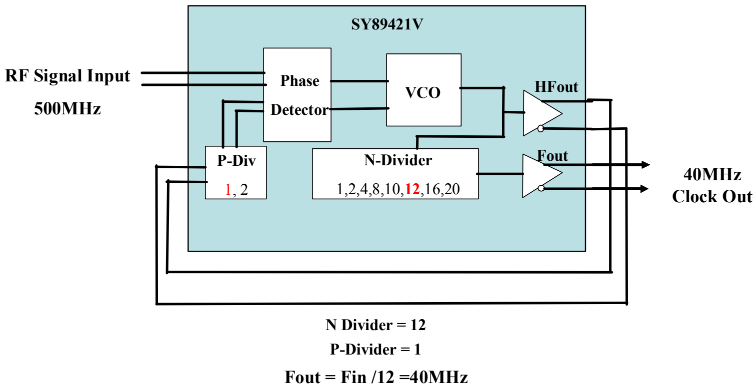

Fig. 10.3-16 Circuit for generating 40 MHz clock with SY89421V

2. Optical Transfer System

The optical fiber has many advantages, such as the temperature stability, low transmission loss, etc, for the long distance transfer of precise clocks compared to a coaxial cable. We plan to used the phase stabilized optical fiber (PSOF) made by Furukawa electric Co.[13] which has been successfully used in several experiments, such as LEP [14], Spring8 [15], KEKB [16] and KEK-ATF [17], due to its excellent stability against temperature variations. PSOF has a very low temperature coefficient (0.04 ppm/ ^{0}C) [18] compared with that of the ordinary optical fiber(6 ppm/ ^{0}C). For a short distance, 200m or less, PSOF can keep the phase stability without feedback. The time jitter was tested to be 1.1ps with 100 meters fiber cable for 508MHz at KEK[19].

3. Clock Distribution

Since one VME 9U module will assemble 16 FEE channels, a total of 28 VME

9U modules are needed for the whole TOF system at least. A 1:20 clock driver (NB100LVEP221) of On Semiconductor [19] has been considered for the clock fan out. NB100LVEP221 is a LVPECL/LVECL clock driver with 1ps RMS jitters. Two such chips will be enough for all of TOF modules.

By using SY89421V and NB100LVEP211 chips, the circuit which including 40MHz clock generator and fan out will be very simple. It's possible that only one NIM or VME 6U module is used for them. A test board for performance evaluation is under development as shown in the Fig. 10.3-17.

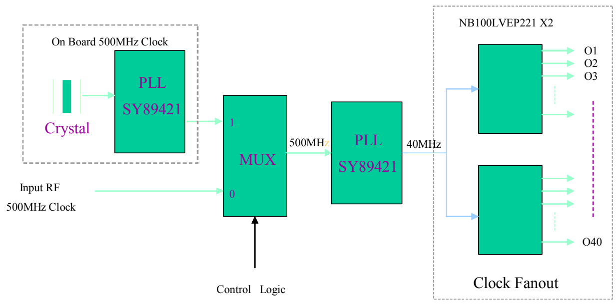

Fig. 10.3-17 Block diagram of clock test board

Summary

TOF frontend electronics is designed to work in pipeline mode with the capability of multi-hits. For time measurement, HPTDC developed at CERN will be our choice, and the time stretcher may be used together with HPTDC depending on the performance of the final version of HPTDC chip. A precise 40MHz reference clock, which is directly from the SC cavity is used for time reference, as well as for whole system as a system clock.

For charge measurement, ATWD chip for the waveform digitalization may be used in order to obtain more information from PMT signal. It is very useful for the walk correction and eliminating backgrounds. Using "Ping-Pang" mode can effectively eliminate the dead time caused by ATWD digitalization time. In addition to waveform digitization, traditional pulse amplitude measurement is also under development as an alternative scheme.

Detailed design of several testing boards is in progress according to the schedule. Table 10.3-5 below lists the Specifications of the TOF electronics system of BESIII.

Table 10.3-5 Specifications of the TOF electronics system

2.1.1.1.1.3.1.1 Electronics Requirements	
Discriminators(leading edge)	896 channels HL: 448 channels LL: 448 channels
Time Measurement	448 channels Barrel: 352 Endcap: 96 HPTDC:56(without TS) HPTDC:28 (with TS) Resolution: 25ps RMS Full Range: 0 ~ 60ns
Charge Measurement	448 channels Barrel: 352 Endcap: 96 ATWD: 224 (ping pang) Crosstalk: < 1% INL: < 2%
Fast Trigger Signals	Barrel: 176 channels (Mean Timer) Endcap: 96 channels
L1 Trigger	Trigger Rate: 4K/S
40 MHz Reference Clock	Fanout: ~ 30 Jitters: <20ps RMS PSOF: 80 meters Signal: LVPECL or LVDS
Pre-Amplifiers	176 (CCT)
Card Package FEE Clock Fanout & others:	 VME 9U NIM or VME 6U
TDC Parameters	
Bin size	25ps (Without TS) 100ps (With TS)
Dynamic Range	21 bit
Input Signal	LVDS
Clock	40MHz
Package	BGA
Time Stretch factor	4
ADC Parameters (ATWD)	
Resolution	10 bits
Sample Rate	> 1GSPS
Input Range	0~3V
Clock	40MHz

Reference

[1] BESIII collaboration, "The BESIII detector (Draft)", Beijing, June 2002

[2] J．Christiansen, "High performance time to digital converter" Version 2.1, July 2002, CERN/EP-MIC.

[3] MAXIM Inc.,
MAX9693 http://pdfserv.maxim-ic.com/arpdf/MAX9691-MAX9693.pdf
MAX9601 http://pdfserv.maxim-ic.com/arpdf/MAX9600-MAX9602.pdf

[4] Analog Device Inc.,
AD96687 http://www.analog.com/productSelection/pdf/AD96685_7_d.pdf

[5] SPT Inc., SPT9693 http://www.spt.com/datasheets/products/9693.pdf;
SPT9689 http://www.spt.com/datasheets/products/9689.pdf

[6] J．Christiansen et al, "A data driven high performance Time to Digital Converter"

[7] Gary. S. Varner, "High Precision Time-Of-Flight: Belle Experience and Future R&D", BESIII meeting, Beijing, June, 2002

[8] Gary. S. Varner's email. Aug. 10, 2002.

[9] Stuart A. Kleinfelder, Gerald T. Przybylski, "Analog Transient Waveform Digitizer R1.1 (V2)", Lawrence Berkeley National Laboratory, July 31, 2001.

[10] JingjinWang et al，"Nuclear Electronics"，page 50, Atomic Energy Press, 1983.

[11] Gary. S. Varner, "A Proposal for a Front-end Fastbus Module to Process the TOF PMT Signals", June 17, 1995.

[12] MICREL Inc., http://www.micrel.com/product-info/products/SY89421V.html

[13] FURUKAWA Electric, http://www.furukawa.co.jp/english/index.htm

[14] L. de Jonge et al, "RF reference distribution for the LEP energy upgrade ", EPAC'94, London, Jul. 1994.

[15]H. Suzuki et al, "Characteristics of RF Reference Signal Distribution for Spring8", The 9th Symposium on Accelerator Science and Technology, Tsukuba.

[16]T. Naito et al., "Performance of the timing system for KEKB", KEK internal, 96-3, 1996.

[17]T. Naito et al., "Timing System of the ATF", ICALEPCS'97, Beijing, Nov. 1997.

[18]T. Naito et al., "RF reference distribution using fibre-optic links for KEKB accelerators".

[19]T. Naito et al, "Synchronization scheme for the KEKB accelerator", CALEPCS'97, Beijing, Nov. 1997.

Muon Counter Electronics

Muon counter (MC) is constructed with 9088 channels (4992 at the barrel and 4096 at the endcup) by Resistive Plate Chambers (RPCs). The tasks of the MC readout system are to transform the information from strips of the RPCs into digital data, handle the data of the event after trigger signal, store the data into the sub-event buffers with the relative header, and wait for calling by DAQ system.

The readout system of the MC contains one VME crate and four power supply crates. In the VME crate there is a readout module containing 40 data chains, each of which is composed of the 256-bit data from the strips of the RPC. The readout system is able to scan 10,240-bit data in parallel in order to satisfy the requirement of the MC.

In addition, the electronics system of the MC contains a test subsystem, which can test the whole readout system online.

Requirement of Electronics Design

(1) Output Signal of Detector

The position information of a particle hit is obtained from the strips of RPCs, whose waveform of the output signal is shown in Fig.10.4-1.

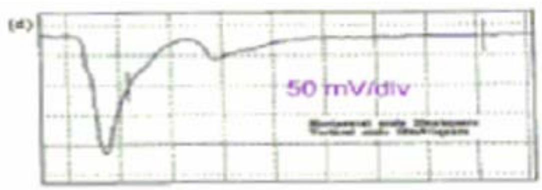

Fig.10.4-1 typical output signal of RPC

The features of the output signal of the RPC are listed is the following:

Typical amplitude(50Ω)	700 mV
Minimum signal amplitude(50Ω)	100mV
Maximum signal amplitude(50Ω)	800mV
Typical signal width	50ns

(2) Hit Rate

The dark rate of the RPC is typically 0.10 Hz/cm^2, hence the accidental hit is below 10 per event. A typical physics event generates at most a few tens of hits.

(3) Deadtime

The readout system of the MC is no deadtime because of the usage of the pipeline in the Front-End Card (FEC).

(4) Threshold

The threshold, which can be adjusted by the software, is the same for all of the discriminators in the FECs. The accuracy of the threshold level is 1%.

(5) Trigger

Trigger latency	6.4 μs
Trigger latency jitter	±200ns
Average trigger rate	4 kHz

(6) Test System

All the test signals of the channels have the same amplitude, with an accuracy of 1%.

The optimization for the performance versus the design of the MC readout system must be considered carefully considering the cost for 9,088 channels.

Configuration of Readout System

The readout system of the MC consists of a readout subsystem, a threshold control subsystem, and a test subsystem. The muon readout system, shown in Fig. 10.4-2, constructed by a 9U VME crate located above the detector, which contains a system control module, a readout module, 4 I/O modules, and 14 JTAG control modules.

1. Control Module

The control module receives the trigger signals (L1, Clock, Check, and Reset) from the trigger system and transmits them to the FECs through the I/O modules. It also receives commands such as setting thresholds testing, etc., and transmits them to the FECs. The control module is also a transceiver which transfers the FULL signal between the readout module and FECs.

2. I/O Module

The VME crate contains four I/O modules, each of which consists of 12 I/O sockets connected by a data chain, to satisfy 36-40 data chains of the design requirements. The I/O module drives and transmits the signals of the clock and trigger to all the FEC's, the signal ReadoutBufferFull signal from the readout module to the FEC's, and the signal FECBufferFull signal from the FEC's to readout module.

3. Readout Module

The readout module is responsible for all the operation relative to data readout. It not only reads and suppresses the data from all the data chains, constructs the sub-event data to save into the buffer, and requests the interrupt to the DAQ system to processing the sub-event data, but also communicates the Full signals to the FEC's to control the data transmission. The readout module checks and resets L1 signal and sends the Buffer FULL and RERR signal to the trigger system. It controls the reading and suppressing of the FEC data, requesting interrupt to DAQ, counting and resetting the trigger number. One readout module can in principle read all the data of the muon event since the event sign is only 600-byte and the total data rate is only 2.4Mbyte/s (refer to paragraph 10.4.3). However, due to the limited area of one VME module, it is possible that multiple reading module are necessary and data have to be transferred to DAQ by the mode of Chained Block Transfer(CBLT).

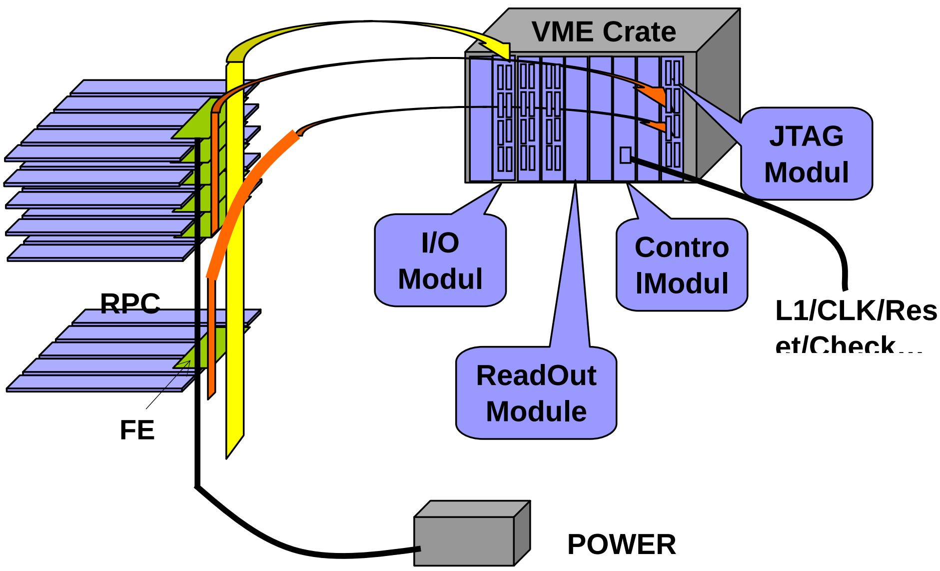

Fig.10.4-2 Configure ratios of electronics system of MC

4. Frond-End Card

The 16-bit data from the strips are read and stored in parallel into a 16 bits shift registers, which are connected to a 16-shift daisy chain. A total of 16 FECs compose one FECs Daisy-Chain, which covers 256 strips. The data of each chain as position information, are transferred bit by bit to the readout module in VME crate through the I/O modules using differential LVDS signals. Each data of the chain will be stored temporarily in the relative data chain buffer of the readout module after the data suppression, then all the chain data will be stored into the sub-event data buffer to waiting for the DAQ processing.

The whole system consists of 36-40 chains, each contains 256-bit. Therefore it can represent position information of 10,240 channels and satisfy the requirement of the muon readout system.

In each FEC there is a DAC chip, which is used to generate the test signal. When a test command goes to the test signal generator located in the system control module in the VME crate, the generator transforms the command into series timing pulses for controlling the DAC, and then sends the timing pulses to FEC through the I/O module. The timing pulses set the DAC chip which deliver a test signal to each input port of the channels' comparators to test the FEC operation.

The principle of the threshold setting circuit is the same as the test circuit. The timing pulses are generated by the threshold controller in the system control module, sent to the DAC to generate the threshold level at each of the input ports of the discriminators in the FEC.

5. JTAG Module

The JTAG module gets the FPGA setting command from the VME BUS, transforms the command into the JTAG control timing, and sends to the FECs. The muon readout system contains 14 JTAG modules, each of which has 12 slots on the panel of the module (1 slot for 4 FEC's JTAG setting). Therefore, the JTAG modules satisfy the requirement of the whole readout system.

Readout System

1. Front-End Card (FEC)

The FECs are located in the RPC detector, whose block diagram is shown in Fig. 10.4-3.

The task of the FEC is to transform signals form the strips into bit map through the discriminator, store the data into the buffer on the FEC for 6.4 μs, waiting for a trigger signal. Events with a trigger will be transmitted into the chain event buffer in the VME readout module others will be cleared, the buffer will be filled by the next event input signals.

The analog signal from the strip of the RPC is transformed into digital signal via the discriminator on the FEC through twisted flat cable. The data of 16 channels are stored in the FIFOs of the FPGA waiting for the trigger signal. The output of the shift registers of the FPGA becomes 16-bit serial stream to be connected to the next FEC in the daisy chain mode when the trigger signal occurs. There is also an “OR” gate of 16 inputs to generate a FAST-OR signal for the trigger system (not shown in the Fig.10.4-3).

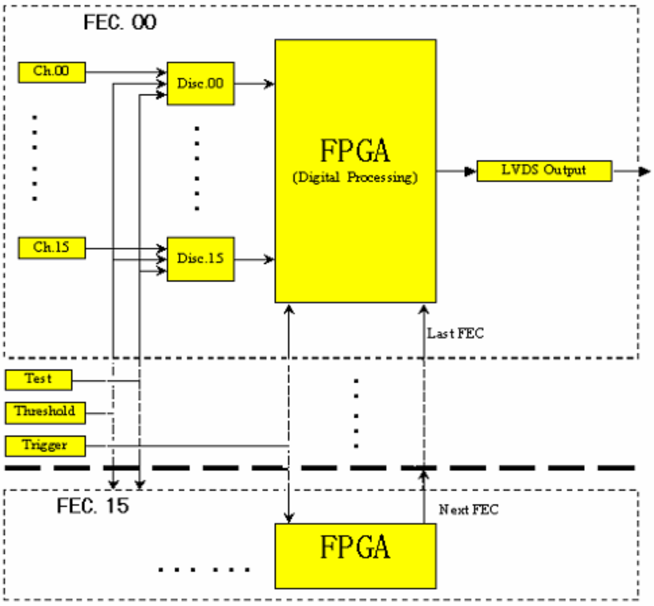

Fig.10.4-3 Block diagram of FEC

The block diagram of the FPGA is shown in the Fig.10.4-4, also in this figure it shows that the pipeline technique is used in the FPGA to avoid the deadtime of the readout system.

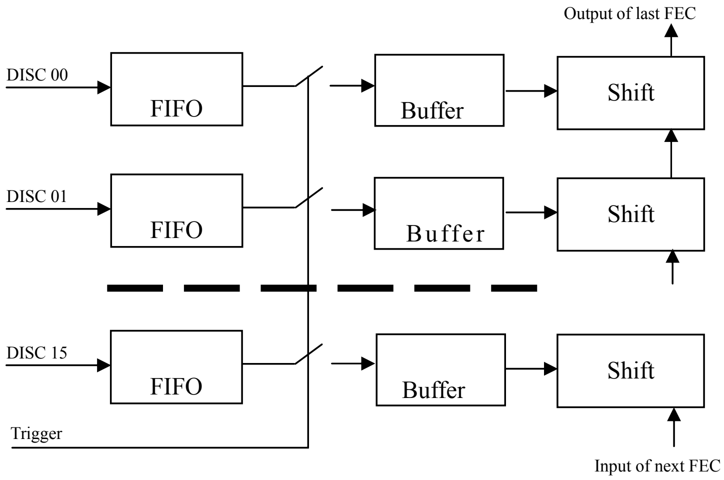

Fig.10.4-4 Block diagram of FPGA

There are two buffers in each FPGA. The first buffer is FIFO used as the pipeline buffer, whose depth is equal to the total among of data during the trigger latency including possible jitter. The second buffer is for storing the data and avoiding data loss when the trigger signal occurs again during the time when good event are being transmitted into the VME readout module through the 18 m twisted flat cable using LVDS logic. Please refer to the Appendix A for the estimation of the depth of the second buffer in the FEC.

The upset of the FPGA may appear due to the huge discharge during the time of the beam loss, sometimes even leads to the physical damage of the FPGA. Meanwhile, the Single Event Upset (SEU) and Single Event Latch-Up (SELU) could appear due to radiation damage. To prevent the FPGA chips in the FECs from the above problem, a reload cable of the FPGA, a monitoring circuit for checking SEU, SELU and operating current of the FPGA are incorporated in the FEC design. The monitoring circuit will have a warning-message in order to reloads the FPGA code or cuts the current of the power supply of the FPGA if the FPGA chips have problems. The current limit for avoiding the FPGA SELU must be studied under the irradiation test of the FPGA chip in order to ensure the reliability of FEC.

2. VME Readout Module

Data coming from FECs will be suppressed at first, and then stored into the chain event buffers. One VME readout module, which contains 40 data chains, is able to receive the data from all the channels of the system in parallel. Data in chain event buffers will be stored into a sub-event buffer with a data header, such as the trigger number and the operation number, waiting for the DAQ processing.

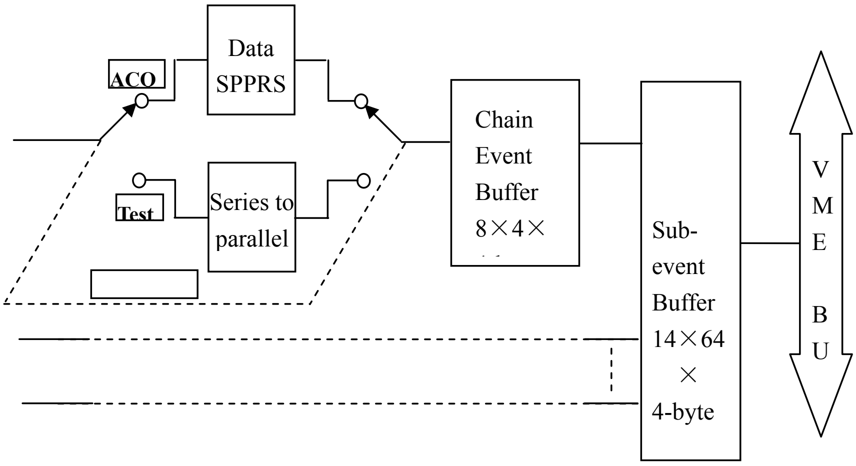

Fig.10.4-5 Block diagram of VME readout module

The block diagram of the VME readout module is shown in Fig.10.4-5. The module works in the test mode when the switch is at the position of test.

(1) Data suppression

The RPC of the MC is a low occupancy detector. A physic event can generate at most a few tens of hits.

There are two methods of data suppression we can think of zero suppression and format, suppression by the FEC.

As shown in Fig10.4-6, the data suppression by the FEC is to store all the data of 16 channels of a FEC if any of the 16-channel is non-zero. The 10-bit code expresses the address of the FEC; and the 16-bit code expresses the data of 16 channels, one for each channel.

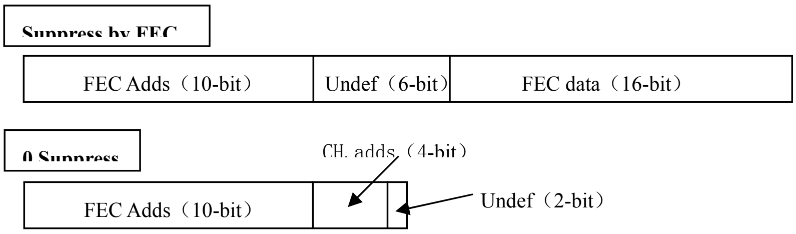

Fig.10.4-6 Two methods data suppression

The method of the zero suppression is to remove all zeros and only the datum 1 is stored. The 10-bit code expresses the address of the FEC and the 4-bit code expresses the channel address in a FEC.

Let's now compare data rate for these two suppression schemes. For each physics event, the total number of hits is assumed to be 100 and each hit has 5 channel (strip) signals. In the scheme of data suppression by the FEC the 100 hits of the RPC are divided into two parts: the first part (50 hits) has all the 5 channels for each hit distributed in one FEC, then its compressed data are

4 bytes/FEC x 50 FEC = 200 bytes

The second part (another 50 hits) has the 5 channels for each hit distributed in two FEC, the compressed data are

4 bytes/FEC x 50 FEC x 2 = 400 bytes

The compressed data for an event is 600 bytes; and the data rate after compressing with a trigger rate of 4 kHz is 2.4 Mbytes/sec.

In the scheme of zero suppression, the data are encoded for individual channels, so the total number of channels for 100 hits is

100 channels x 5 = 500 channels

The total amount of data is

2 bytes x 500 = 1 Kbytes

Hence the data rate after compressing with a trigger rate of 4 kHz is 4 Mbytes/sec.

The data rate of the zero suppression is more than that of the suppression by the FEC. We choose the suppression by the FEC in our readout system of the MC.

(2) Depth of the chain event buffer

The size of the chain event buffer can be a 2 x 4-byte matrix for one bank of event, but more banks are necessary in order to avoid the loss of good data if the trigger signal occurs during the data transmission from the chain event buffer to the subevent buffer.

The readout system may lose 1.97 event data at a trigger rate of 4 kHz for 8 hours if 6 banks of the chain event buffer are used. This data loss is negligible, and the chain event buffer does not contribute to the deadtime of readout system.

The estimation of the depth for chain event buffer is described in detail in appendix A.

(3) Depth of the subevent buffer

The size of the subevent buffer is a 64 x 4-byte matrix for 16 chains of data, as a bank of the subevent buffer. However, we need more banks in the subevent buffer in order to avoid the data loss if the trigger signal occurs during the DAQ processing.

The readout system will lose 1.13 event data in 4 kHz trigger rate for 8 hours if 12 banks of the chain event buffer are used. This event data loss is negligible.

The estimation of the depth for subevent buffer can be seen in the appendix A.

Test System

The test system for the readout system consists of a test control module in the VME crate, and a test function generator in the FEC.

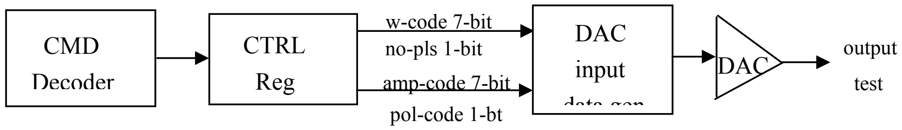

Fig.10.4-7 Block diagram of the test system

The test control module sends commands to the FEC after receiving them from the VME bus. The test command is transformed into serial control timing pulses by the input timing generator in the test control module through the command decoder and the control register. The timing pulses are sent to the test function generators on the FECs through the I/O module in the VME crate to set the DAC chip, which generates analog signals according to the timing to feed comparators on the FEC.

The test system has the following commands:

TWE – write the control register to control the output signal (yes/no);

TWC– write the control register to adjust the width, the amplitude, and the polarity of the signal.

The block diagram of the test system is shown in Fig.10.4-7.

In the Fig.10.4-7 the data of the command in the control register generated by the command decoder, are 7-bit width code, 1-bit yes/no code, 7-bit amplitude code, and 1-bit polarity code. These DAC setting cod are sent to DACs on the FEC to generate analog signals.

Threshold-Setting System

The principle of the test system and the threshold-setting system is almost same.

The difference is just that the threshold-setting system offers a level, which is not an analog signal as that of the test system.

The threshold-setting system for the readout system consists of a threshold-setting control module in the VME crate, and a threshold-setting generator in the FEC.

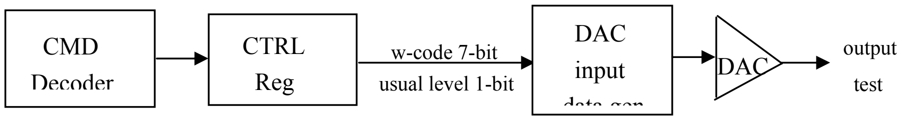

Fig.10.4-8 Block diagram of threshold-setting system

The threshold-setting control module transforms the command into the control data and sends them to the FEC after receiving the command from the VME bus. The threshold-setting command is transformed into serial control timing pulses by the input timing generator in the threshold-setting control module through the command decoder and the control register. The timing pulses are sent to the threshold-setting generators on the FECs through the I/O module in the VME crate to set the DAC chip, which generates a level according to the timing for comparators on the FEC.

The threshold setting system has the following commands:

DWN – write the control register to have the usual threshold level;

DWC – write the control register to adjust the level of the threshold.

The block diagram of the threshold setting system is shown in Fig.10.4-8.

In the Fig.10.4-8 the data of the command in the control register generated by the command decoder, are 1-bit code for usual threshold and 7-bit amplitude code. These DAC setting code are sent to the DACs on the FEC to generate the threshold level.

Errore.

Appendix A

Estimate of the Buffer Depth

(A) Formula of buffer depth

For a buffer with 0-k cells, the input data rate to the buffer complies with the Poisson distribution, i.e.

$$f(t) = \lambda e^{-\lambda t}$$

where λ is the average input data rate. The data service rate out of the buffer complies with the Poisson distribution too, i.e.

$$b(t) = \mu e^{-\mu t}$$

where μ is the average service rate out of the buffer. A state map of the buffer is shown in Fig.10.4-9.

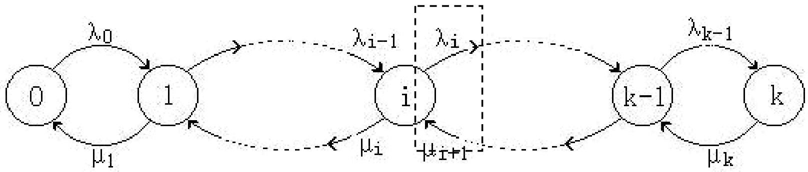

Fig.10.4-9 State map of buffer

The probability of cell i at the dynamic balance follows

$$\lambda_i \cdot P_i = \mu_{i+1} \cdot P_{i+1}$$

$\overline{\lambda}$ and $\overline{\mu}$ denote the average value of λ and μ， we have

$$P_{i+1} = \frac{\overline{\lambda}}{\overline{\mu}} \cdot P_i = \eta \cdot P_i$$

then the probability for the appearance of the k state is

$$P_k = \eta^k \cdot P_0$$

where $\eta = \overline{\lambda}/\overline{\mu}$ is the transferring ratio.

According to the completeness of the probability we have

$$P_k + P_{k-1} + \cdots + P_1 + P_0 = 1$$

i.e.

$$\eta P_k + \eta P_{k-1} + \cdots + \eta P_1 + \eta P_0 = \eta$$

We then obtain

$$P_0 - P_{k+1} = 1 - \eta$$

$$P_0 = \frac{1-\eta}{1-\eta^{k+1}}$$

since $P_k = \eta^k P_0$, the above equation can be expressed as

$$P_k = \frac{1-\eta}{1-\eta^{k+1}} \cdot \eta^k$$

that means, if all the cells of the buffer have data and the data arrive to the cell k under input rate $\bar{\lambda}$ again, the data loss is

$$\Delta\lambda = \lambda P_k$$

The relative data loss in a buffer is

$$\frac{\Delta\lambda}{\lambda} = P_k = \frac{1-\eta}{1-\eta^{k+1}} \cdot \eta^k$$

Using above formula, we can estimate the relative data loss or absolute data loss of a buffer with a depth of k cell.

If a large buffer consists of several banks with the same number of cells, the above formula is valid because the property of a bank is the same for a cell, whose data input rate and data service rate both comply with the Poisson distribution.

(B) Estimation of depth for of buffer in FEC

The data flow is shown in Fig.10.4-10. It is from the FIFO on FECs to the chain event buffer after suppression part in the VME readout module through the LVDS transceiver.

The delay time of the operation, which is the transmitting time for the data from FIFO on the FEC to the buffer of the data chain, is

25 ns＋LVDS delay＋25 ns＋150 ns＋T01 ＝ 350 ns

where the LVDS delay is the time from TTL to LVDS level, which is negligible; T01 includes delay time of the data compression and data storage into chain event buffer, which is about 150ns.

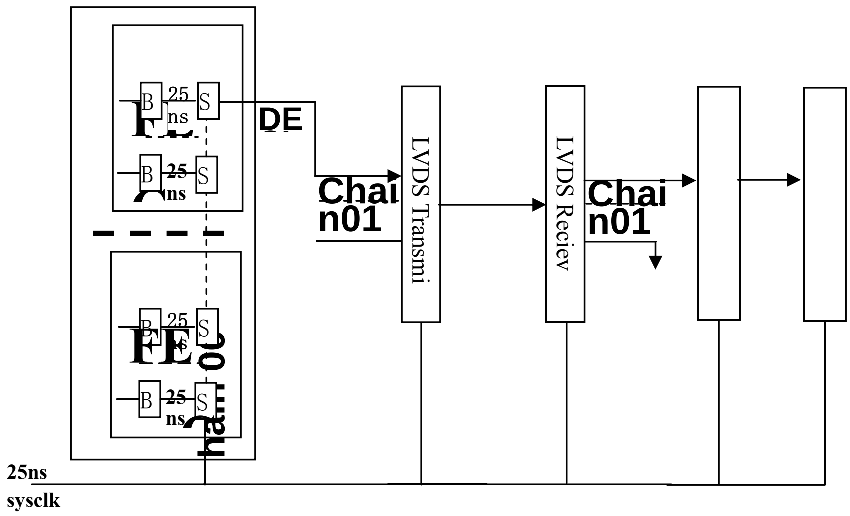

Fig.10.4-10 Data flow of a readout chain

The delay time of all of the data, moving from a 256-shift daisy chain to a chain event buffer, is

$$256 \times 25\ \text{ns} + 350\ \text{ns} = 6400 + 350 = 6.75\ \mu\text{s}$$

Using the above formula, the relative data loss of the FIFO on the FEC is estimated to be 1.40 x 10-8 under the condition of 4 kHz trigger rate, 75.76 kHz (1/6.75μs) service rate and 5 banks. This corresponds to a loss of 1.61 event in 8 hours.

(C) Estimation of the depth for chain event buffer

Using the above formula, the relative data loss of a chain event buffer during the transmission from the chain data buffer into the subevent buffer in the VME readout module is estimated to be 1.71×10^{-8}, under the condition of 4kHz trigger rate, 78.1 kHz (1/12.8μs) service rate and 6 banks. This corresponds to a loss of 1.97 event in 8 hours.

(D) Estimation of the depth for subevnet buffer

If the DAQ data readout rate is 18Mbytes/sec, the event sign is 600 bytes/event, the readout time by DAQ is then about 30μs; the time for sub-event build in the PowerPC is about 20μs; hence the total time for event readout is 50μs.

Using the above formula, the relative data loss from a subevent buffer to the VME readout module is estimated to be 3.28 x 10-9 under the condition of 4kHz trigger rate, 20 kHz (1/50μs) service rate and 12 banks. This corresponds to a loss of

1.13 event in 8 hours.

Trigger System

The trigger system is a fast real-time event selection and control system. It selects interesting events for physics and suppresses backgrounds to a level that the DAQ system can sustain. Since BEPCII will operate with a bunch crossing time of 8ns and a peak luminosity of 10^{33} cm^{-2} s^{-1}, a new trigger system must be built to match the new beam structure and the high event rate.

Estimation of Event Rate

A good understanding of the expected trigger rate for the luminosity of 1033 cm^{-2} s^{-1} is desirable to determine the architecture of the trigger and the front-end electronics. Besides physics events, various backgrounds from the machine and cosmic-rays also contribute to the total event rate. The main backgrounds in BESIII will be the machine backgrounds by Coulomb scattering and Bremsstrahlung with the residual gas and Touscheck scattering in the single bunches. A good way to estimate machine background rate is to simulate lost beam particles and synchrotron radiation which can be found in section 4.2. Here we estimate background with our experience at BESII.

Good Physics Events

The peak luminosity of BEPCII is designed to be 1×10^{33}cm^{-2}s^{-1}, the event rate will be 2000Hz and 600 Hz at the J/ψ and ψ′ resonance respectively. The Bhabha event in the detector coverage ($|\cos\theta| < 0.95$) will be about 800 Hz. Although Bhabha event will be used for detector calibration and luminosity measurement, its rate is too high to be acceptable, we will use a prescaler to reduce bhabha event rate.

Cosmic Ray Background

The cosmic-ray flux at Beijing's altitude is 170 m^{-2}s^{-1}. The full size of the BESIII detector is roughly the same as that of BESII, so the cosmic-ray event rate will be about 170 m^{-2} s^{-1} $\times$ 3 m $\times$ 3 m = 1500 Hz. At BEPC/BESII, 95% of the cosmic-ray background is suppressed by the TOF signal with a time window of 40ns and only 1Hz is recorded with further help of the Vertex Chamber. While in BEPCII the bunch spacing is too small to use a time window, and there will be no vertex chamber, we will use MDC trigger to reduce the cosmic-ray rate to less than 200Hz.

Machine Background

The machine background is mainly caused by the lost beam particles and its interaction with the detector. The beam current of BEPCII will be 40 times higher than that of BEPC with only a half beam lifetime (τ_{BEPCII} =3.5~3.8hr). Therefore the electron lost rate, correspondingly the beam background, will be 80 times of that of BEPC. Electron and positron lost rate is estimated to be (dn / dt) = 8.7×10^{8}/s. Suppose the lost electrons and positrons are distributed uniformly around the BEPCII ring, the number of lost e^{+}, e^{-} hitting the detector is $(dn/dt)_{BESIII} \approx 1.3\times10^{7}$/s, i. e., a background event rate of 13MHz. This is a conservative estimation, because the lost of electron and positron would be mainly around the quadruple, not uniformly along the beam pipe. Fig.11.1-1 is a measurement of background from an inner single wire of MDCII versus the beam current in BEPC. With the experience of BESII trigger, we estimate the beam background which may pass the trigger is about 2000Hz.

Fig.11.1-1. Background rate from one wire in the first layer of MDC Vs beam current

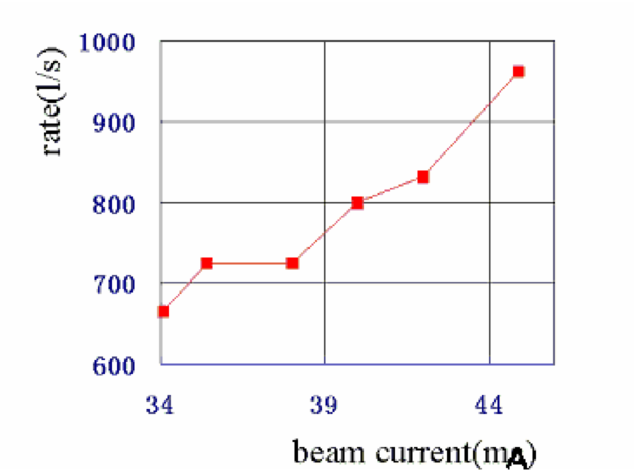

Total Event Rate

The BESIII trigger system should suppress the event rate from 1.3×10^{7} Hz to a maximum event rate of about 4000Hz, including 2000 Hz from physics, which is sustainable for the DAQ system.

Requirement of BESIII Trigger

The design goal of the trigger system is to keep the total dead time at a level of a few percent, similar to that of BESII. This was achieved by designing a trigger system with several levels, the lowest level is very fast and may suppress most of the backgrounds without dead time, and the high level is very complex but may introduce a small dead time. This scheme can not be used in BESIII because we face different constrains.

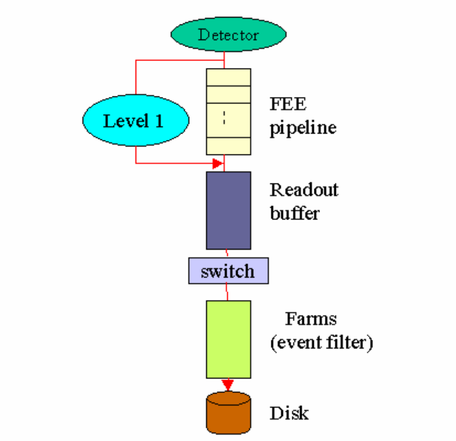

Fig.11.2-1 BESIII event flow chart

Unlike in BEPC where the bunch spacing is 800ns which leaves trigger system enough time to process various sub-detector signals and make the decision before next collision, in BEPCII the bunch spacing is only 8ns, which is too short to generate any trigger. This situation is further complicated by the fact that the arrival time of the Time of Flight (TOF) signal has an intrinsic spread of 30ns due to the different decay products of the J/ψ and ψ ' resonance with different momenta at different hitting position of the scintillater. It is impossible to identify a single bunch, and to determine which bunch an event originated from by hardware. This fact allows to set the trigger sampling period several times longer than the bunch spacing, and to simplify the design of the pipeline components. The period is chosen to be 25ns which is three times of the bunch spacing, so the signals from different sub-detectors will be binned into 25ns wide time slices and be processed in each pipeline step.

The TOF signals will be ready in 30ns after the collision， While it is 400ns for MDC due to the drift time of electrons. The trigger signal goes to the digitization card which is placed near detectors through a long cable for the signal delay. The trigger system needs time to process and synchronize all signals from sub-detectors. There must be a latency for the trigger signal to be delivered, within which signals from detectors are processed in FEE and kept in FEE pipeline buffer, until the trigger system completes the level 1 decision.

Therefore the BESIII trigger system will be in two levels, level 1 for hardware trigger and level 3 for software event filter as shown in Fig.11.2-1. Signals from different sub-detectors are split into two paths, one is digitized and stored in the pipeline of front-end electronics (FEE), the other is fed to the level 1 hardware trigger to be processed for further trigger decision. The latency between the level 1(L1) trigger signal and the event time origin is set to be 6.4μs. Data are moved from the FEE pipeline to the buffer when a L1 signal presents. The DAQ system reads the event data from each sub-detector buffer, packs them into an event, and sends them to the online farm where the level 3 trigger (software filter) filters the background events further.

Structure of Trigger System

The BESIII trigger system consists of MDC, TOF, EMC, Track Matching, and global trigger subsystems as shown in Fig.11.3-1. Electronic signals from sub-detectors are received and processed by the appropriate circuits in VME crates to

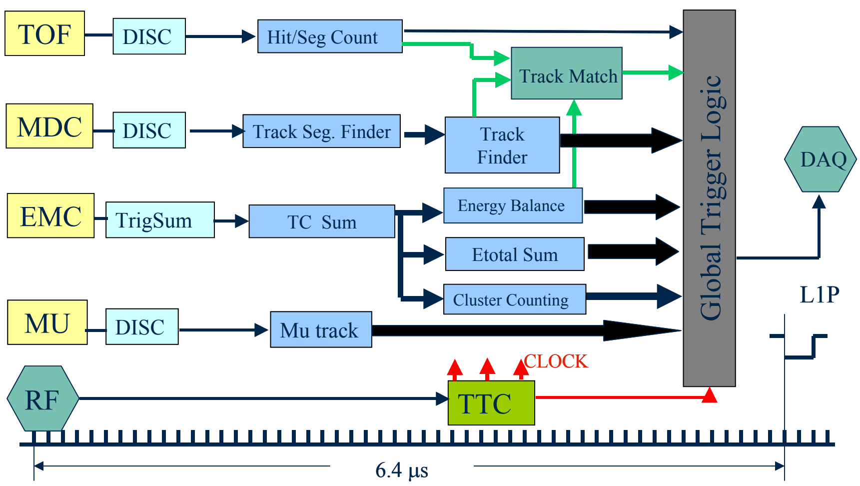

yield basic trigger information such as the hit counts in TOF, track counts in the drift chamber, the cluster count and topology in the electromagnetic calorimeter. These information from sub-systems are correlated to track matching and sent to global trigger logic (GTL) which generates an L1 strobe every time a valid trigger condition is satisfied. The timing and control circuitry conditionally pass the L1 signals to the fan-out modules for distribution to the data acquisition system (not shown here).

MDC Trigger

The function of the MDC trigger is to select charged tracks with a certain transverse momentum and rejects charged background, and provides information like number of tracks and angle/position of tracks to track matching and global trigger subsystem.

The drift chamber consists of 6860 small cells in the inner chamber (8 layers) and outer (35 layers) chambers. All cell signals will be used in trigger system and are arranged as axial wire layers (AX) and stereo wire layers (ST). There are 5 Axial super layers (SL) and 7 stereo super layers, each with 4 wire layers (WL) (the last superlayer has only 3 layers), as shown in Table 11.4-1.

Table 11.4-1 Parameters of the MDC trigger

Super Layer	Wire Layer	# of sig.				# of WL in SL	Symmetry	Total sig. in SL	# of pivot cells SL
		L1	L2	L3	L4				
SL-1	ST-1/2/3/4	40	44	48	56	4	1/4	188	44
SL-2	ST-5/6/7/8	64	72	80	80	4	1/8	296	72
SL-3	AX-9/10/11/12	76	76	88	88	4	1/4	328	76
SL-4	AX-13/14/15/16	100	100	112	112	4	1/4	424	100
SL-5	AX-7/18/19/20	128	128	140	140	4	1/32	536	128
SL-6	ST-21/22/23/24	160	160	160	160	4	1/32	640	160
SL-7	ST-25/26/27/28	192	192	192	192	4	1/32	768	192
SL-8	ST-29/30/31/32	208	208	208	208	4	1/32	832	208
SL-9	ST-33/34/35/36	240	240	240	240	4	1/32	960	240
SL-10	AX-37/38/39/40	256	256	256	256	4	1/32	1024	256
SL-11	AX-41/42/43	288	288	288	0	3	1/32	864	288
	Total	6860						6860	1764

Simulation of MDC Trigger

The MDC trigger is very important and a critical part for rejecting backgrounds. A Monte Carlo simulation has been made to explore MDC trigger scheme. The geometry together with a track is shown in Fig.11.4-1.

In the simulation, we define the second layer of each super layer as pivot layer (PL), and the number of cells of PL as the number of pivot cells (NPC) of that super layer.

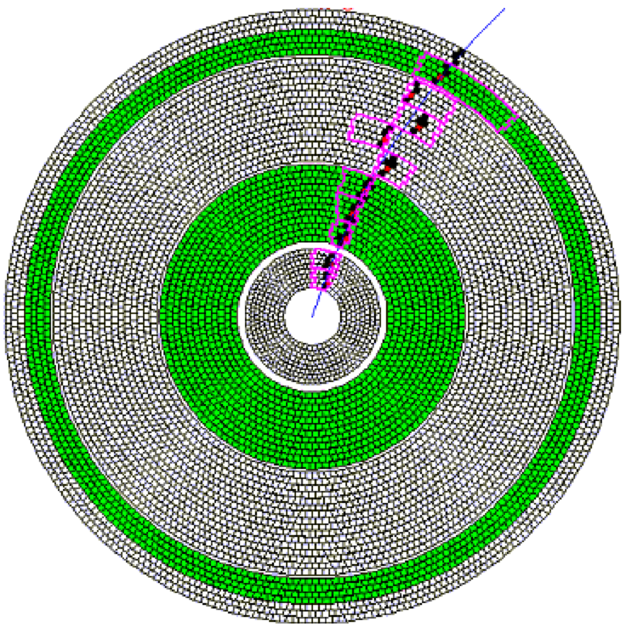

Fig.11.4-1 Simulation of MDC cells, layers, super layers, super cells and track segments

Assuming a particle with a large transverse momentum passes a super layer and leaves a track segment through pivot B1. If there are hits in each of the four layers, the pattern must be one of the 8 combinations under 4/4 group for B1 in Fig.11.4-2. If one hit is missing, the pattern must be one of the combinations under 3/4 group for B1. These combinations are also valid for other pivot cells. If we ask for all four layers with hits, called 4 out of 4, and when we find one of the 8 combinations of cell B1, a track segment through B1 in this super layer is found. Similarly, if we ask only 3 layers with hits, called 3 out of 4, and we find one of the 22 combinations, a track segment through B1 in this super layer is found. In this way we can find track segments (TSF) information in each super layer.

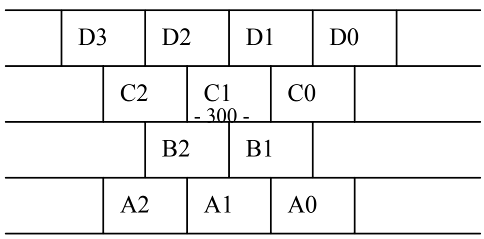

(layer B as pivot layer)

4/4 group	3/4 group
B1 pivot cell:	
A0*B1*C0*D0	A0*B1*C0+A0*B1*D0+A0*C0*D0+B1*C0*D0
A0*B1*C0*D1	A0*B1*C0+A0*B1*D1+A0*C0*D1+B1*C0*D1
A0*B1*C1*D1	A0*B1*C1+A0*B1*D1+A0*C1*D1+B1*C1*D1
A0*B1*C1*D2	A0*B1*C1+A0*B1*D2+A0*C1*D2+B1*C1*D2
A1*B1*C0*D0	A1*B1*C0+A1*B1*D0+A1*C0*D0+B1*C0*D0
A1*B1*C0*D1	A1*B1*C0+A1*B1*D1+A1*C0*D1+B1*C0*D1
A1*B1*C1*D1	A1*B1*C1+A1*B1*D1+A1*C1*D1+B1*C1*D1
A1*B1*C1*D2	A1*B1*C1+A1*B1*D2+A1*C1*D2+B1*C1*D2
B2 pivot cell:	
A1*B2*C1*D1	A1*B2*C1+A1*B2*D1+A1*C1*D1+B2*C1*D1
A1*B2*C1*D2	A1*B2*C1+A1*B2*D2+A1*C1*D2+B2*C1*D2
A1*B2*C2*D2	A1*B2*C2+A1*B2*D2+A1*C2*D2+B2*C2*D2
A1*B2*C2*D3	A1*B2*C2+A1*B2*D3+A1*C2*D3+B2*C2*D3
A2*B2*C1*D1	A2*B2*C1+A2*B2*D1+A2*C1*D1+B2*C1*D1
A2*B2*C1*D2	A2*B2*C1+A2*B2*D2+A2*C1*D2+B2*C1*D2
A2*B2*C2*D2	A2*B2*C2+A2*B2*D2+A2*C2*D2+B2*C2*D2
A2*B2*C2*D3	A2*B2*C2+A2*B2*D3+A2*C2*D3+B2*C2*D3
Each pivot cell Bi has 8 combinations	each pivot cell Bi has 26 combinations

Fig.11.4-2 TSF track finding logic

Looking at the 3 out of 4 combinations, we see the A1*C1*D1 is in combinations of both B1 and B2, that is, when there are hits in A1, C1 and D1, both pivot cell B1 and B2 are having a track segment. This kind of ghost tracks is treated as the following: if there is a hit in B2, we set pivot cell B2 having segment only with combination A1*B2*C1*D1. When there is a hit neither in B1 and B2, then we set B1 having segment with A1*C1*D1 combination. Similarly, A1*C1*D2 is assigned to B2 and A1*B1*C1*D2 to B1.

Combinations for all pivot cells in all SL are called track segment configuration data. It should be pointed out that the above is true only for tracks with high transverse momentum and there are same number of cells in each layer of the super layer. Real number of combination should be calculated by Monte Carlo simulation.

Table 11.4-1 is a simulated number of combinations in different super layers for a track with P_t>120MeV/c. We see that number of combinations becomes larger for the outer super layer.

Table 11.4-1 Simulation of TSF combinations in different super layers

SL	1	2	3	4	5	6	7	8	9	10	11
# of combinations	13	11	17	26	30	30	34	48	56	84	139

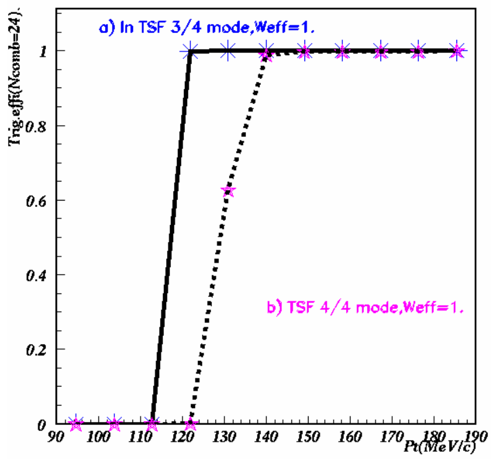

Fig.11.4-3 Trigger efficiency vs track Pt

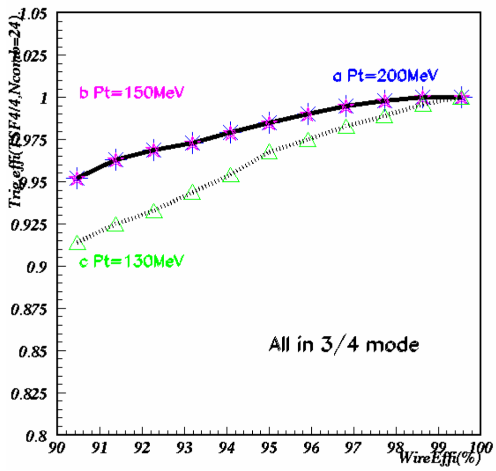

Fig.11.4-4 Trigger efficiency vs wire efficiency

Two trigger schemes have been used in the simulation. In the first scheme, both axial and stereo super layers are used and we define 32 super cells (SPC, some track segments be or-ed together) in each of the super layers, which will simplify the implementation. With the track segment information of a charged particle, we test if the SPC makes a full track (from first to tenth super layer) or short track (to fifth super layer) in Binary Link Track (BLT, see later), and also check if it has transverse momentum over a preset momentum threshold with Pt Discriminator (PTD, see later). If a track passes these checks then it's a good track. In the second scheme only axial super layers are used. We take fifth SL as the reference layer and check other SL's for a track. If a predefined combination of hits in all four SL's is found, then a long track is found. If a predefined combination of hits in SL3/4/5, then a short track is found. Fig.11.4-3 shows the trigger efficiency for single track as a function of the transverse momentum. It can be seen that 3 out of 4 logic in TSF is very effective for improving trigger efficiency. Taking into account the wire inefficiency with 3 out of 4 logic we found that the trigger efficiency is still high for a track of Pt=150, as shown in Fig.11.4-4 even for wire inefficiency of 96%. The cosmic-rays with a distance to the vertex more than 10 cm are mostly rejected. The trigger efficiency for physics channels and background rejection ability will be studied further.

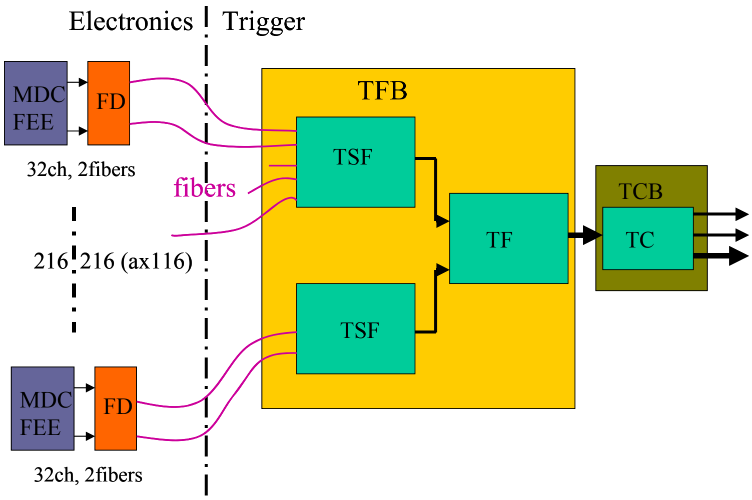

Fig.11.4-5 A scheme of MDC trigger

Implementation

The MDC trigger is composed of track segment finding (TSF), Track Finding (TF) and a Track Count (TC), as shown in Fig.11.4-5 At present only axial wires will be used for tracking.

All 32 signals from MDC discriminator module are first grouped into two 16 bits and be serialized into one stream with a serializer and then transmitted to trigger via a fiber transceiver. After being received and deserialized, some of these signals are sent out to neighboring cards, and some signals from other neighbor cards are stretched as shown in Fig.11.4-6. To minimize the inefficiency caused by possible dead cells, an input register is used. Signals are fed to the TSF engine (TSFE), implemented by the Xilinx FPGA chip with CLB or LUT to look for track segment. When the TSF find a track segment, the information will be send to the TF.

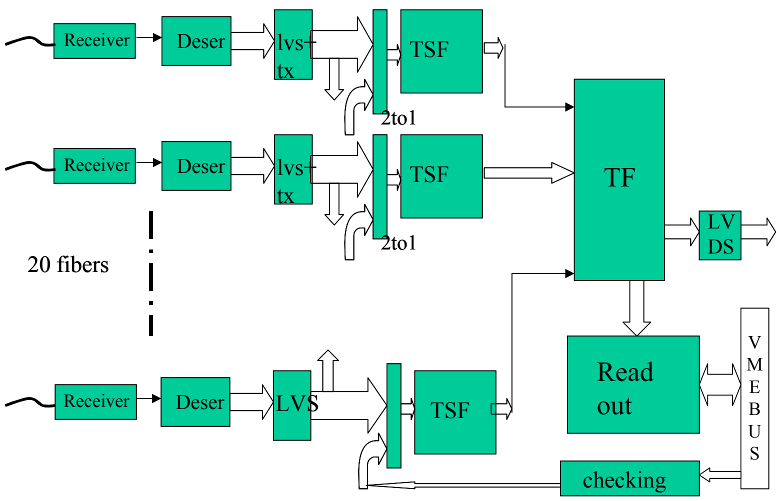

Fig.11.4-6 Block diagram of TSF card

The function of TF is to look for short and long tracks as defined in simulation section. This function is realized by TF engine in a FPGA chip. The circuit of this engine is stored in a PROM and downloaded at power-up. The TSF cells in SL5 is used as a reference layer for long and short track finding. The combinations of track segments (TSF) with predefined momentum are stored in a look up table (LUT). The checking of long tracks for a cell in SL5 requires all the pivot cells in eleventh super layer being reference cells, and pivot cells in seventh, fourth and third super layer (all axial super layers) to be in the saved patterns.

The checking of short tracks takes pivot cells in the seventh super layer as reference cells, and pivot cells in the fourth and third super layers becomes one of the predefined patterns.

The TRKCNT module calculates the number of tracks that passed the TF checking.

TOF Trigger

The TOF trigger provides precise timing signal, the hit number and topology information to the GTL. Fig.11.5-1 is a block diagram of TOF trigger system. There are 352 TOF signal in the barrel. Both photo-multiplier signals from a scintilator are discriminated first and then fed to a mean timer to get a precise time. This signal is in coincidence with signals in another layer in a known range to form a TOF hit. The signal of endcap scintilator comes from one end without mean timer. All signals from barrel and endcap scintilators are "OR-ed" together to form the timing signal. After simple calculation the signal of the hits number greater than 1 and 2, as well as the position information are fed into track matching and global trigger.

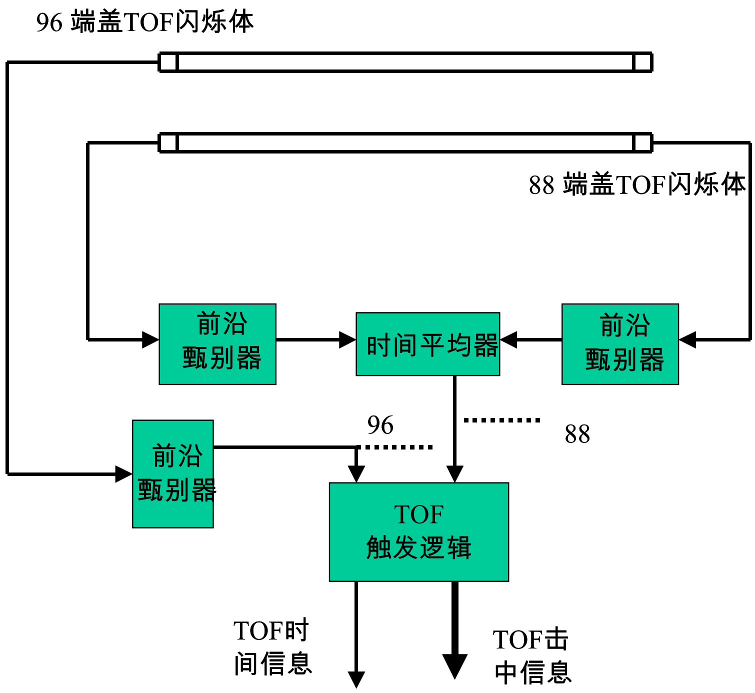

Fig.11.5-1 Block diagram of TOF trigger

EMC Trigger

General Description

The Electromagnetic Calorimeter (EMC) comprises of $\theta \times \phi = 44 \times 120 = 5280$ CsI crystals in barrel, and 992 Crystals in each endcaps. It is used to detect photons and electrons, to select Bhabha and pure neutral events.

The EMC trigger should provide flexible and effective trigger conditions to select neutral, Bhabha and charged events together with other sub-detectors, to reject-cosmic rays, beam background and to participate in the matching logic with the Main drift chamber (MDC) and the Time-of-Flight (TOF) system.

Compared with the MDC and the TOF, the EMC can detect more types of particles, which makes particle counting available for trigger. Almost all the energy of incidence photons and electrons are deposited in EMC, which plays a key role in the selection of Bhabha and neutral events. Especially, the neutral events can only be triggered by the EMC.

The design of the EMC trigger system should coordinate with other subtrigger systems. They should be complementary with other sub-detector trigger conditions.

Based on above considerations, three kinds of trigger conditions are implemented in the EMC trigger sub-system, the total energy, the energy balance and the cluster counting. They are complementary to have a high efficiency and reliability trigger.

Simulation

A simulation for the EMC trigger system is performed. The charge from two preamplifiers of a crystal are added on, and gains and light yield of crystals are corrected one by one with a precision of 10%, corresponding to a 4-bits precision. Monte Carlo simulation shows that 20% gain precision can be accepted, as shown in Fig.11.6-1.

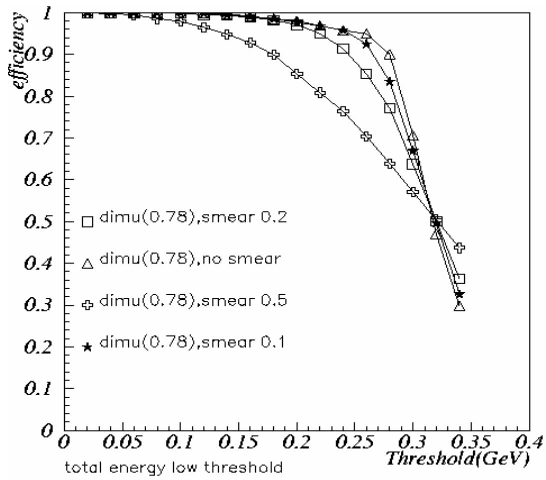

Fig.11.6-1 The influence of crystal gain non-uniformity

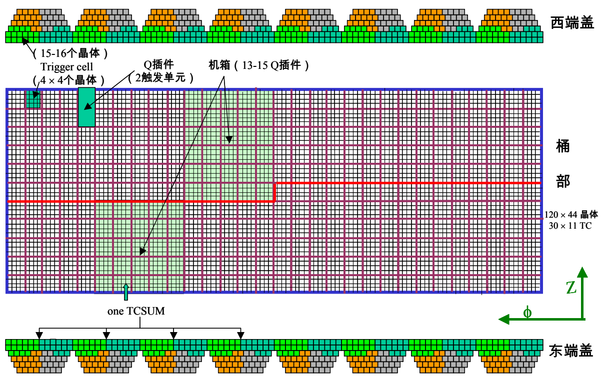

Fig.11.6-2 The trigger cell division

The gain-adjusted signals are fast-shaped, and added into a group of 8 crystals in FEE to form the TrigSum signals, which are then sent to EMC trigger system.

TrigSums are added into a group to form a Trigger cell energy sum (TCSums) on TCSUM(BTCSUM, ETCSUM) boards.

A trigger cell is defined as adjacent $\theta\times\phi=4\times4$ crystals, and there are a total of 330 trigger cells in the barrel region. Each end-cap are divided into $\theta\times\phi=2\times16$ trigger cells. In total, there are 394 trigger cells, and the detailed division is shown in Fig.11.6-2.

The trigger cell size is studied carefully in order to guarantee most of the electron energy deposits in one trigger cell. The simulation shows that the suitable trigger cell size is 4×4, as shown in Fig.11.6-3.

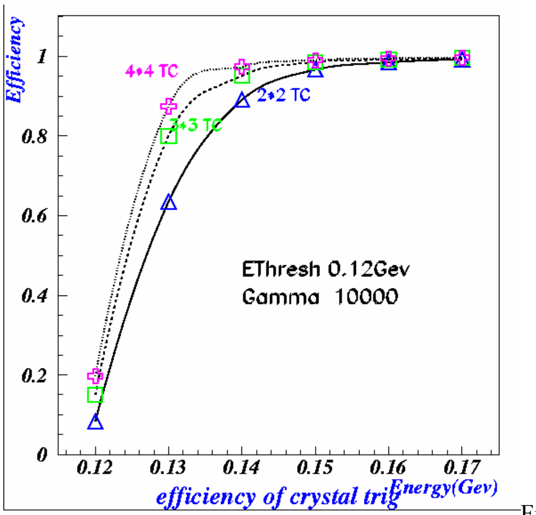

Fig

Fig.11.6-3 The decision of trigger cell size

There are three thresholds on TCSum boards, which are the gate threshold (gate_TH), low and high energy threshold of trigger cells (TC_THL and TC_THH).

A low threshold about 50MeV is set for TCSums to form signals for cluster counting, low energy balance, and neutral timing. A high threshold at about 300MeV is set for TCSums and the high energy balance trigger. The output of TCSums exceeding the gate threshold will participates in the energy summation to form the total energy trigger. This threshold can reduce the influence of incoherent and coherent noises along with the baseline pileup effect. With 1MeV incoherent gaussian noise for each crystal and 20MeV gate threshold for each trigger cell, the efficiency of trigger as a function of threshold with and without the gate threshold is shown in Fig.11.6-4. It can be seen that using the gate threshold improves performance dramatically.

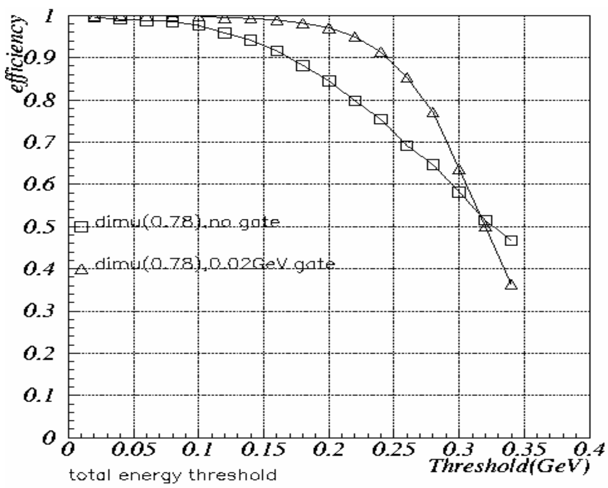

Fig.11.6-4 The influence of electronic noise

The gated outputs of TCSums (gatedsums) are added further to form total energy sum on the BESUM(EESUM) board, as shown in Fig.11.6-5. Three thresholds are set for the total energy trigger. In addition to a threshold for debugging purpose, a low threshold is used to suppress electronic noise and a high threshold is used to help select Bhabha and neutral events and to exclude cosmic background. The high threshold should guarantee a comparably high efficiency for charged events. The low energy threshold of total energy sum is set at about 150MeV, and the high energy threshold is set at about 1GeV.

The total energy trigger conditions, energy balance trigger conditions and particle number trigger conditions are all sent to Global Trigger Logic (GTL) after time-alignment.

The Hardware Implementation

The hardware implementation of the EMC trigger depicted in Figure 11.6-5, consists of three type of boards: energy summing (BTCSUM/ETCSUM), total energy sum（BESUM/EESUM）and cluster counting(ACNT). Two Signals from EMC FEE(a sum of 8 crystals) first added together and then compared with TC_th to have position and timing information. The sum of all signals are also available for local total energy, which are summed in BESUM/EESUM board to have total energy. There are three thresholds for barrel and two thresholds for endcap as total energy trigger conditions: Etot_l, Etot_M and Etot_H in barr and Etot_L and Etot_H in Endcap. The cluster information from TCSUM board are used to obtain the number of isolated clusters in barrel and endcap and their position information. All boards will be VME 9U boards.

Track Matching

The MDC, TOF and EMC trigger subsystems can provide information to

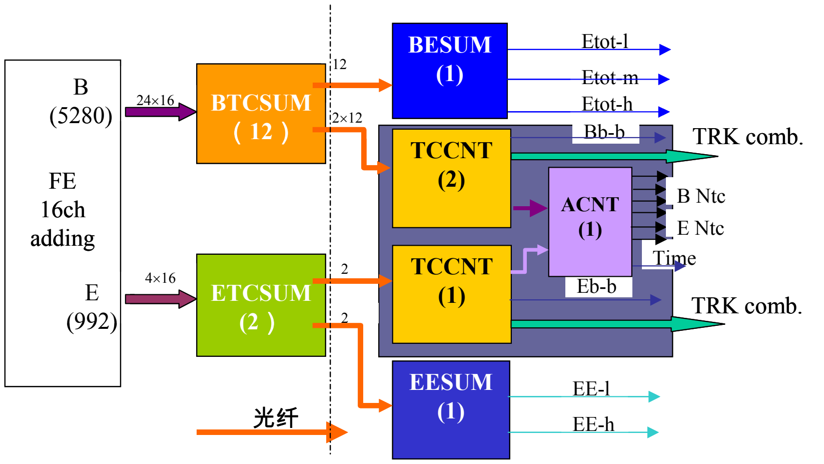

Fig.11.6-5 the EMC trigger sub-system

identify particle trajectories. Track Matching(TM) logic matches these conditions radially to find a global track to further suppress backgrounds. Barrel Track Matching(BTM) matches long track from MDC trigger with corresponding TOF hits and EMC clusters. Endcap Track Matching (ETM) matches short tracks from MDC trigger with corresponding cluster from Endcap EMC. The block diagram is shown in Fig.11.7-1.

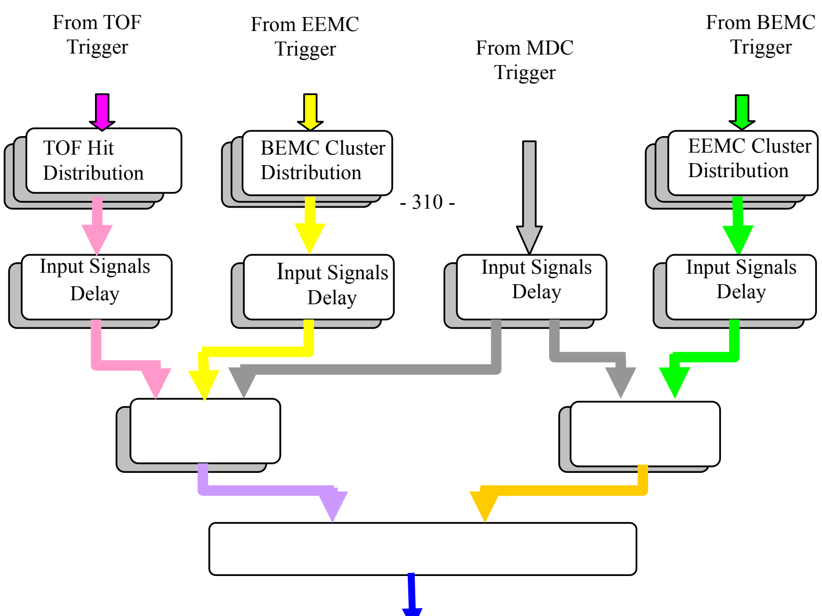

1. TOF Hit Distribution (THD)

In order to match with MDC, the hit signals from TOF must first be grouped with MDC tracks. Since MDC has 32 sectors, each corresponds to several TOF cells. The combination logic of a TOF matched cell is realized with a PLD device.

2. EMC Cluster Distribution (ECD)

The EMC clusters will be also matched with MDC sectors. This logic is put on EMC trigger Master Board using PLD device.

3. Programmable Input Signal Delay (ISD)

The programmable ISD board delays the signals from MDC, TOF and EMC of the same event with different arrival time for synchronization. The delay time is adjustable with VME commands.

4. Barrel Track Matching (BTM)

If a long track from MDC matches with TOF hits, we have a ATRK(MDC&TOF). If it also matches with the EMC cluster, we have a BTRK (MDC&TOF&EMC). These matching bits are kept in a buffer. When a Level 1 (L1) trigger signal occurs, they are readout for debugging and online monitoring.

5. Endcap Track Matching(ETM)

If a short track from MDC matches with EMC clusters forming CTRK (MDC&EEMC), they are readout by DAQ for debugging and monitoring.

6. Matched Track Counting(MTC)

The MTC board calculates the number of ATRK, BTRK and CTRK, and sends these signals to global trigger. The following conditions

ATRK≥1, ATRK≥2, ATRKBB,

BTRK≥1, BTRK≥2, BTRKBB,

CTRK≥1, CTRK≥2, CTRKBB,

are stored in a trigger table of the global trigger.

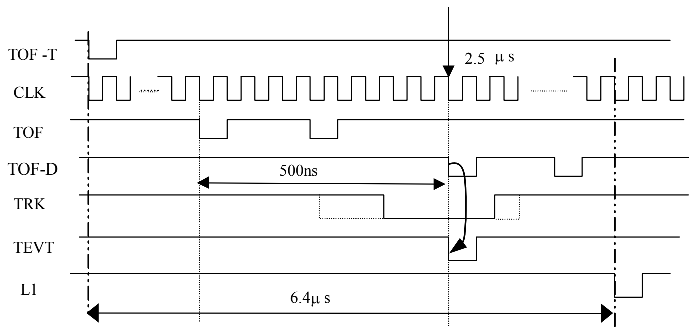

7. Online Testing of Track Matching

There should be an online test for the track matching on each module or in an independent module. It can be used to check the function and timing of each module, and also for the connection between modules. Well defined data of 256 bits can be fed into the trigger subsystems, and move with the pipeline clock. The results can be readout from BTM or MTC, to check against predicted results in order to find out possible faults.

Global Trigger and Timing Control

The tasks of global trigger include collecting signals from sub-detectors and making trigger decision based on the trigger table, providing pre-scaling ability for certain type of events, determining event timing, strobing the L1 signal 6.4μs after the collision, and providing pipeline clock and control signals for the whole trigger system. Fig.11.7-2 shows the timing sequence of the global trigger. The live and dead time of the DAQ system are also recorded. Trigger signals from subsystems of the same event are first delayed to be synchronized and then are checked against the trigger condition at each cycle of the pipeline clock. If they satisfy the trigger condition in the table, a trigger event (TEVT) signal is generated. TOF timing signal (TOF-T) or EMC timing signal(EMC-T) is used to determine the exact time (6.4μs after collision) to strobe out TEVT as L1 signal. For event with charged tracks the time is determined by TOF-T, while for event with only neutral particles, the time is determined by EMC-T.

The global trigger consists of programmable Input Signal Delay(ISD), programmable trigger decision, programmable prescaler, scalers and timing control logic as shown in Fig.11.8-1. They

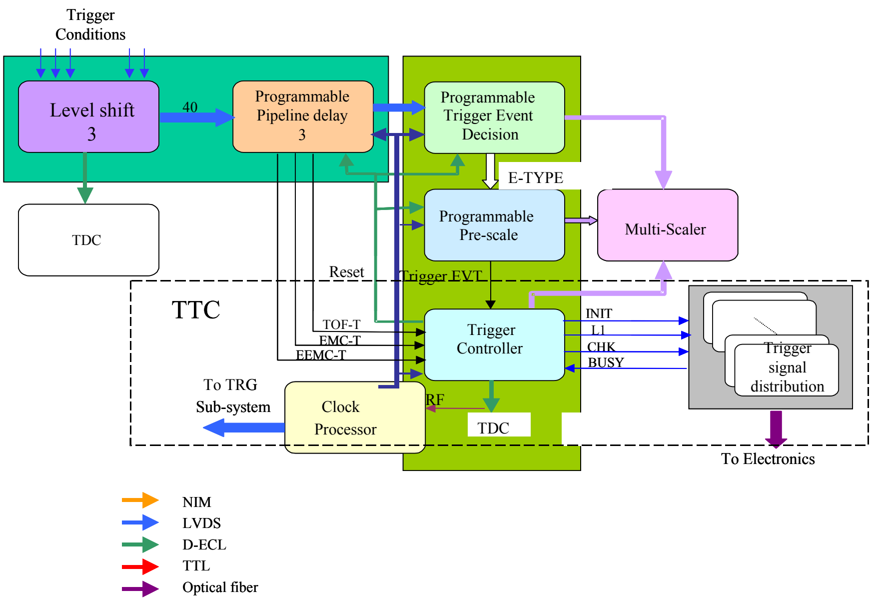

Fig.11.8-1 Block diagram of global trigger and timing control

are described in detail in the following.

Programmable Input Signal Delay(ISD)

The programmable ISD board delays the signals from MDC,TOF and EMC of same event with different arrival time in order to be synchronized. The delay time is resettable with VME commands. ISD type A (ISDA) accepts LVDS signals and ISD type B (ISDB) accepts NIM signals.

Programmable Trigger Decision(PTD)

The trigger decision logic finds the combination of trigger conditions matching with the preloaded trigger table and delivering the corresponding event type. The event can be classified as charged (Charge), neutral(Neutral), di-mu (DMU), small angle bhabha (EBB), large angle bhabha (BB), and cosmic ray (COSM) etc.

The trigger decision logic works in pipeline mode and may use Look Up Table(LUT) to make decisions. The trigger conditions are used as the address of the LUT, and the event type as the output. Combinatory logic can also be used in the trigger decision logic.

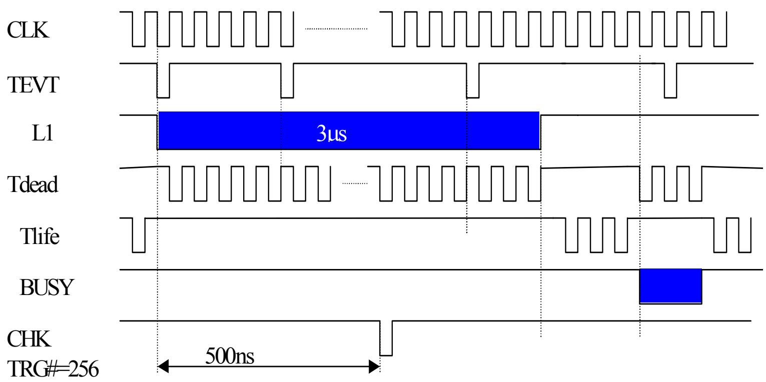

Fig.11.8-2 Timing sequence of L1 and DAQ signals

Pre-scaler (PRE-S)

With a high luminosity, the trigger rate will be very high. To decrease the trigger rate, some type of events like Bhabha can be scaled down with a known factor by a pre-scaler besides suppressing as much as possible backgrounds. The scaler must be programmable from 0 to 256. TEVT signal is produced by “OR-ing” all the 8 prescaled event type signals.

Trigger Timing and Control

The trigger timing and control (TTC) logic (the dash-lined box in Fig.11.8-1) is the heart of the trigger system. TTC will divide RF clock to have a 40MHz clock which will be used as trigger pipeline clock and controls the output of L1 signal.

1). TOF-T signal is used to determine the event time for charged event. EMC-T is used for neutral event. TOF-T has higher priority.

2). If there is a TEVT signal, L1 signal will be strobed out synchronized with the clock.

3). Trigger number counter (TRGC, 8bit, Max 256 events) increases one with the L1 signal. When TRGC reached 256, a check signal (CHK) will be issued 500ns after the L1 signal for system wide trigger number TRGN checking. TRGN will be used as the event packing tag.

4). A BUSY signal from DAQ when the buffer is full blocks the issuing of L1 signal.

5). Dead time and live time will be recorded to correct for the efficiency. The timing is shown in Fig.11.8-2, where the TEVT denotes a good event. The L1 signal will be given together with TOF-T or EMC-T. A delay of 3μs after L1 is required by A/D feature extraction. In this period the trigger system is still working which might produce another TEVT, but new L1 is blocked, causing an event lost. Also the BUSY signal cause dead time as indicated by the shadow. Tdead and Tlife is the number of clocks in dead time and live time respectively.

6). The control logic should provide means for automatic and manual system initialization and for blocking the trigger system from working.

7). Some signals should be recorded by ADC and TDC for function checking and monitoring.

8). There will be one or two modules to accept DAQ status signals such as BUSY, fanout clock and control signals.

Global Scalers

The global trigger uses two kind of scalers to check and monitor the system status. The console scalers are used for instant checking of different signal rates. The online scalers are used to record information for offline analysis. Some data like trigger conditions, event types, TRGN, prescalers contents, live time and dead time etc. are recorded in global scalers.

Trigger Pipeline Clock

The trigger pipeline clock is produced by dividing the RF clock with a 50% duty cycle. A local clock of 40MHz will also be implemented in the case without collision.

The timing and control logic can be explained in 6 states shown in Fig.11.8-3. The hardware is designed as the state machine. After system initialization the system is in wait state(WAIT). When TEVT comes, the machine is in the state waiting for TOF-T or EMC-T(WAITT). When a timing signal comes the machine moves to L1PASS state. After this state, the machine moves to WAITT state automatically waiting TEVT signal again. These are four main working states. Others are the initialization state and the trigger masking state. If the machine move in WAITT state, but no TOF-T and EMC-T signals come in a predefined time (say 1 second), the machine is recovered automatically to WAIT state.

Data Acquisition System

BESIII Data Rate

BEPCII is designed with a peak luminosity of $10^{33}cm^{-2}sec^{-1}$. After the Level 1

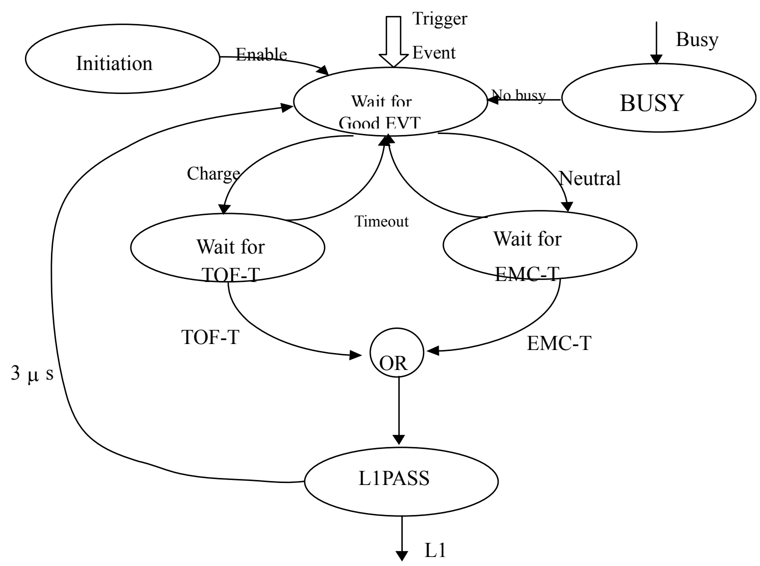

Fig.11.8-3 State flow chart of global trigger

trigger, the event rate is estimated to be around 4000Hz at J/ψ peak. A pipelined front-end electronic system is required and the BESIII DAQ system is designed to satisfy the requirement of event readout and processing with such a high event rate.

The performance of the DAQ system is determined by the trigger rate and the event size. The total number of electronics channel is more than 40K, among which there are 20K ADC and TDC channels. Assuming an occupancy of 15% for MDC T channel, 17% for EMC, 1% for MUC and 10% for others, the estimated total data rate is listed in Table 12.1-1. As a comparison, the data rate of BESII in listed in the last row.

Table 12.1-1 Established data rate of BESIII

Sub-detector	Number of Channels	Crate Data Rate (Mbytes/s)	Farm Data Rate (Mbytes/s)	Record Data Rate (Mbytes/s)
MDC（T+Q）	13600	46.6	28	21
EMC	6272	24.8	17	13
TOF+CCT	896	2.3	1.6	1.2
μ	9088	2.4	1.6	1.2
Trigger	400	6.4	6.4	4.8
Sub-total	**30256**	**82.5**	**54.6**	**41.2**
BESII	**20000**		**0.04**	**0.04**

The BESIII data acquisition system is designed with a capacity of 80Mbytes/s for the front-end readout, 50Mbytes/s for the online farm processing and 40Mbytes/s for the tape-recording after the Level 3 trigger. Compared with BESII, the BESIII DAQ system has a much higher design target both in scale and in performance.

System Architecture

The BESIII data acquisition system consists of the readout system, the online control and monitoring system, the calibration system and other support/service systems.

The main tasks of the BESIII DAQ system are the followings: collecting event data from the front-end electronics after Level 1 trigger; transferring data fragments from each VME readout crate to the online computer farm through two levels of computer pre-processing and high speed network transmission; assembling data fragments into event data, filtering the event data, and then recording the selected event into a persistent media.

In order to read out large amount of data from the front-end electronics system and reduce the dead time, the BESIII DAQ system adopts multi-level buffering, parallel processing, high-speed VME readout and network transmissions techniques. The key issue is to solve the “bottleneck” caused by the VME readout and the network transmission.

To accomplish above tasks, the DAQ system are designed to have the following functions:

（1） To collect data from the VME readout modules (ADC and TDC) at high speed and fully utilize the bandwidth of the VME bus; to assemble the data fragments from front-end electronics into sub-events;

（2） To provide necessary hardware and software protocols that ensure correct readout and transmission;

（3） To design and implement the online software system, including event filtering, mass storage, run control, information monitoring and condition adjustment;

（4） To provide system calibration, readout electronics calibration and data pre-processing;

（5） To provide “Exception Handling” functions, such as valid or wrong operations, buffer overflow and some other failures. To provide debugging, testing/diagnostic functions for the hardware and software of the electronics and trigger system, as well as failure finding and failure recovering functions;

（6） To design and implement the online database management system and its interface with the offline analysis system.

In the system architecture, the DAQ system must have high reliability, stability and scalability and also be easy for upgrade. The system devices and software development tools adopt as many existing products as possible, in order to follow closely the technical trends and have good cost performance ratio.

The BESIII DAQ system is designed based on advanced computer and network technologies and multi-level parallel data collecting/processing schemes. The lowest level is the VME readout crates, each holding a system controller and some FEE readout modules (ADC and TDC). There are no more than 16 FEE modules in each crate, each having no more than 1024 electronics channels. The VME processor, a MVME2431 embedded single board computer, is used to collect, pre-process and transfer data. Several readout crates are connected to a readout PC through fast Ethernet, thus constituting a readout branch. All the readout branches are connected to the online computer farm through gigabit switch, constituting the backbone of the DAQ data flow. Sub-event packages, coming from each readout branch, are assembled in the online computer farm. After being filtered and processed, events are recorded in persistent media. The configuration is shown in Fig.12.2-1.

The BESIII DAQ system provides also other control and test functions. In the stage of system design, it is required to define the interface and driving mode between the DAQ system and the front-end electronics system, as well as the interface between the DAQ and the trigger system. It is also required that the control, calibration, testing and failure diagnosis functions of the entire system and each sub-systems be taken into consideration at present. Furthermore, the DAQ system must provide a series of service functions, such as recording power supplies of magnets, electronics power supplies, high voltage system and accelerator parameters; system initialization; downloading program/parameters; delivering and executing commands.

Software development of the BESIII DAQ system is quite a software engineering project. It is necessary to consider the quality and standardization of the software, which rely on the powerful management of software engineering. The readout controller software will be written in C language and run in the real-time operating system VxWorks. The readout PCs and online computer system software will be written in C++ and run in Unix/Linux. In order to store and use the operation parameters, environmental data, standard database technique based on SQL language will be used in the BESIII DAQ system.

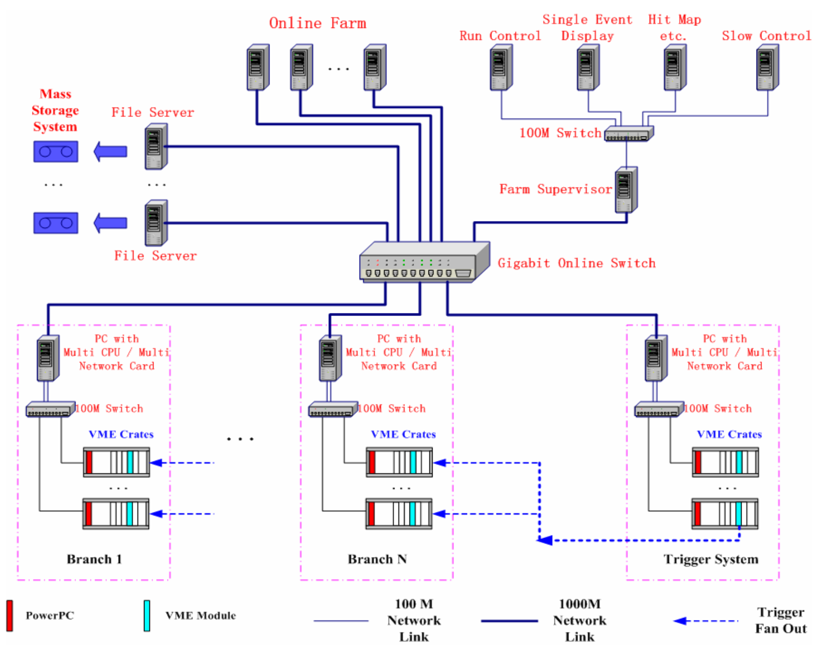

Fig.12.2-1 Architecture of the BESIII DAQ System

System Requirements

The design of the BESIII DAQ system is complicated because Level 1 trigger rate is 200 times higher than that of the BESII, the event size is 6 times larger than that of the BESII and the data rate is more 1000 times than that of the BESII. Thus three kinds of key techniques must be considered during the system design:

(1) For readout system configuration, it is important to match data bandwidth with data throughput;

(2) For system architecture, it is important to build an integrated DAQ system together with the front-end electronics system and the trigger system, including the implementation of sub-system testing, system initialization, system control and monitoring.

(3) For the software developing, we must follow the rule of software engineering, and continue to improve the software process.

According to the information provided by each sub-system, the basic readout configuration of the BESIII DAQ system is shown in Table 12.3-1. There will be about 48 readout crates and less than 16 readout branches. It is estimated that the online computer farm consists of more than 30 PCs and a Mass Storage System with a capability of 240Tbytes/5years. Other supporting systems, such as the calibration system, will also be built on a large scale.

Considering the non-uniformity of data distribution, the designed BESIII DAQ system requires the throughput of readout crate to be 3.2Mbytes/sec in order for the system to accomplish data acquisition task with a shortest dead time. Therefore, high-speed VME bus readout methods and fast Ethernet are applied.

Table 12.3-1 Configuration of Readout Devices

Sub-system	Number of Channels	Number of Readout Modules	Number of Readout Crates	Number of Readout Branches
MDC（T+Q）	13600	224	16	4
EMC	6272	208	16	4
TOF+CCT（T+Q）	896	28	2	1
MUON	9088	40	4	1
Trigger	400	160	10	2
Total	30256	804	48	12

In order to collect data and transfer them to the online system, event fragments are assembled first within readout crates and readout PCs. It is required that the data readout mode and data format for both the front-end electronics system and the trigger system are almost the same in order to process and assemble the event fragments correctly.

To build an operational BESIII DAQ system, it largely depends on the correct linkage of system devices, logic signals agreement and the integrated software design. The electronics system and the trigger system are also required to provide all necessary information of hardware facilities. For the software design of the DAQ system, it is important to correctly comprehend and execute hardware functions and make the best use of all hardware resources. It will greatly enhance the software system with more functions such as failure finding, testing/diagnosis, task recovering, exceptional handling of functional modules and dead channel processing, etc.

In order to guarantee the quality and the performance of the software, commercial products of the developing tools will be used. Software engineering standard will be applied throughout the software design, its implementation and management. The software system should be designed to possess good reliability, maintainability, scalability and portability. In addition, it is important and required to have a good documentation, which will help to manage the archives in the future.

Readout System

One of the key technical challenge of the BESIII DAQ system is to read out data from the front-end electronics at a high enough speed. There are “bottleneck” of the data flow in the system caused by the VME access speed and the network bandwidth. From the test results of a few I/O devices, it takes more than 1μs for one 32bit read, which means 3Mbytes/sec when reading from VME bus to MVME2431 memory by using Programmed I/O mode. While with the 32bit DMA mode, it could be more than 13Mbytes/sec (<300ns/32bit read). Therefore, DMA mode will be used in VME readout in order to fulfill the requirements of the Data Readout.

The capability of network transmission is also an issue related to the readout system. According to our testing results, the point-to-point transmission speed for 100M Network may reach 10Mbytes/sec in the circumstances of 12-port fast Ethernet switch hub and multiple network adapters installed in each readout PC. This kind of point-to-point connection enables each network adapter to connect to its corresponding readout crate, while the gigabit network adapter installed in the readout PC connects the PC to the online switch. This configuration constitute a readout branch, which has the following functions:

（1） To collect event fragments from readout crates and assemble them into the tagged sub-event packages.

（2） To control and monitor data stream and commands stream.

（3） To transfer event fragments to online PC farm via gigabit network.

The performance of the readout system is mainly determined by the data throughput of the readout crate, i.e. the comprehensive capability of the data readout from VME bus, data pre-processing and data transmission over the network.

The data throughput of the readout system has a close relationship with the design of the front-end electronics modules. For the DMA mode of the readout, each module should have global buffers on board and supports VME Block Transfer. With the zero suppression on board, and the total number of channels no more than 1024 per crate, the total data to be transferred at 4000Hz will be about 3.2Mbytes/s. Therefore, according to the general estimations of VME access speed, the network transmission speed and the data to be read out satisfy the requirements for the data readout of 1024 channels under 4000Hz trigger rate.

The readout system adopts Motorola MVME2431, a VME processor module with a good cost/performance ratio, as the system controller. MVME2431 is configured with the PowerPC750 32-bit microprocessor, 32MB of on-board ECC SDRAM, 8MB on-board flash memory for user-specified requirements, 10M or 100M Ethernet interface, D64 (MBLT)/D32/D16/D8 VME bus to local bus interface and DMA transfer mode. In addition to the data readout from VME crate at high speed, the system controller will perform other tasks, such as (non)linear correction, interrupt processing, task scheduling, device control and monitoring.

BESIII Online System

The main task of the BESIII online system is to read out data from FEE, build and filter the events and finally write the selected events to a persistent media.

The BESIII online system includes event building, event filtering, event classification, data storage, operation control, event display, histogram display, process monitoring, etc. Fig.12.2-1 shows the block diagram of the BESIII Online system.

(1) Event Building

A multi-step event building technique will be adopted by the BESIII online system, as shown in Fig.12.5-1. The first step of the event building is to assemble the data in VME crates. After receiving a good event signal provided by the trigger system, the PowerPC in the VME crate will read out data from electronics modules. Data fragment is assembled and stored in memory after corrections. All readout crates work in parallel. The second step is to assemble the data in branch level. Several VME crates are grouped in a branch and each crate is connected to a readout PC with multi-CPU and multi-network card via a fast Ethernet switch. Data in all VME crates within a branch is sent to the readout PC. Data fragment is assembled to a sub-event data, and stored in memory by the readout PC. There may be one or more branches for each sub-detector according to its number of channels. The third step is in event level. A node of the BESIII online PC farm assembles sub-events distributed in readout PCs via a gigabit Ethernet switch, the event is built and passes the event filter. Finally the filtered event is sent to the online file server to be recorded on the tape. All data fragments of an event are unique numbered by the trigger segment and a time stamp.

A sub-event in one branch can be sent to one node of online PC farm, at the same time, sub-events of other events in other branches can be sent to other nodes of the online farm with the technique of parallel event building with a switch. So the high speed and parallel event building can be achieved with advantages of scalability, high reliability and the best price performance ratio.

The latency of Ethernet switch affects the data transfer rate. To reduce the transfer frequency, the size of the data package should be as big as possible. Using the multi-step event building technique, data are assembled gradually from the distributed front-end electronics to the online PC farm. To reduce the delay time of the switch at lower levels at such a high event rate, it is necessary to pack several events into a big package before transferring via Ethernet switch.

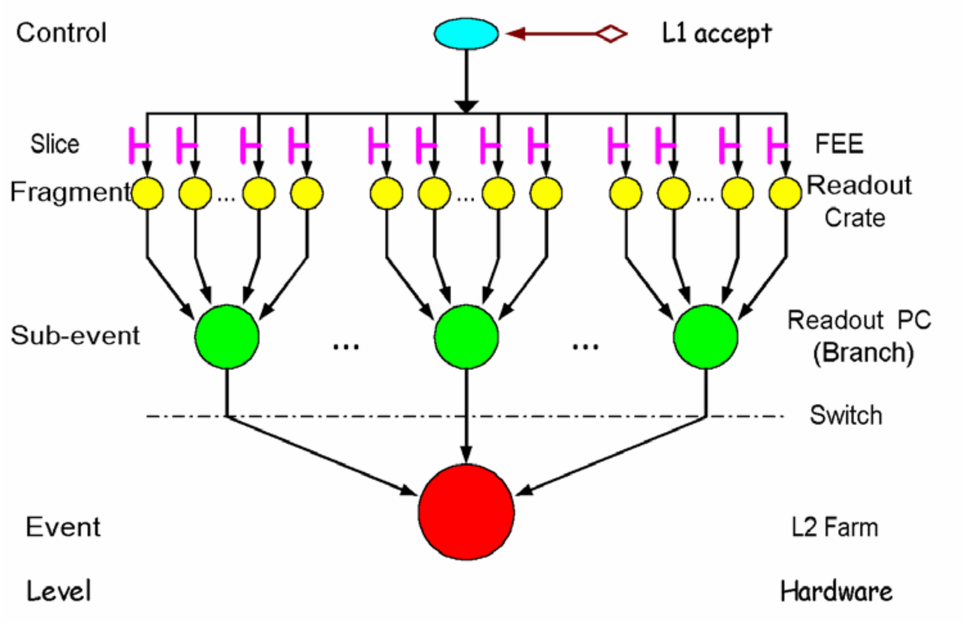

Fig.12.5-1 Topology of event building of the BESIII DAQ system

(2) Online Data Flow

The data flow of the BESIII online system is showed in Fig.12.5-2 and described in detail as follows.

① The readout PC informs the online farm supervisor that a data fragment is ready to be read out with a trigger number after assembling the data in a branch level;

② The online farm supervisor informs one of the idle online PC farm nodes to read out the corresponding data block with the trigger number after receiving all the event ready signal from the readout PCs;

③ The node n of the online PC farm reads out the corresponding data fragment in all readout PCs with the trigger number;

④ The node n of the online PC farm starts to build, format, filter and classify the event, and sends the results to the online file server;

⑤ After receiving data from the node n of the online PC farm, the online file server informs the online farm supervisor that the event data with the trigger number has been processed, and writes the data to the disk and/or tape after a given number of events;

⑥ The Online farm supervisor informs the node n of the online farm and all the readout PCs to free the memory with the trigger number.

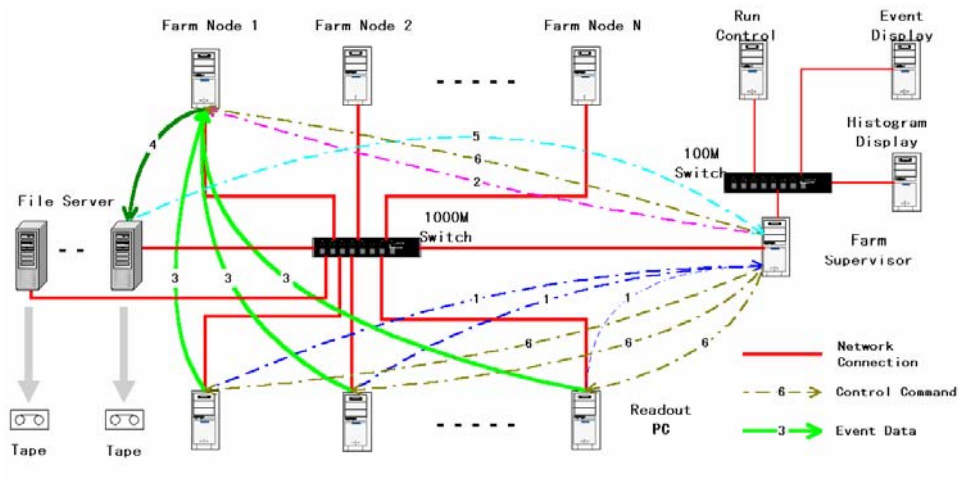

Fig.12.5-2 The data flow of the BESIII online system

The online farm supervisor should be a highly reliable workstation. There are 2 queues in the supervisor. One is the queue of event number to be assembled, which comes from the level 1 trigger; the other one is the queue of free nodes of the online farm. According to the 2 queues, the supervisor informs an assigned node to read out the proper data fragments from the readout PCs. All the data processing tasks are done on the assigned node of the online farm.

(3) Online Filtering

Online event filtering is also called level 3 software trigger, which is software based running on a farm node after the event building. The filter process suppresses the background to reduce the data rate to magnetic media. To compare with the hardware trigger, more flexible and more sophisticated algorithm can be adopted in the software trigger, such as fast tracking in MDC, fast cluster finding in the electromagnetic calorimeter, etc. The cosmic-ray background and beam lost background are suppressed by using the event vertex information from the MDC. The Bhabha sample, useful for detector calibration and luminosity measurement is selected by using the MDC tracking and EMC cluster information. The $\mu^+\mu^-$ sample can also be selected by using the information from MUON counter. During the event filtering, the farm nodes accumulate various histograms and classify event type as hadron, Bhabha, $\mu^+\mu^-$, cosmic, etc. The information is transferred to the host computer for monitoring.

One of the following two methods, or both of them may be adopted in the filter algorithm:

–Digital filtering with complete data using algorithm similar to the trigger system;

–Developing more sophisticated filtering algorithm, such as track reconstruction and cluster finding.

The final event rate recorded on the magnetic media will be reduced to 3000Hz if the filter can suppress 50% of background.

The online farm, consists of high performance PCs, may also do real time event reconstruction, using the same code as the offline as the first round of event reconstruction. Rolling calibration technique may be used in the real time event reconstruction.

(4) Event Record

The event rate to be recorded by the BESIII DAQ system is about 3000Hz after the online event filtering. The average size of event data is about 12Kbytes. So the data rate to the magnetic media is estimated to be 40Mbytes/sec. The event data after filtering are transferred to the online file server via the gigabit Ethernet switch.

The online file server is two high performance workstations with multi-CPU, multi-network cards, disk arrays and tape library. Event data are assembled to a run on the file server, written to disk file and recorded to magnetic media. The data are also transferred to the computer center via network.

(5) Host System

The host computer provides a man-machine interface to control the operation of the BESIII and monitor the process of experiment. It consists of several high performance workstations and/or PCs with distinct usage, such as run control, single event display, histogram display, run status display, etc.

① Run Control

As a man-machine interface, it accepts various run commands, such as calibration, pedestal run, normal data taking etc., and sends the command to all readout PCs and all nodes of the online farm via network. The readout PC and farm node will execute the program corresponding to the command. Parameters of experimental process and configuration of the DAQ system are also controlled by the host computer.

② Data Monitoring

With the powerful CPU, the PC farm can do histogram accumulation and event classification during the filter processing. The host computer can extract a histogram data from any farm node, sum up histogram data from all farm nodes and view event display from any farm node randomly. Combining the luminosity event rate and the information of event classification, the host computer may calculate and display the online production cross section for different physics processes and physical integrated luminosity. In addition, the host computer periodically monitors various count rates, such as luminosity, trigger rate, dead-time, count rate of each sub-detector, etc., displays their variation with time and alarms if necessary. The host computer will also display and handle the error report message from each sub-system and farm nodes.

(6) Database Management System

The BESIII DAQ system is to build an online database management system. The main parameters of run status, environment and other shared parameters are provided via this database, which can ensure the safety of these data. The event data will not be stored in the online database directly. The online database is estimated to be less than 40Gbytes/year, and it will be managed by the SQL language based free software, such as MySQL PostgreSQL, etc.

Other Supports

During the construction and operation of the data acquisition system, some support systems are to be built up, such as the calibration support system, the failure diagnosing system, the data flow monitor and the network monitor.

(1) Calibration

Calibration involves determination of parameters for converting digitized data like ADC and TDC counts into physics data such as energies and coordinates. Another type of calibration is for diagnostics, such as the determination of system errors and failure positions, and checking the function/performance of the devices.

Calibration will be designed either for global or local run mode for each sub-detector and can be run in either step or normal continuation mode.

(2) Diagnosis

Since the scale of the BESIII data acquisition system is huge and complex, it is necessary to detect any hardware and software failures/errors as soon as possible in either running mode or static state checking mode. Diagnosis is very useful in the stages of electronics design and system debugging. Their running modes will be in either global or local.

(3) Data Flow Monitor

The fast network technique will be cosmically used in the BESIII data acquisition system, so it is needed to consider the safety and performance of the network. The BESIII network environment and data flow monitor system will provide friendly user interface to monitor all cases of the BESIII network in a dynamic way, in order to determine and adjust any system configuration in the stage of design or running.

Offline Computing System

Overview

The BES detector has been in operation for more than 12 years, and the BES offline data analysis environment has been developed and upgraded along with the development of the BES hardware and software. At present the BES data are processed on both HP-UNIX farm system and PC-farm system. The network system consists of a 1000Mbps optical fiber network together with a distributed 100Mbps fast Ethernet system, as well as a 100Mbps FDDI local area network.

Based on the existing BES computing environment, following points should be taken into account for the future BESIII offline computing system and software environment:

- The system should be set up by adopting or referring to the latest technology commonly used in HEP community, both in hardware and software, in order to benefit the collaboration and to have easier exchanges with other experiments.
- The system should support hundreds of the existing BES software packages and should serve for both experts of the BESII software and new members in the collaboration.
- Many of the BESII packages will be modified or re-designed to suit for the new computing environment.

The BESIII computing facility and software system will operate for many years. Thus they should have the scalability to keep up with the development of the technology in both the hardware and software. It should be highly flexible, powerful, reliable and easy for maintenance.

Requirements

BESIII Data Yields

The peak luminosity of the BESIII at the J/ψ resonance will be about $10^{33}\,\mathrm{cm}^{-2}\,\mathrm{s}^{-1}$. The event rate recorded on tape is estimated to be about 3000 Hz. and the event size is about 12 Kbytes/event for raw data, 24 Kbytes/event for reconstructed data(Rec.) and 2 Kbytes for summary data(DST).

Assuming BESIII will take J/ψ data at the begin of the data taking for one year or more, and then move to ψ' data energy region. So the maximum data yields per year is about 1×10^{10} J/ψ data. The total data size in first years: $12\times10^{3}\times1\times10^{10}\approx120\times10^{12}$ bytes. Detail information is listed in table 13.2-1.

Table 13.2-1 Estimate of the BESIII data yields in the first year

Data type	Event size(k bytes)	Total Data size(10^{12}bytes)
Raw	12	120
Rec.	24	240
DST	2	20
M.C. Rec.	24	120
M.C. DST	2	20
Total		640

Data Storage and Management

All kinds of data, including raw data and reconstructed data, are stored in tapes mounted on Robot in the computer center. The total amount of raw data in 5 years is estimated to be about 240×10^{12} bytes, which includes 120 Tbytes of J/ψ data and 120 Tbytes of ψ', D and Ds data. Suppose the data reconstruction is repeated three times per year, the total size of the Rec. and DST data will be about 1440 Tbytes and 120 Tbytes respectively. The size of Rec. and DST data from Monte Carlo simulation will be about the same as that of real data.

All of raw and Rec. data, about 3120 Tbytes, will be put on the tape library. A total of 240 Tbytes DST data will be stored on a disk array accesse via high-speed network system. Details are listed in table 13.2-2.

Table 13.2-2 Requirements of the tape and Disk space for BESIII Data

Sort of data	Amounts of data (Tbytes)	Device
Raw	240	Tape Lib.
Rec.	1440	Tape Lib.
DST	120	Disk
M.C. Rec.	1440	Tape Lib.
M.C. DST	120	Disk

CPU Power Requirement

According to the experience of data processing at BESII, required CPU power for data reconstruction is about 20s×MIPS per event. Suppose the total active running time of the computer is about 2×10^7 second per year, and the data reconstruction is repeated three times a year for improving calibration and reconstruction, the required CPU power is about 130000 MIPS. Details are listed in table 13.2-3.

Table 13.2-3 The CPU power required for handling the BESIII data.

Job type	Speed/Event (MIPS×s)	Total event (10^{10})	Total CPU (MIPS)

Data Rec.	20	4	40000
MC Sim.	100	1	50000
MC Rec.	20	4	40000
Total			130000

Bandwidth for Data Transfer

The bandwidth required for online data transfer from the online computing system to the offline data server should be more than 400 Mbps, which is determined by the product of trigger rate times the event length, i.e. 4000×12Kbytes×8. It also requires that the network system should be highly stable and secure to avoid event losses.

The bandwidth required for data transfer from the data server (i.e. RAID disk) to the reconstruction farm depends mainly on the processor speed of selected machines. The higher the processor speed, the larger the bandwidth required. Due to very high data traffic in the local network, it is necessary to create an isolated BES computing environment, which is separated from other part of the IHEP network, and can ensure a reasonable efficiency in data transfer.

Computing Enviroment

The main tasks of the BESIII Computing Environment can be divided into four parts: The first one is the various data handling such as the data reconstruction and offline analysis; The second one is the transport of various data; The third one is storage and management of various data and documents; The fourth one is the communication between users and system devices.

To satisfy these requirements, the system to be built should have good performance, including stability, reliability and flexibility, with a reasonable and acceptable cost. Also the rapid development of advance technology in both computer hardware and software should be followed closely so that we can benefit from the latest development of technology. Especially a high-speed network is essential for mass storage system, such as a robot tape library and a disk array. Fig.13.3-1 shows a preliminary scheme of the computing system for the BESIII. The main considerations are the following:

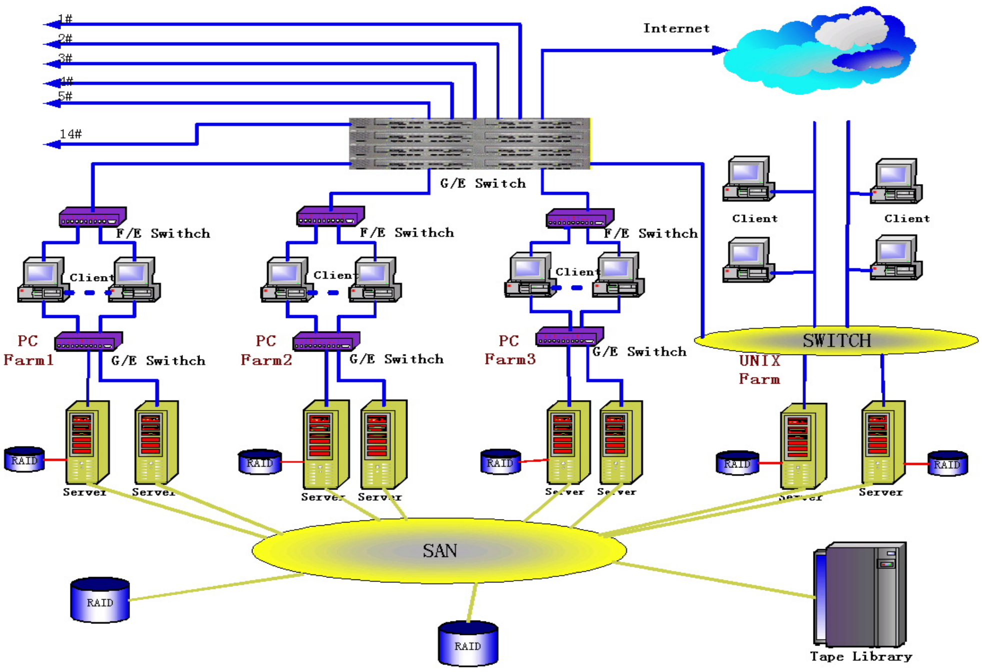

Fig.13.3-1 The scheme of the BESIII computing system

CPU type and architecture: A high quality computing system based on PC/Cluster or PC/Grid technology will be taken. The CPU type can be any or all of Intel、AMD or IA64.

Data storage: The BESIII Storage System will adopt the visual technology of the Disk Array and Tape library with HSM(Hierarchical Storage Management). A SAN(Storage Area Network) construction can satisfy the requirement of large amount data storage, high access speed and expandability. In such a system, all the sub-storage system such as the Disk Array and the Tape Library, are connected through a switcher and are independent from the server.

Network and I/O control: In order to increase the data access speed and to reduce the interference, a second network based on SAN will be adopted to separate data transfer and normal network traffic. In addition, all nodes will have both 100TX/1000TX network cards, in which 100TX provides traditional TCP/IP services while 1000 TX provides NFS services.

System software: The BESIII offline computing system will mainly adopt free software to reduce the cost and to have an easier exchange with other experiments in the world . The main components are the following:

- RedHat/Linux as the system operation software;
- Castor or MySQL or PostgreSQL for database system;
- PBS for the batch system;

- YP for user management and auto-mount for document management.

Offline Data Analysis System

The main task of the BESIII software system is to convert raw data of the detector responses into physics results. It consists of a main framework, the data reconstruction and calibration package, the Monte Carlo simulation of physics processes and detector responses, the database management and interfaces, various utility packages, and user's physics analysis packages. It should also manage documents, software codes and libraries. The system should take the advantages of the Object Oriented technology by using the C++ computer language, while still keeps the possibility to incorporate some of the existing BES Fortran software packages. The system would also be taken into account practical needs, such as usability, stability and flexibility, and to accommodate conflicting needs between experts and novices.

1. Framework of the BESIII Offline Software

In order to take advantages of the modern technology and utilize common tools of other HEP experiments in the world, the main framework of the BESIII offline software will be based on the Object-Oriented methodology and C++ language, and take into account the following points:

- It should support some of the existing BES packages written in Fortran language;
- It should use as much as possible existing HEP libraries.
- It should provide a uniform data management, code and library management, and database access.

The BESF as the BES III software framework, based on the Belle analysis Framework (BASF)[7], has been developed in the summer of 2003. In order to make the framework more flexible and robust, be able to handle offline data and MC events as well as online Event Filter (EF) system, some software components and infrastructures are taken from other experiments such as the Service in Gaudi [8] and data management infrastructure from the Babar software.

The major packages of the BESF framework are shown in Fig.13.4-1. In which the BesKernel is the core part of the framework that implements the control on data processing. It depends on other four packages: the EventIO package managing event input and output, the UserInterface package providing friendly interface for running jobs, the Panther[9] package that is an integral data management system and the BesEvent package implementing the interface to the ProxyDict originally developed in the Babar experiment. The ROOT and CERNLIB are the only two external libraries needed by Histogram package.

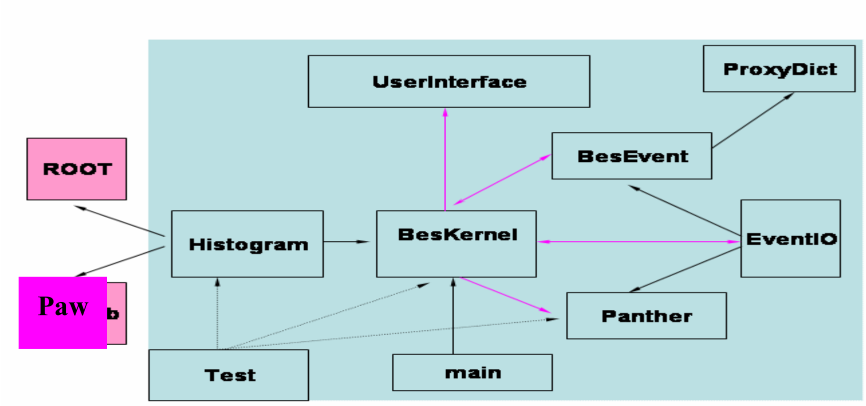

Fig.13.4-1 Software packages and dependencies in the BESF

2. Calibration and Reconstruction

Most of the sub-detectors of the BESIII are different from that of the BESII, therefore the calibration and reconstruction code will mostly be re-written. Whether it is written in C++ or in Fortran, the software system should have a well separated calibration and reconstruction sequence, with a modular structure so that any changes of an intermediate step will not result in modifications of related code in a later stage. If C++ is adopted, some of the objectivity should be compromised, for example, data and operation should be well separated.

The main tasks of the reconstruction include track finding and fitting, cluster finding, shower fitting and reconstruction, scintillation timing reconstruction, muon track finding in muon chambers and particle identification.

Data calibration will be done at various stages, both online and offline. Calibration constants will be stored in a database. It is also foreseen to have several calibration iterations so that data will be processed several times over a year.

3. Monte Carlo Simulation

Most of the event generators of the BESII can be re-used although some modifications may be needed. The simulation of the detector response will be a new package based on the GEANT4 program while a Fortran code based on the GEANT3 program in Fortran will be kept as a backup and for comparison. Detailed simulation of the drift chamber resolution using output of Garfield will be investigated. Light transport in scintillators of the Time-of-Flight system and the time resolution can be well simulated using GEANT4.

The BESIII simulation packages based on Geant4[1], BOOST, consists of three main parts, the event generator, the particle tracking and the detector response. The XML[5] language will be used for the detector description. The “raw” data format is used for the final output of BOOST. Right now, the hit information from most sub-detectors can be used to test or tune the offline reconstruction program.

4. Common Tools and Libraries

Commonly used CERN libraries, both in C++ and in Fortran, will be used extensively. Physics analysis will be based on HBOOK, PAW, PAW++, ROOT, MN_FIT, Fitver and so on.

Some of the BESII libraries in Fortran, such as Telesis for kinematical fitting, events vertex fitting and event-kink fitting can be re-used.

The database of the BESIII contains the detector geometry, calibration constants, detector running status and conditions, environment parameters, etc. Some of the tables in the offline database are kept identical with that of the online database while some other tables will only appear in one of the two databases. The database will be managed by a free software based on SQL language, such as PostgreSQL, MySQL or MiniSQL.

Commercial software packages can also be used, as long as it is well received by the HEP community. For example, the software code will be managed most likely by CVS, RCVS, AFS or DFS and so on.

2.1.1.2 References

[1] http://cern.ch/geant4

[2] http://www.slac.stanford.edu/bfroot/computing/offline/simualtion/web

[3] http://cmsdoc.cern.ch/oscar

http://atlas.web.cern.ch/atlas/groups/software/oo/simulation/geant4

[4] http://www.thep.lu.se/~torbjorn/pythia.html

[5] http://gdml.web.cern.ch/gdml

[6] http://root.cern.ch

[7] Itoh, R., BASF - BELLE AnalysiS Framework, Talk given at Computing in High-energy Physics (CHEP 97), Berlin, Germany, 7-11 Apr 1997

[8] Barrand, G. and others, GAUDI - A software architecture and framework for building HEP data processing applications, Comput. Phys. Commun., 140(2001) 45-55

[9] Shojiro Nagayama, Panther User's guide version 3.0

[10] http://lhcb.web.cern.ch/lhcb/

Mechanical Integration and Service Utilities

Constrains and Requirements

The BESIII detector will be installed in the existing experimental hall to replace the BESII detector. Therefore the BESIII mechanical integration design is constrained by the following conditions:

(1) There are two steel rail pads on the floor of the experimental hall built for moving the whole BES detector in and out from the beam line position. The pads were welded with high density reinforce cast in the concrete. The distance between the two pads from their inside is 3900mm, the width of each pad is 995mm, and the height from the pad surface to the beam line is 3700mm.

(2) The maximum allowed weight for the floor was designed to be 40 tons per square meter.

(3) The capacity of the crane is 50 tons.

(4) The length of the hall along the beam line is 18000 mm. Facing the center of the accelerator, it is 7000m on the left and 11000mm on the right.

(5) The distance from the center of the BES detector to the north wall of the hall is 6000mm.

(6) The width of the main gate is 5500mm and the height 6000mm.

The weight and dimensions of detector pieces and installation tools must match these requirements for transportation into the hall and installation of the BESIII detector.

Requirements for the mechanical integration design are as follows:

(1) To provide all necessary support and adjustments for all sub-detectors so that they can be finally positioned within the tolerance.

(2) To provide convenient access to sub-detectors when maintenance is required, such as access to the drift chamber when wires are broken, this requires the opening of endcap yoke and removing of endcap EMC.

(3) The re-position of any parts of the iron return yoke should guarantee that the change of the magnet field configuration is within the tolerance.

(4) Providing route and space for cables, cooling pipes and gas pipes. The resulted fringe field should be minimized.

Ba

octa

stru

and

and

The

mm.

into

stru

of th

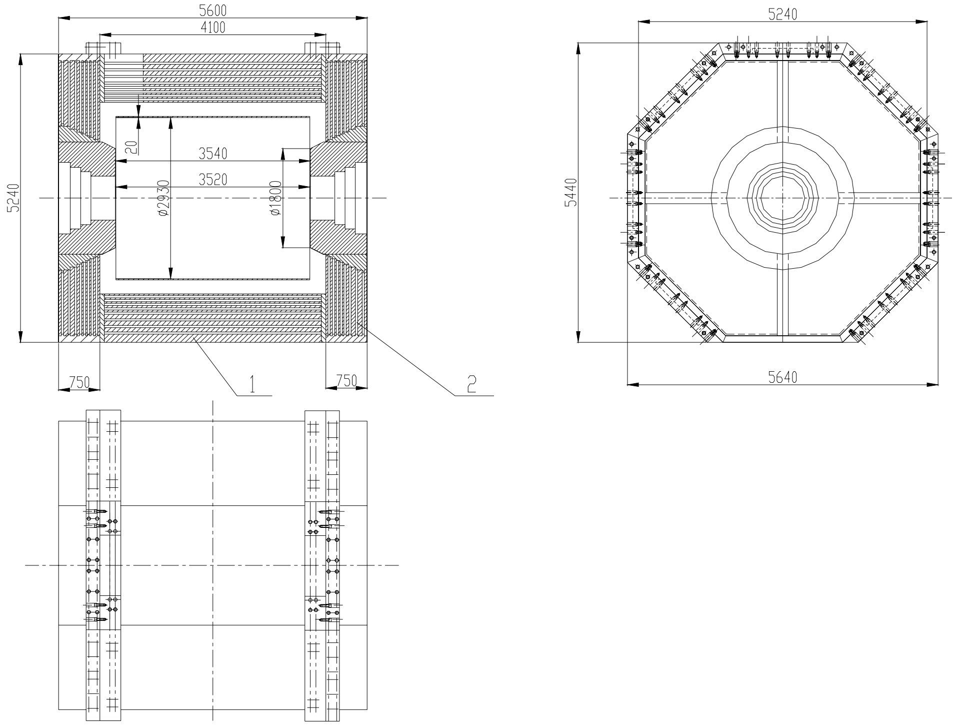

Fig.14.2-1 Over all view of the iron yoke

Due to the large thickness (150mm) and width (2112.49mm) of the outer layers of the octagonal plates, the raw material must have width about 2300mm. But the largest width of the steel plate that can be produced by continuous casting in domestic factories is 1200mm.Therefore each plate of the outer octagonal has to be divided in to four pieces along the axis. Then the continuous casting plate is fabricated into a 1200X2112.49X80mm plate. Four of this kind of plates horizontally put together to form a plate of an octagonal plan.

The barrel structure must have enough rigidity against the magnetic force when the magnet is in operation and must support all sub-detectors of about 50 tons. It is desirable that the structure is assembled instead of welding. Welding in the experimental hall must be avoided since it will cause deformation, leading to errors beyond the tolerance.

The supporting for the solenoid dewar is an adjustable structure with 8 parts, made of 8 triangle spaces between the inner octagonal plate of the barrel yoke and the dewar; All inner sub-detectors will be supported by two stainless steel cylinders with a flange inserted in the dewar.

Compared to several different designs, a structure with stepped plates conjunction was selected. Fig.14.2-2 and Fig.14.2-3 show the structure of stepped plates conjunction with 9 layers forming a unit. The stepped plates have a length of 4100 mm and a width of 85mm. On one side, the surface is cut to the stepped

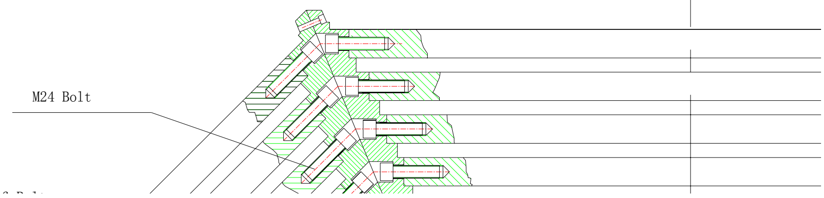

conf
outsi
insid
side
stepj
dew

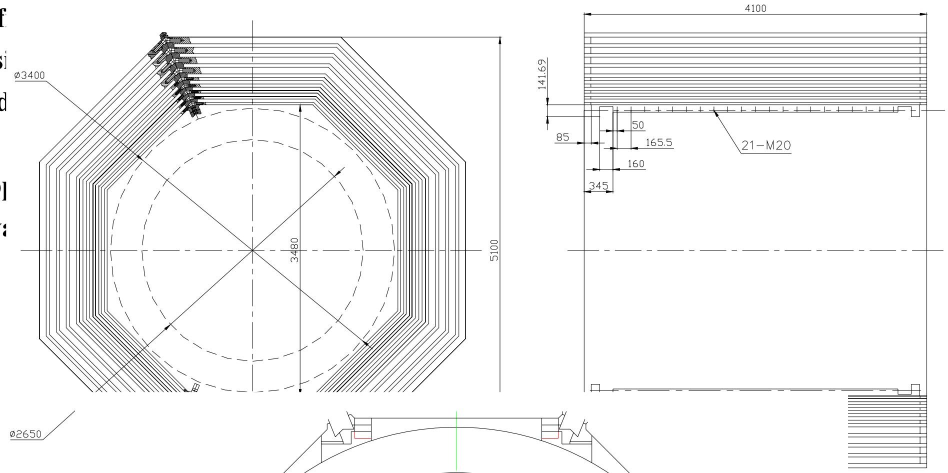

The i ... e pre-
assemblin ... ining
to save ti ... , this
structure ... mm.

1. Su

The l ... tons.
Fig.14.2-4

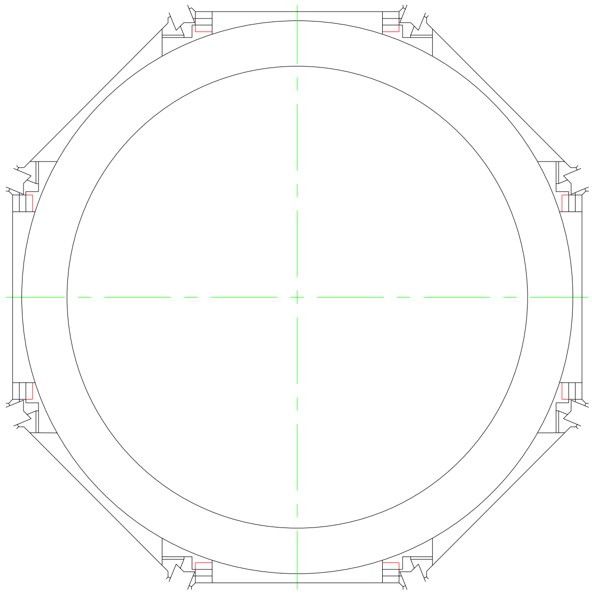

Fig.14.2-4 Dewar support in the barrel iron yoke

These supports are fixed on the 8 corners of the octagonal respectively. Each support are welded two blocks on both side of the step plate for positioning, and at the corresponding position, welded position blocks on both ends of the solenoid dewar. When the solenoid is installed at the designed position, we need to place the key blocks, axial position blocks and radial position blocks, adjust the position of dewar through placing different thickness of the position blocks.

2. Conjunction of the Barrel Iron Yoke with the Cylinder

For extracting the read out cables and utilities from the barrel, it is necessary to make a slot with 1100x 80mm on every terminal surface of the barrel of yoke. It provides the cable channel and in the mean-time leaves every

corner of the octagonal to contact the end yoke for magnetic flux loop to reduce the fringe field.

A cylinders is located on each side of the dewar for supporting sub-detectors. The two cylinders have a good rigidity and will be used for the mapping system before installation.

The support structure of cylinder with flange is shown in Fig.14.2-5. In this

desig
thick
exter
x 80

adde
inne
are f
sand

Su

time
and

2660
total

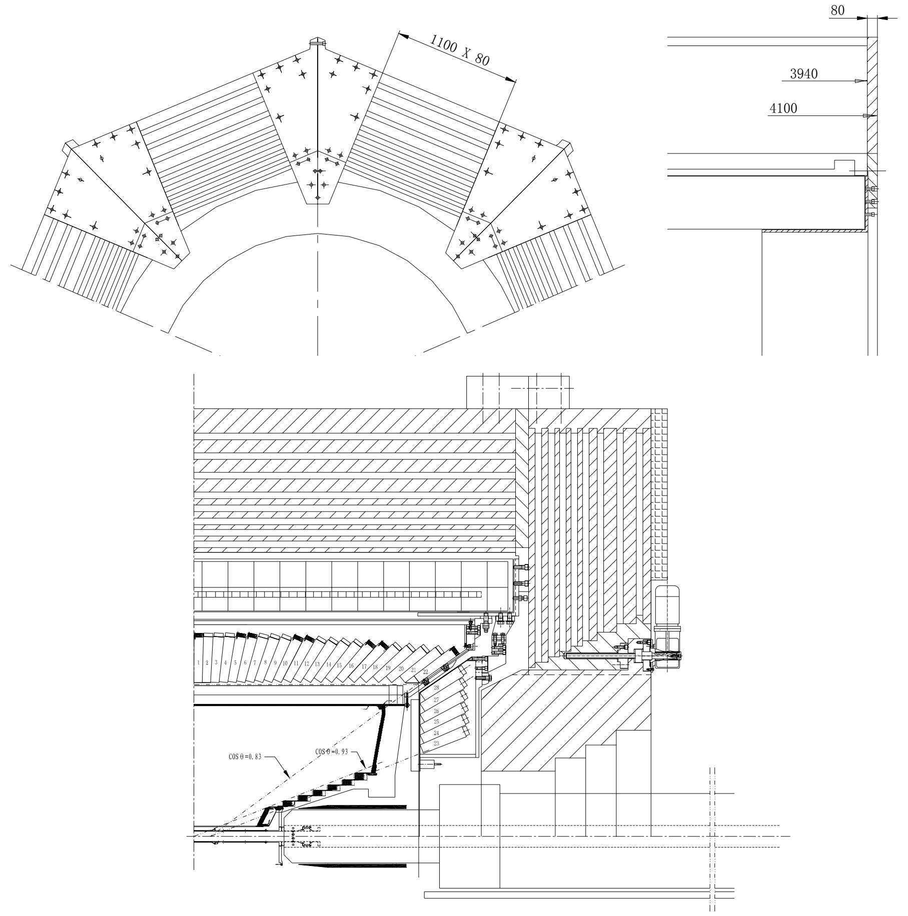

Fig.14.3-1 Support structure of the inner sub detectors

The main idea for the support structure is to reinforce the conical section of the barrel calorimeter to be a rigid body as shown in Fig.14.3-1. The 8 angle pieces are screwed to the conical section of the calorimeter in horizontal and the cylinder in vertical. These screws can be removed for adjustment and final fixing of the calorimeter.

The barrel of time-of-flight-counter will be bounded on the outer cylinder of

the drift chamber by nylon strip. This is the best way to save the radial space.

The outer diameter of the drift chamber is 1620mm, the length is 2400 mm and the total weight is about 1 ton. The extended cylinder sleeves are connected to the bottom of the conical section of the barrel calorimeter by some angle pieces.

This structure of design takes into account the limited space between the time-of-flight-counter and the end cap EMC calorimeter. Another ideal design is being discussed on fixing the drift chamber to a stainless ring attached on the bottom of the conical section if there are enough space.

The end calorimeter has a conical disc shape separated into two parts. The outer diameter of it is from 1000 to 3440 mm and the thickness is 340mm. The end cap time-of-flight-counter with the weight of 1.5 tons is bounded on the front-end of the calorimeter by 8 angle pieces, which are connected with the barrel calorimeter by adjusting screws.

Structure of the End Yoke and Its Opening Mechanism

The end yoke of the BESIII detector with the weight of 52 tons consists of two half parts. The end yoke is designed to move on a rail supported by a base for its heavy weight. As the end yoke is higher and thinner compared with barrel, also looks like a wall, the security should be taken into account. In order to prevent the end yoke form turning over, an oriented cross rail on the top of the barrel yoke and two boom sheaves on the top of each half of the end yoke are designed. Each half of the end yoke will be driven by a system consisting of a motor, a reducer and a screw rod. The power of each motor is 7.5kW. The end yoke moves on the base rail at a speed of 1 meter per minute. Its stroke is 2m. The oriented cross rail on the top of the barrel yoke can also be used as a base for the top platform of the BESIII detector, as shown in Fig. 14.4-1.

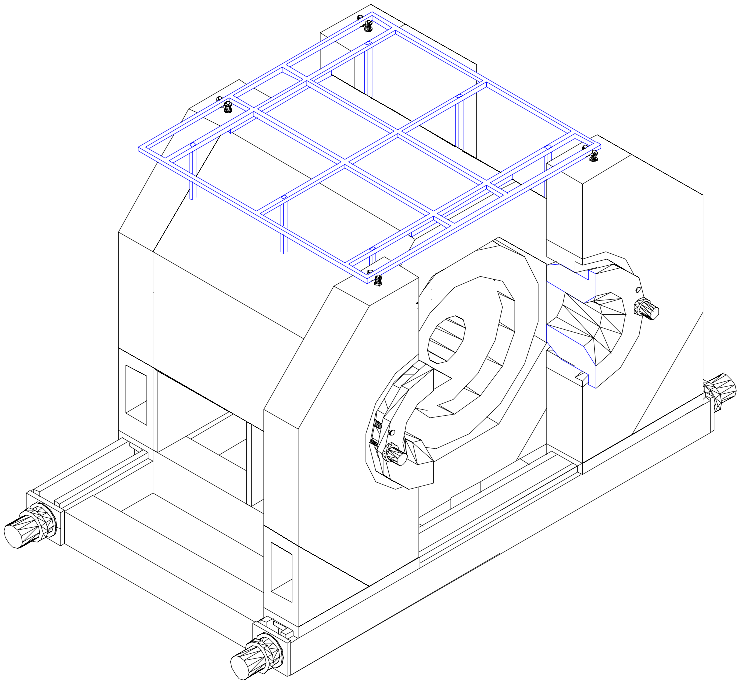

Fig. 14.4-1 The opening and closing structure for the end yoke of BESIII

The pole tip of the end yoke is stored out the interaction point (IP). Enable the moving of the end yoke without interference with barrel yoke the pole tip is designed to be removable along the beam line relative to the whole end yoke. So it can pull the pole tip out along the beam line before opening the end yoke and the entire end yoke just need to move along the x-axis.

As the pole tip of the end yoke is not symmetrical in both x-axis and z-axis, it is difficult to find the center of the gravity. Pilot holes in the pole tips and pilot poles installed in the end yoke make the moving of the pole tip smoothly. Each half of the pole tip will be driven by a system consisting of a motor, reducer and a screw rod. The power of each motor is 3kW. The speed of the pole tip is 1 meter per minute and the stroke is 300mm.

The motor for the end yoke and the pole tip adopts an alternating-current motor with a reducer. The control system selects the digital frequency inverters to guarantee a smooth startup or stop of the end yoke weighting 52 tons. Some approach switches at proper position along the base rail are designed. The butterfly buffer springs are set at both ends of the rail to avoid accident.

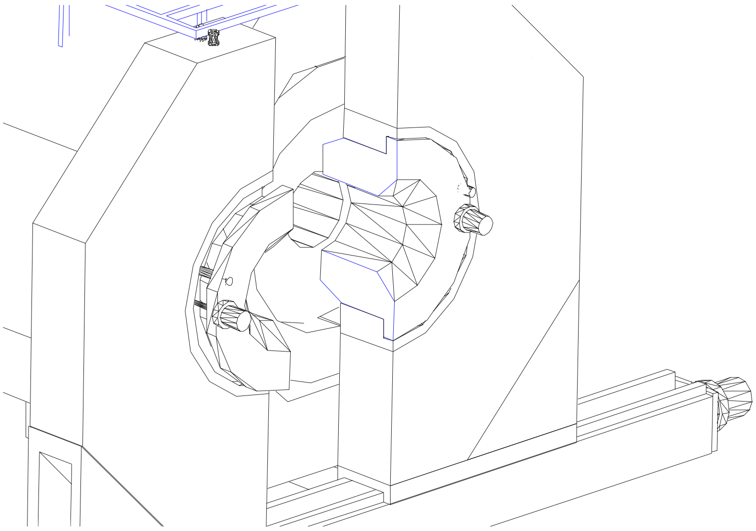

Fig. 14.4-2 The moving structure of the pole tip relative to the end yoke

When the end yoke is to be opened, the first thing to do is to pull the pole tip out along the beam line, then move out the end yoke. The whole process will be automatically finished in 5 minute. Fig.14.4-2 shows one of the moment of this process, in which the right half of the end yoke and the pole tip are in cut-off state, the left half of the end yoke is in opening state and the pole tip has been pulled out to the limited position.

Supporting and Moving System of the Endcap EMC

Maintenance for the drift chamber requires easy opening of the endcap calorimeter, which consists of two half cones. The moving system of the end cap calorimeter must move in three direction, 850mm along z axis, 500mm along x axis and 2200mm along y axis to prevent the calorimeter from colliding with the quadrupole SCQ and the barrel yoke.

There are three options for the moving system of the end calorimeter. The first is a set of three-dimensional sliding tables. The second is a multi-bar cargo boom. The third is a curving guide way.

Fig.14.5-1 shows the operating principle of the sliding tables. It has a long suspension arm. The size of this mechanism is fairly large and the end calorimeter is easy to quiver during the moving because of the too long suspension bar.

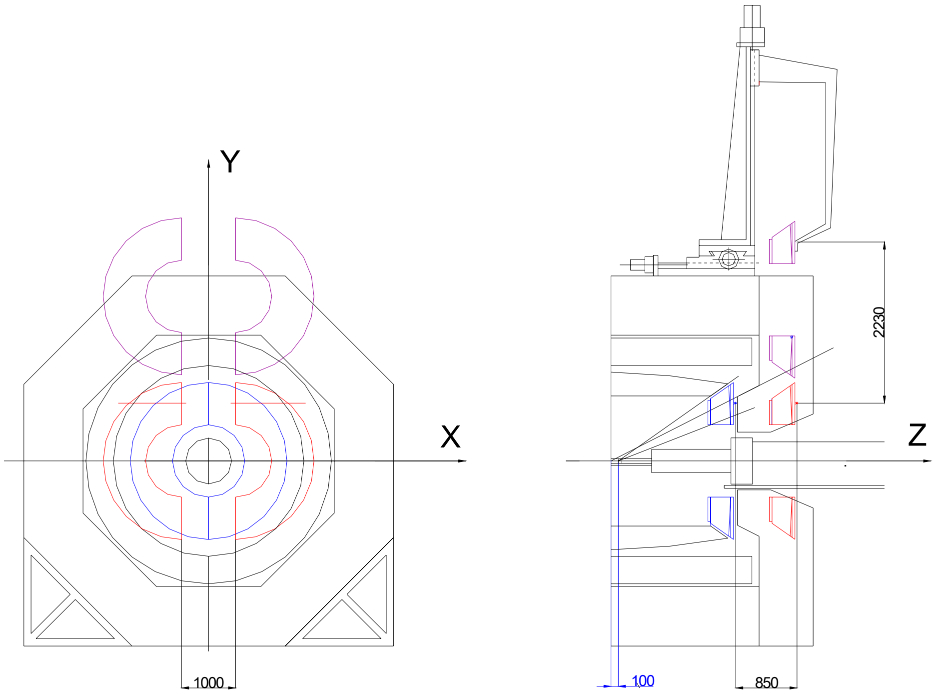

Fig.14.5-1 The moving system(option I) of the endcap calorimeter

The multi-bar mechanism is shown in Fig.14.5-2. In fact, it is a magnifying mechanism and the ratio is 4:1, so the stroke of the vertical slide piece is only 550mm and the horizontal is only 250mm. Compared with the Option 1, the base dimension is smaller and the structure of this mechanism is more compact. A parallelogram mechanism of the lift arm is designed to keep the end calorimeter stationary during the suspending and moving, and the parallelogram mechanism with double rods has the better rigidity and the weight of the suspending system is lighter. However the design for overlapping parts of the mechanism is more complex.

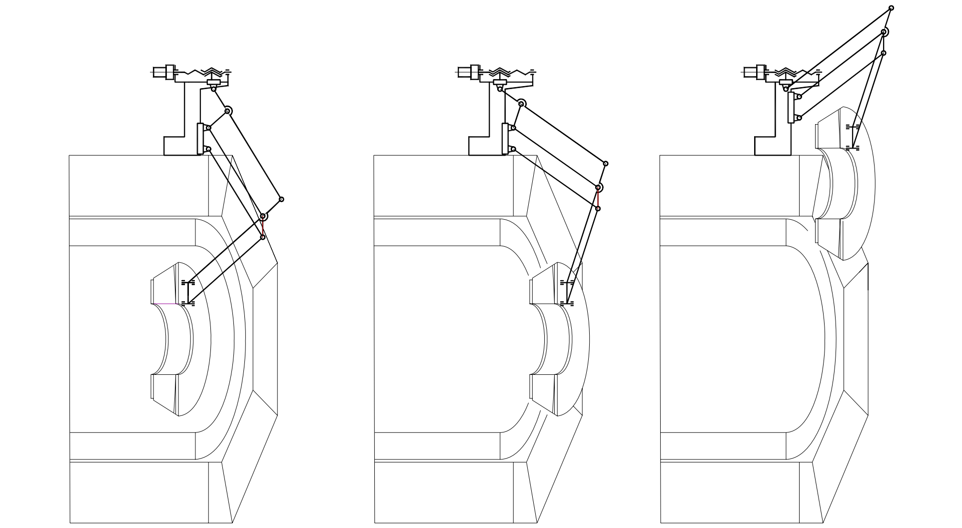

a) Working position

b) Moving off with 25 direction z

c) Moving up along degrees for direction y

Fig. 14.5-2 The moving system (option II) of the end cap of calorimeter

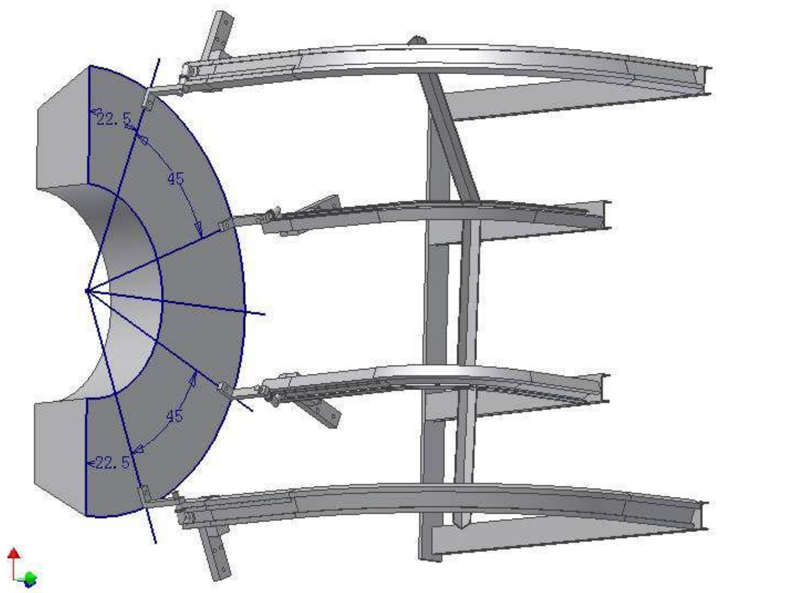

Fig. 14.5-3 The moving system (option III) of the end cap of calorimeter

In the first and the second options, the end calorimeter are suspended on the sky, hence it looks like not very safe during the maintenance of the inner detectors. Moreover the base of the moving systems must be fixed at the top of the yoke, hence it is difficult to be realized since there are other system such as the top guide rail of the end yoke and the chimeny of solenoid on it.

Fig. 14.5-3 shows the third way of the curving guide. It is safe because its base is fixed at the end surface of the barrel yoke and the endcap calorimeter is not necessary to be suspended. During the movement of the calorimeter along the curving guide way a larger space is occupied, so another better option is to use a X-Z double layer guide way moving system, which will ensure a smooth and stable moving.

Base of Magnet Yoke and the Moving of BESIII

The barrel magnet yoke and the endcap magnet yokes with its rails are mounted on a base. The total length for the left and right end yoke is 10.03m. In order to have enough stability and rigidity, the two rails of the end yokes are connected by six crossbeams.

Both rails of the end yokes are set on the base, but they cannot be welded together because of the required precision of the rail. There are accurate surfaces and holes for the bolts on the base to fix the base rail. The base can be moved to the interaction point on the slide pads along the direction x, from the south to the north. The entire detector is driven using a motor and a windlass which exist in the hall. When the entire detector is moved, four Teflon plates are installed below the base for reducing friction. The contour of the base is 10300mm long and 5600mm width.

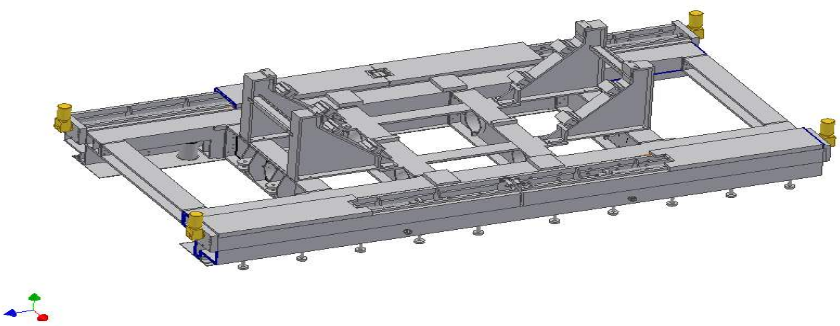

Fig.14.6-1 The connection of the rail of the end yokes

The base and the six cross beams of the rail can be made to an integrated part, as shown in Fig.14.6-1, but the dimension of the door in the hall and the transportation of the detector must be considered.

The horizontal position control of the base is realized by the ready-made slide pads and guide board used for BES-I before. The vertical position adjustment is by lifting the detector through the four hydraulic pressure jacks, and place different adjustable blocks under the bottom of base.

Support System and Assembly of the Detector

Assembly of the Readout Electronics

1. Crates and Racks of Readout Electronic

Eliminato:

All the detector signals will be read out by electronics which has 30K signal channels in total. The number of cables is about 1.50k. There are about 150 crates and 50 racks to be arranged around the BESIII detector and about 20 racks in the counting room.

In order to reduce the noise or crosstalk, it is necessary to build independently the device ground and the safety ground. It is desirable that the two ground nets is far away from the accelerator and the synchroradiation ground net systems.

All of the racks will be arranged as Fig.14.7-1. The total number of the cables and crates are shown in Table 14.7-1.Summarizing the heat power generated by electronics is shown in Table 14.7-2.

2. Cabling, Cooling and Gas Tubes

There are all together 6860 sense wires in Drift Chamber(DC). Since one preamplifier board can handle 8 signal channels, there are about 900 cables for DC in total. The 176 signal cables and 176 high voltage (HV) cables in the barrel TOF will be out from each end of BESIII. The heat generated by the beam pipe, electronics and photomultipliers of the inner detectors must be removed by adequate liquid coolant. All the cables of DC and TOF, cooling and gas tubes will go through the 40mm gaps between the barrel and endcap calorimeters.

The barrel and endcap calorimeter have a total of 6272 signal channels, in which 3136 read-out cables will go out from both ends of the detector. For endcap TOF, 48 signals and 48 HV cables will go through the gaps between the SCQ and the end-cap calorimeter, and then go through the gap behind the end cap to the flute. In addition, all of the temperature monitoring cables, cooling pipes, gas tubes, etc. will go out from the body of the BESIII also. Therefore, all of the cables, pipes, tubes have to go through the flute between the barrel and the end yokes. There are 8 such flutes at each end. The size of each flute is $80\times1100\text{mm}^2$.

Cables coming from gaps will go along the body of the BESIII via cable trays and bridges to the electronics hut.

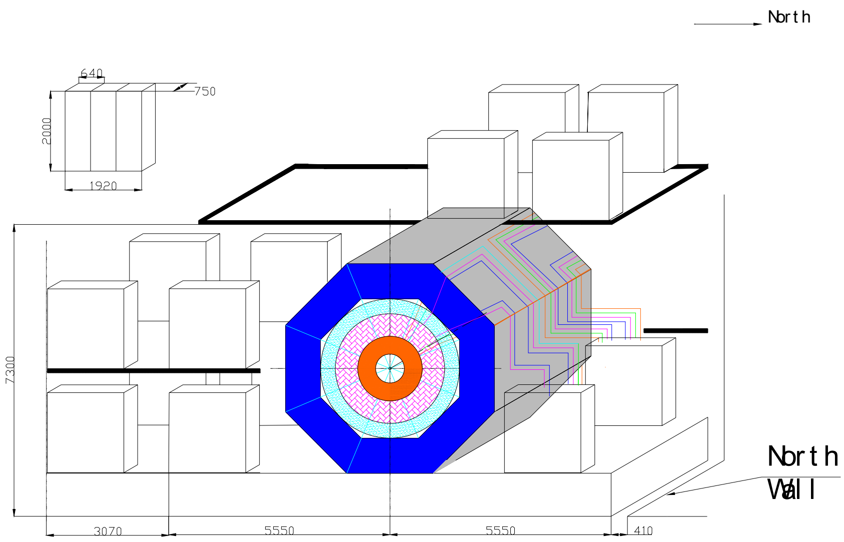

Fig. 14.7-1 Layout of the electronics rack of the BESIII detector

Table 14.7-1 Number of cables, crates and racks

Name	Total Signals	Cable/each end	NIM Crate	VME/6u Crate	VME/9u Crate	HV Supply	Rack
DC	6860	HV-480 Signal-450	12	1	16	1	9
ESC	6272	3136	48	0	18	0	18
TOF	448	HV-224 Signal-224	2	0	8	3	4
μ Chamber	9088	HV-136 Signal-284	2	3	5	2	5
DAQ	/	/	0	0	0	0	20*[1]
Trigger	/	/	1*[1]	2*[1]	3+4*[1]	0	1+3*[1]
LM	12	6+6	4	0	0	0.5	1
Monitor	4	2+2	2	2	0	0.5	1
Online							1
Slow-Control							1
Magnet							1
Total	~29500	6565	70+1*[1]	6+2*[1]	50+4*[1]	8	42+23*[1]

Note： *[1]To be placed in counting room.

*[2] Crates with no special note will be placed in the BES hall.

Table 14.7-2 Heat source of the BESIII detector

Sub Detector	Power/each (w)	Quantity	Power consumption(Kw)	Total(Kw)
DC-VME	1000	17	17X1.4	~24
DC-Preamp.	50mw/channel	6860	0.34	~24.34
EMC-VME	1000	18	18X1.4	~49.54
EMC-NIM	800	48	38.4X1.4	~103.3
EMC-Preamp.	200mw/channel	6272	1.26	~114.56
TOF-Barrel	1/pm	176 X 2	0.352X1.4	~115.05
TOF-End cap	1/pm	48 X 2	0.096X1.4	~115.2
μ Chamber	150mw/channel	9088	1.36	~116.56
μ-VME	1000	8	8X1.4	~127.76
Trigger	1000	3	3X1.4	~131.96
Slow-Control	800	4	3.2X1.4	~136.44
HV Power	850	7	5.95X1.4	~144.77
Beam Pipe	100	1	0.1	~144.87
ISPB	985 Kcal	2	2.3	~147.17
Q1 & Q2	6832 Kcal	2	15.9	~163.07

Cooling Pipes

The environmental temperature of BESIII is required to be controlled to $21^0C \pm 3^0C$ during the operation. In areas such as DC and CsI calorimeter, the temperature is required to be $21^0C \pm 1^0C$, hence all the heat generated by the front electronics of the calorimeter should be removed with adequate liquid coolant. In addition, the low voltage supplies will generate also a large amount of heat, which should be removed with cooling water. All the electronics crates are also cooled with dry air. Fig.14.7-2 shows the arrangement of cables, pipes and tubes around BESIII.

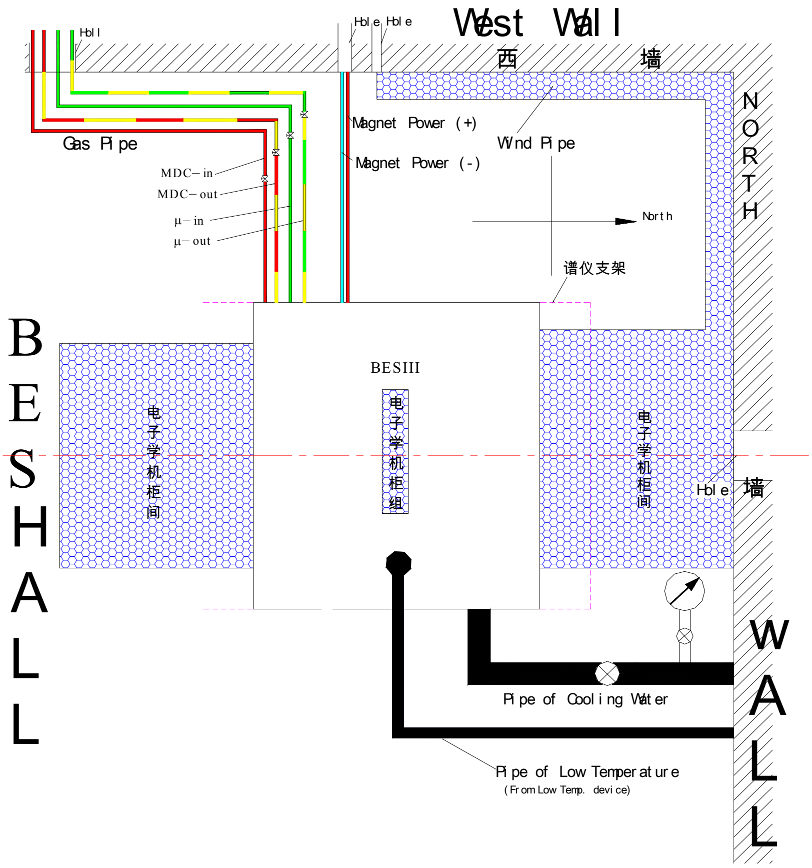

Fig.14.7-2 Layout of various pipes of BESIII

Gas System

There are two gas systems for two type of gasous detectors of the BESIII, The drift chamber (DC) and the μ chamber. The gas system consists of the chamber, the gas supply, the mass flow control system, the electro-polished stainless steel pipes, the pressure regulator, the storage buffer and the supplementary system. The gas supply provides pure gases such as liquid He, Ar, C_3H_8, C_4H_{10} and F134A($C_2H_2F_4$). The mass flow control system is the essential component of the system which controls ratios of various gases.

The gas system of the drift chamber is shown in Fig.14.7-3. The DC holds a gas volume of approximately 5m^3 filled with a gas mixture of 60% He and 40% C3H8. The layout of the gas system for the μ chamber is shown in Fig.14.7-4.

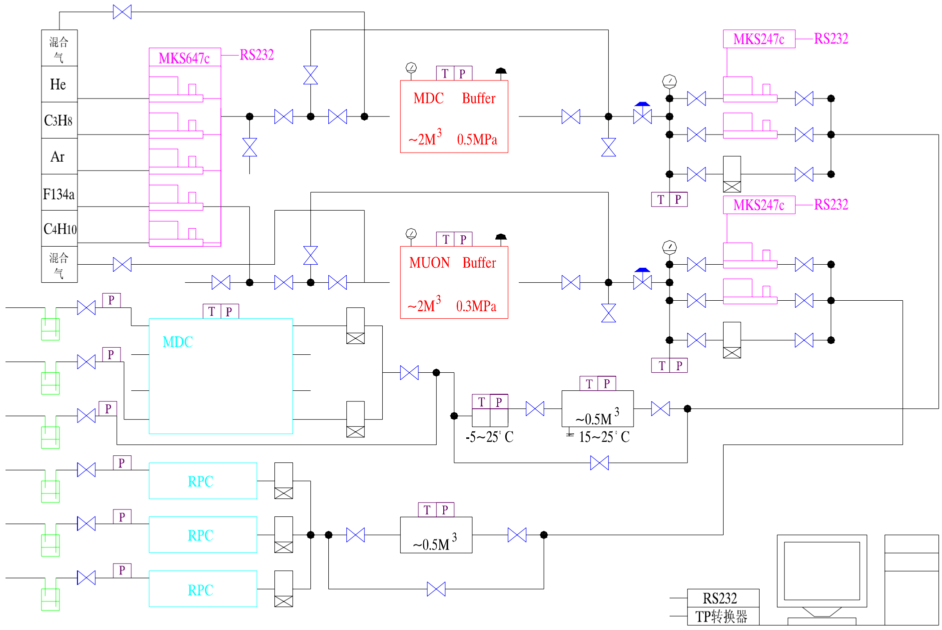

Fig. 14.7-3 Gas system of the drift chamber

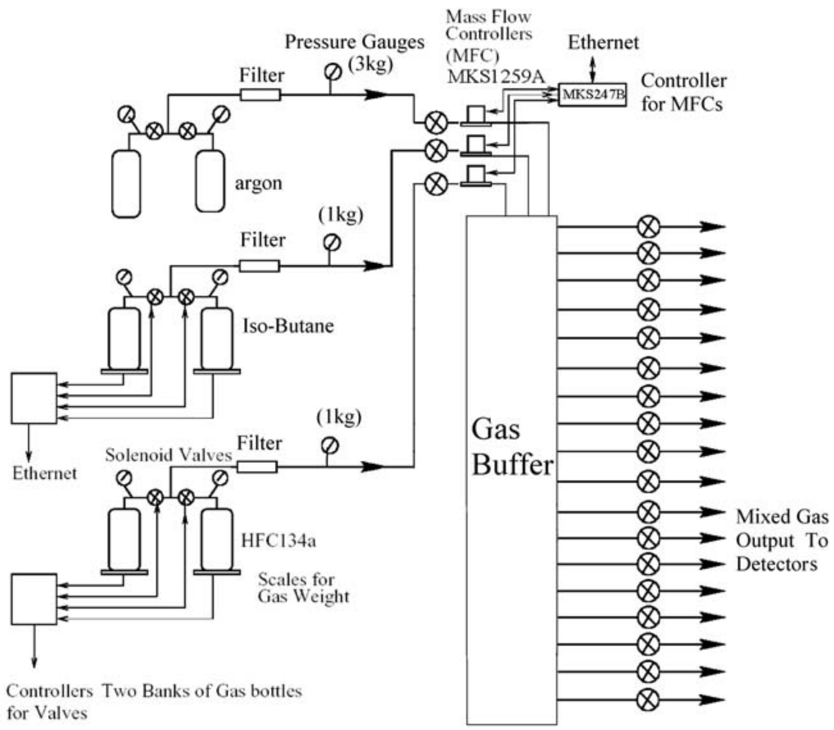

Fig. 14.7-4 Gas system of the μ chamber

The Dose Monitoring System of BESIII

1. The Integral Dose System

Since the performance of the CsI(Tl) crystal calorimeter will be degraded due to the radiation damage, the radiation dose absorbed by CsI(Tl) crystal should be known. Knowing the relation between the integral dose absorbed by crystals, and the energy response a correction can be made for such damage effect.

The monitoring system consists of radiation sensitive FET(RadFET), which is used to measure the integral dose absorbed by crystal. A total of 80 detectors will be installed to monitor the dose distribution in the calorimeter.

Main components of the monitoring system are detector, front end electronics (FEE) and read out system.

RadFET is a special field effect transistor (MOSFET) used for real time measurement of the integral dose with a good linearity.

Fig.14.7-5(a) shows the working principle of the RadFET in positive bias, a constant current for the RadFET, the change of voltage between S and G gives the integral dose. Fig.14.7-5 (b) shows the working principle of the RadFET in zero bias voltage. The depletion thickness in this mode is much less than that in positive bias, hence the sensitivity decrease and the relation between ΔV and the integral dose is not real linear. However this mode has a larger dynamic range, the system is relatively simple (only two cables), and it's also easy to exchange different detectors.

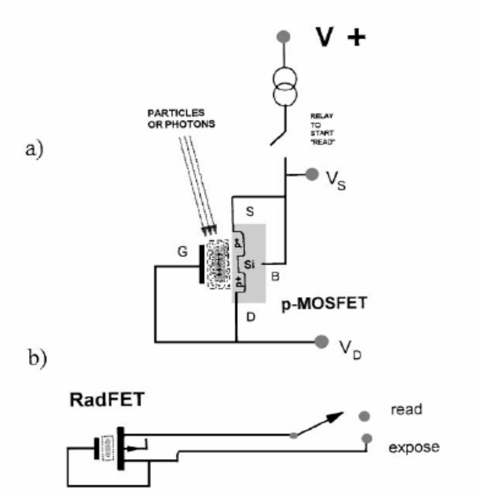

Fig.14.7-5 The work principle of RadFET

The output of each RadFET connects to a cable of 1-3meters long, a total of 32 such cables connect to the electronics board (RMB) which consists of three parts: the constant current source, the A/D converter which can be used for multi-channels and the controller. The system needs 20 seconds to scan all the channels, and it have a very good ability to work in an environment with strong electromagnet interference.

2. The Differential Dose System

The beam pipe of the BEPCII is made of Beryllium(Be) which can be damaged due to very high beam background.

This system use PIN Diode as a detector to measure the dose rate near the beam pipe, and it can also give an alarm signal or a signal to the control room to stop the beam.

In order to protect the electronics from the possible damage due to extremely high radiation dose only the detector and FEE are located near the pipe. The read out system connected to the detector via a long cable is in the electronics hall.

Fig.14.7-6 shows the configuration of the system.

The detector measures the change of dose rate as a function of time .The sensitivity and dynamic range should satisfy experimental requirements and it should have a good energy response, good radiation hardness with the capability of temperature compensation.

There are two readout methods: A/D converter or current integral, both satisfy requirements of the sensitivity, the dark current and the temperature response, as shown in Fig.14.7-7.

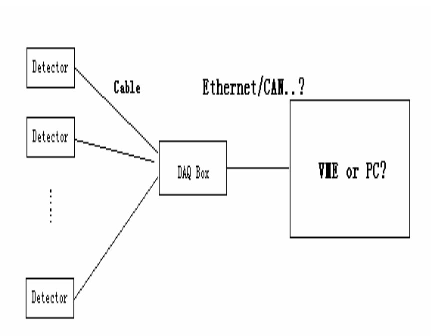

Fig.14.7-6 diagram of system

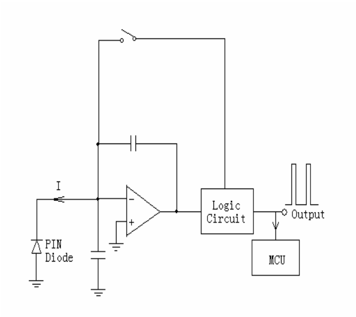

Fig.14.7-7 Diagram of integral current

Slow Control System

1. System Structure

The slow control system consists of independent subsystems that are used to monitor and control individual sub-detectors. It consists of environment monitoring, gas system, high voltage system, and security interlock. Every system has its own host computers for signal detection, data acquisition and automation. Through a 100M Switch, subsystems are connected to the main control computer which is connected to the on-line system through a 100M Switch. Every subsystem works independently from each other and can receive instructions from the main computer for executing monitor and control tasks.

2. Hardware Implementation

Three different buses (USB, one wire bus, CANE) are used in the BESII slow control system and each has its merits respectively. The bus structure diagram of the slow control system is show in Fig.14.7-8. The USB/one wire bus is adopted in special instruments that produce indirectly or directly the signal of voltage and current. The high voltage system uses the CANE bus which are connected to the PCI interface of the computer. The security interlocking of BEPCII and BESIII is achieved with the combination of GI and IMTV by the computer in the BESIII Slow Control system.

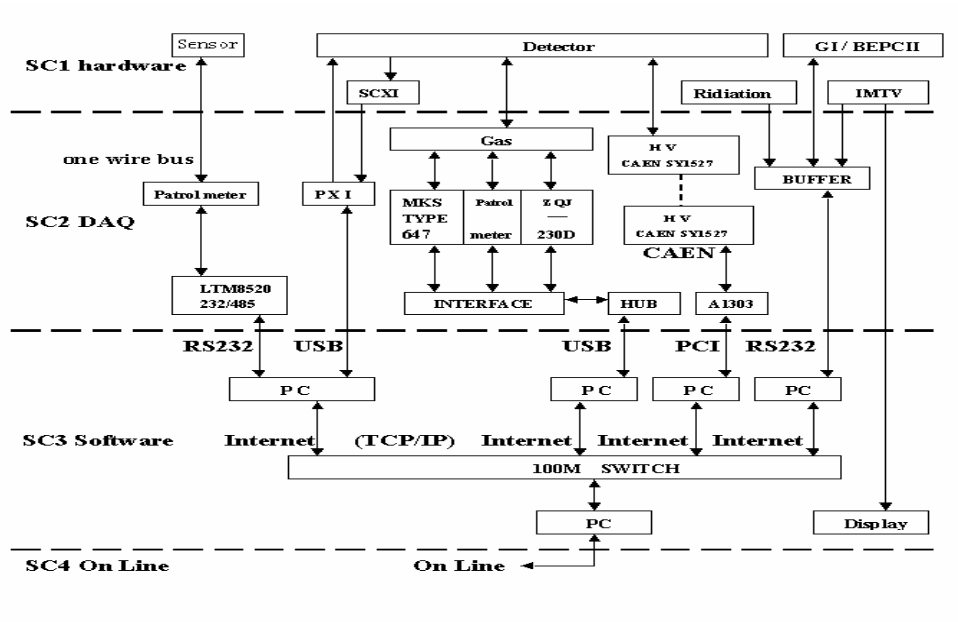

Fig.14.7-8 The bus structure diagram of the slow control system

The one wire bus is used in the condition monitoring system of the slow control with the block diagram shown in Fig.14.7-9.

Important parameters relative to physical data and operation are saved in the operation databases. In term of the detectors' request, it is imperative to realize audio and optical alarms for vital parameters. Utilizing PLC controller, the reliability is assured in the gas controlling system, whose block diagram is shown in Fig.14.7-10.

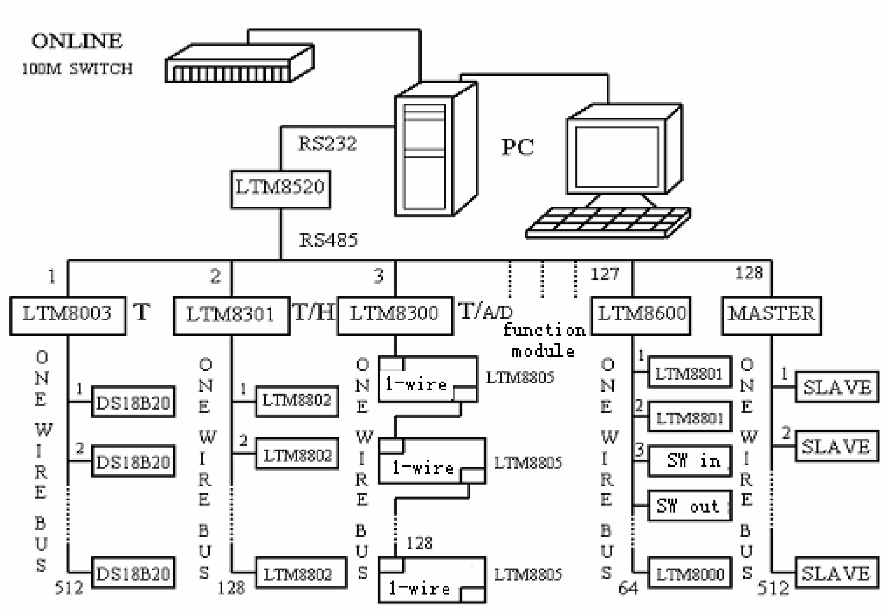

Fig.14.7-9 The block diagram of the condition monitoring subsystem

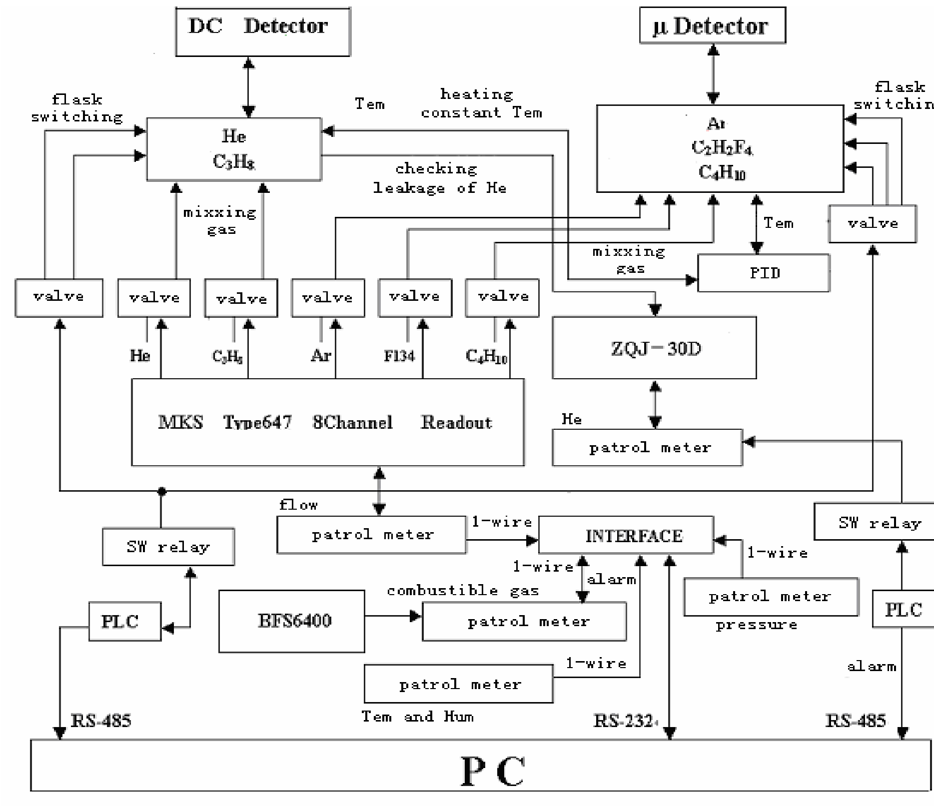

Fig.14.7-10 the block diagram of the gas slow control system

Three sub-detectors, MDC, TOF and μ chamber, have high voltage subsystems in which the power supply module is controlled by a computer via a PCI interface card. The block diagram is shown in Fig.14.7-11.

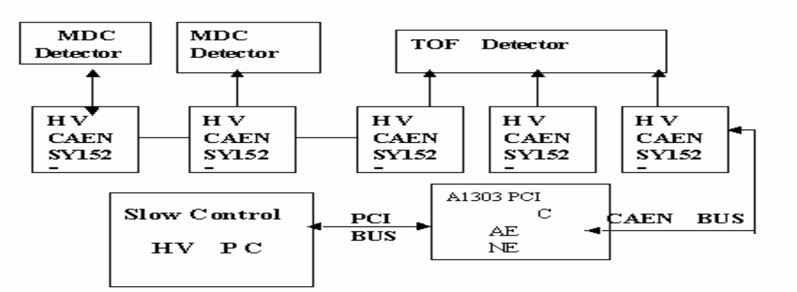

Fig.14.7-11 The block diagram of high voltage system

3. Software Implementation

There are several choices for an unified software, such as Epics, Labview, Fix, etc.

EPICS is a free software, and Fix is an expensive commercial software, but they all need standard hardware, hence expensive devices to support them. Labview is a graphics program designed to support “virtual devices”, which also needs expensive hardware to configure it and only suitable for lab type application.

In order to have a software which can support a variaty of hardware devices at a reasonal price. We choose the GMCC for the BESIII Slow control system.

GMCC has an abundant device drivers and drive development tools. For example, it supports the popular serial port devices, ISA and PCI bus, and dynamic data exchange (DDE) device driver. GMCC can collect and record I/O variables in real time, display real time data in graphics or tables, record history data and display history trend graph.

The slow control software system applies Object Oriented Programming methods hence the detail information of the device is hidden to the user program. Device parameters such as the address, the number of channel, the information of channel and so on, are obtained from the pertinent database. The online database records the state of the detector and environmental parameters, which will be used for online environmental monitoring and trouble shooting. Some of these parameters, useful for the offline analysis, will be transfered to offline database in an antomatic and timely manner. The software structure of the slow control system is shown in Fig.14.7-12.

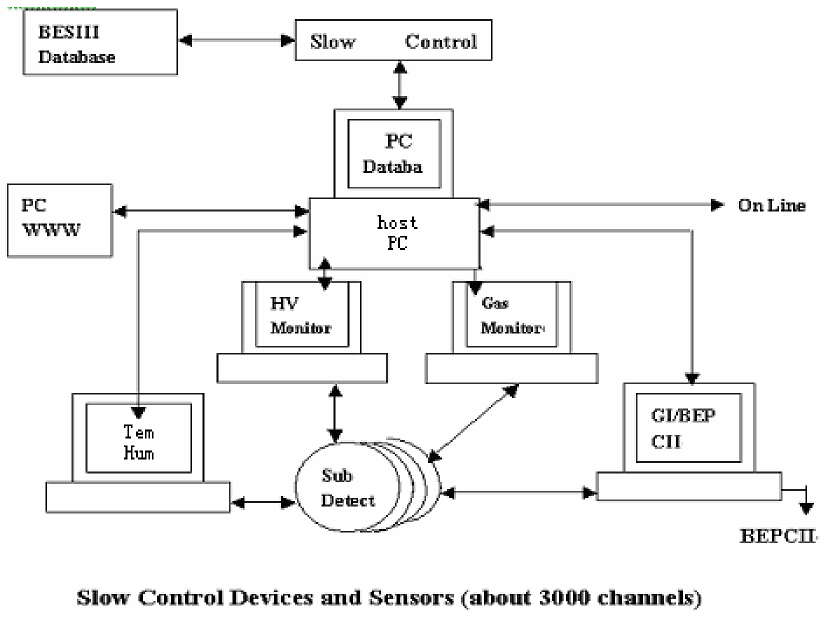

Fig.14.7-12 Software structure of the slow control system